

Development of Novel Gearbox Lubrication Condition Monitoring Sensors in the Context of Wind Turbine Gearboxes

Candidate: Andrew Hamilton

1st Supervisor: Dr. Francis Quail

2nd Supervisor: Prof. David Infield

Wind Energy Centre for Doctoral Training
Department of Electronic and Electrical Engineering
University of Strathclyde
Glasgow G1 1XW

June 2015

Declaration of Authenticity and Author's Rights

This thesis is the result of the author's original research. It has been composed by the author and has not been previously submitted for examination which has led to the award of a degree.

The copyright of this thesis belongs to the author under the terms of the United Kingdom Copyright Acts as qualified by University of Strathclyde Regulation 3.50. Due acknowledgement must always be made of the use of any material contained in, or derived from, this thesis.

Signed:

Date:

Contents

Index of Figures.....	vi
Index of Tables	xi
Abstract.....	xii
Acknowledgements.....	xiii
Funding	xiii
Chapter 1 – Introduction	1
1.1 Background	1
1.2 Condition Monitoring of Wind Turbine Gearboxes	2
1.3 Objectives and Methodology.....	3
1.4 Novel Contributions	4
1.5 Thesis Structure	5
1.6 Publications Related to Thesis Research.....	6
Chapter 2 – Wind Energy and the Gearbox.....	7
2.1 EU Renewable Energy Roadmap	7
2.2 UK White Paper on Energy 2007	7
2.3 Wind Energy.....	9
2.4 Modern Wind Turbine Design	10
2.5 Drivetrain.....	12
2.5.1 Gearbox	13
2.5.2 Gears	14
2.5.3 Bearings.....	17
2.5.4 Lubrication System	18
2.5.5 Torque Loading.....	18
2.5.6 Reliability.....	19
2.6 Conclusions	21
Chapter 3 – Gearbox Failure Mechanisms.....	22
3.1 Non-Lubricant-Related Failures	23
3.2 Lubricant-Related Failures	24
3.2.1 Hertzian Fatigue	24
3.2.2 Wear Fatigue	26
3.3 Particle Number.....	30
3.4 Conclusions	31
Chapter 4 – Gearbox Lubrication	32
4.1 Lubricant Properties	32
4.1.1 Mineral Lubricants	33
4.1.2 Synthetic Lubricants.....	34
4.1.3 Viscosity.....	35
4.1.4 Hydrodynamic Lubrication	37
4.1.5 Additives	38
4.2 Lubricant Degradation.....	42
4.2.1 Acidity.....	43

4.2.2	Water Content	43
4.2.3	Oxidation.....	44
4.2.4	Temperature	45
4.3	Application Methods	45
4.3.1	Splash Lubrication	45
4.3.2	Pressure-Fed Lubrication	46
4.4	Conclusions	47
Chapter 5 – Gearbox Lubrication Condition Monitoring		48
5.1	SCADA and Vibration Analysis	49
5.2	Offline, Online and Inline Sensing.....	51
5.3	Currently Deployed Lubrication Monitoring Sensors.....	52
5.3.1	Light Source Particle Counters	52
5.3.2	Electromagnetic Particle Counters.....	55
5.3.3	Temperature Sensors.....	57
5.3.4	Dielectric Loss Factor Lubrication Sensors	58
5.4	Applicable Lubrication Analysis Techniques	59
5.4.1	Ferrography.....	59
5.4.2	Infra-Red Spectroscopy.....	60
5.5	Conclusions	62
Chapter 6 – Development of Lubrication Wear Sensor		63
6.1	Test Rig Layout	64
6.2	Test Rig Components	66
6.2.1	Rig Pipework.....	66
6.2.2	Mono CMM263 Progressive Cavity Pump.....	67
6.2.3	Lubricant Reservoir and Heater Elements	68
6.2.4	Measurement Sensors.....	69
6.2.5	Particle Delivery Valves	70
6.2.6	Inline Filters	71
6.2.7	Data Acquisition and Rig Control.....	72
6.2.8	Test Lubricant	73
6.3	Active Pixel Sensors.....	74
6.4	Active Pixel Sensor Device Selection	76
6.5	Sensor Assembly Design and Construction	79
6.6	Light Source	82
6.7	Digital Image Processing.....	83
6.7.1	Object Detection and Recognition	84
6.7.2	Greyscale Conversion	85
6.7.3	Histogram Processing	87
6.7.4	Binary Conversion	89
6.7.5	Edge Detection.....	90
6.7.6	Morphological Image Processing.....	94
6.8	Development of Image Capture and Analysis Software	97
6.8.1	Sensor Calibration and Adjustments.....	97
6.8.2	Main MATLAB Program Image Capture Subroutine	98
6.8.3	Initial Image Processing Subroutine and Object Detection	100
6.8.4	Object Analysis Subroutine.....	102

6.8.5	Data Export Subroutine.....	105
6.8.6	User Interface	106
6.9	Testing Methodology	107
6.9.1	Lowest Particle Size Testing.....	107
6.9.2	Particle Morphology Detection.....	109
6.9.3	Flow Rate Limits.....	110
6.9.4	Lower Light Level.....	110
6.10	Conclusions	111
Chapter 7 – Development of Lubrication Quality Sensor		112
7.1	Gearbox Lubrication for Experiments.....	112
7.2	FTIR Analysis of XMP 320	113
7.2.1	Experimental Samples.....	114
7.2.2	Sample Preparation	114
7.2.3	Comparison XMP 320 Experiments	116
7.3	Sensor Design.....	118
7.3.1	Sensor Layout	118
7.3.2	Selection of Light Source.....	119
7.3.3	Selection of Photodetector	123
7.3.4	Circuit Design	124
7.3.5	Circuit Mounting on Pipe.....	128
7.4	Testing Methodology	130
Chapter 8 – Experimental Results.....		132
8.1	Wear Particle Sensor Experimental Results	132
8.1.1	Particle Size Testing.....	132
8.1.2	Misidentification of Particles	139
8.1.3	Effect of Mixed Samples on Detection Levels	140
8.1.4	Closing and Opening.....	141
8.1.5	Improvements for Particle Detection	144
8.1.6	Particle Morphology Detection.....	146
8.1.7	Flow Rate Limits.....	151
8.1.8	Lower Light Level.....	152
8.2	Lubricant Quality Sensor Experimental Results	155
Chapter 9 – Conclusions and Future Work.....		158
References		I
Appendix A: Applicable Lubrication Analysis Techniques.....		i
A.1	Photoacoustic Spectroscopy	ii
A.2	Fluorescence Spectroscopy.....	iii
A.3	Karl Fischer Water Test.....	vii
A.4	Viscometers	ix
A.4.1	Capillary Tube Viscometers	ix
A.4.2	Rotary Viscometers.....	ix
A.4.3	Solid State Viscometers	x
A.5	Scanning Electron Microscope.....	xii
A.6	Atomic Spectroscopy.....	xv
A.6.1	Inductively Coupled Plasma Mass Spectroscopy (ICP MS)	xv

A.6.2 Flame Atomic Absorption Spectroscopy (FAAS)	xv
A.6.3 Optical Emission Spectroscopy (OES)	xvi
A.6.4 Laser-Induced Breakdown Spectroscopy (LIBS)	xvi
A.7 Summary of Technologies Reviews	xvii
Appendix B: MATLAB Code for Wear Sensor	xix
B.1 Main MATLAB Program Image Capture Routine	xx
B.2 Initial Image Processing Subroutine and Object Detection	xxi
B.3 Object Analysis Subroutine	xxii
Appendix C: IR Absorbance Spectra and Additional Information	xxiii
C.1 Enlarged IR Spectra of XMP	xxiv
C.2 XMP320 Individual Spectra	xxv

Index of Figures

Figure 2.1. Comparison of UK energy generation in TWh by source from 2006-2014.....	8
Figure 2.2. Wind speed variation over 7 hours for an onshore turbine.....	10
Figure 2.3. Siemens 3MW 3 bladed HAWT wind turbine.	11
Figure 2.4. Basic layout of wind turbine drive train.	12
Figure 2.5. Two parallel gears with centred shafts.	14
Figure 2.6. Interaction of gear teeth to transfer motion and power with pitch line indicated.	15
Figure 2.7. Two helical gears with intermeshing teeth.	15
Figure 2.8. Epicyclic gear with 4 planet gears (blue), central sun gear (yellow) and annular gear (red). Planet gears drive rotation of carrier (green).....	16
Figure 2.9. 2 stage epicyclic gearbox with 3rd stage parallel gears.....	16
Figure 2.10. Deep groove ball bearing with exposed inner race.....	17
Figure 2.11. Input torque loading into gearbox through main shaft during application of mechanical brake.	19
Figure 2.12. Failure frequency and downtime for wind turbine components per turbine.	20
Figure 4.1. Cracked tooth completely detached from gear.	23
Figure 4.2. Development of pitting due to direct contact between two surfaces.	24
Figure 4.3. Helical gear teeth with severe pitting and spall formation.	25
Figure 4.4. Spherical wear particles 40 μm diameter.	26
Figure 4.5. Progression of wear fatigue of a bearing and race.....	27
Figure 4.6. Abrasive wear particle with small holes from successive compressive loading.....	28
Figure 4.7. Adhesion of wear surface due to surface roughness and thin film.	28
Figure 4.8. Scuffing wear particle with major axial dimension of 150 μm	29
Figure 4.9. Scoring wear in which particles are formed.	29
Figure 4.10. Cutting wear particle 500 μm in length.	30
Figure 4.11. 1.5 MW onshore wind turbine gearbox cumulative particle count	30
Figure 5.1. Thin layer of lubricant in one dimensional flow.	35
Figure 5.2. General effect of temperature on the viscosity of lubricants. Different grades of lubricant (ISO 320, 150 and 68) have different VI profiles.	36
Figure 5.3. Chemical structure of 2,6 ditert-butyl-4-methyl phenol (benzene inner structure).	39

Figure 5.4. Effect of viscosity modifiers on viscosity index.	39
Figure 5.5. Chemical structure of zinc-dialkyldithiophosphate with ‘R’ representing general alkyl groups that may be utilised.....	40
Figure 5.6. Chemical structure of a spiro-bicyclodiphosphite with ‘R’ representing general alkyl groups that are selected depending on the base lubricant structure.	41
Figure 5.7. Diethanolamine salt of carboxylic acid is a common friction modifier.	42
Figure 5.8. Polyisobutylene molecule can be used alone or in conjunction with succinimides.....	42
Figure 5.9. From <i>left to right</i> : hydroxyl, carbonyl and carboxylic acid.....	43
Figure 5.10. Hydrolysis reaction of an ester (‘R’ represents a general molecule) [79].	44
Figure 5.11. Oxidation of a hydroxyl group.	45
Figure 5.12. Meshing gears with splash lubrication provided by reservoir at base. ...	46
Figure 5.13. Pressure-fed lubrication system with main components labelled.....	47
Figure 6.1. Conceptual wind turbine communication model based on IEC 61400-25 series.....	49
Figure 6.2. Inline, online and offline sampling of lubrication.	51
Figure 6.3. Operation of particle counter based on laser light extinction [94]	53
Figure 6.4. Equivalent diameter of a 2D object with area A.....	54
Figure 6.5. Effect on particle orientation based on a circular particle analysed using light extinction at different angles.....	54
Figure 6.6. Particle counter using a flow spur to reduce flow cross-sectional area..	54
Figure 6.7. Change in coil inductance is used to detect particles.	55
Figure 6.8. Magnetic flux detection (<i>left</i>) and collection (<i>right</i>) sensors measuring flux (Φ).....	56
Figure 6.9. Trends of gearbox oil temperature rise vs. square of rotor velocity []. ..	57
Figure 6.10. Increasing conductivity increases $\tan \delta$ of lubricant.	58
Figure 6.11. Operation of a ferrogram with particles deposited along plate according to mass.....	59
Figure 6.12. First 3 vibrational modes for a simple molecule.	60
Figure 6.13. Amount of IR radiation absorbed for each particular component of a sample.	61
Figure 7.1. Schematic of physics simulation rig used for testing sensors.....	64
Figure 7.2. Photograph of simulation rig.	65
Figure 7.3. Rig with 300 mm copper pipe sections visible.....	66
Figure 7.4. Mono CMM263 Progressive Cavity Pump.	67

Figure 7.5. Reservoir with 6l of XMP320 lubricant contained inside.	68
Figure 7.6. Flowmeter, thermocouples and pressure sensors located on the rig.....	69
Figure 7.7. Two isolation valves to allow wear particle regimes to be introduced...	70
Figure 7.8. 10 mm filter is last component before lubricant re-enters reservoir.....	71
Figure 7.9. CRIO-9022 Real-Time PowerPC Controller.....	72
Figure 7.10. Charge transfer operation of a CCD chip. Losses can occur when electrons are not transferred fully, resulting in pixel degradation.	74
Figure 7.11. A standard 3T APS cell layout.	75
Figure 7.12. Readout procedure for an array of APS sensors.....	76
Figure 7.13. APS Array visible in centre of exposed webcam device.....	78
Figure 7.14. 100 and 500 μ m circular printed on dot captured with webcam at 10 mm distance.....	78
Figure 7.15. Proposed layout of sensor assembly.....	79
Figure 7.16. Rig with 300 mm copper pipe sections visible.....	79
Figure 7.17. Cross section of acrylic and copper pipe section join.....	80
Figure 7.18. Plastic mount for webcam to allow flat connection with acrylic piping.	81
Figure 7.19. Acrylic piping with taped and exposed sections visible.....	81
Figure 7.20. Light source position below APS sensor (N.B. box shield is placed over assembly to reduce incident of ambient light).	82
Figure 7.21. Example of image processing where an image of the University of Strathclyde is converted to a binary image.	83
Figure 7.22. Difference between object detection and object recognition.....	84
Figure 7.23. Example of greyscale conversion.	86
Figure 7.24. Example of histogram based on number of probability of pixels belonging to certain grey levels.	87
Figure 7.25. Difference in greyscale histograms for images with and without particles.	88
Figure 7.26. Example showing the uncertainty in estimating object size using greyscale (left) compared with binary (right).	89
Figure 7.27. Left - Ideal digital edge with sharp change in grey level profile. Right - Ramped digital image with a ramped change in grey level profile.....	91
Figure 7.28. Left – Image of multiple particles in lubricant. Right(L) – Magnitude of gradient between pixels. Right(R) – Direction of gradient using Prewitt method.	91
Figure 7.29. Median filtering of a 3x3 pixel array where the individual pixel values are sorted and the median is found.....	92

Figure 7.30. <i>Left</i> – X-direction operator (columns), <i>Right</i> – Y-direction operator (rows).	92
Figure 7.31. G_x (in red) is applied to matrix A , values are calculated by multiplying each value of G_x to corresponding A value, each product is summed into $O_x(1,1)$. ..	93
Figure 7.32. The process of object dilation. Note the structuring element has its origin at centre of blue cross.	94
Figure 7.33. The process of object erosion. Note that it is not the exact inverse of dilation.	95
Figure 7.34. <i>Above</i> – Opening operation on left image. <i>Below</i> – Closing operation on left image.....	96
Figure 7.35. Total FOV for webcam and AOI used in image acquisition.	98
Figure 7.36. 465KB sample image showing the 6x6 mm area of interest and several particles.	99
Figure 7.37. 2x 750 μm particles. <i>Left</i> – Image from APS, <i>Right</i> – Conversion of image using Otsu’s method into bi-modal.	100
Figure 7.38. <i>Left</i> - 4 connectivity, <i>Right</i> – 8 connectivity for centre pixel.	101
Figure 7.39. Initial ‘disk’ structuring element with radius of 5 pixels (diameter of 9).	101
Figure 7.40. Example images of regular objects used to test shape parameters.	102
Figure 7.41. Object shape parameters for square and rectangular test objects.	104
Figure 7.42. Object shape parameters for circular and ellipsoidal test objects.....	104
Figure 7.43. User interface showing current image, bi-modal conversion and particles classed as discrete objects by the morphology subroutine.	106
Figure 7.44. Basalt spherical particles used for size testing and other experiments.	107
Figure 7.45. Basalt spheres particles suspended in oil under microscope inspection. <i>Left</i> – 476 μm , 490 μm and 498 μm particles. <i>Centre</i> – 483 μm particle. <i>Right</i> – clustered particles ranging from 127 – 145 μm	109
Figure 7.46. Sample of wear particles used for testing morphology.	109
Figure 8.1: <i>Left</i> - New sample, <i>Middle</i> - Used test rig sample, <i>Right</i> - Used gearbox sample.	112
Figure 8.2. IR absorbance spectrum of XMP 320 lubricant using FTIR analysis. .	113
Figure 8.3. IR spectra of new XMP 320 lubricant samples.	115
Figure 8.4. IR Spectra for 3 samples of unused XMP320 from a new container. ..	116
Figure 8.5. Comparison of XMP 320 Spectra from each group of lubricants.	117
Figure 8.6. Layout of pipe and desired location of main components.....	118
Figure 8.7. Beam divergence across lubricant and glass.	119
Figure 8.8. Transmittance spectrum for BK7 glass.	121

Figure 8.9. Sample transmittance spectrum for XMP320 test lubricant	121
Figure 8.10. Responsivity/wavenumber relationship of a photodetector OSD15-5T.	123
Figure 8.11. Driver circuit for laser diode using TinyCAD® open source software.	125
Figure 8.12. Increasing depletion zone due to reverse bias of voltage.	126
Figure 8.13. CA3140 op-amp with pin connections indicated [].....	128
Figure 8.14. Reverse bias photodetector driver circuit using TinyCAD® open source software.....	128
Figure 8.15. Circuit mounted on copper pipe.	129
Figure 8.16. Sealed end of pipe to allow samples to be held while IR sensor transmits voltage signal.....	130
Figure 8.17. Photodetector output connected to ADC1 of Arduino microcontroller.	131
Figure 8.18. Arduino program used to view and log voltage signal.	131
Figure 9.1. Focal length, f , field of view, FOV , and camera offset length, L_{os}	132
Figure 9.2. Summary of 50 mg samples of geometric mean 136.9 μm	133
Figure 9.3. Sample of images from Test #1 of 125 - 150 μm particles to determine detection rate.	134
Figure 9.4. Summary of particles detected for 50mg samples of geometric mean 487.3 μm	135
Figure 9.5. Single 475 - 500 μm particle in original, binary and unique identifier.	136
Figure 9.6. Assumed particle distribution in ISO 21501-3:2007.....	137
Figure 9.7. Misidentification of lubricant as an object.	139
Figure 9.8. Large 500 μm particles disrupt ability for detection subroutine to discern smaller particles.	140
Figure 9.9. 125-150 μm particles in clusters. Image was passed into closing/opening operations to improve number of discrete particles.	141
Figure 9.10. Conversion of image with clustered particles using closing and opening with circle structuring element.....	142
Figure 9.11. Opening operation of captured wear particle image.....	143
Figure 9.12. Image with no particles present with application of Otsu's finding difference in greyscale and applies boundary conditions.	144
Figure 9.13. Total particles detected for different size ranges for mixed particle samples.....	146
Figure 9.14. Summary of morphology detection for frame #32 during of Test 1... ..	147
Figure 9.15. Objects 1 and 3 with non-standard morphological features.	148

Figure 9.16. Summary of morphology detection for frame #108 during of Test 2.	149
Figure 9.17. <i>Left</i> - Object with low solidity. <i>Right</i> - Object with high solidity. Green indicates convex area. Outer red line indicates bounding box.	150
Figure 9.18. Average number of particles captured for flow rates of 12 and 24ml s ⁻¹ .	151
Figure 9.19. Comparison of linear trend lines for low and normal light level conditions.	153
Figure 9.20. Above - normal light level conditions. Below - reduced light level conditions.	153
Figure 9.21. Despite low light levels, small 125µm particles could be distinguished from lubricant.	154
Figure 9.22. Returned voltages signals from microcontroller for all 3 fluid types.	155

Index of Tables

Table 4.1. Difference between major mineral oil groups.	33
Table 4.2. Basic process to create synthetic oil and polyalphaolefin.	34
Table 5.1. Categories for non-ferrous and ferrous particles.	60
Table 6.1. MobilGear XMP Series Lubricant Characteristics .	73
Table 6.2. Summary table of webcam characteristics.	77
Table 6.3. Sample of data shown in Excel worksheet.	105
Table 6.4. Individual Particle Mass for Diameter Limits.	108
Table 6.5. Total number of particles for 50mg samples.	108
Table 6.6. Summary of flow rate test regimes	110
Table 7.1. Summary of laser diode characteristics used in selection process.	122
Table 7.2. Resultant beam profiles for at length l = 19mm.	123
Table 7.3. Main OSD photodiode characteristics used in selection process.	124
Table 8.1. Summary of structuring elements applied and various differences in parameters.	142

Abstract

Wind power has become established as an alternative power source that forms a significant proportion of national energy generation. An increasing proportion of turbines is being constructed offshore to exploit higher average wind speeds and to avoid development issues associated with onshore wind farms. Isolated locations and unpredictable weather conditions lead to increased access costs for operators when conducting scheduled and unscheduled maintenance and repairs. This has increased interest in condition monitoring systems which can track the current state of components within a wind turbine and provide operators with predicted future trends. Asset management can be improved through condition based maintenance regimes and preventative repairs. Development of novel condition monitoring systems that can accurately predict incipient damage can optimise operational performance and reduce the overall level of wind turbine generation costs.

The work described in this thesis presents the development of novel sensors that may be applied to monitor wind turbine gearboxes, a component that experiences relatively high failure rates and causes considerable turbine downtime. Current systems and technology that may be adapted for use in wind turbine condition monitoring are evaluated. Lubrication related monitoring systems have been identified as an area that could be improved and are divided into those that track liberated wear material suspended in the lubricant and those that assess the state of the lubricant itself.

This study presents two novel lubrication based gearbox monitoring sensors that potentially offer a low cost solution for continuous data capture. The first demonstrates the potential for active pixel sensors such as those found in digital cameras to capture images of wear particles within gearbox lubricants. Particle morphology was tracked in this system, allowing the type of particles to be correlated with the type of wear that is generated and a potential source. The second sensor uses a targeted form of infra-red absorption spectroscopy to track changes in the lubricant chemistry due to the increase in acidity. Ensuring the lubricant is functioning correctly decreases component stress and fatigue, reducing maintenance requirements.

Acknowledgements

I would like to express gratitude and thanks for support of the following people without whom this work could not have been achieved.

Alison Cleary, whose knowledge, advice and encouragement allowed the development of the sensor work contained in this thesis.

Francis Quail, who as my main supervisor who initiated the research and provided resources and advice during my studies.

Drew Smith, who gave encouragement and guidance during difficult periods during my studies.

David Infield, for providing support and advice during the final stages of my Ph. D.

Pawel Niewczas, who kindly review my work and offered advice.

David Brown Gear Systems, for providing lubricant samples sensor development advice.

Neil Hunt and the members of staff from the Multidimensional Spectroscopy Group who provided help and advice in FTIR analysis of lubricant samples.

The Electronic and Electrical Engineering Workshop staff, who helped build the test rig that allowed the demonstration of the wear particle sensor.

Funding

The research was funded by the EPSRC (project reference number EP/G0377728/1) through the Wind Energy Systems Centre for Doctoral Training with additional support from the Centre for Advanced Condition Monitoring.

Chapter 1 – Introduction

This chapter outlines the context and motivation for the research described within the thesis. The objectives and methodology for the research and the overall thesis structure are then described.

1.1 Background

In recent years the development of renewable energy resources has become a major governmental policy of the United Kingdom and other European Union (EU) nations [1]. Severe environmental damage has been linked to traditional energy sources such as coal and has become of concern to the general public. Energy security has also become an issue with the majority of gas and oil being imported, placing the supply of fuel out of the direct control of EU governments.

These factors have encouraged governments to develop their renewable energy resources. In most European countries, few suitable sites for hydroelectric dams remain without substantial ecological-urban impact. Solar energy has seen development in regions with suitable weather conditions but remains relatively expensive due to cost of panel fabrication. Geothermal requires very specific site conditions to be economical for development. Exploitation of tidal energy using barrages and wave capture has seen success with several new devices being tested in the UK and other countries. However, large scale deployment has not occurred.

Wind energy has become the dominant source of renewable energy after biomass for a variety of reasons. A relatively mature technology combined with an abundant energy source has enabled thousands of wind turbines to be deployed globally. Despite this, wind energy faces unique technological problems. Component failure has been a key problem and has limited the overall availability of energy capture and increased the cost of energy due to the expense of repairs. In particular, the gearbox that is used to increase the rotational speed for the generator is responsible for significant periods of wind turbine downtime [2]. Reducing this failure rate has acted as a driver for the research described within this thesis.

1.2 Condition Monitoring of Wind Turbine Gearboxes

Condition monitoring systems (CMS) encompass a broad range of techniques that are used to determine the performance of machines and other equipment to predict faults, failures and assist in asset management. The developments of such approaches arose from a need to prevent machines from running until failure, resulting in costly repairs, replacements and long periods of downtime. CMS are increasingly used within the wind energy industry as they allow operators to assess the current state of entire arrays of turbines in remote locations.

The wind turbine gearbox experiences transient loads in excess of 2 MNm and sustained loads of 0.5 MNm [3]. The highly variable loading regime causes the failure of numerous components within the gearbox such as the low speed bearing and planetary gear teeth.

It has been demonstrated that CMS techniques when employed correctly can extend gearbox operational lifetime, reduce costs associated with failures, improve safety and in many cases increase operational performance [4]. The wind industry has seen increased application of CMS techniques for a variety of components since large scale turbine deployments [5]. Insurance companies made basic CMS a requirement for certification for wind turbine operators, in effect making systems standard within the wind turbine [6].

Failures within the gearbox are often related to the lubricant that reduces friction between interacting components such as bearings and gearing. Wear particles suspended within the lubricant cause fatigue and wear within several gearbox components. When the lubricant quality degrades, the separating layer between components reduces and fatigue through metal-on-metal contact increases due to increased localised stress. Monitoring these two conditions is crucial for reducing maintenance costs and maximising wind turbine availability.

The most common types of gearbox lubrication sensors are particle counters and temperature sensors. Particle counters track the total amount of wear that has been liberated from the surface of gearbox components and correlates the total mass to

expected failures based on previously measured data. Temperature sensors are used to correlate failures which have been observed when the component temperature rises significantly. However, in both sensors the specific fault and failure mechanism cannot be determined accurately. It is believed that novel sensors can be developed that provide data which can be correlated better to component failure and consequently improve the overall understanding of the gearbox condition. By using a larger number of sensors than is currently used, a greater understanding of the gearbox condition may be found.

1.3 Objectives and Methodology

The research is focussed on developing condition monitoring sensors that can improve current fault prediction strategies within the wind turbine gearbox. The main objectives are as follows:

- Understand the failure mechanisms that occur within the gearbox.
- Understand the current state of the art within CMS for wind turbine gearboxes and identify any limitations or improvements.
- Develop novel sensor concepts or improvements that will improve understanding of gearbox health.
- Construct sensors and assess them on their ability to track their relevant parameters.
- Document sensor performance and identify improvements.

Briefly, the research methodology consisted of:

- Develop understanding of the wind turbine gearbox, the conditions in which they operate, the failure mechanisms that occur and how they develop.
- Perform a literature review of the state of the art in CMS for wind turbine gearboxes and identify improvements. Identify other CMS techniques that may be applicable.
- Outline novel sensor concept development plans and document how they may improve gearbox condition monitoring.

- Develop a laboratory method of testing sensors that is representative of an operational wind turbine gearbox.
- Develop a data acquisition system that will allow any data obtained from the novel sensors to be processed quickly and displayed
- Evaluate sensors and data acquisition system on their ability to track parameters in real-time and present data.
- Evaluate the fulfilment of the studies objectives and give recommendations for improvements or future development.

1.4 Novel Contributions

This thesis presents the development of novel lubrication monitoring sensors for wind turbine gearboxes. The main contributions to knowledge are as follows:

- A prototype in-line wear particle sensor based on an imaging sensor that detected particles through light extinction.
- Demonstration of real-time categorisation of test wear particles by shape and size in real-time using software developed in the MATLAB environment.
- System integration of wear particle sensor into functioning data capture and analysis system on a scaled gearbox lubrication system test rig.

1.5 Thesis Structure

The structure of the thesis reflects the development process of the novel sensors which began with understanding the wind turbine gearbox, assessing current CMS, developing a research methodology for sensor development and evaluating sensor performance.

Chapter 1	Describe objectives, methodology, novel contributions and related publications
Chapter 2	Introduce the background of wind energy development with focus on the gearbox; introduce failure mechanisms and causes.
Chapter 3	Describe in detail gearbox failure mechanisms, with focus on failures related to lubricant performance.
Chapter 4	Introduce wind turbine gearbox lubrication and discuss the causes of degradation.
Chapter 5	Discuss current condition monitoring technologies used in wind turbines, their advantages and potential new sensors design.
Chapter 6	Describe the development and testing methodology for a novel sensor that monitors wear particles within the lubricant.
Chapter 7	Describe the development and testing methodology for a novel sensor that tracks changes in infrared absorbance in lubricant.
Chapter 8	Present experimental results and discuss sensors performance and discuss improvements.
Chapter 9	Present conclusions and future work.
Appendix A	Additional information of condition monitoring systems for Chapter 5.
Appendix B	MATLAB code for wear particle sensor described in Chapter 6.
Appendix C	Absorbance spectra of analysed lubricant samples described in Chapter 7.

1.6 Publications Related to Thesis Research

The work describing development of the active pixel sensor in Chapters 4, 5 and 6 was contained within the following publications:

- **Hamilton A.**, Quail F., “*Development of a Low Cost Lubrication-Based Wear and Colour Monitoring Sensor for Wind Turbine Gearboxes*” European Wind Energy Association (EWEA) Conference, Vienna, Austria, 2013.
- **Hamilton A.**, Cleary A., Quail F., “*Development of a Novel Wear Detection System for Wind Turbine Gearboxes*” - IEEE Sensors Journal (2013).
DOI: 10.1109/JSEN.2013.2284821

The papers described the development and testing of the wear sensor on its ability to detect particle morphology.

Research into infra-red absorption spectra in Chapter 7 was used in the following publication:

- Parker M., Cleary A., **Hamilton A.**, “*Practical Online Condition Monitoring of Gearbox Oil Using Non-Dispersive Infra-Red Sensors*” Renewable Power Generation Conference, Naples, Italy, 2014.

The conference paper described the development of a lubricant condition sensor based on absorbance of infra-red light from a broadband source.

A summary of the state of art describing the different types of gearbox condition monitoring techniques was presented in the following journal publication:

- **Hamilton A.**, Quail F., “*Detailed State of the Art Review for the Different Online/Inline Oil Analysis Techniques in the Context of Wind Turbine Gearboxes*” - Journal of Tribology (2011).
DOI:10.1115/1.4004903.

The paper summarised a number of current techniques used as well as technology that may be adapted.

Chapter 2 – Wind Energy and the Gearbox

The energy policy of the United Kingdom (UK) has been influenced by domestic concerns and international obligations through its membership of the European Union (EU). This has resulted in a policy that favours development of renewable resources and promotion of energy conservation.

2.1 EU Renewable Energy Roadmap

In 2007 the European Commission (EC) published a Renewable Energy Roadmap, laying out a legally binding target of 20% of total energy supply to come from renewable sources by 2020 [7]. The purpose of the roadmap was to reduce member states dependence on imported fuels and reducing carbon dioxide emissions. In 2008 the national targets were set, with the UK required to contribute 15% of energy from renewable sources by 2020 [8].

2.2 UK White Paper on Energy 2007

In response to the requirements of the EC, the current UK energy policy was set out in the 2007 Energy White Paper [9]. It established reducing domestic carbon dioxide emissions and developing clean energy sources to reduce dependence on imported fuels as the two main challenges. To achieve these, four goals were set:

- Reduce total carbon dioxide (CO₂) emissions by 80% by 2050.
- Maintain and enhance reliable energy supplies.
- Promoting competitive markets in Europe to improve productivity
- Ensure all households would be adequately heated and insulated.

The Department of Energy and Climate Change (DECC) was created in 2008 to coordinate implementation of the policy [10]. Development of renewable energy was considered a key strategy to achieve several of the stated goals. It was recognised that the UK has some of the best renewable energy resources in Europe, with high average wind speeds and numerous suitable locations for tidal power stations [11].

Despite the drive to develop renewable energy resources, coal and gas still dominate, accounting for over 66% of total energy generation. Coal has remained the biggest contributor since the construction of the National Grid but its dominance is set to reduce significantly as older coal fired stations are decommissioned [12]. It is expected that almost 30GW of new generation capability is required to be operational by 2030 to compensate for the combined loss of older coal and nuclear power plants. The generation breakdown in 2012 is detailed in Figure 2.1.

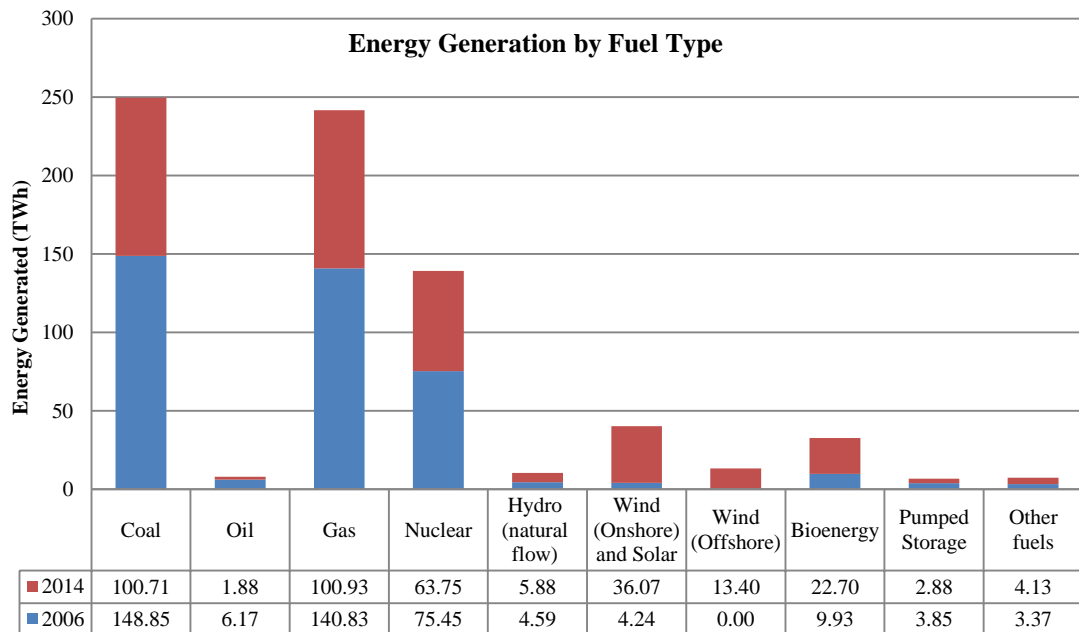


Figure 2.1. Comparison of UK energy generation in TWh by source from 2006-2014 [13].

Renewable energy sources account for 13.4% of total UK generation, with combined onshore and offshore wind being the largest single source (7.6%). However, when compared to 2006 before the current EU and UK legislation concerning energy was adopted, the renewable contribution was just over 5.8%, with offshore wind almost non-existent. This rapid increase in offshore deployment can be attributed to a variety of different factors. Public opinion is more favourable compared with onshore turbines due to lower visibility of offshore. Offshore regions experience higher average wind speeds with reduced turbulence and variations in wind direction [14]. The future generation profile is expected to have a significantly higher contribution from offshore wind energy based on the number of approved wind farms [15].

2.3 Wind Energy

The underlying relationship between wind speed and energy is defined as:

$$P_w \propto v_w^3, \quad \text{Eq. 2.1}$$

where P_w is the energy extracted from the wind and v_w is the speed of the wind [16]. It can be seen that since P_w varies cubically with v_w the energy that can be captured will increase dramatically over a short range of wind speeds. Consequently the forces exerted upon mechanical components during power transmission will vary proportionately to v_w^2 .

This relationship becomes increasingly important when the high variability of the wind is considered. Turbulence refers to variations in the wind speed over a time period of less than 10 minutes [16]. Variations over longer periods are normally related to factors such as season and height which are predictable within certain limits. Turbulence is more complex and is caused by air density changes related to thermal variations and local geography. These features add complexity to the friction of the ground, creating these short term variations. The turbulence intensity is the measurement of the overall turbulence and is defined as:

$$I = \frac{\sigma}{\bar{U}}, \quad \text{Eq. 2.2}$$

where σ is the standard deviation of wind speed variations about the mean of the wind speed U (m s^{-1}) over a 10 min interval. In general the turbulence intensity is greatest close to the ground and reduces with height. However, most wind turbines operate between 60 and 160 m (accounting for sweep area of the rotor). This region experiences significant turbulence. An example of a typical wind load that a turbine will experience over 7 hours is shown in Figure 2.2. During this sequence the average wind speed is 8 ms^{-1} but changes rapidly from each 1 s interval so the rotor and drivetrain do not experience a constant wind speed for any significant period of time. As a consequence of the wind variation, the gearbox experiences large variations in torque transmitted from the rotor through the drivetrain.

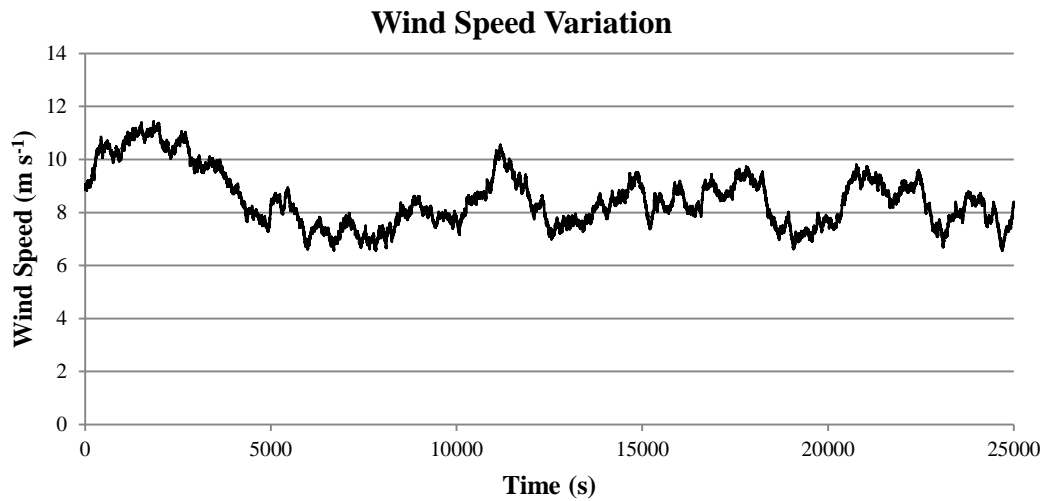


Figure 2.2. Wind speed variation over 7 hours for an onshore turbine [17].

2.4 Modern Wind Turbine Design

Modern wind turbines have their designs rooted in the ‘Danish concept’ which was initially developed in the late 1950’s. The 1973 oil crisis in which saw large increases in the price of crude oil prompted further development and research of alternative energy sources which accelerated the development of wind power [18]. Currently the most common design is known as a horizontal-axis wind turbine (HAWT) and is characterised by an electrical generator is contained within a nacelle at the top of a tower with a rotor that faces upwind (see Figure 2.3).



Figure 2.3. Siemens 3MW 3 bladed HAWT wind turbine [19].

The generator is connected to a rotor through a drivetrain and gearbox. 3 blades are most commonly used as they provide an optimal smoothness in rotational speed weighted for cost when compared with 2 and 4 bladed turbines [20]. Smoothness refers to the small changes in angular velocity that occur due to inertial variation. These variations are mainly caused by blades passing in front of the tower which creates periodic variations in the wind flow around the blade. Whilst 4 blades provide reduce the effect of these periodic variations, the benefits are reduced when the additional cost of a blade and extra weight are considered.

The overall rotor dimension has grown considerably from 15 to over 125 m diameter over a period of 30 years. The power rating has also increased proportionally with industrial turbines now commonly rated at 2-3 MW for onshore developments and 3 MW for offshore [21]. It is expected that 5 MW turbines will become standard for offshore wind farms whilst onshore development may stay at the current 3 MW standard.

2.5 Drivetrain

The drivetrain transfers rotational energy from the rotor to the generator. In the majority of wind turbines, the drivetrain consists of a main shaft which connects the rotor and gearbox together. The shaft rests on 1 or 2 main bearings which are connected to the nacelle base plate. The output shaft of the gearbox is connected via a flexible coupling to the turbine generator. The general layout is shown in Figure 2.4. The drivetrain is often the source of failures as the large amount of energy captured by the rotor must be transferred through all the components and into the generator [2]. Large transient loads which occur during periods of high turbulence or turbine shutdown will impact throughout the drivetrain.

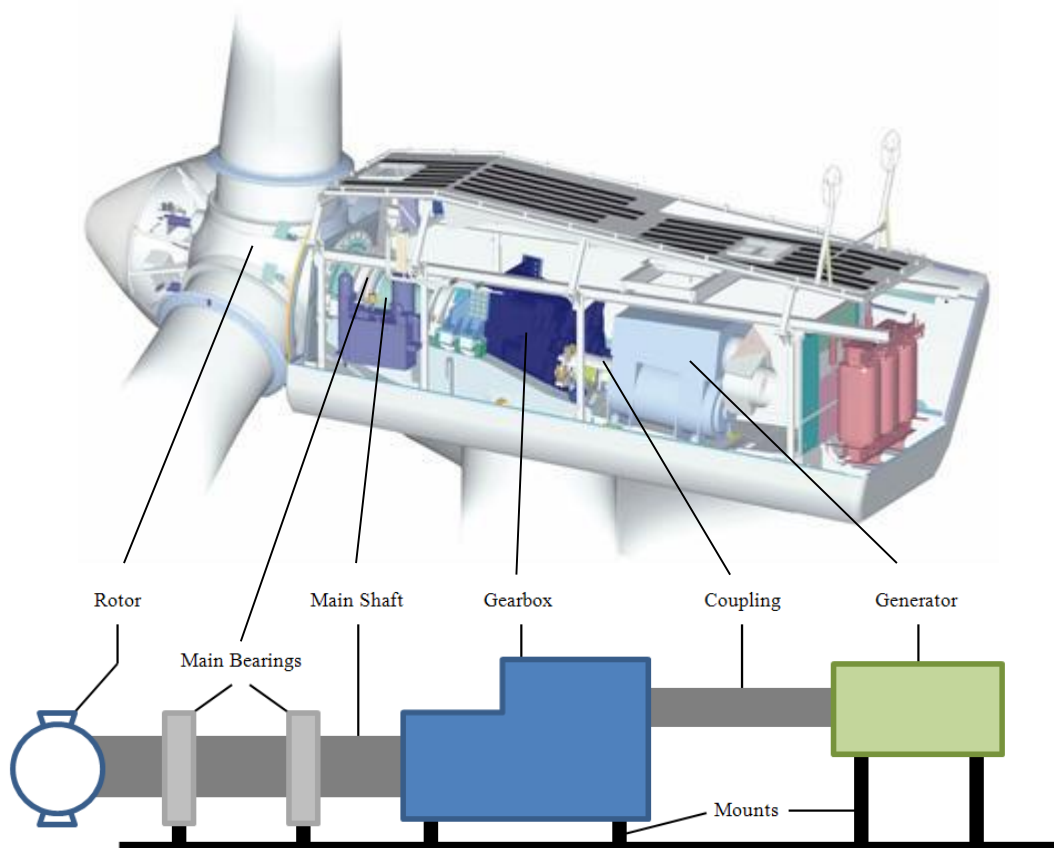


Figure 2.4. Basic layout of wind turbine drive train [22].

2.5.1 Gearbox

Gearboxes (or specifically transmission systems) are the assembly of mechanisms that transfer the rotational force of a shaft onto a different component. As the force is acting at a specific distance around the shaft axis, the effect is considered as torque:

$$\tau = r \times F, \quad \text{Eq. 2.3}$$

where τ is torque, F is the applied force and r is distance from the axis to the force. Within rotational machinery, the transfer of force is between different shafts with the intention of increasing torque whilst reducing speed. Force is also transferred between internal bearings, gears and the outer casing. This arrangement is found most commonly in combustion engines where the rotational speed generated is far too fast to be utilised. Transmission systems are also used where the source of power cannot be located close to where the application of power is desired. The basic equation that defines the relationship between shaft power (P), angular speed (ω) and torque (τ) is defined as

$$P = \tau \cdot \omega, \quad \text{Eq. 2.4}$$

Wind turbine gearboxes have the unusual purpose of increasing shaft rotational speed at the expense of torque. The overall shaft direction remains the same but is transferred between parallel shafts onto the flexible generator coupling. The rotational speed of the wind turbine rotor depends on the wind speed, the turbine type and the power rating. 2 MW turbines may have optimal rotational speeds of 16.7 rpm whilst smaller 300 kW turbines may operate at 48 rpm to create a sufficient voltage and current within the generator. However, due to constraints on components weight and size in wind turbine nacelles, large generators that could operate at such low speeds are often impractical. To compensate, smaller induction generators with limited pole pairs can be used in conjunction with gearboxes that increase the rotational speed of the shaft to more appropriate values. Step up ratios of 1:30 or more are common in larger rated turbines to increase the shaft rotation to approximately 1500 rpm [23].

2.5.2 Gears

Motion and power from the driving shaft is transmitted onto a secondary shaft by using meshing gearing. The most common type of gears are spurs (an example shown in Figure 2.5). In the majority of applications, the transmission of power is to be uniform so that movement in the driving gear will result in a proportional movement in the driven gear (an elliptical gearing system may be used for non-linear angular momentum such as assembly lines)

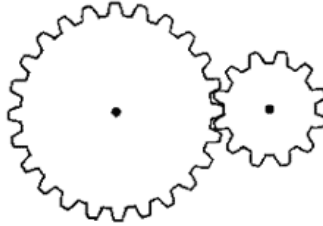


Figure 2.5. Two parallel gears with centred shafts.

The most important aspect of gearing is the ability to use gears with different number of teeth so the power can be transferred whilst altering the rotational speed and consequently the torque. This relationship is known as the gear or speed ratio and is defined as:

$$R = \frac{\omega_I}{\omega_O} = \frac{N_O}{N_I}, \quad \text{Eq. 2.5}$$

where R is the gear ratio, ω_I is the input gear angular velocity, ω_O is the output gear angular velocity, N_I is number of teeth on the input gear and N_O is the number of teeth on the output gear. Speed ratios are used in ratio calculations as torque ratios are not exact due to mechanical losses that vary dependant on the loading and required speed. An involute gear profile is used to allow several teeth to be in contact simultaneously and to gradually transfer force across the tooth surface. This provides a more uniform transfer of power and reduces noise and heat (see Figure 2.6). The pitch line velocity is the speed at which the point of contact between the gear teeth travels in relation to the tooth surface.

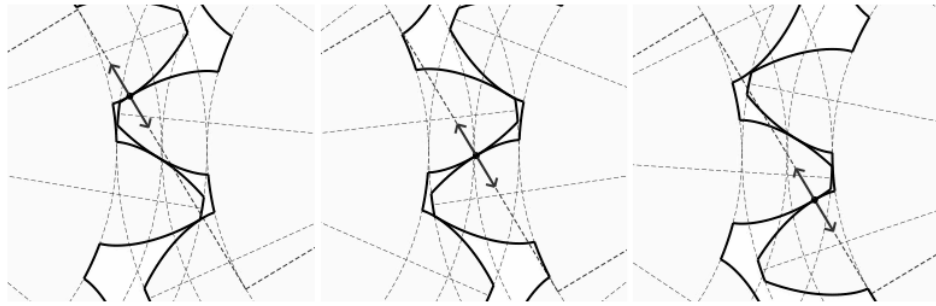


Figure 2.6. Interaction of gear teeth to transfer motion and power with pitch line indicated.

1 MW rated and above wind turbines have gearboxes that use helical spur gears with an epicyclic arrangement. Helical teeth are set at an angle along the circumference of the gear as shown in Figure 2.7. Helical gears have a larger tooth face width, allowing the transfer of force to occur over a longer distance which can reduce contact pressure and wear fatigue. This reduces noise and heat further, but allows thrust forces along the axis of a shaft to be transferred. This can result in undesirable forces within the gearing and onto secondary shafts. Helical gearing is used for higher speed ratios of 1:8 but with a small increase in mechanical losses when compared with standard spurs.

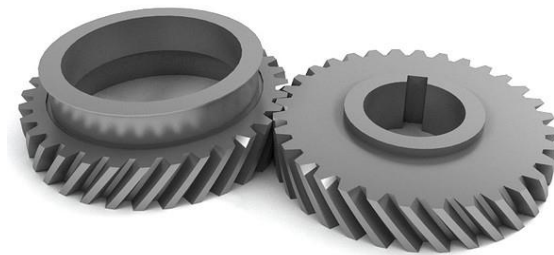


Figure 2.7. Two helical gears with intermeshing teeth.

Epicyclic (or planetary) gearing is a method of achieving a very high speed ratio within a small volume. The primary shaft connects to a carrier plate on which multiple planet gears are fixed. The planet gears drive a central sun gear that drives the secondary shaft. The planet gears also mesh with a surrounding annular gear that is fixed to the gearbox casing and is stationary (see Figure 2.8).

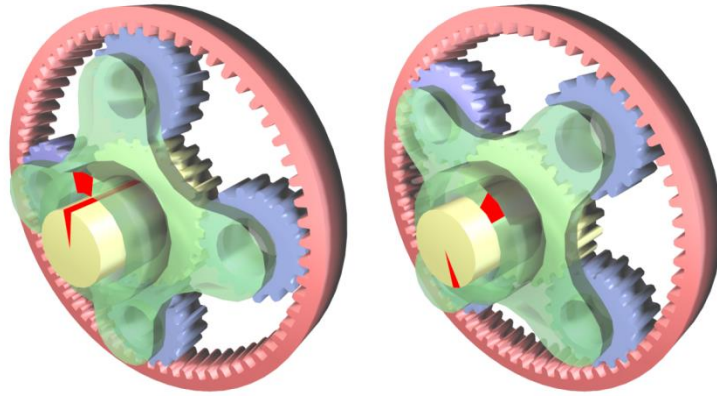


Figure 2.8. Epicyclic gear with 4 planet gears (blue), central sun gear (yellow) and annular gear (red). Planet gears drive rotation of carrier (green) [24].

The planet gears are free to rotate around the axis of the primary shaft. In this arrangement the power from the primary shaft is split equally between the planet gears, allowing smaller individual gears to be used rather than using 2 larger parallel gears. The speed ratio is typically 1:4 but varies depending on the manufacturer. In order to increase the output shaft to the required rotational speed, multiple stages may be used, where the secondary of one epicyclic gear serves as the primary for another epicyclic stage. Most +1 MW wind turbines use at least a two stage epicyclic gearbox. The final stage generally uses a single parallel gear pair for the final stage as the heat generated by epicyclic gears is significant. Lubricant is required on meshing gear teeth to prevent direct contact between surfaces and to remove excess heat.

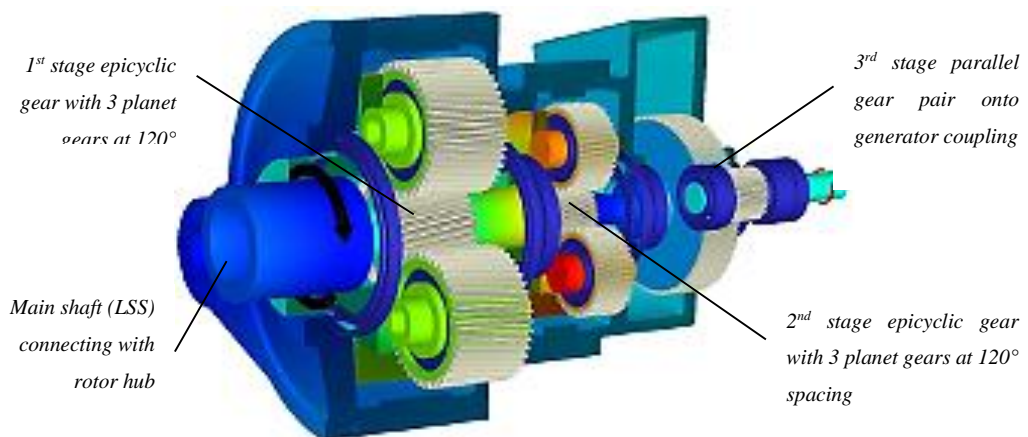


Figure 2.9. 2 stage epicyclic gearbox with 3rd stage parallel gears [25].

2.5.3 Bearings

Bearings are used within gearboxes to allow axial rotation of a shaft while fixing their absolute position with minimal loss of mechanical energy from friction. Ball bearings are the most common type found within the gearbox. The bearing consists of 2 races which enclose the balls. The outer race is normally stationary whilst the inner race is free to move and is connected to the shaft. The races may be designed to have a groove to prevent ball movement laterally from the shaft axis (see Figure 2.10).



Figure 2.10. Deep groove ball bearing with exposed inner race [26].

Bearings are lubricated like gear teeth and the bearing housing is designed to allow fluid to be pumped into the bearing and removed to facilitate heat dissipation. Industrial bearings are designed to fulfil their operational life without failing 90% of the time which is known as the L10 standard (i.e. 1 in 10 identical bearings is expected to fail). However, in wind turbine gearboxes, bearings frequently fail before reaching this target due to the early onset of failure mechanisms [27].

2.5.4 Lubrication System

The basic purpose of the lubrication system includes ensuring that various interacting gearbox components have a lubricant film at contact points to prevent direct interaction, removing excess heat generated and preventing corrosion due to environmental contaminants. It is an essential system which is required to maintain continuous and efficient operation of the gearbox.

The overall chemistry of lubricants designed for wind turbine gearboxes shares many similarities with conventional applications of machinery oil. However, there are a number of differences to allow for the unusual operational environment, the stochastic load regime and the requirement for infrequent lubricant changes. (N.B. oil nomenclature varies depending on context, for example, in academia and industrial environments. Alternative terms and names are listed where possible). The gearbox lubrication system will be discussed in detail in Chapter 4.

2.5.5 Torque Loading

Torque is reacted in the gearbox through the main shaft and casing which is connected to the rotor hub. Wind turbine gearboxes are designed to withstand torque between zero and the rated value over the lifetime of the wind turbine. However, in reality the rated torque is breached regularly under the following conditions [28]:

- Slow pitch response to changing wind load on fixed speed turbines resulting in abnormal loading on rotor.
- Dynamic magnification of torque loads due to drive train excitement at resonant frequencies.
- Application of mechanical brakes during high winds or emergency situations in turbine design where brakes are located on high speed shaft.

When these events occur significantly higher torques are transferred into the gearbox. During emergency shutdowns, an additional problem occurs where the torque loading will rapidly fluctuate causing dynamic stress cycles upon gearbox components (see Figure 2.11).

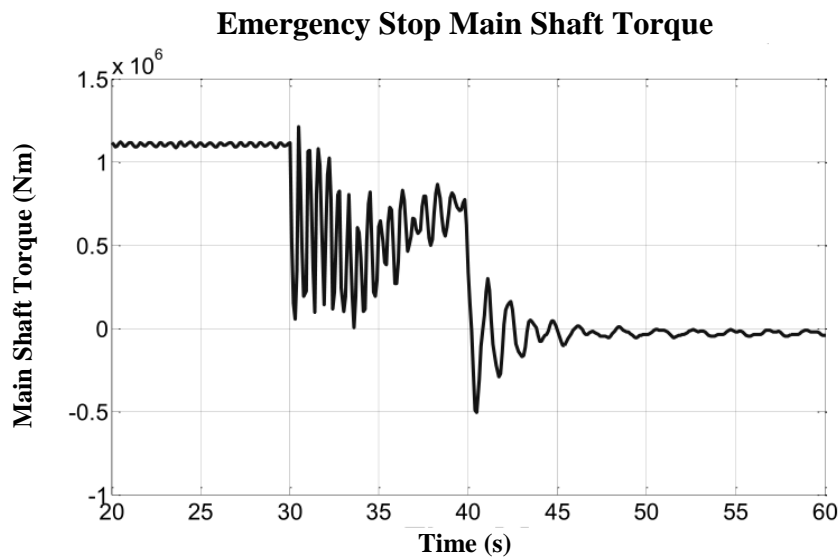


Figure 2.11. Input torque loading into gearbox through main shaft during application of mechanical brake [29].

These torque loads have been correlated with gearbox failures in a number of studies and have been associated with poor reliability [29].

2.5.6 Reliability

Various studies have been conducted to collate failure data and establish which wind turbine components fail most frequently. The number of days which the turbine was not operational was also tracked. The Scientific Measurement and Evaluation Programme (WMEP) was a study conducted on over 1500 wind turbines in Germany. The wind turbines ranged in size, mechanical configuration and age. The aim was to collect and analyse over 64000 maintenance and repair reports to provide accurate data on the failure and turbine down-time on various turbine sub-components. The reliability statistics are shown in Figure 2.12.

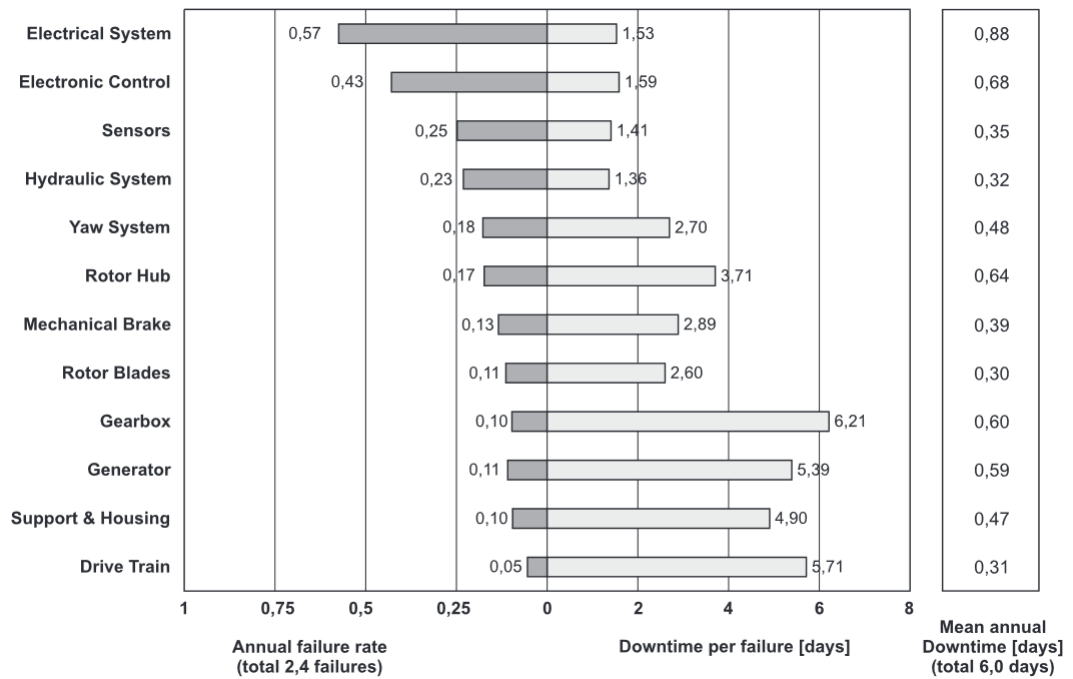


Figure 2.12. Failure frequency and downtime for wind turbine components per turbine [2].

Smaller components such as control and sensors systems had relatively high failure rates but required less down time of the turbine to fix. The gearbox failed relatively infrequently, but was responsible for the largest average turbine down-time when it did fail. In addition, the gearbox as an individual component has a high cost. An £800 bearing can fail, leading to the replacement of a £300,000 gearbox with a £50,000 per day hired crane, excluding the costs incurred from downed electricity production [28,30]. Similar studies conducted on UK wind farms have shown that the gearbox is responsible for the largest turbine downtime [31]. UK wind turbine operators and original equipment manufacturers (OEMs) are often reluctant to publish failure rates.

Within the gearbox, bearing failures account for over 60% of all sub-component failures, followed by gear teeth [28]. Several studies into the cause of high failure rates have found that shaft misalignments combined with extremely large transient loads are the cause [32]. In order to meet renewable energy targets, wind technology must be reliable enough to match the stability of supply that is delivered by traditional power sources such as nuclear and fossil fuels. The gearbox has been identified clearly as problematic which justifies further research into understanding and reducing failure rates that affect the component [33].

2.6 Conclusions

The gearbox has been identified as problematic component that can incur large costs for wind turbine operators. Peak and transients loads in excess of 2 MNm are leading to increased component failures. These problems will be exacerbated when more wind farms are located offshore due to greater forces, more isolated conditions and increased access costs [34]. Understanding the reasons for failures will allow development of solutions that may reduce wind turbine operational costs.

Chapter 3 – Gearbox Failure Mechanisms

In this chapter the mechanisms that cause key gearbox components to fail are discussed. Understanding of these mechanisms is an important stage to developing novel condition monitoring sensors.

Wind turbine gearboxes experience mechanical failures similar to other lubricated machinery that are well documented from industrial experience in other fields [35]. There are two broad categories for failure mechanisms: non-lubrication-related and lubricant-related. Development of a failure mechanism in one category may cause an actual failure in the other category. This distinction is known as primary and secondary modes of failure [36]. In the case of a broken gear tooth, the failure mode may be a fracture breakage due to repeated dynamic loading fatigue. However, the cause of the damaging dynamic load may be an uneven tooth surface caused by scuffing. In this case, the primary failure mode is scuffing whilst the secondary failure mode is fracture breakage. The distinction is important as scuffing is directly related to an inadequate lubricant boundary layer, allowing frequent metal-on-metal contact. Direct contact between components surfaces causes material to be removed and transferred into the surrounding lubricant.

3.1 Non-Lubricant-Related Failures

Non-lubrication-related failures (NLRF) are caused by material weakening through cyclic loading. When the gear teeth or bearings are continuously loaded and unloaded, small cracks (known as subsurface fatigue) develop in regions of stress concentration, for example at the gear tooth root [37]. These can combine or one may propagate sharply, resulting in a fracture. A broken gear tooth may result in enormous damage to the rest of the gearbox whilst a bearing failure may cause significant damage to the shaft it is supporting.



Figure 3.1. Cracked tooth completely detached from gear [38].

NLRF's unrelated to any primary failure mechanism are usually an unavoidable feature of mechanical systems but can be designed for by analysing the expected loading regimes over the desired lifetime. Standard methods of fatigue prediction include S-N curves that derive a relationship between stress (S) and number of cycles (N) of that stress based on measured test samples of materials [39]. Miner's rule approximates the number of cycles until failure based on aggregating the damage caused by varying levels of stress with different cycles [40]. A number of refinements and improvements upon these prediction methods have been applied to wind turbine gearboxes in an effort to predict when failures will occur [41,42]. The complexity of the drivetrain with multiple flexible objects and dynamic harmonics combined with the stochastic wind loading has created great difficulties in establishing accurate models for failure events. Additional data sources may aid modelling by allowing basing failure prediction on multiple parameters and not solely on wind loading [43].

3.2 Lubricant-Related Failures

Lubricant-related failures (LRF's) are mechanical faults that arise from or are accelerated by poor lubricant performance. If the correct lubricant with associated additives is applied to the components, the failures are a result of lubricant degradation or contamination as opposed to using a lubricant with inadequate properties. LRFs have a significant advantage over NLRFs as the failure mechanisms tend to produce wear particles that become suspended within the lubricant. These wear particles can be analysed using condition monitoring methods to identify the source of wear and the degree of damage [44].

3.2.1 Hertzian Fatigue

Hertzian fatigue covers a group of contact fatigue mechanisms that were first described by Heinrich Hertz [45]. They describe the mechanisms by which material from a surface is liberated by contact stress with another material. Within gearboxes, this occurs when the lubricant film is either insufficient in depth or surface roughness allows material to penetrate the film.

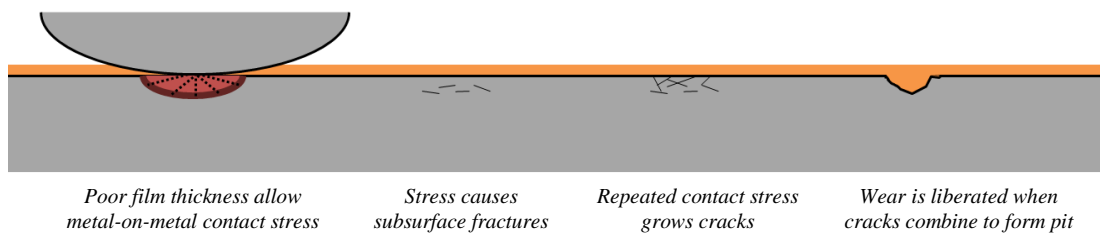


Figure 3.2. Development of pitting due to direct contact between two surfaces.

The most common Hertzian fatigue mechanism is pitting (see Figure 3.2) [46]. Pitting is a fatigue related mechanism where a small crack develops at the surface or just below. The cracks generally propagate a relatively short distance perpendicular or parallel to the surface until they branch out or return to the surface. Groups of these cracks may combine so that small chunks of the surface are liberated, creating a pit. If several pits combine, a larger pit will form which is referred to as a spall. The pit is usually visible to the naked eye once it has fully developed (see Figure 3.3).

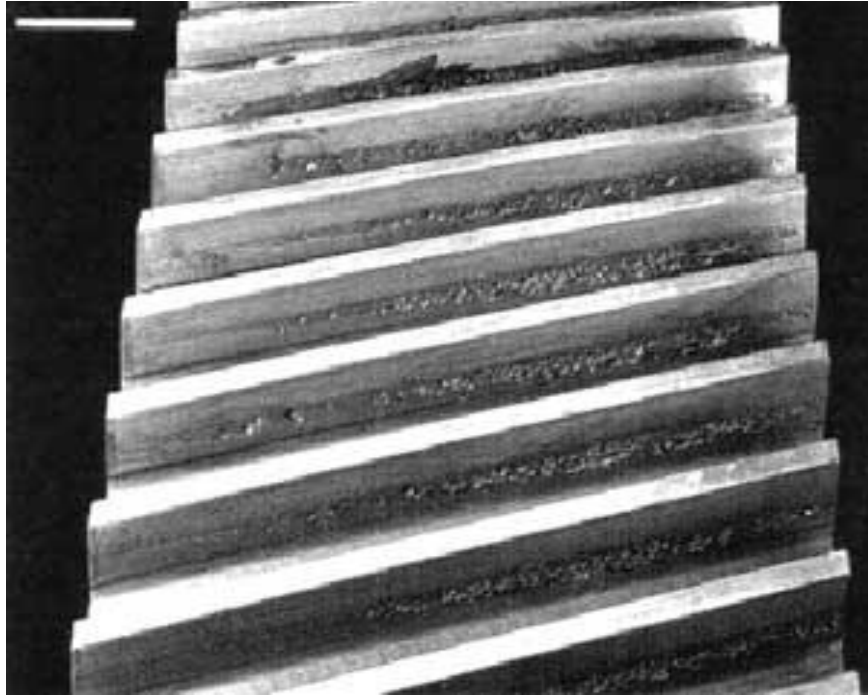


Figure 3.3. Helical gear teeth with severe pitting and spall formation [47].

Pitting can be initiated due to a number of factors. Water contamination of the lubricant can corrode the metal surface through ionising hydrogen atoms. The presence of wear particles within the lubricant can also cause a break in the lubricant film, resulting in localised increases in pressure on the metal surface. Defects within the metal such as impurities or cracks during manufacturing can also initiate pitting [48]. Pitting undergoes several identifiable stages from initiating where progressively larger material is liberated from the pit until it is considered a spall. Pitting is more commonly found on gear teeth but can also be found on severely damaged bearings [49].

Wear particles liberated from pitting vary dependant on the pit severity. In early stages particles are irregular shapes with major axial dimensions of $5\mu\text{m}$. Major axial dimension is the longest straight line measurement possible within a 2D object. As the pit enlarges and develops into a spall, larger spherical particles are liberated. These particles are known as spalls and are shown in Figure 3.4.

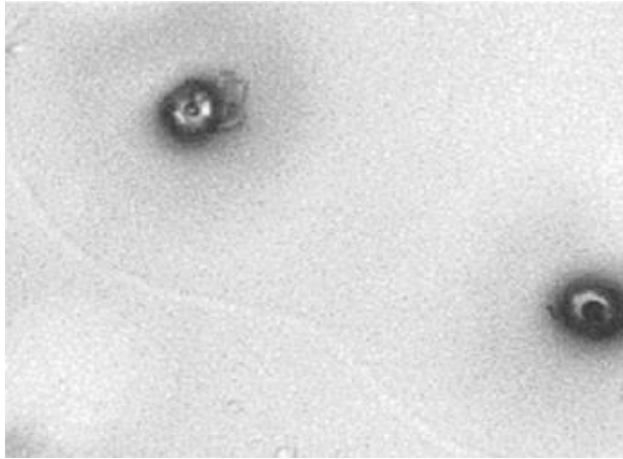


Figure 3.4: Spherical wear particles 40 μm diameter.

Micropitting is identical to pitting with the only difference being the actual size of the pits [46]. In general, the pits are in the order of 5 to 10 μm deep and appear to the naked eye as a frosting or a grey mark upon a smooth metallic surface. Components that have undergone hardening through chemical and thermal processes are susceptible due to the increase in surface roughness. This causes the lubricant film to fall between peaks across the surface and allow direct metal contact between surfaces. Micropitting is commonly found in rolling element contacts such as bearings due to the repetitive stress that locally deforms the curved surface [50]. Wear particles liberated from micropitting are identical in shape to standard pitting wear particles but range from having 2 to 5 μm major dimensions.

3.2.2 Wear Fatigue

Wear fatigue is damage to the surface of machine components through the action of discrete particles [46]. The initial source of wear particles varies but is generally from the gearbox itself through Hertzian fatigue. Material in the bearing and gear teeth surfaces from manufacturing are often liberated quickly during initial run in. These particles are usually filtered out but a significant number may remain or liberate at a later time. A small number of external contaminants may enter the gearbox during maintenance or operation such as silica (sand) in desert wind farms.

Abrasion is the most common wear-related fatigue mechanism where particles suspended in the lubricant break the film layer and penetrate the surface of a

component. The action normally requires the particle to be compressed between two surfaces such as 2 gear teeth or between the bearing and inner/outer race. In Figure 3.5 the abrasive effect is shown for a bearing and race. The particle travels with the lubricant flow and enters the surface interface. The particle is large enough in diameter to break the film thickness (indicated in orange). Once compressed between the two surfaces, the particle exerts a compressive force upon each surface and is compressed itself. Once the particle has passed through the interface, the surfaces of the bearing and race will have suffered localised Hertzian fatigue. A small amount of particles may also be liberated with each successive particle passing. The particle itself is now compressed and hardened further, increasing the damaging impact it may have upon other components.

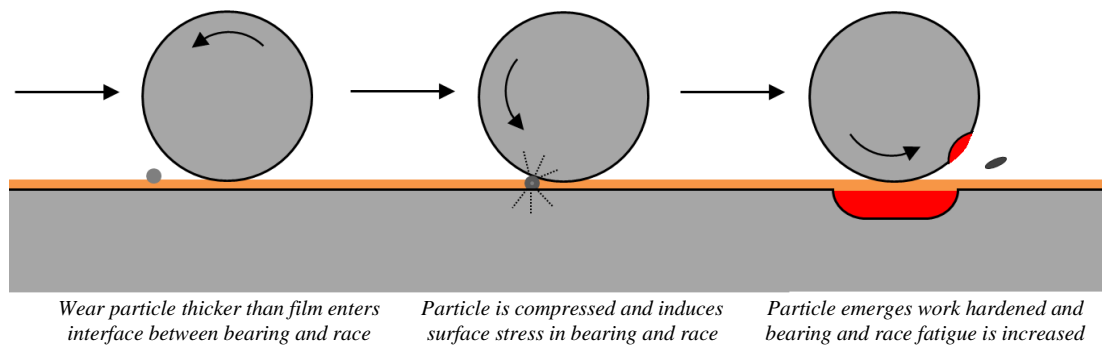


Figure 3.5. Progression of wear fatigue of a bearing and race.

Abrasive wear particles tend to be flat in shape and have an approximate 20 to 60 μm major axial dimension with a length to thickness ratio of 30:1. The overall shape is generally ellipsoidal with a rough perimeter as shown in Figure 3.6.

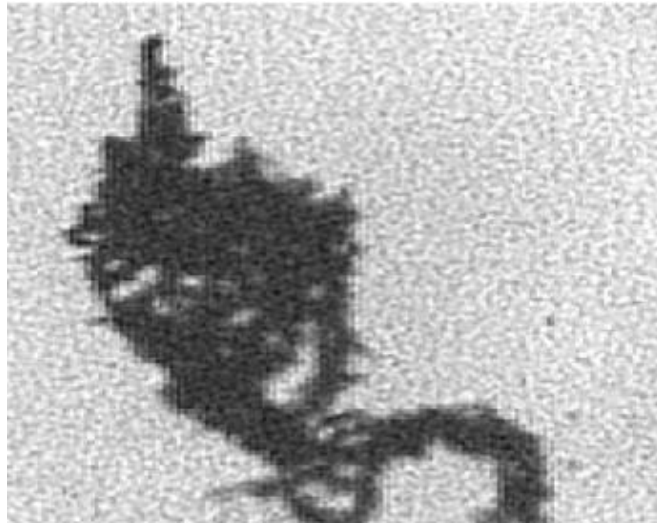


Figure 3.6. Abrasive wear particle with small holes from successive compressive loading [51].

Adhesion wear is the direct interaction of metal resulting in the plastic deformation of the surface. In this process inadequate lubricant film thickness allows two metal surfaces to rub, for example two gear teeth. The surfaces move in opposite directions and small variations can interact, creating independent wear particles and transferring material. Adhesion is a beneficial process during initial operation of the gearbox as it removes any imperfections on the surface of components from manufacture and so increases the average lubricant film thickness [52]. The process becomes problematic when other fatigue mechanisms have increased surface roughness.

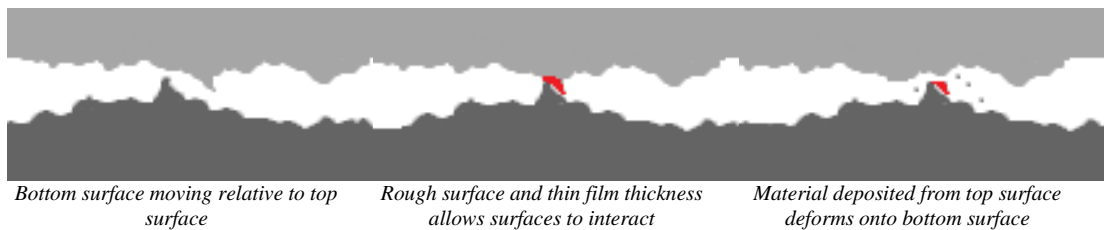


Figure 3.7. Adhesion of wear surface due to surface roughness and thin film.

Adhesion is classed as mild if the upper surface is only affected where metal is oxidised or has bonded with any additives. Once a breach has been made into the surface, adhesion becomes more damaging and increases the presence of wear particles and the probability of abrasive fatigue. When wear particles are liberated due to severe adhesive action, the term scuffing is used. The particles produced from this

mechanism are usually in the order of 5 to 15 microns in length, 1 micron in thickness and shaped like platelets (see Figure 3.8).

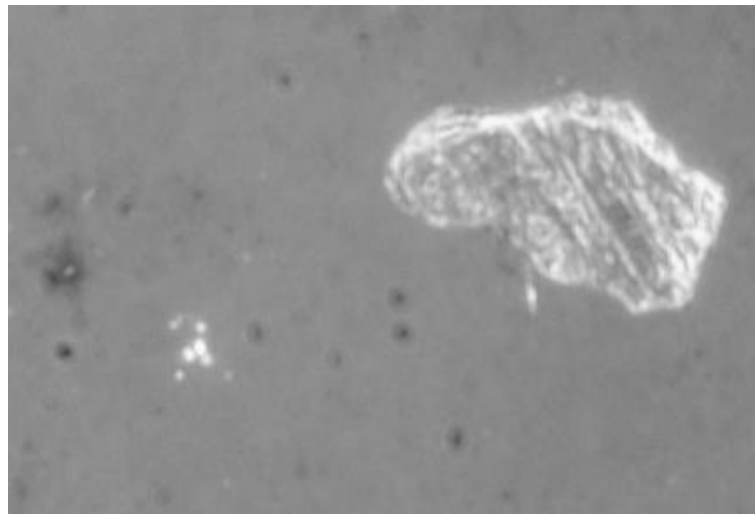


Figure 3.8. Scuffing wear particle with major axial dimension of 150 μm .

Scoring is another fatigue mechanism resulting from adhesion. In this method, imperfections in material surfaces give rise to localised nodes that are significantly stronger than the surrounding material from hardening. The nodes are able to remove material from a different surface that is relatively weaker as shown in Figure 3.9.

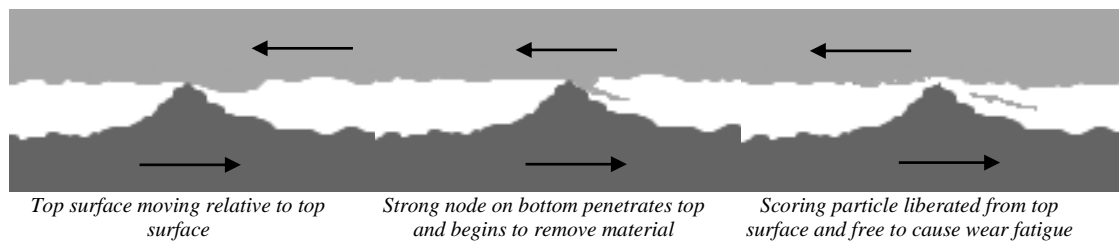


Figure 3.9. Scoring wear in which particles are formed.

Since the force is concentrated on a smaller area, the particles formed are usually in the order of 25 to 100 microns long, 1 to 5 microns wide and have a coarse appearance as shown in Figure 3.10. Cutting wear particles are not common in a machine that is operating correctly. Localised stronger nodes are normally found deeper within materials and so their presence indicates severe wear has occurred. Extreme loads can also cause scoring due to the temporary reduction in lubricant thickness.



Figure 3.10. Cutting wear particle 500 μm in length [51].

3.3 Particle Number

Since component erosion will inevitably occur within the gearbox, the quantity of particles present in the lubricant is indicative of component fatigue. The rate of particle liberation is an indicator of the current state of several components in the gearbox. During normal operation, the rate is normally low with small amounts being found due to excess material in the manufacturing process or certain weak points along the component surface. As this rate begins to increase along with a total increase in the particle quantity, there is a strong indication that one or several components are beginning to degrade. In Figure 3.11 an example of inline gearbox wear particle trending is shown obtained from a particle counter sensor.

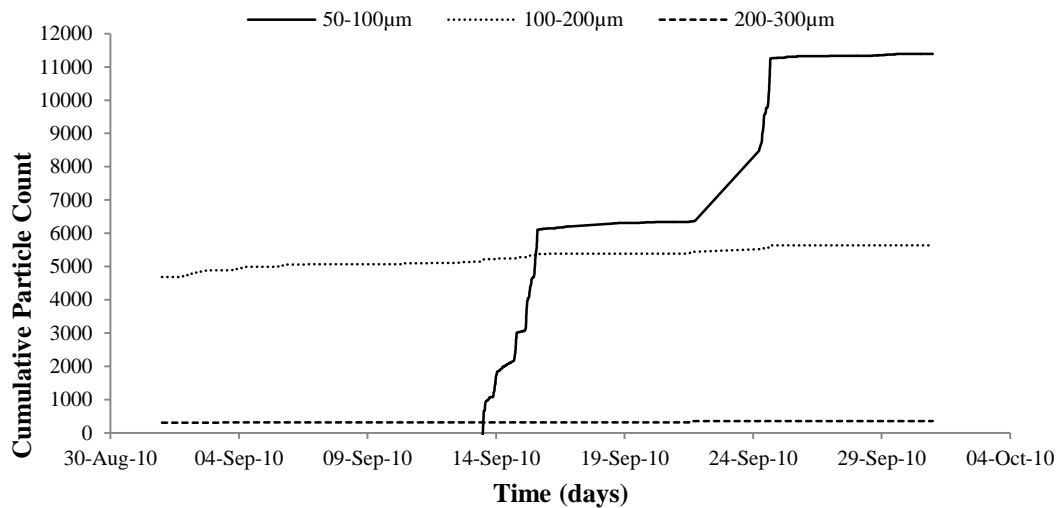


Figure 3.11. 1.5 MW onshore wind turbine gearbox cumulative particle count [53].

The particle liberation regime is not a smooth or an easily interpreted trend. Due to the complex design of the lubrication system with different components, channels and lubricant reservoirs, particles can become trapped for extended periods of time and remain undetected. Inevitably, a steady accumulation of normal wear particles can be released simultaneously and give a false impression of a large fault which can be seen in the 50-100 μm trace in Figure 3.11 beginning 14th September and 22nd September. The larger particle trend lines do not exhibit this behaviour and increase approximately linearly over time. Correct positioning of the wear particle sensor is important. Tracking the cumulative detection of different size classes of particles and using suitable analysis algorithms allows wind turbine operators to assess the current state of the gearbox and specific components. However, only the major axial dimension is captured with no indication of the shape or other dimensions.

3.4 Conclusions

Gearbox failures related to the lubricant create wear particles which have dimensions and size related to the type of fatigue mechanism occurring. Bearings and gear teeth suffer from similar faults but also have individual problems that produce different wear types. Particle counting is currently used by industry with distinctions made between particles of different major axial dimension. However, shape and other axial dimensions are not tracked despite the potential to provide additional information on the type of failure that is occurring and which particular components are affected. A review of the current CMS related to wear particles and lubricant condition has been conducted to establish the current limits of detection and to identify improvements or novel concepts that may be applied. The entire review can be found in Appendix A whilst a focussed analysis can be found in Chapter 5.

Chapter 4 – Gearbox Lubrication

In this chapter, the chemistry of lubricants will be discussed in detail. Wind turbine gearbox lubricants are required for the following functions:

- **Film Thickness** - provide interacting gearbox components with an adequate lubricant film at contact points to reduce direct interaction.
- **Heat Removal** - remove heat generated within components to reduce fatigue and prevent corrosion through thermal effects.
- **Corrosion Prevention** - prevent contaminants from directly attacking exposed metal surfaces.
- **Wear Removal** - remove wear material to prevent damage mechanisms described in the previous chapter.

Lubricants consist of a base oil which provides the majority of the chemical properties that allow them to achieve the listed functions. However, a single molecule cannot fulfil all criteria effectively and so chemicals known as additives are mixed with the base oil to compensate. Over time the lubricant composition begins to change due to degradation mechanisms until it cannot function adequately. Certain condition monitoring techniques track these degradation mechanisms. Understanding these mechanisms is necessary to assess if improvements are necessary in the current CMS.

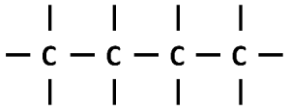
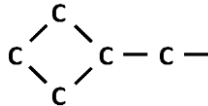
4.1 Lubricant Properties

The overall chemistry of lubricants designed for the wind turbine gearboxes share many similarities with conventional applications of machinery lubrication. However, several variations are required so the lubricant can perform under the varying loads of a normal wind regime. Lubricants are broadly classed into two groups based on their source: mineral and synthetic lubricants. Both are used for lubricating the wind turbine gearbox but synthetics are gradually becoming more dominant in 1 MW and higher rated wind turbines.

4.1.1 Mineral Lubricants

Mineral lubricants are a broad range of oils that have been derived from non-vegetable sources. The most common source is from the fractional distillation process of crude oil when petroleum is manufactured. Crude oil may be a mixture of different oil types which can be broadly split into 3 categories: paraffinic, naphthenic (or *cycloalkanes*) and aromatic as shown in Table 4.1. Each of these have useful characteristics that are appropriate for different lubricant purposes making the location highly important. The geological source is a major factor in the composition of crude oil, with some being dominated by a single type, with others being more equally mixed.

Table 4.1. Difference between major mineral oil groups.

Type	<i>Paraffinic</i>	<i>Naphthenic</i>	<i>Aromatic</i>
General Structure	 <p><i>Straight chain molecules with one main carbon chain with possible branches and other elements. Consists of single bonds so is fully saturated.</i></p>	 <p><i>Contains at least one ring of carbon atoms and may be part of a larger long chain molecule. Consists of single bonds so is fully saturated.</i></p>	 <p><i>Contains a benzene ring which consists of unsaturated carbon atoms potentially allowing other atoms to bond.</i></p>
Sources	<i>Nigeria, USA, Venezuela</i>	<i>North Sea, South Sudan, Saudi Arabia</i>	<i>Russia, Turkmenistan, USA</i>

Each category has distinct advantages and all are used for machine lubrication. Crude oil normally contains all three categories with some being more dominant than others. During fractional distillation where crude oil is separated by chemical weight, most aromatic compounds are removed and base stocks of oil consist of either mainly paraffinic or naphthenic.

In terms of lubricant properties, the overall subgroup of oil type largely determines the initial viscosity index (VI). Mineral oils suffer from several weaknesses which can affect lubricant performance, despite extensive methods to remove them [71]. The presence of sulphur (S), phosphorus (P), and carbon double bonds (C=C) are all detrimental to the lubricant by changing the viscosity.

4.1.2 Synthetic Lubricants

Synthetic lubricants are long chain hydrocarbons that were developed to address many of the problems found with source contaminants in mineral oil. Advances in chemical polymerisation allowed basic hydrocarbon monomers to be formed into complex and useful compounds. Several base compounds may be used such as olefin oligomers, neopentyl polyol acids, dibasic acid esters and alkylated aromatics [54,55]. The base compound is selected on its ability to form stable hydrocarbon formations with specific properties. Generally, synthetic lubricants are manufactured to have specific properties such as high VI, oxidative resistance or high shear strength [56]. The main problem with many synthetics is their susceptibility to thermal degradation so better suited for low temperature applications below 200°C [57].

Table 4.2. Basic process to create synthetic oil and polyalphaolefin.

Stage	Description	Structure
1	<i>Ethene/ethylene is used as a base group due to the simple structure and presence of a double bond</i>	$\begin{array}{c} \text{H} & & \text{H} \\ & \diagdown & / \\ & \text{C} = \text{C} \\ & / & \diagdown \\ \text{H} & & \text{H} \end{array}$
2	<i>A hydrogen free radical is introduced which wants to form bonds</i>	$\text{CH}_3 - \text{H}_2^+$
3	<i>Larger compounds from and usually stabilises at 10. The oil is now paraffinic and can be processed further</i>	$\begin{array}{cccccc} \leftarrow & \text{CH}_2 & - & \text{CH} & - & \text{CH}_2 & - & \text{CH} & - & \text{CH}_2 & - & \text{CH} & \rightarrow \\ & & & & & & & & & & & & \\ & & & \text{R} & & \text{R} & & \text{R} & & & & & \end{array}$
4	<i>Monomer alpha olefin is shown. This can be polymerised into polyalphaolefin by breaking the C=C. Several of these can be joined together to create a lubricant with a backbone and branches</i>	$\leftarrow \text{CH}_2 - (\text{CH}_2)_7 - \text{CH}=\text{CH} \rightarrow_x$

A large number of wind turbine gearboxes use polyalphaolefin (PAO) as the base stock for gearbox lubricants (see Table 4.2). They have better oxidation prevention properties at higher temperatures compared with mineral oils and have inherently low contaminants. However, it is actually a poorer lubricant than most mineral oils due to the absence of impurities such as sulphur and nitrogen oxidative compounds which have strong positive and negative charges. This causes polarisation of individual

molecules which increases fluid friction. Lower fluid friction within synthetic lubricants reduces viscosity which is undesirable when separating interacting components. Viscosity in PAO's is improved by including additives that disrupt molecule shape.

4.1.3 Viscosity

Viscosity is a measurement of the internal friction within a liquid at a given temperature. However, there are two main ways in which viscosity is defined: dynamic and kinematic. Dynamic (also known as absolute) viscosity of a fluid is defined as

$$\eta = \frac{\tau}{(du/dz)}, \quad \text{Eq. 4.1}$$

where η is the dynamic viscosity, τ is the shear stress and du/dz is the shear strain rate [58]. The shear strain rate is the velocity gradient across a fluid with depth dz and du is the velocity difference between the top and bottom surface as shown in Figure 4.1.

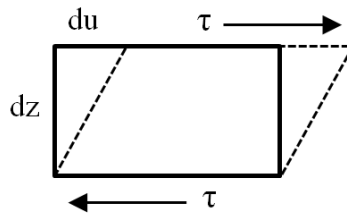


Figure 4.1. Thin layer of lubricant in one dimensional flow.

Dynamic viscosity is a measurement of resistance to flow and shear force within a fluid due to internal friction. It can be quantified by measuring the force required to move fluid through a confined space at a constant rate. Rotary viscometers determine dynamic viscosity by measuring the required torque to rotate a metal spindle within a fluid at a constant rotational speed. However, kinematic viscosity is more commonly measured and is defined as:

$$v = \frac{\eta}{\rho}, \quad \text{Eq. 4.2}$$

where ν is the kinematic viscosity, η is the dynamic viscosity and ρ is the density of the fluid. Kinematic viscosity (whilst intrinsically measuring the same physical property) is defined differently from dynamic viscosity in that the fluid's resistance to flow and shear due to gravity. It is determined using viscometers that measure the time taken for a fluid sample to flow through a known pipe diameter with known surface roughness. The time can be correlated accurately to kinematic viscosity [58]. Viscosity is the most important characteristic of a lubricant as it will determine the film thickness that separates interacting components. Calculating the required film thickness is component dependent, but is a function of fluid viscosity, velocity and external pressure:

$$h_{min} \propto \frac{\eta u}{f}, \quad \text{Eq. 4.3}$$

where h_{min} is the film thickness, η is the dynamic viscosity, u is the velocity and f is the unit pressure of the lubricant [59]. As the loading increases, the film thickness decreases. If the velocity or viscosity increases, the thickness increases. Viscosity is affected by a variety of factors including, lubricant degradation, acidity and water contamination, but it is mainly affected by temperature as shown in Figure 4.2 [60].

Effect of Temperature on Dynamic Viscosity

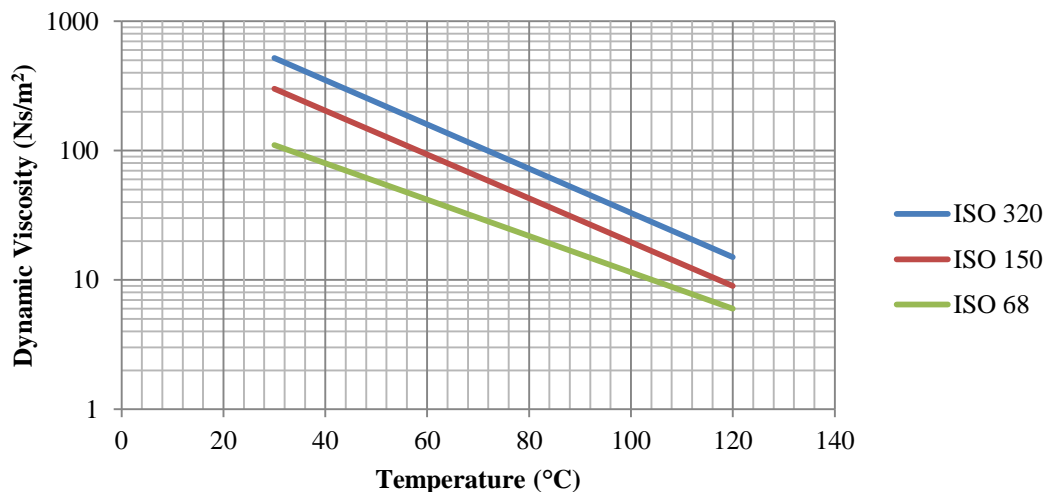


Figure 4.2. General effect of temperature on the viscosity of lubricants. Different grades of lubricant (ISO 320, 150 and 68) have different VI profiles [60].

The three traces in Figure 4.2 show different grades of lubricant. All three ISO grades reduce in dynamic viscosity with increases in temperature but ISO 68 has an overall

lower viscosity compared with ISO 320. As temperature is so significant, industrial lubricants are required to publish their viscosity index (VI). VI is a measurement that combines the kinematic viscosity of a fluid at 40°C and 100°C using ASTM standard D2270 in order to characterise the lubricants performance under varying temperatures. An ideal lubricant would maintain the same viscosity for any temperature range. Whilst this is impossible to achieve, mixing certain lubricants together or adding additives can reduce the viscosity variation over a set temperature range. VI is measured by comparing the kinematic viscosity of the test lubricant to two other known lubricants. All 3 lubricants must have the same kinematic viscosity at 100°C, but all have different kinematic viscosities at 40°C. The VI is then defined as:

$$VI = \frac{L_{st} - U_t}{L_{st} - H_{st}} \times 100, \quad \text{Eq. 4.4}$$

where VI is the viscosity index of the test lubricant, L_{st} , H_{st} and U_t are the kinematic viscosities at 40°C of the first known lubricant, the second known lubricant and the test lubricant respectively [58]. A high VI (between 80 and 110) indicates that the decrease is less severe than a lubricant with a low VI (35 or below). Synthetic lubricants used in large wind turbines can have VI of 95 or higher [61].

When viscosity is reduced, the fluid film covering components shrinks and increases the probability of contact, resulting in wear and degradation. In addition, the lubricant ability to remove wear particles by suspension is also affected by viscosity. Once the viscosity is reduced, larger particles are harder to move and may remain near to contact surfaces, breaking lubricant films and causing further damage.

4.1.4 Hydrodynamic Lubrication

When lubricating inter-meshing or point contact components such as gear teeth and bearings, the film thickness critical in reducing the probability of mechanical failure. When assessing the minimum film thickness, the lambda ratio is used:

$$\lambda = \frac{h_{min}}{[(\Delta_a^2 + \Delta_b^2)]^{1/2}}, \quad \text{Eq. 4.5}$$

where h_{min} is the minimum film thickness, λ is the lambda ratio, Δ_a is the root mean square (RMS) of the primary surface per unit area and Δ_b is the RMS of the secondary surface per unit area [62]. The root of the sum of the surface RMS values provides an equivalent surface roughness as the surface topography will vary over a given region. When the ratio is greater than 1, the two surfaces are not in contact (known as full elastohydrodynamic lubrication). In this lubrication regime, mechanical wear is negligible and contact mainly occurs during extreme load scenarios. If the surface roughness increases or the film thickness decreases, the lambda ratio can drop below 1. The frequency and severity of surface contact increases until the ratio drops below 0.3. At this stage, the surfaces are essentially in direct contact with minimal or no lubricant film.

4.1.5 Additives

Gearbox base lubricants lack many properties that are necessary to ensure effective component lubrication and durability [63]. Synthetic lubricants lack characteristics that are found in standard mineral lubricants and so require additives to simply match performance. However, they are now more commonly used in wind turbine gearboxes due to longevity and superior anti-corrosion properties [61]. Different chemical compounds can be added to the base lubricant to create or enhance desirable properties and remove or reduce damaging ones.

4.1.5.1. Rust Inhibitors

Rust inhibitors (RIs) are added to a lubricant due to the likelihood of contact with steel and other metals susceptible to oxidation. For this reason they are included in the majority of gearbox lubricants. RI's constitute approximately 0.25% of the total lubricant volume, with larger or smaller proportions depending on the operational environment of the machinery. The most commonly used molecule is a hindered phenol that functions by readily reacting with free oxygen molecules which may otherwise react with the lubricant or any susceptible machine components. A commonly used RI is 2,6 ditert-butyl-4-methyl phenol (shown in Figure 4.3) which is based on a hindered phenol [64]. Monitoring the quantity of unreacted RI's is desirable

to ensure oxidation rates remain low. Temperature is a significant factor on the specific type of RI to use.

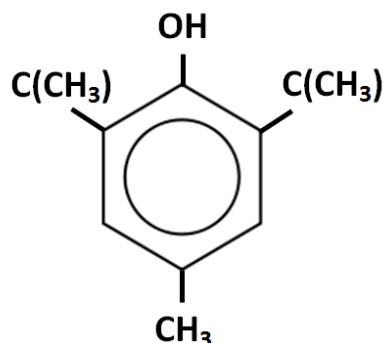


Figure 4.3. Chemical structure of 2,6 ditert-butyl-4-methyl phenol (benzene inner structure).

4.1.5.2. Viscosity Index Modifiers

Viscosity modifiers are used to change the VI for lubricants that are expected to operate under a range of temperatures. The aim is to reduce changes to viscosity as a function of temperature (see Figure 4.4) so that the lubricant remains effective in maintaining the relative distances between interacting components. Polyalkylstyrenes, olefin-copolymer and polyacrylate may be used as modifiers [65].

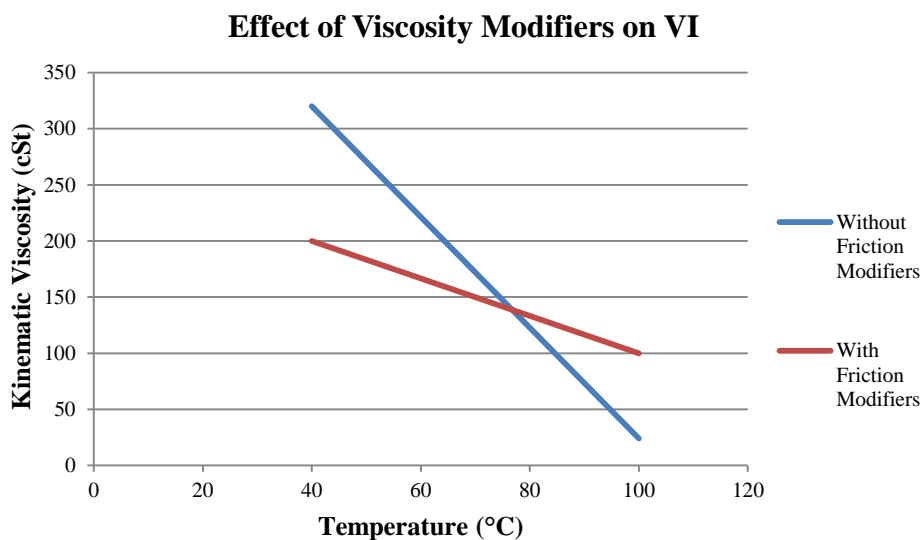


Figure 4.4. Effect of viscosity modifiers on viscosity index.

They operate by disrupting the natural structure of the base oil. For example, paraffinic lubricants tend to settle into flat, stratified layers due to their long chain structure. This increases viscosity at lower temperatures. The modifiers work by disrupting the lubricant with structural ‘branches’ that push between layers of lubricant, preventing the formation of stable flat layers. A negative effect of VI modifiers is the relationship between dynamic and kinematic viscosity defined in Eq. 4.2 in may not hold. The lubricant may act as a non-Newtonian fluid where the viscosity may not vary proportionally to the shear stress and shear strain rate as defined in Eq. 4.1 because it will cause localised changes in density

4.1.5.3. Anti-Wear Additives

Anti-wear additives (AW) are included in lubricants to reduce surface particle liberation within machinery. The additive operates by bonding with the metallic surface of components to create a sacrificial barrier layer that will erode over time [66]. This protects the metallic surface from wear associated with boundary lubrication conditions. The additive also acts as a rust inhibitor by preventing oxidation of metallic surfaces. AW’s constitute approximately 0.3 – 1% of the total lubricant volume, depending on the type of AW used, the material composition of the components and the type of machine operation. An example group of AW additives is monomeric zinc dialkyldithiophosphates (ZDDPs) with its structure shown in Figure 4.5.

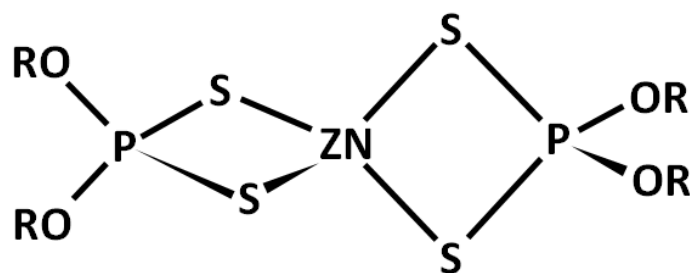


Figure 4.5. Chemical structure of zinc-dialkyldithiophosphate with ‘R’ representing general alkyl groups that may be utilised.

Prolonged use of anti-wear additives can corrode components over time due to the chemical bonding with the surface. However, higher wear particle liberation rates occur in components that do not have AW's included in their lubricant profile.

4.1.5.4. Extreme Pressure

Extreme pressure (EP) additives are used to prevent high loads from causing direct surface interaction that could not be prevented by the base lubricant alone. EPs are designed to form a secondary protective layer under high pressures when the normal lubricant film has failed. Their chemical structure has one part of the molecule which interacts with components surfaces, whilst the other interacts with the lubricant. This allows the additive to disperse evenly throughout the lubricant and surface areas. Spiro-bicyclodisphite is a commonly used EP additive and is shown in Figure 4.6 [67].

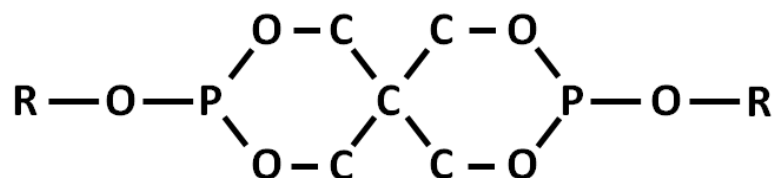


Figure 4.6. Chemical structure of a spiro-bicyclodiphosphite with 'R' representing general alkyl groups that are selected depending on the base lubricant structure.

When extreme loads occur, the lubricant film begins to decrease in thickness and the local temperature begins to rise. This temperature rise acts as a catalyst for EP additives to react with the metal surface. In this process, a variety of new compounds are created that are dependent on the type of EP used. These compounds create a new film to prevent surface contact, reduce friction and reduce wear liberation. A large variety of chemical compounds can be used with some that are both temperature and pressure dependent and other which rely only on pressure. Compounds based on boron, phosphorus, sulphur and chlorine are typically used. The film layer that is produced typically consists of metal salts such as iron chlorides and phosphides.

4.1.5.5. Friction Modifiers

Friction modifiers account for approximately 1% of the total volume of lubricant and are commonly manufactured using rapeseed oil. Their structure allows them to alter

the surface friction of machinery components by using polar compounds that have a high affinity for metallic surfaces such as diethanolamine salt of carboxylic acid shown in Figure 4.7 [68].

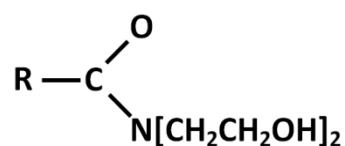


Figure 4.7. Diethanolamine salt of carboxylic acid is a common friction modifier.

4.1.5.6. Dispersants

Dispersants (shown in Figure 4.8) are only used in gearboxes if significant amounts of copper are used for various components [69]. Originally chlorine was used but has been banned due to the health issues associated with the compounds formed after continuous operation. Dispersants function by disrupting layers found in paraffinic lubricants which lower the overall viscosity.

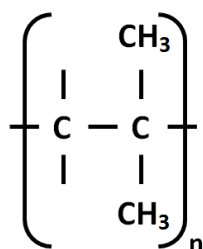


Figure 4.8. Polyisobutylene molecule can be used alone or in conjunction with succinimides.

4.2 Lubricant Degradation

Lubricant properties change over time due to sustained use and through contamination. Eventually the lubricant will no longer be able to form an adequate film boundary between surfaces. The main causes of lubricant degradation are increased acidity, water contamination, oxidation and prolonged high temperatures.

4.2.1 Acidity

The level of acid in lubricating oil can be affected by a number of factors but is primarily related to the amount of water, oxidation levels and types of additives. The most common types of acid found in gearbox lubrication are oxoacids, which are composed of one oxygen atom, one hydrogen atom bonded to the oxygen atom and one other element, usually carbon. Within the broad area of oxoacids, the most common group of acids to be found are carboxylic acids, nitric acid and sulphuric acid [70]. The presence of the nitric and sulphuric is usually attributed to combustion products of an engine and so are less commonly found within wind turbine gearboxes. An example of carboxylic acid formation is shown in Figure 4.9.

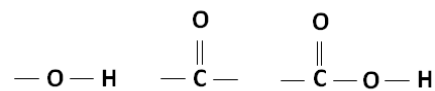


Figure 4.9. From left to right: hydroxyl, carbonyl and carboxylic acid.

Its presence is usually detected by the carbonyl group that is attached, either by a chemical reaction that breaks the double bond or by spectroscopic methods. The standard method of quantifying lubricant acid content is the Total Acid Number (TAN). TAN is the ratio of a standard base, usually potassium hydroxide (KOH), which is required to neutralise the acid present in the oil compared with the total volume of lubricant.

4.2.2 Water Content

Water can exist in oil in 3 different states: dissolved, emulsified and free with each of these causing different problems for lubrication effectiveness:

- **Dissolved** – Water molecules are low in concentration throughout the lubricant and cannot be visibly observed. The concentration may vary between 200-600 ppm depending on the lubricant type and temperature.
- **Emulsified** - The total amount of dissolved water has exceeded the lubricant capacity and small droplets can be identified visually.
- **Free** - Concentration of water has increased high enough that layers of water may form. These are normally observed in lubricant reservoirs.

The presence of free water in lubricating oil will cause corrosion to any metallic components. Contact with iron and oxygen will result in various iron oxides (rust) forming. This will cause contamination of the lubricant due to rust particles, surface damage due to the formation of oxides, scoring and block cooling passages. The corrosion can lead to ionic compounds existing within the oil, further disrupting its chemical properties. Emulsified water can cause several changes to occur to additives, depending on their chemical composition. Since a large number of commercial synthetic lubricants rely on the properties of additives, changes are significant. Hydrolysis is the process of water breaking down a compound by using its two ionic components, H^+ and OH^- . These ions will try and bind with different parts of a polymer, resulting in its structural breakdown, causing reduced lubricant effectiveness, changes to viscosity and potentially greater corrosion due to the presence of free ionic molecules.

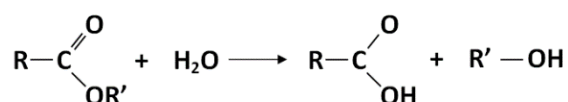


Figure 4.10. Hydrolysis reaction of an ester ('R' represents a general molecule) [70].

In Figure 4.10, a hydrolysis reaction is shown of an ester, often found in a variety of lubricants and oils [71]. In addition to splitting the structure, 2 hydroxyl groups are created which may react with other groups, further destabilising the lubricant. When water disassociates into oxygen and hydrogen, several problems can occur. Oxidation rates are accelerated due to the presence of oxygen and also metal particles which have formed oxides. Hydrogen will cause embrittlement of the iron, weakening steel components. As these cracks grow, failure probabilities increase.

4.2.3 Oxidation

Oxidation levels can be established by monitoring reaction by-products such as ketones, esters, aldehydes, carbonates and carboxylic acids [72]. Some of these molecules are dissolved in the oil or remain suspended due to the additives in the oil. The effect of prolonged oxidation is that the lubricant becomes more acidic which leads to corrosion and can also change the viscosity. The additional oxygen atoms can

either change the structure or break it up entirely into new molecules, both of which have serious consequences for the operating condition of the lubricant.

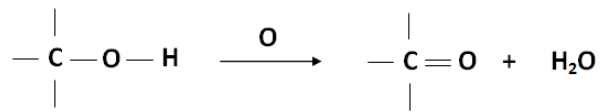


Figure 4.11. Oxidation of a hydroxyl group.

In Figure 4.11, oxidation of a hydroxyl group is shown. First, the creation of water is significant for the reasons mentioned in the previous section. The reaction also results in a carbonyl group (C=O), which can become carboxylic acid if there is another hydroxyl group attached. Other effects of oxidation include by products, such as hydroperoxides which can become large polymers long enough to start sludging in the oil [73]. This process can increase the viscosity significantly, adversely affecting the lubricants performance.

4.2.4 Temperature

The temperature of the lubricant is important due to its effect on the parameters already mentioned. As the temperature increases, rates of oxidation increase, viscosity decreases, lubricant components begin to suffer from thermal degradation and additives can become unstable. Whilst relatively simple to measure, temperature is still critical. High temperatures can also break down larger synthetic polymers into smaller molecules.

4.3 Application Methods

Two main methods exist for applying lubricant to the required gearbox components with the average pitch line velocity (see Section 2.5.1) determining which is used.

4.3.1 Splash Lubrication

In this method the component is submerged in a lubricant bath to a sufficient depth so that during operation it will pick up an adequate amount of lubricant and disperse it during mechanical interaction. As several different components usually require lubrication within a gearbox, it is most common to find that the casing is used as the

lubricant bath. The design of the casing should ensure that all components are splashed with a sufficient amount of lubricant. Due to the simple nature of the method, maintenance and monitoring requirements are low: it is only necessary to ensure that the lubricant remains clean and that the viscosity index does not alter over time to prevent excessive heating. The type of monitoring is also limited as the lubricant forms one unit and may only be assessed for oil quality and not component state. Wind turbines gearboxes for small scale turbines commonly use this type of lubrication system as the pitch line velocities are generally low.



Figure 4.12. Meshing gears with splash lubrication provided by reservoir at base.

4.3.2 Pressure-Fed Lubrication

For gearboxes with a higher average pitch line velocity, pressure-fed systems (also known as force-fed) are used. The exact configuration is component specific but in general lubricant is delivered from a reservoir using a pump to specific locations of the gearbox via feed lines. The components are normally encased so that lubricant is fed into one side and extracted from another. This continual circulation allows the lubricant to enter heat exchanges to facilitate component cooling as shown in Figure 4.13.

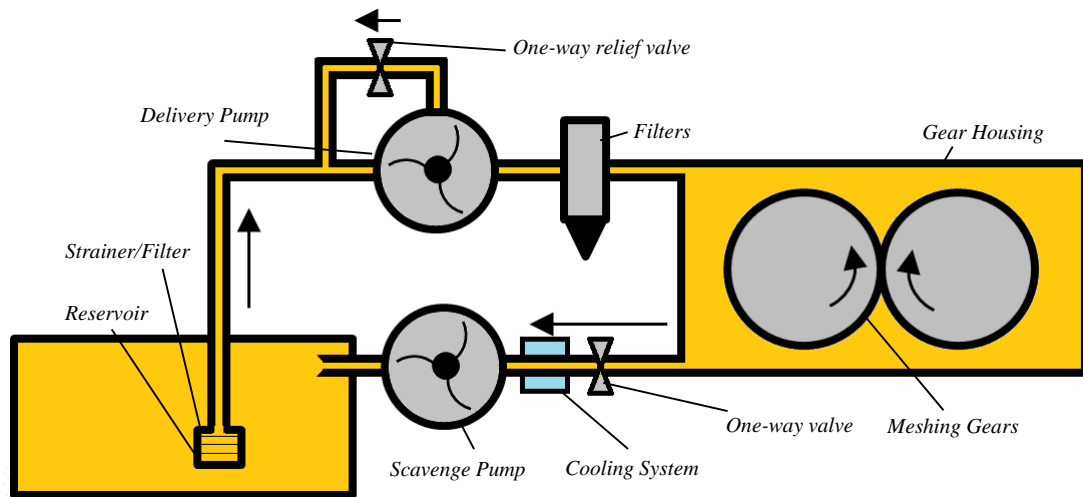


Figure 4.13. Pressure-fed lubrication system with main components labelled.

One consequence of the closed flow system is that liberated wear material from components will flow around with the lubricant. The particles are filtered out to prevent additional damage to components. However, sensors may be placed on the scavenge line that can monitor fluid. Several filters are normally used that target specific particle diameters (initially larger particles are removed with the sieve size gradually decreasing until in the final filter the smallest particles are removed). Pressure-fed lubrication systems normally serve the entire gearbox, depending on the gearbox configuration. This means that all wear particles from different components are mixed together which adds complexity to analysis methods.

4.4 Conclusions

The majority of large wind turbines use synthetic lubricants to ensure an adequate film thickness between contacting surfaces in the gearbox. Viscosity is the key parameter and can be reduced by a number of degradation methods, increasing the probability of destructive wear mechanism. Pressure-fed lubrication system offer an analysis advantage as wear particles may be monitored before filtering. Understanding which condition monitoring methods can be applied for this arrangement should be investigated.

Chapter 5 – Gearbox Lubrication Condition Monitoring

There has been considerable debate within the wind industry over the use of CMS; for example the economic benefit of certain CMS techniques has come under scrutiny for onshore turbines [74]. The need of CMS for offshore applications is widely accepted due to the higher costs associated with distance, weather conditions and the scale of maintenance intervention [75].

In this chapter, the various condition monitoring techniques currently used for gearbox lubrication will be summarised and assessed [76]. Whilst current systems do offer robust analysis, it is believed that by developing novel sensor techniques or improving existing methods, it will be possible to obtain new data types based on previously unrecorded parameters. Alternative technologies are also considered and are summarised in Appendix A and the most promising are discussed. The following criteria are used to assess each technique:

- Allow a new data source to be effectively tracked that improves understanding of the lubricant condition.
- Sensor could be feasibly deployed remotely and operate in a turbine nacelle.
- Relatively low cost so technique could feasibly be adopted by wind turbine operators.

Technology that was considered but not developed were those that could not fulfil these criteria. For example Karl Fischer tests require liquid iodine to determine water concentration. Fluorescence spectroscopy could create accurate spectra of the lubricant indicating quality but is expensive in its current form so is unlikely to be adopted by operators. Supervisory Control and Data Acquisition (SCADA) and vibration analysis are briefly discussed as they form a major component of robust condition monitoring systems. However, the sensory technology that drives their data capture (accelerometers for vibration, temperature sensors and piezoelectric resistors for SCADA) are mature and well established. Research into condition monitoring using these methods has focussed mainly into improving data analysis techniques. Better condition monitoring may be achieved by combining improved lubrication CMS with vibration analysis [77].

5.1 SCADA and Vibration Analysis

SCADA refers to computer-based industrial systems that provide up to date information on the performance of a machine. Typical monitored signals include:

- Wind speed derived from nacelle anemometer readings
- Generator rotational speed
- Power output derived from the electrical converter
- Rotor yaw based on position of nacelle

Unlike other industries SCADA is generally not used to control the operation of turbines and focusses on monitoring. Control is managed by a wind turbine controller system that automatically manages operational aspects such as yaw and blade pitch.

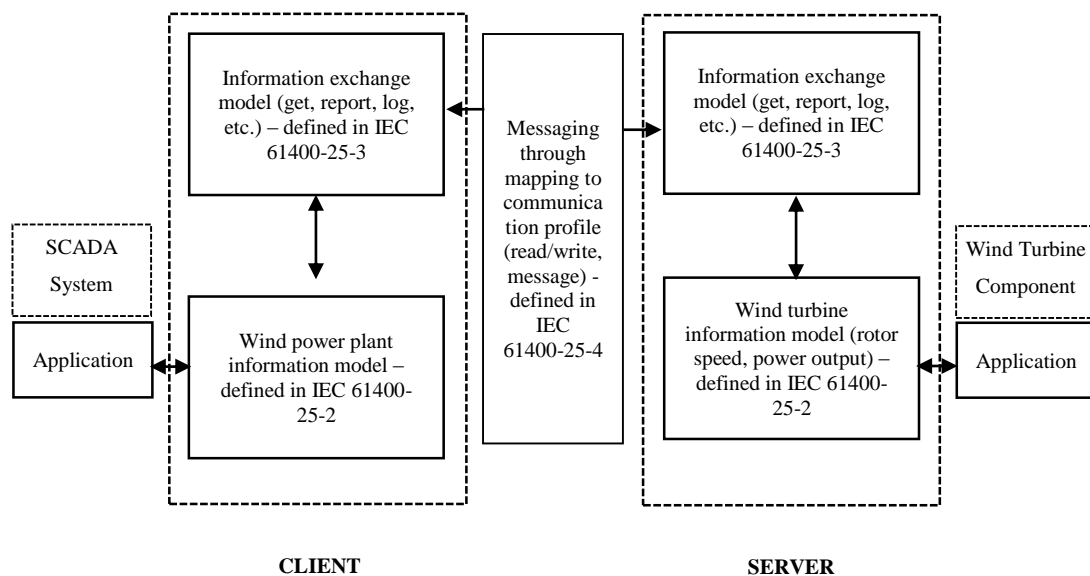


Figure 5.1. Conceptual wind turbine communication model based on IEC 61400-25 series.

An example of the communication model used in SCADA systems is shown in Figure 5.1. A large amount of SCADA data is collected directly from the wind turbine controller system, however, various SCADA systems now monitor signals from other sources as well [78]. The exact data collection, analysis types and reporting methods depends largely on the SCADA system designer. In general, commercial SCADA systems provide a graphical display of real time data trends including component temperatures, the generator speed, the wind speed and the power output. Clustering

algorithms are commonly used to interpret the data and decide if the wind turbine is performing optimally for the give conditions [79]. If suboptimal performance or degradation is detected, a warning is given to the user.

Gearboxes running under normal operating conditions will produce characteristic vibration signatures dependant on the interaction of rotating shafts, gear teeth meshing and other dynamic components. These vibrations are expected and the gearbox is designed to ensure the impact on internal components is minimal. However, when faults begin to develop, the vibration frequency and amplitude will alter due to the changes in component interaction. For example, if the rotor shaft develops a small misalignment, new displacements with the same frequency as the rotor can be detected. The vibration measurement may consist of displacement, velocity or acceleration, whilst the measurement may be absolute or relative [80]. These vibrations will also affect the first stage of the planetary gearbox, leading to a new vibration signature of the gear teeth.

SCADA data analysis is a major research area in condition monitoring of wind turbines. However, there is little improvement that can be achieved in the physical sensors that are to track key parameters. Temperature sensors are either thermocouples or resistive temperature detectors (RTDs) which can provide accurate data. Power datum is recorded by monitoring the generator output through the electrical control. Gearbox condition monitoring through vibrations signals is a vast subject with many different analysis approaches. The field is constantly being improved through better modelling and fault correlation analysis [81]. In terms of sensors, vibration CMS may be improved by including additional accelerometers to increase the total number of data sources [82].

5.2 Offline, Online and Inline Sensing

Condition monitoring systems can be categorised as either offline, online or inline [83]. Offline methods are those that require a trained operator to take data measurements at the target component. For example, in helicopter maintenance, lubricant samples will be extracted from the engine and may be analysed on-site or sent to a laboratory. In both cases, data can only be extracted when the helicopter is not operational.

Online techniques are those that have a condition monitoring system in place that can extract data from a component without the need for a human operator. However, the CMS will only extract data periodically due to the nature of the component or the limitations of the condition monitoring system. An example is magnetic particle counters that measure the change of inductance on the surface of a probe due to wear accumulation. Once a certain threshold of accumulation is achieved, the sensor reports a total mass of particles that have been detected. The sensor then flushes the probe by de-magnetising and allowing the particle to flow away. The sensor is classed as online as it can only report when a certain threshold of wear particle mass has accumulated, rather than instantaneous wear total. Other online systems include destructive sampling methods that burn a small sample of lubricant to determine quality through spectroscopic analysis. In this case, the system is limited to online analysis as lubricant cannot be continuously destroyed. In Figure 5.2, the difference between different analysis types are shown. It can be seen that online can require a test spur from the main flow to allow extraction.

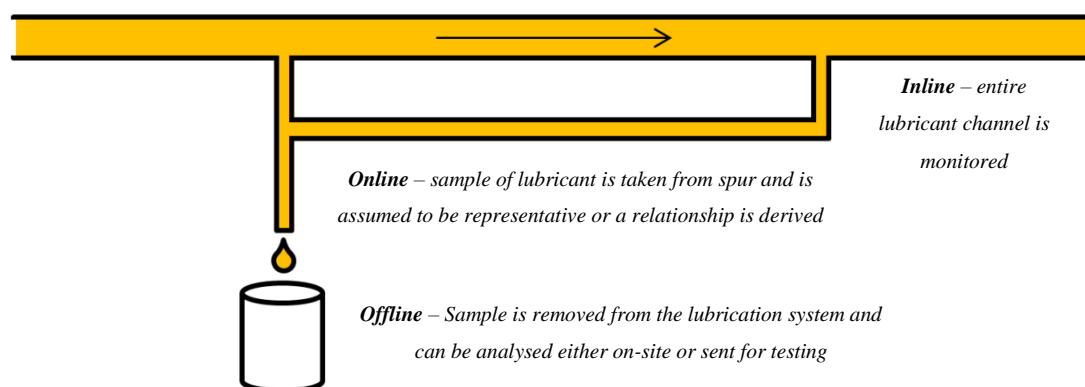


Figure 5.2. Inline, online and offline sampling of lubrication.

Inline methods are those that extract data and report continuously. An example is inductive coil lubricant sensors that report changes to the field of inductance due to changes in the lubricant composition from contaminants or wear. The voltage signal is continuously generated and reported. This chapter will focus on online and inline sensing technology as these are the most relevant categories when condition monitoring of remote wind turbines in onshore and offshore environments. However, offline methods that may be adapted into online are also discussed.

5.3 Currently Deployed Lubrication Monitoring Sensors

Due to the rapid development of wind farms worldwide and the need for condition monitoring, a large number of condition monitoring systems have been deployed in wind turbines. Crabtree et al have summarised current CMS in wind turbines in annual reports with the most recent from 2014 [84]. Vibration analysis using accelerometers is the most common condition monitoring technique used for gearbox analysis. Lubrication analysis using particle counters has also become more common since 2010 [84]. Some CMS will monitor several components simultaneously but may only have one single sensor monitoring the gearbox. For conciseness, only sensors related to gearbox condition will be discussed.

5.3.1 Light Source Particle Counters

Light source wear particle counters refer to sensors that quantify the number of discrete wear particles that passes through a lubricant channel. The sensors work on the principle that light passing through a highly opaque fluid will be affected by the presence of solid particles. This can be achieved using the following methods:

- **Light extinction** – the reduction in the total light passing through opaque fluid is correlated to the size of particles.
- **Light scattering** – the scattering of total light passing through opaque fluid is correlated to the size of particles.

Light extinction normally uses a laser source combined with a photodetector that generates a voltage or current signal that is relative to the total incident light upon the photodiode surface (total illuminance). When a particle passes between the laser

source and photodetector, the illuminance will reduce proportionately to the size of the particle [85].

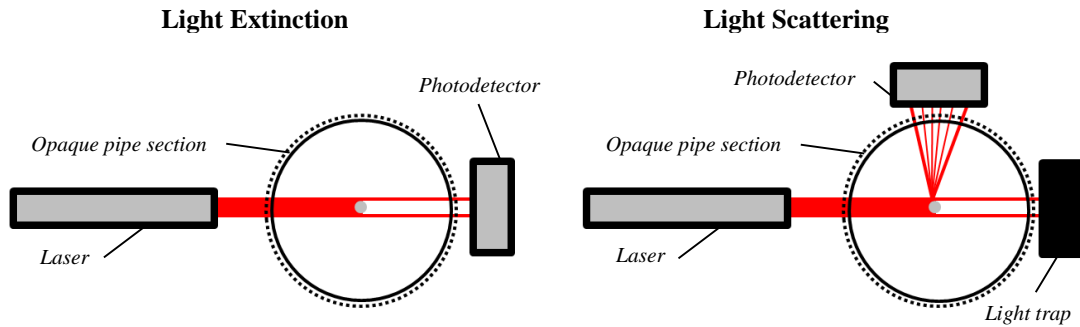


Figure 5.3. Operation of particle counter based on laser light extinction [85]

Light scattering also uses a laser source but with a photodetector at 90° to the laser source. When a particle passes in front of the laser source, light is reflected in different directions which can be detected by the photodetector. As the majority of particles are metallic with highly reflective surfaces, larger particles will have a greater scattering effect on the laser light. The operation of light extinction and scattering are shown in Figure 5.3. Some particle counters use both extinction and scattering by replacing the light trap with a second photodetector [86]. Laser light is normally used as it has a high degree of spatial coherence, reducing errors arising from signal loss.

In both methods the voltage or current generated by the photodetector is correlated to overall particle size experimentally [87]. Particle size is defined using the equivalent diameter of a non-circular object:

$$x_{eq} = 2 \sqrt{\frac{A}{\pi}}, \quad \text{Eq. 5.1}$$

where x_{eq} is the equivalent diameter of the object and A is the area [88]. The area is derived from the voltage signal of the photodetector. In this method, the particle is defined by x_{eq} and is assumed to be circular (see Figure 5.4). No morphological features are extracted by such particle counters.

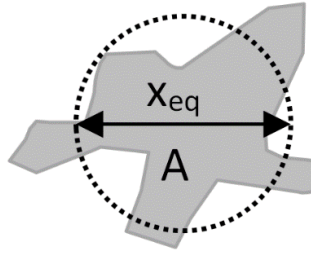


Figure 5.4. Equivalent diameter of a 2D object with area A.

Particle orientation is a problem for optical particle counters. They report a voltage signal based on a single light source and detector which means that if a flat particle is rotated in a particular orientation, its 2D orthographic projection may not be representative (see Figure 5.5).

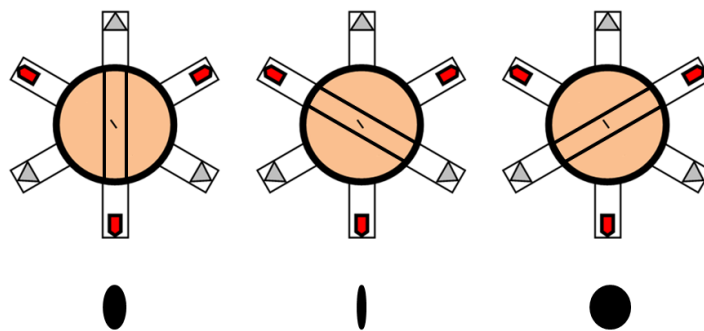


Figure 5.5. Effect on particle orientation based on a circular particle analysed using light extinction at different angles.

In pressure-fed lubrication systems, the lubricant channel diameter may be as large as 20 mm. Wear particles are in the order of microns and so a large number may be present within the cross-sectional flow of the lubricant. In order to detect individual particles, a spur line is taken from the lubricant channel which will remove lubricant. This spur line is much narrower and reduces the potential of 2 particles to pass the laser source at the same time. In this arrangement, online detection can only be achieved as the entire lubricant channel is too large to monitor effectively. It is assumed that the oil assessed is a random sample of the lubricant.

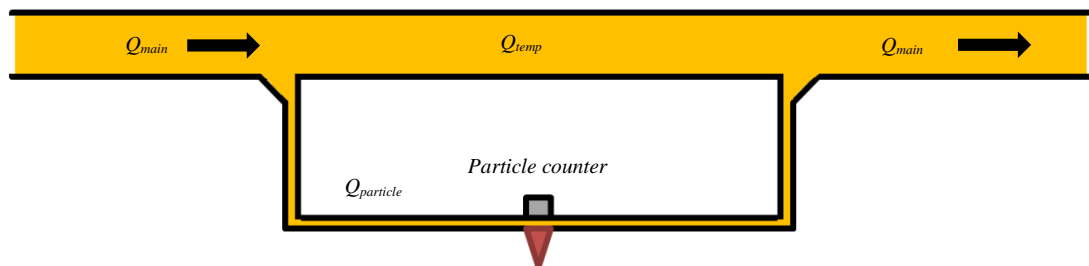


Figure 5.6. Particle counter using a flow spur to reduce flow cross-sectional area.

5.3.2 Electromagnetic Particle Counters

Electromagnetic particle counters are those that measure the change in electromagnetic properties of the oil caused by the local presence of metallic wear particles in the lubricant.

5.3.2.1. Inductance Sensor

Inductance sensors operate on the principle that the inductive field of a coil of wire will change when a metallic particle passes through it [89]. The sensor uses a non-metallic section of piping that is adapted to allow the lubricant channel to be sampled. The section has copper wire tightly wound around it (see Figure 5.7). The inductance of the coil is found when clean lubricant flows through it. When metallic particles pass through in the lubricant, the inductance will change, depending on the particle mass and whether it is ferrous or non-ferrous. The coils inductance is defined as:

$$L = \frac{\mu N^2 A}{l}, \quad \text{Eq. 5.2}$$

where L is the coil inductance, μ is the magnetic permeability, N is the number of turns, A is the area of the coil and l is the coil length [90]. The presence of ferrous particles will increase the magnetic permeability proportional to the mass of the particle, increasing inductance. Non-ferrous wear particles (from bearings and gears plated with molybdenum and other metals) increase resistive losses in the coil, reducing the inductive field.

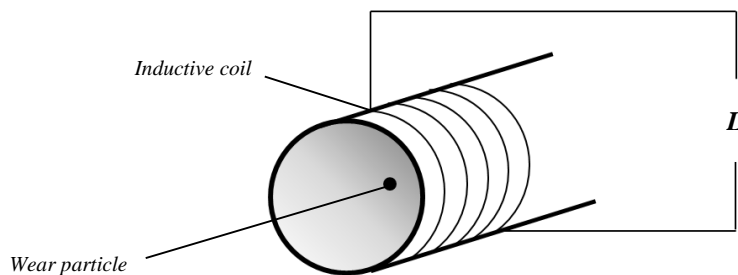


Figure 5.7. Change in coil inductance is used to detect particles.

The basic layout of an inductance sensor is shown in Figure 5.7. As inductance sensors can distinguish between ferrous and non-ferrous particles, it is possible to identify

components with known compositions. However, the particle size cannot be discerned, only total mass [89]. Similarly to laser counters, online detection can only determine an accurate total particle number by reducing the lubricant channel diameter. Inline sensors are used but track total liberated particle mass rather than discrete particles.

5.3.2.2. Magnetic Flux Sensors

Magnetic flux sensors monitor the change in a fixed magnetic field caused by ferrous particles. The field will be relatively weak so particles can continue to flow within the lubricant. A monitoring circuit will record the change in magnetic flux due to the presence of ferrous particles [91]. Inline monitoring can be achieved but would provide a general total of ferrous wear detected. Online sampling using a narrow spur line allows individual counting and classification by mass size.

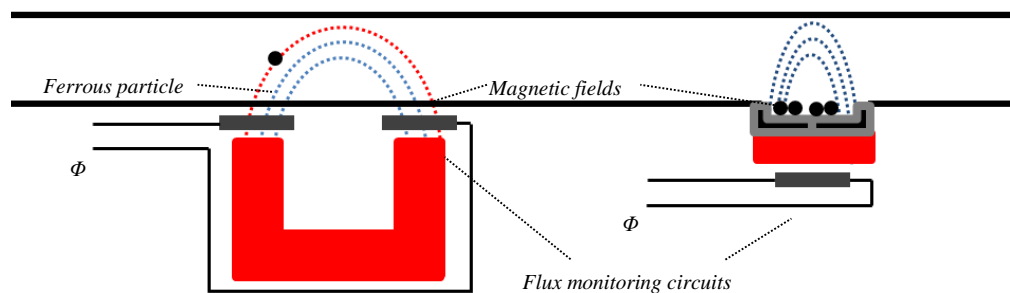


Figure 5.8. Magnetic flux detection (*left*) and collection (*right*) sensors measuring flux (Φ).

Others magnetic flux sensors use a strong field to pull particles out of the flow and deposit them on a desired surface. The field is only strong enough to hold a certain mass of ferrous material and when this is exceeded, the sensor ‘flushes’ by demagnetizing temporarily to allow a new period of deposition. The sensor reports a complete deposit which is correlated to the mass of particles. Only a general level of wear can be assessed in this method rather than an individual count and classification by mass. The basic layout of magnetic flux sensors are shown in Figure 5.8. In both methods, other metals such as molybdenum cannot be detected reliably [92].

5.3.3 Temperature Sensors

One of the earliest and most commonly monitored relationships is between the temperature of lubricant and gearbox condition. It has been demonstrated that a 10°C increase in the lubricant temperature can be correlated to earlier failures for the same relative power output [93]. As indicated in Figure 5.9, it can be seen that there is a significant correlation between higher lubricant temperatures and reduced period until failure. The 3 traces indicate the temperature of the gearbox lubricant at different rotational speeds in revolutions per minute squared (RPM²). At higher RPM², the lubricant has a higher temperature as more thermal energy is required to be dissipated due to increased work effort. However, an abnormally high lubricant temperature has been linked with a shortened period until the gearbox fails. It can be seen in Figure 5.9 that if the gearbox lubricant temperature is approximately 5-8°C for a given rotational speed, the period until failure decreases from 6-9 months to 3 months (indicated by the different traces).

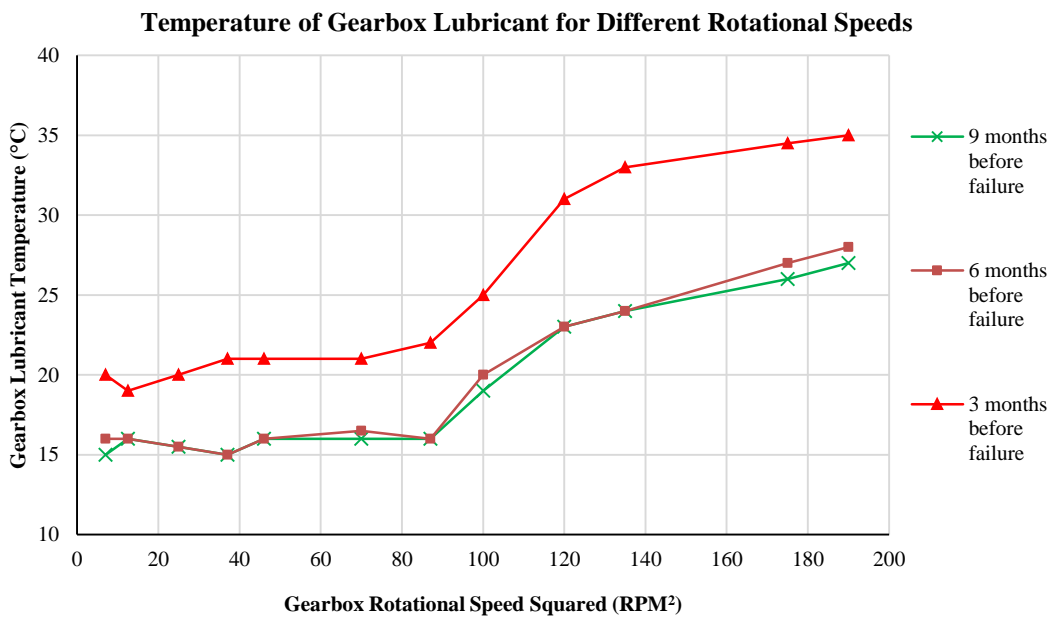


Figure 5.9. Trends of gearbox oil temperature rise vs. square of rotor velocity [94].

However, the physical temperature sensors do not require further development due to the maturity of this technology. Improving this method relies on applying data analysis methods that can correlate different temperature profiles to known fault conditions and mechanisms.

5.3.4 Dielectric Loss Factor Lubrication Sensors

The dielectric loss factor (DLF) is the ability of a dielectric material to dissipate electromagnetic energy into heat. As discussed in the previous chapter, lubricant degradation is associated with the formation of acidic compounds, increased water contamination and oxidation products. These compounds are classed as dielectric as they can be polarised by applying an electric field to them. The DLF is often called the tan delta and is defined as:

$$\tan\delta = \frac{\omega\epsilon'' + \sigma}{\omega\epsilon'}, \quad \text{Eq. 5.3}$$

where $\tan\delta$ is the loss tangent, ω is the angular frequency of the electrical field wave, ϵ' is the real component of the lubricant's permittivity (resistance to forming an electrical field), ϵ'' is the imaginary component of the lubricant's relative permittivity and σ is the conductivity of the lubricant. Initially, the lubricant will have a small loss due to its low composition of dielectric material. As degradation causes the emergence of water and acidic compounds, the DLF begins to increase due to the higher conductivity and higher relative permittivity (with the imaginary permittivity being the major component) [95].

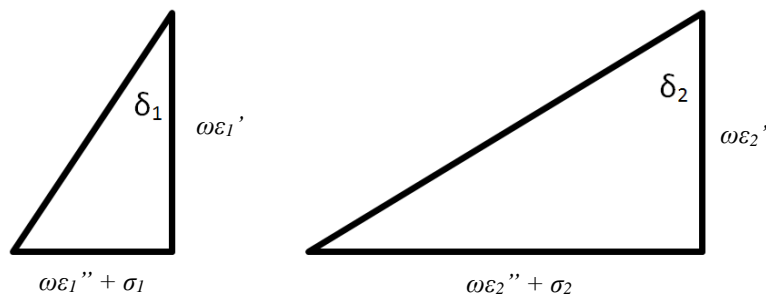


Figure 5.10. Increasing conductivity increases $\tan \delta$ of lubricant.

One of main issues with measuring DLF is the cause of the change in the lubricant condition is difficult to discern without additional data. It is also influenced by wear debris so must be used with a particle counter to compensate. In addition, some additives have dielectric properties and are gradually consumed through continuous use [96]. This may lead to a decrease in the DLF which may negate any increase due to degradation contaminants.

5.4 Applicable Lubrication Analysis Techniques

A review of current lubrication techniques and technology that could potentially be applied was conducted to assess the current state of the art [97]. A summary of the review can be found in Appendix A. The review concluded found that a diverse range of technologies exist that could be adapted for use as an inline/online gearbox lubrication sensor. However, the most promising technologies were ferrography and infra-red spectroscopy due to a combination of cost, complexity and practicality.

5.4.1 Ferrography

Ferrography is a process that separates magnetic and non-magnetic particles from oil and then uses an optical imaging sensor to analyse them. The first stage is to create slides called ferrograms (see Figure 5.11) for observation. The oil sample is diluted and allowed to flow down the ferrogram that is at an angle and has a magnetic cylinder underneath. The angle means that the magnetic field experienced is weaker at the start and stronger at the end. This causes larger ferrous particles to deposit at the start and smaller ferrous particles at the end [98].

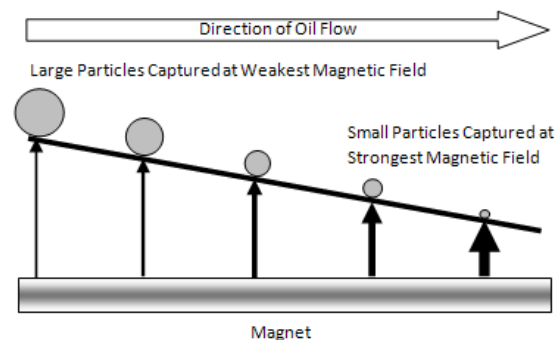


Figure 5.11. Operation of a ferrogram with particles deposited along plate according to mass.

Non-ferrous particles are deposited on the slide at locations depending on the concentrations of ferrous particles. If there were no ferrous particles in the sample, relatively few non-ferrous particles would be captured in the ferrogram despite high concentrations in the sample. The slide is then washed to remove any lubricant and is ready for analysis using a bichromatic microscope. A reflecting red light source is situated above the sample and a green transmitting light source is situated below. They transmit through glass which has been selected to prevent absorption of light. A digital

camera is used to take images that can then be classified. The categories of particles used by technicians are summarised in Table 5.1. In addition, the size and shape of particles can also be classified.

Table 5.1. Categories for non-ferrous and ferrous particles.

Non-Ferrous	Ferrous
White Nonferrous Particles	High Alloy Steel
Copper Particles	Low Alloy Steel
Babbitt Particles	Dark Metallic Oxides
Contaminants	Cast Iron
Fibres	Rust (Iron Oxides)

There is high potential to develop ferrography as a sensor. Online ferrographs have been created recently which use digital image processing in order to identify particles [98]. Currently accuracy and reliability depend on many different factors such as the flow rate of lubricant, the magnetic field strength and the distribution patterns of deposited particles. A key advantage of this system is the images captured are available for analysis using image processing techniques.

5.4.2 Infra-Red Spectroscopy

Infra-red spectroscopy (IRS) operates using the principle that chemical bonds will absorb a unique wavelength of infrared radiation (IR) corresponding to their resonant frequency [99]. This is the frequency at which a particular mode of the molecule will vibrate at when suitably excited. Figure 5.12 shows the first 3 modes of a simple molecule.

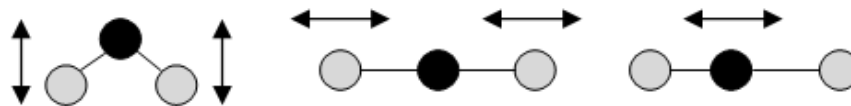


Figure 5.12. First 3 vibrational modes for a simple molecule.

Absorption IRS is the most common method used to identify molecules. In its simplest form, a beam of monochromatic IR radiation is directed at a reference sensor to detect the wavelength emitted [100]. The same beam is then directed at the sample with a

sensor positioned underneath that will detect if the beam passes through or has been absorbed and the process is repeated for the desired range of IR wavelengths. The main problem with this method is the length of time it requires to analyse all the desired wavelengths. However, a process known as Fourier Transform Infrared Spectroscopy (FTIR) may be used instead. Instead of using a monochromatic source, a ‘broadband’ beam consisting of a range of wavelengths will be passed through the sample and the values of wavelength which are absorbed are recorded by the sensors. This process is repeated several times, but using different combinations of wavelength values in order to establish separate data points which can be interpreted using Fourier mathematics.

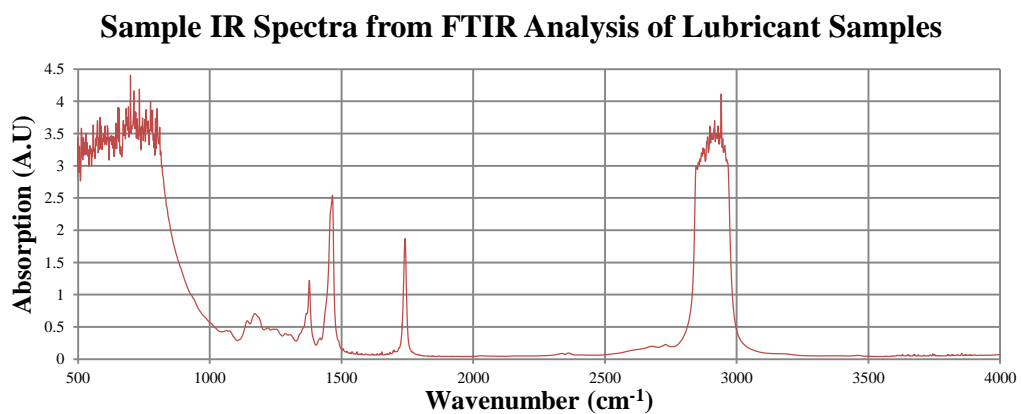


Figure 5.13. Amount of IR radiation absorbed for each particular component of a sample.

IRS can produce absorption spectra as shown in Figure 5.13. It shows which frequencies of IR radiation are absorbed and to which degree. These spectra can provide information regarding the lubricant condition. For example carbonyl is a major indication of the level of oxidation in a lubricant. It consists of a double bonded carbon and oxygen molecule ($C=O$) that is connected to a larger lubricant hydrocarbon. The wavelength which will be absorbed by this bond is approximately $1720-1740\text{ cm}^{-1}$ [101]. A defined peak at this wavenumber can be observed in Figure 5.13. Other peaks and other spectral features can indicate other lubricant parameters [102]. However, an additional complexity arises when additives are included. There are currently commercially available hand held IRS devices which have the ability to measure TAN, TBN, oxidation, nitration, sulfation, glycol, water and glycerine within 1 minute [103]. However, the unit cost of each device is high.

5.5 Conclusions

Wear particle counters that are commonly installed as part of gearbox CMS do not report particle morphology, a major indicator of gearbox failure mechanisms. In addition, fully inline monitoring cannot be achieved with light source particle counters as the flow volume must be reduced to allow analysis. Offline particle analyses techniques like ferrography often use microscopes and digital cameras to produce high resolution images of wear. Developing a sensor that can combine the inline capabilities of wear particle detectors with the morphological analysis of ferrography, a new data source may be tracked that can be correlated to failure mechanisms in the gearbox. The main challenges of such a sensor would be capturing images of sub 500 μm wear particles in real-time with sufficient accuracy to determine morphological features. The proposed sensor system would require application of real-time image processing combined with an appropriate image sensor and tested on a representative pumped lubrication system found on wind turbine gearboxes.

Similarly, infra-red spectroscopic analysis was identified as a potential technology that could be adapted into a low-cost lubrication monitoring sensor. Since full IR is costly and the necessary equipment precludes use in a wind turbine nacelle, the main challenge is to develop a more focussed system that used the same principles. Gearbox lubricant IR spectra have shown that degradation is observed at specific wavebands, rather than across the full spectra. For example increased oxidation can be correlated to changes in absorbance at 1720 cm^{-1} which reduces the importance of monitoring other wavebands. Development of a system that would target specific IR wavenumbers of key lubricant conditions may allow costs to be reduced while providing accurate data on the lubricant condition.

Chapter 6 – Development of Lubrication Wear Sensor

From the conclusions in Chapter 5 it was decided to develop an inline sensor that could function in a similar manner to online ferrography. In this chapter the development stages of the novel wear sensor from concept to testing are described. The wear sensor design was based on the principle of using active pixel sensors found in imaging devices to capture images of particles in a format that allowed quick and efficient analysis of shape from which wear characteristics could be determined.

To allow representative testing of the wear sensor, a lubrication simulation rig was developed to simulate a circulatory closed loop gearbox lubrication system. The rig is described briefly to indicate the conditions under which sensors could be tested.

Development of a novel wear sensor that may analyse particles for shape began by investigating the application of digital imaging based on technology found in devices such as webcams and digital camcorders. Advances in digital video hardware have lowered the cost of high resolution active pixel sensors (APSs) which are found in a variety of household technology. Webcams and other optical systems are available with high video resolution and frame rates, allowing a high level of detail to be captured at a low cost. When coupled with focussing equipment such as lenses, it is possible to capture images of very small objects with a large amount of clarity. It was considered that these APSs may be capable of providing inline, real time images of particles suspended in wind turbine gearbox lubricant [98].

6.1 Test Rig Layout

The rig was developed within the University of Strathclyde under a joint project between the Wind Energy Centre for Doctoral Training, the Department of Electronic and Electrical and the Department of Mechanical and Aerospace Engineering. The schematic of the rig layout is indicated in Figure 6.1 and the actual rig is shown in Figure 6.2. The system was required to simulate a closed loop lubrication system and the following features were included:

- Oil tank to house an industrial standard lubricant.
- A pump capable of delivering flow across a range of conditions.
- Heating system to create changes in temperature.
- Modular pipe network for integration of sensors.
- Measurements sensors and instrumentation for monitoring and control.

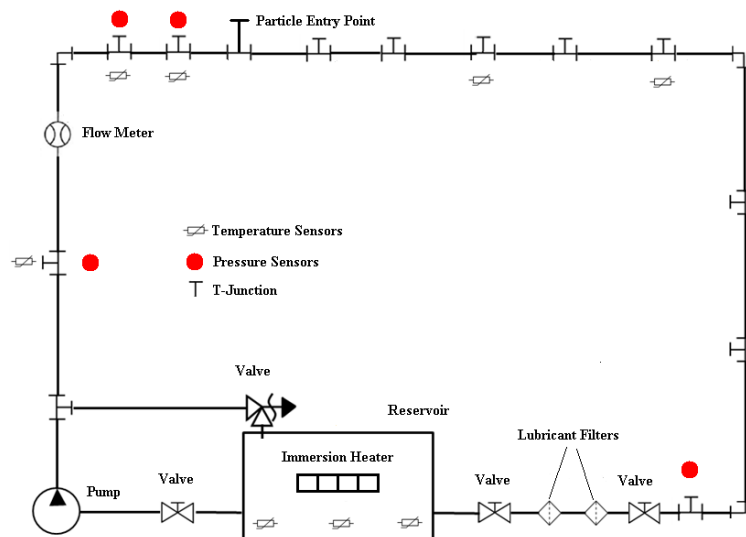


Figure 6.1. Schematic of physics simulation rig used for testing sensors.



Figure 6.2. Photograph of simulation rig.

6.2 Test Rig Components

The construction of the test rig was undertaken by the University of Strathclyde's Mechanical and Electronic and Electrical Engineering workshops. Individual components were sourced from different manufacturers and were integrated into the rig also by the Electronic and Electrical Engineering workshop staff.

6.2.1 Rig Pipework

The test loop framework was approximately 1 m in height with a breadth of 2 m, giving a total pipe length of 6 m. Standard 15 mm copper piping with associated fittings was selected for the pipework due to its robustness, ease of forming and wide availability (see Figure 6.3).

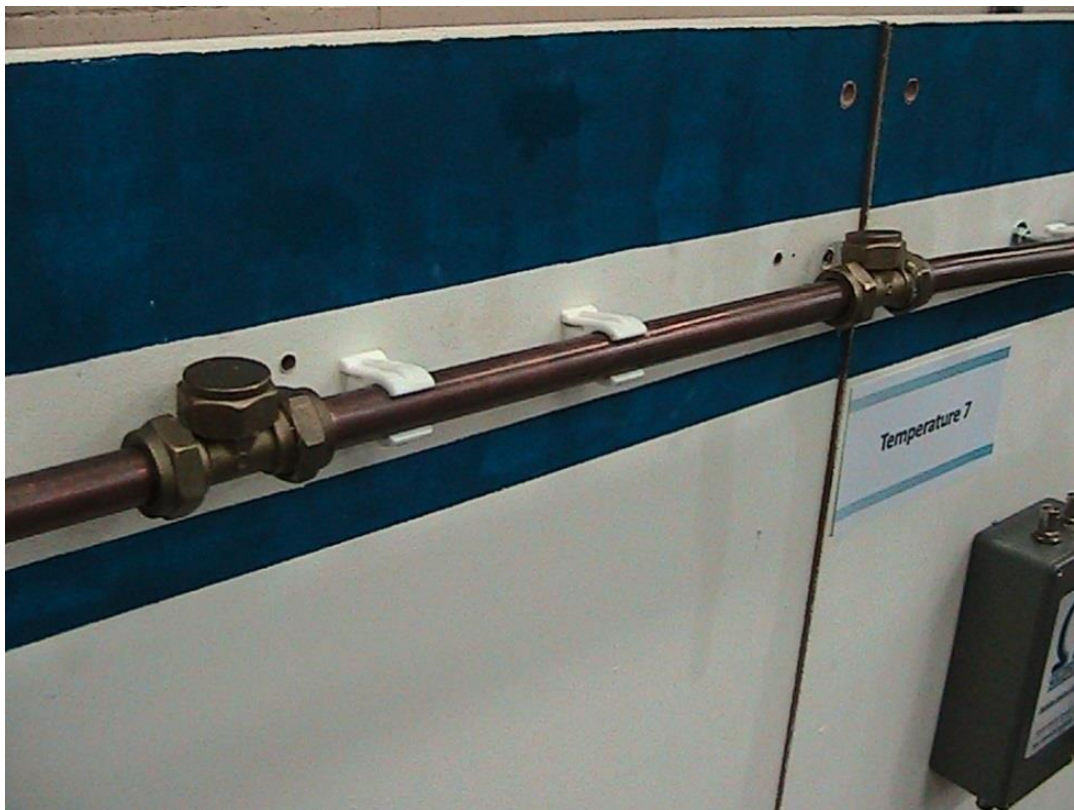


Figure 6.3. Rig with 300 mm copper pipe sections visible.

6.2.2 Mono CMM263 Progressive Cavity Pump

A rotary positive displacement pump was selected over kinetic pumps as perform better when inducing flow in high viscosity liquids like lubricants. Positive displacement raises the pressure of the fluid drawn into the cavity between a rubber stator and helical rotor. The fluid will exit with constant flow rate at given speed regardless of the discharge pressure. The rotational speed of the pump is proportional to the volume transferred.

A Mono CMM263 progressive pump was selected as it had a maximum flow rate $0.0265 \text{ m}^3/\text{min}$ with a 25.4 mm inlet valve (see Figure 6.4). This meant it was capable of providing a 7.5 m suction head which was adequate for the system requirement of 5.09 m head [104].



Figure 6.4. Mono CMM263 Progressive Cavity Pump [104].

6.2.3 Lubricant Reservoir and Heater Elements

The lubricant tank was a steel construct with one side removed and replaced with 10mm thick polycarbonate for viewing. The tank had one inlet and outlet screw adapter to which the 15 mm copper pipe was attached. Two immersion heaters were incorporated into the tank through circular openings. A 22 mm fill port allowed lubricant to be poured into the tank. The oil reservoir holds approximately 12 l of lubricant with 2 l held within the pipework (see Figure 6.5).

The heating element was selected by calculating the energy required to heat 10 l of lubricant from 20 to 50°C within 60 mins. The heaters used to meet this specification were two 400 W stainless-steel EMH series from Omega Components. The rig may operate under pressure if the reservoir was sealed, however, it was generally operated at atmospheric conditions. A series of valves also allows the flow to be constricted or blocked.



Figure 6.5. Reservoir with 6l of XMP320 lubricant contained inside.

6.2.4 Measurement Sensors

Four MPX5700D piezoresistive transducers were incorporated to measure the pressure within the system (see Figure 6.6) [105]. The sensors operate by measuring the change in depth of the piezoelectric material which created a change in resistance.

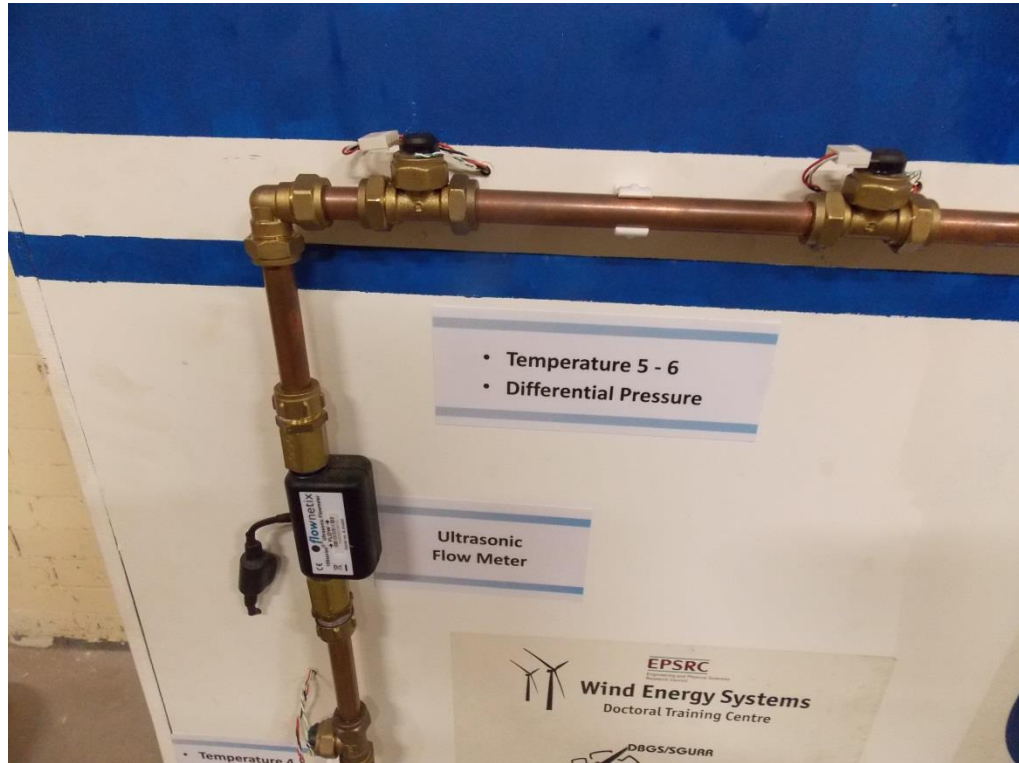


Figure 6.6. Flowmeter, thermocouples and pressure sensors located on the rig.

A FlowNetix ultrasonic flowmeter was used to track the instantaneous flow rate [106]. The sensor measured the feedback of ultrasonic pulses within a small chamber and passes on a square wave signal with the amplitude proportional to the flow rate and the breadth to the volume of flow. K type thermocouples were incorporated to sense the temperature at the lubricant tank, pump, filters, pressure sensors and pipe fittings [107].

6.2.5 Particle Delivery Valves

Wear particles were introduced into the lubricant flow by incorporating two isolator valves with a 100 mm gap between them (see Figure 6.7). Both valves were initially secured when a new flow regime began to ensure no leaks occurred. The top valve could then be released so particles mixed in lubricant could be poured in. The top valve would be closed and the bottom opened until the end of the current test.

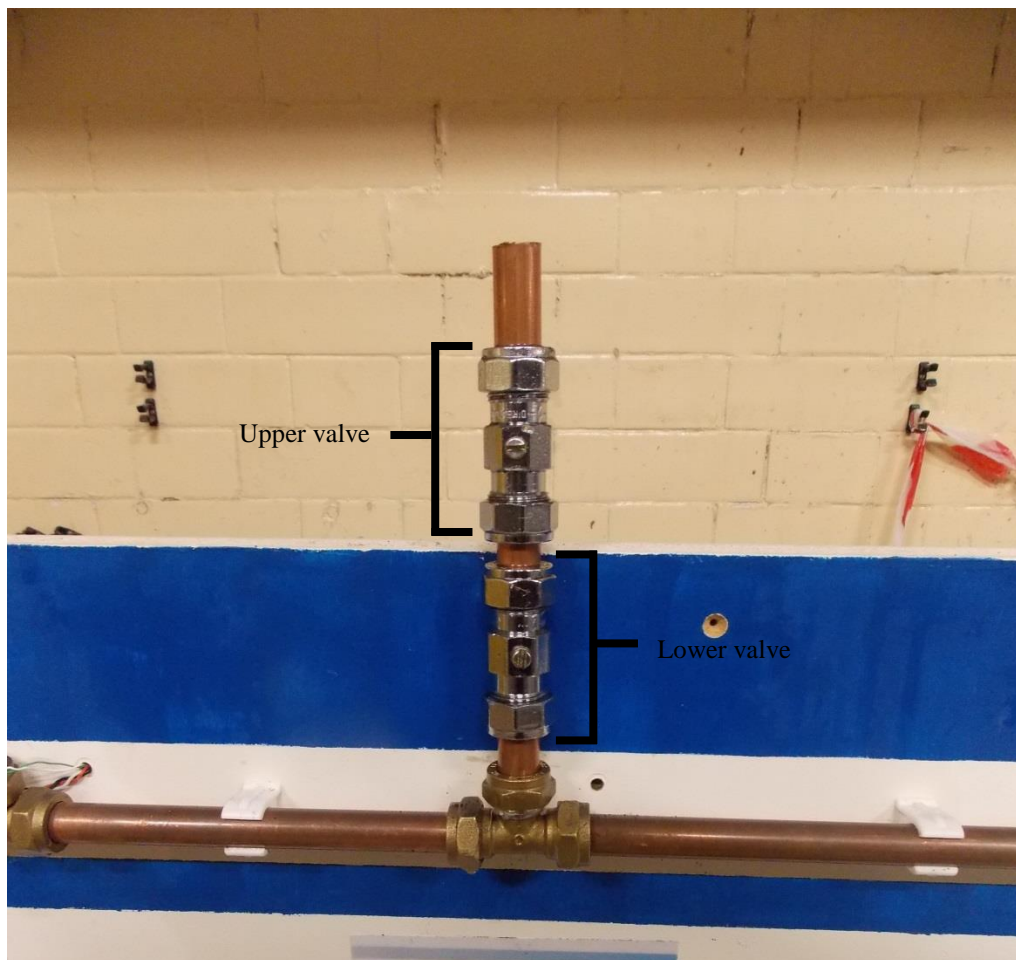


Figure 6.7. Two isolation valves to allow wear particle regimes to be introduced.

6.2.6 Inline Filters

A 10 μm Parker Lubrication 18P Series high pressure membrane inline filter and a 400 μm inline filter were used to remove wear particles from the rig (see Figure 6.8). This meant that particles could be introduced into the lubricant and then removed. These were necessary to ensure that some testing regimes did not cross-contaminate other experiments. The filters required regular cleaning to ensure they remained functional and to ensure uniform test conditions.



Figure 6.8. 10 mm filter is last component before lubricant re-enters reservoir.

6.2.7 Data Acquisition and Rig Control

The test rig incorporated National Instruments hardware and software to capture and present data for analysis. The CompactRIO (cRIO) is a programmable automation controller consisting of a real-time controller which executes LabVIEW Real-Time applications [108]. These are developed using LabVIEW on a computer before being exported to the cRIO. The controller can perform analysis, control tasks, log data, display user interfaces on monitors and communicate with any modules connected (see Figure 6.9). The input/output modules interface sensors with the cRIO, allowing data capture and can be used for a variety of measurement types including voltage, current, strain, accelerometers and thermocouple.



Figure 6.9. CRIO-9022 Real-Time PowerPC Controller [108].

On the rig, the cRIO was used to control the flow rate of the lubricant and the temperature of the sump heaters. Flow rate was controlled by sending the measured flow rate from the ultrasonic flowmeter back to the cRIO where proportional-integral-derivative control was used to set the pump speed. A similar system was used to control the temperature of the lubricant using the thermocouples.

6.2.8 Test Lubricant

MobilGear XMP 320 lubricant was selected for testing for this study as a widely used wind turbine gearbox lubricant. The lubricant also had an adequate viscosity index for use in the test rig to test sensors. Many gearbox lubricants would have too great a viscosity at the temperature ranges which tests could be conducted in the current laboratory. The lubricant characteristics are shown in Table 6.1.

Table 6.1. MobilGear XMP Series Lubricant Characteristics [109].

	XMP 100	XMP 150	XMP 220	XMP 320	XMP 460	XMP 680
<i>ISO Viscosity Grade</i>	100	150	220	320	460	680
<i>Kinematic Viscosity @ 40° C (cSt)</i>	100	150	220	320	460	680
<i>Kinematic Viscosity @ 100° C (cSt)</i>	11.1	14.6	18.8	24.1	30.6	36.9
<i>Viscosity Index, ASTM D 2270</i>	96	96	96	96	96	89
<i>Pour Point, °C, ASTM D 97</i>	-30	-27	-24	-18	-12	-9
<i>Flash Point, °C, ASTM D 92</i>	250	258	272	268	270	272
<i>Density @15.6° C, ASTM D 4052, kg/l</i>	0.890	0.896	0.900	0.903	0.909	0.917
<i>Weld Load, kg</i>	250	250	250	250	250	250
<i>Load Wear Index, kgf</i>	45	45	45	45	45	45
<i>Sea Water</i>	Pass	Pass	Pass	Pass	Pass	Pass

6.3 Active Pixel Sensors

APSs were first described in the 1960's during the development of passive pixel sensors to replace vacuum-tube imaging devices such as cathode rays [110]. The main distinction between the two types is the inclusion of an in-pixel amplifier [111]. Modern APSs have their origins in work conducted by Eric Fossum in the early 1990's to create miniature charged coupled devices (CCDs) for image capture in NASA projects [112]. During that period, CCDs were the main type of image sensor used in industrial applications and consumer devices such as video cameras.

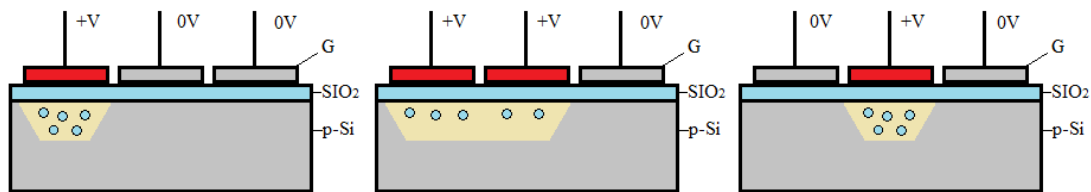


Figure 6.10. Charge transfer operation of a CCD chip. Losses can occur when electrons are not transferred fully, resulting in pixel degradation.

CCDs operate by incorporating a lens to focus light onto a photoactive region comprising of individual pixels. The light causes a proportionate charge to accumulate (dependent on intensity and wavelength of light). A second region then transfers the individual charges via a serial register into an amplifier which converts the entire charge into a voltage signal that can be measured. However, CCDs have several problems that become more apparent when using small mobile devices such as cameras.

CCD's are a capacitor array of photoactive material (generally silicon) which will generate a charge proportional to the intensity of incident light. The array is reset and exposed to an image which is captured by the capacitors. To convert the charges into a recognisable digital signal, each column of the array transfers the charge to the adjacent capacitor. At the end of each column a charge amplifier increase the signal amplitude. In the process, the entire image is converted into a series of voltage signals appropriate for digital processing. However, the transfer of charges requires relatively high power and perfect charge transfer. The capacitor transfers its accumulated charge by switching on the successive gate voltage of each pixel and switching off the

preceding gate voltage as shown in Figure 6.10. If any charge is lost, the final signal will be degraded and may not represent the incident light level accordingly. CCDs also suffer from ‘blooming’ where intense light can cause a large charge to accumulate in one pixel region and spread to nearby pixels. Integrating CCDs with complementary metal–oxide–semiconductor (CMOS) circuitry used for on-chip signal and image processing (for example digital cameras) is also difficult with high manufacturing costs [112].

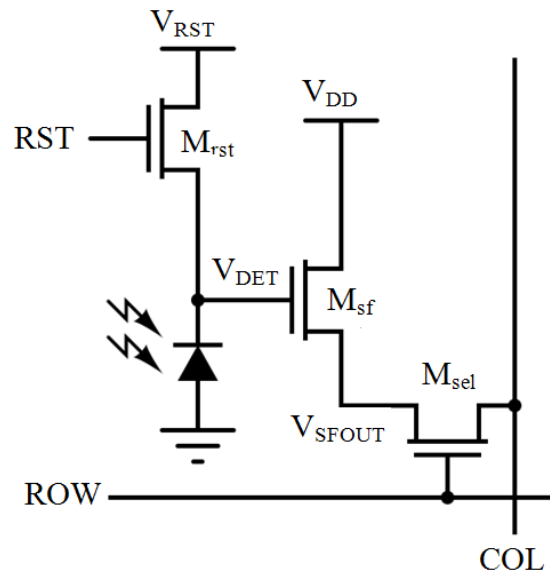


Figure 6.11. A standard 3T APS cell layout.

APSs operate by performing the charge to voltage conversion within each individual pixel in the array, commonly found in an arrangement known as a 3T cell [113]. In this system, the photodetector generates an electrical charge proportionate to the intensity and wavelength of the incident light, as shown in Figure 6.11. The photodetector is connected to reset transistor, M_{rst} . If the reset signal (RST) is initiated, the reset transistor connects the photodetector to the reset voltage, V_{rst} . This removes the charge that has been generated by the incident light. If the reset gate is not initiated, the charge generated by the photodetector develops a voltage signal, V_{det} , which enters the gate of the read out transistor, M_{sf} . This read out transistor acts as source follower, where the drain for the gate and the voltage source, V_{DD} , is shared. When a path from the transistor voltage source and ground is made when V_{det} enters the gate, an output voltage, V_{sfout} is generated that is close to V_{det} . The input impedance for the gate is

extremely large, so M_{sf} does not drain any of the charge from the photodetector. In this way the output voltage, V_{sfout} , will be a proportionately amplified value of V_{det} without altering the signal source. The circuit now has a voltage signal based on the incident light that can be readout using the ROW and COL connections.

Normally several thousand 3T cells are contained within a single array in a standard row and column formation. A control circuit is used to select which row is desired to be read. When this occurs a voltage is sent along ROW to the gate of the selection transistor, M_{sel} . This causes V_{sfout} to transfer to the output COL. The voltages for each column for that particular row are then stored and the control circuit switches to the next row. Once all column values for every row have been collected, an image can be derived based on the value of the voltage signals at every position of the APS array. The process is illustrated in Figure 6.12. To allow a new image to be captured, the reset signal is initiated for all 3T cells within the array and new signals are generated.

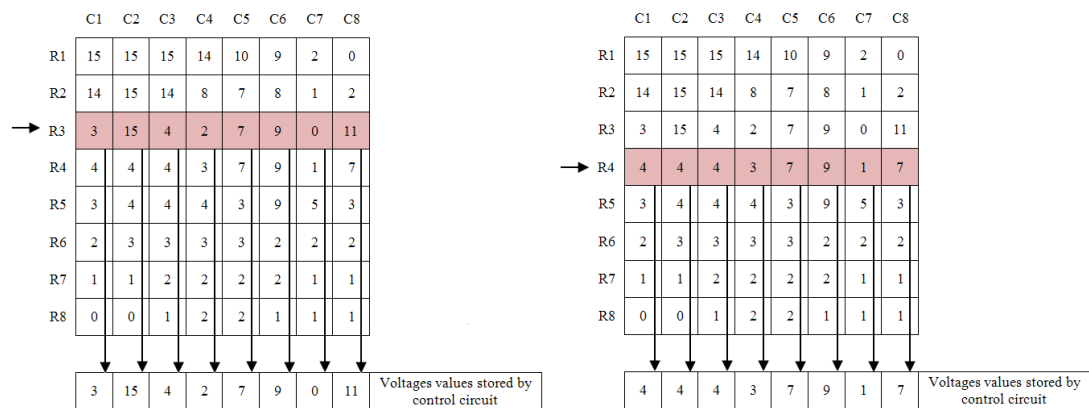


Figure 6.12. Readout procedure for an array of APS sensors.

6.4 Active Pixel Sensor Device Selection

A wide range of devices incorporate APS sensors for generating images and videos. Webcams were selected as the most suitable device for the following reasons:

- Most webcams use a USB connection, allowing them to be connected to computers where the test software would be developed.
- Integrated CMOS signal transfer between USB and pixel array allows the principle of the sensor to be tested rapidly.

- Generally low cost of the devices allowed greater freedom to experiment.
- The MATLAB Image Processing Toolbox included driver software that allowed most webcams to be instantly identified and operated without manufacturer software [114]. This software was identified early on as a likely candidate for developing the capture and analysis program.

Several standard webcams were purchased with different total pixel numbers and optimal focal range. A summary of the different types is shown in Table 6.2.

Table 6.2. Summary table of webcam characteristics.

Manufacturer	Resolution (MP)	Focal Length (mm)	Focus Type
Bush	1.5	5	Manual
Bush	3.1	4	Manual
Microsoft	2.2	5	Automatic
LG	3.2	4	Automatic

Manual focus webcams used a small lens that could be moved to varying distances from the APS array. This allowed the webcam to focus on objects within 10mm of the array which made them ideal for lubricant channel sensor development. It was also expected that during installation of the webcam onto various test rigs, the lens may move slightly. The manual focus allowed small corrections to be made. In addition, the test rig recirculatory feed and scavenge circuit had an inner diameter of 13.6mm. It was expected that heavier particles would traverse the pipe near to the bottom whilst lighter particles remain suspended in the faster central region. The distance between the two regions may be of the order of 10mm so in order to detect particles accurately, the lens needed to be focussed on the region of interest.

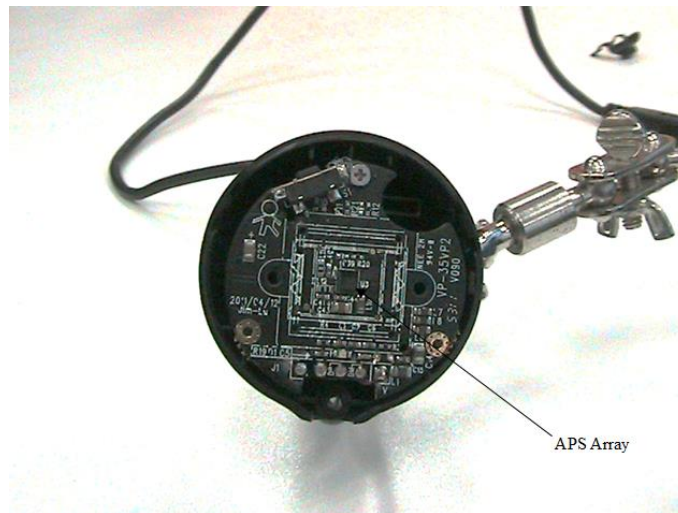


Figure 6.13. APS Array visible in centre of exposed webcam device.

Automatic focus webcams used digital image processing to determine the optimal focal length based on the contrast of the presented image. This prevented manual selection of a desired focal range and so the sensor development continued with only manual focus webcams. The 1.5 MP Bush webcam was selected due to its larger focal length and manual focus (see Figure 6.13). The webcam was stripped of excess packaging to allow easier manipulation when mounting the camera on the sensor assembly. Initial testing of the webcam using factory installed software confirmed that videos and images of stationary objects (such as printed dots) with a $100\mu\text{m}$ major dimension within 10mm distance of the lens could be captured (see Figure 6.14).

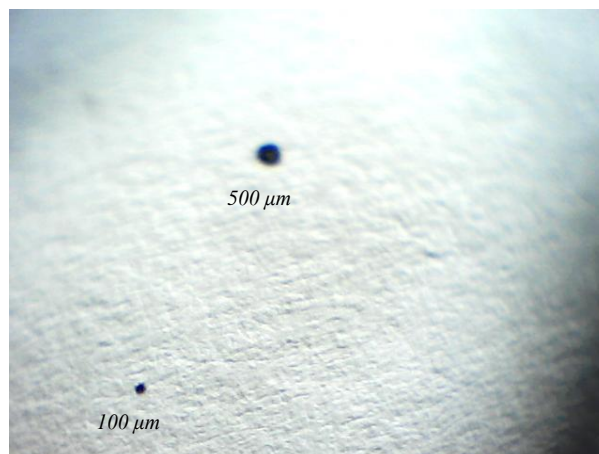


Figure 6.14. 100 and $500\mu\text{m}$ circular printed on dot captured with webcam at 10 mm distance.

6.5 Sensor Assembly Design and Construction

The next stage was to develop an assembly that would allow the sensor to be integrated with the simulation test rig and also view the fluid adequately in order to capture particle images. The schematic layout is shown in Figure 6.15.

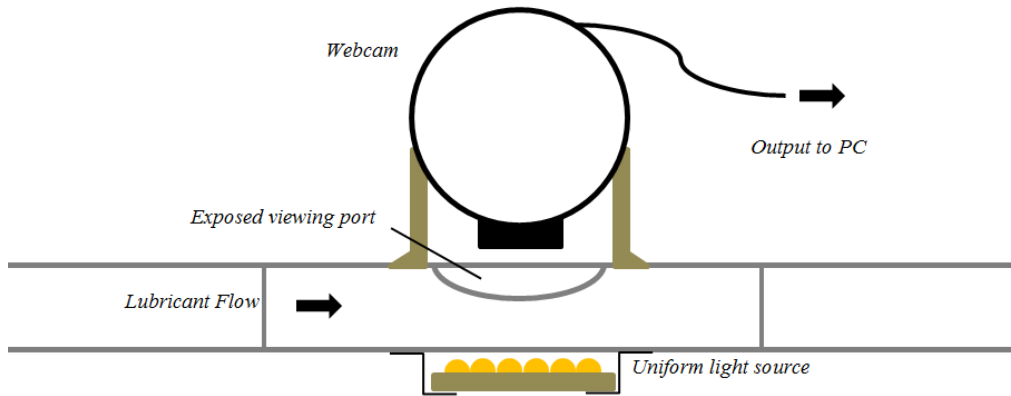


Figure 6.15. Proposed layout of sensor assembly.

The test rig pipework consisted of 15mm diameter copper piping approximately 300mm length connected together with straight brass couplings. The intention was to fit the assembly in one of these sections as shown in Figure 6.16.



Figure 6.16. Rig with 300 mm copper pipe sections visible.

The main challenge was setting the webcam to view the fluid which would require piping made of an opaque material suitable for pressurised conditions. Perspex or acrylic cylindrical piping was sourced that could connect securely with the straight

couplings. The curvature of these pipes acted as a lens, disproportionately increasing the appearance of particle flowing within. This effect may be exploited to increase the size of particles which may be undetectable by the APS array. However, the magnification was not uniform, with particles traversing in the centre region magnified disproportionately compared to particles close to the lubricant-pipe boundary. Square acrylic piping was tested and offered the following:

- Uniform and unmagnified representation of the particles.
- Mounting of the webcam was relatively simple due to the regular shape.
- 2 webcams may be mounted at 90° to each other for developing 3D particle images.

The main problem with square acrylic piping was adapting the ends to fit the circular copper piping or couplings. 10x10 mm acrylic piping was selected which could fit inside two 50 mm sections of 15 mm copper piping once the acrylic corners were sanded down slightly. The inner dimensions of the pipe was 6x6 mm. Epoxy resin was then used to seal the gapes left as shown in Figure 6.17.

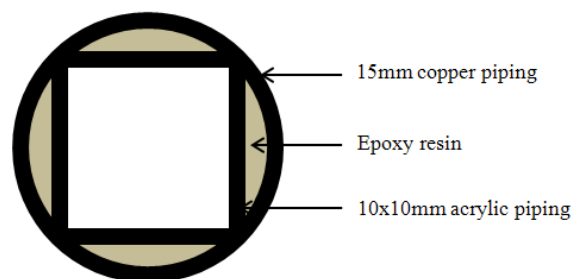


Figure 6.17. Cross section of acrylic and copper pipe section join.

The 2 sections of copper piping allow easy connection with the couplings at either end of the section. The test rig was run at 15 ml s^{-1} for a continuous period of 30 minutes in which no leaks were observed. Due to the change in cross sectional area from 134 mm^2 to 36 mm^2 , the lubricant velocity increased significantly within the acrylic section.

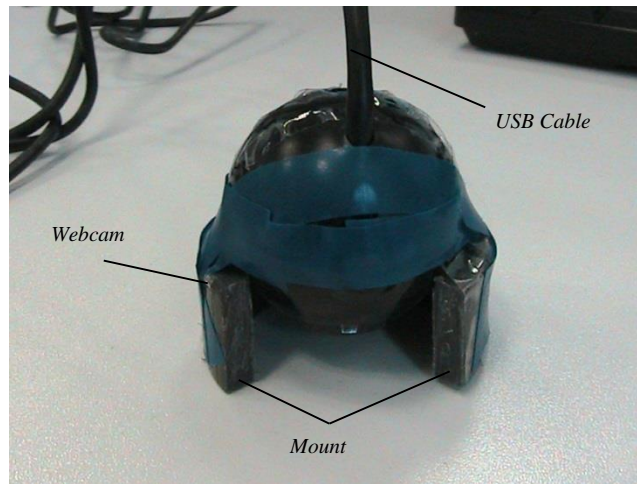


Figure 6.18. Plastic mount for webcam to allow flat connection with acrylic piping.

A small mount was constructed from 60 mm diameter piping with a short section removed to allow access to the manual focus as shown in Figure 6.18. The mount was secured to the pipe using a weak adhesive that could be broken to allow readjustments. The webcam was secured to the mount using electrical tape that could be removed and re-applied to adjust the camera orientation.



Figure 6.19. Acrylic piping with taped and exposed sections visible.

The acrylic pipe was wrapped with white electrical tape to prevent capture of images outside of the pipe. A small window was left to allow the webcam ‘line of sight’ with the pipe. The electrical tape had a secondary purpose as a light source diffuser. APSs can perform poorly in low illumination environments and wear particles may be not be detected [115]. The tape allowed a number of light sources to be placed in close proximity whilst reducing the overall intensity (see Figure 6.19).

6.6 Light Source

A number of light sources were trialled with the basic webcam software running to determine the best type. LEDs were ultimately used for the following reasons:

- Low power consumption which added to the concept of small scale sensor development.
- Low emitted heat which could cause damage to the nearby lubricant or sensor assembly.
- Availability of diffuse type LEDs which provided a more uniform background light source for the acrylic piping.

A small torch with an array of 7 LEDs powered by two 1.5V batteries was selected for use (see Figure 6.20). It was decided that designing an integrated light source that could be controlled would be too time consuming and not appropriate until after the concept had been proven.



Figure 6.20. Light source position below APS sensor (N.B. box shield is placed over assembly to reduce incident of ambient light).

6.7 Digital Image Processing

Digital image processing is the use of computer based algorithms to modify images (an example is shown in Figure 6.21). In some applications, image processing is purely to enhance features for aesthetic purposes. However, in many industrial applications, image processing techniques are combined with signal processing to extract meaningful information from the images. An example of such a system would be a police traffic camera that can record a car registration plate in real time using optical character recognition algorithms [116]. Humans can distinguish and interpret a vast number and variety of objects through the combination of the eye and the cognitive power of the brain. Numerous sophisticated object detection and recognition algorithms currently exist that aim to replicate this same functionality, with differing advantages dependant on the application [117].



Figure 6.21. Example of image processing where an image of the University of Strathclyde is converted to a binary image.

Digital image processing is a vast and complex subject area. Consequently the application of techniques within the subject was focussed on developing the prototype of the wear particle sensor. The following section aims to describe the relevant areas of digital image processing and the logic used to create the sensor software. The overall purpose of was to detect wear particles within an image captured by the APS sensor and extract meaningful information by manipulating the images into a more appropriate format.

6.7.1 Object Detection and Recognition

In object detection, the algorithm is trying to find a known object within a given image. The two inputs for this process are typically known information about an object and an image that may contain the known object (or a close approximation of that object). The output is generally a marker or a bounding box indicating the location of the object contained in the image, if it is present.

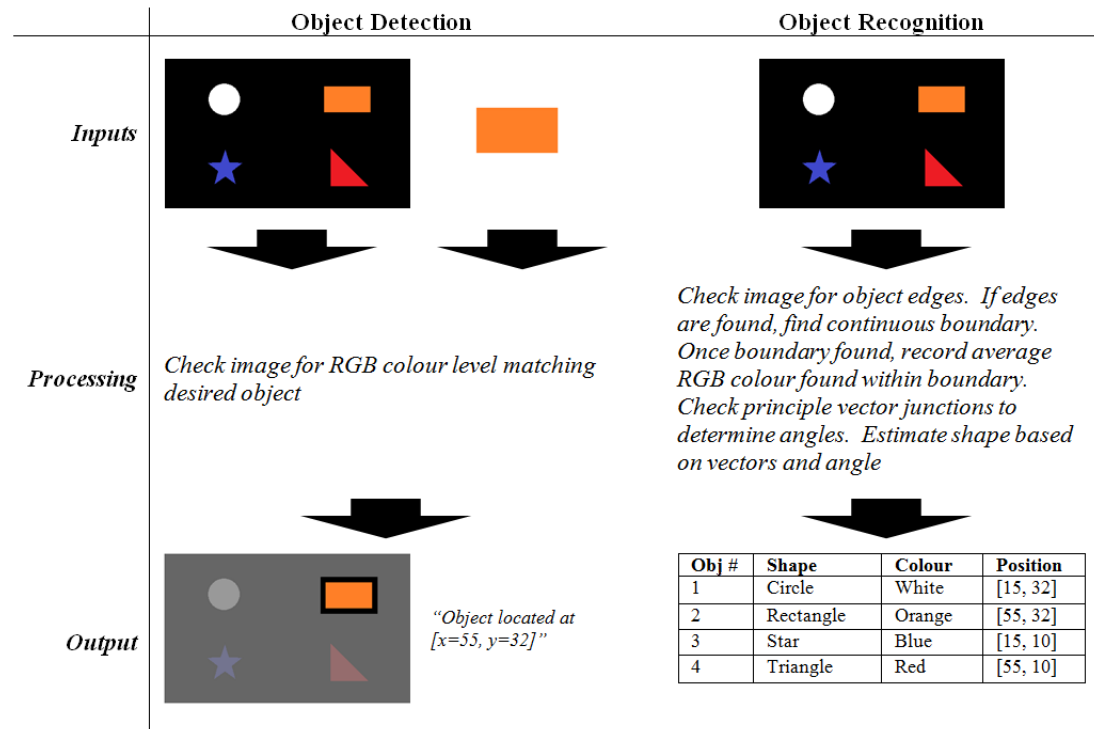


Figure 6.22. Difference between object detection and object recognition.

In object recognition, the algorithm is trying to determine what the object is depicted in the image. The input to the process is only the image whilst the output is usually an index of the detected objects with any classifications the algorithm may have made. A visualisation of the difference between the processes can be seen in Figure 6.22. Using this example, it can be seen that during object detection, this particular algorithm determines if an orange rectangle is present in the image by matching the RGB colour level. In this process, it is assumed that only rectangles may have the colour orange and so this allows a reasonably simple method for detecting the object. If other shapes in the image used the same colour, a problem would exist as the algorithm would incorrectly detect other shapes as an orange rectangle. Size and relative proportions

are also not considered which makes this detection algorithm highly sensitive to changes in the input images.

Using the same example but for object recognition, the algorithm assumes that the image background is black and objects in the foreground will be distinguished by a colour change. The edges of the object are determined by seeing if there is a change in the RGB value of a pixel traversing across the image. Once a change is detected, the algorithm begins to detect the object boundary by progressing through adjacent pixels for similar pixel RGB levels until the original point is reached. The shape is determined by analysing the approximate vectors that define the boundary. In the majority of image processing applications both processes are required.

Digital images in general are created by using a combination of colour components that create the effect of a single colour (in the context of a human eye). The most common method in digital imagery is to use the Red Green Blue (RGB) colour space. In this method, each pixel of an image has 3 components that indicate the level of each RGB colour which create the overall pixel. Other colour spaces exist for different applications within digital image processing. Colour images can provide information that is of importance in certain applications. For CCTV cameras, detecting the colour of a car is desired if the registration cannot be discerned. However, in difference applications the colour may not be of great importance, rather the relative difference in light and dark sections is important, known as intensity [118]. In these applications, the image may be converted to greyscale to reduce the image complexity which can aid in data analysis and faster processing.

6.7.2 Greyscale Conversion

Greyscale conversions are used for a variety of different functions such as reducing the complexity of the image to allow fast analysis. The colour of the wear particles was not expected to provide much data in terms of material composition and so preserving the RGB colour values was not a priority. It was also expected that the image would be further transformed into binary black and white, necessitating an intermediary greyscale conversion.



Figure 6.23. Example of greyscale conversion.

In many applications, the converted greyscale image is required to match the luminance of the original image (see Figure 6.23). This aids in maintaining features which are considered important. In terms of the wear sensor, this will allow the background lubricant to remain relatively bright compared to the darker particles in the foreground. The webcam captures images using the RGB colour model in which red, green, and blue are used as basic components for creating all other colours. The greyscale transformation for maintaining luminosity from an RGB imaged can be defined as:

$$GS_{pixel} = 0.21R_{pixel} + 0.71G_{pixel} + 0.07B_{pixel}, \quad \text{Eq. 6.1}$$

where GS_{pixel} is the converted grey value of the original $pixel$, R_{pixel} is the level of red, G_{pixel} is the level of green and B_{pixel} is the level of blue [119]. However, the simplest RGB to greyscale conversion is defined as:

$$GS_{pixel} = \frac{(R_{pixel} + G_{pixel} + B_{pixel})}{3}. \quad \text{Eq. 6.2}$$

The sum of all RGB components is averaged per pixel [119]. This can reduce contrast of the image as points of extremely light or dark colour can be reduced depending on the individual values of RGB. Both methods would be trialled in the sensor programming to assess if either has a noticeable impact the ability to distinguish particles from the surrounding lubricant.

6.7.3 Histogram Processing

A histogram of an image is the graphical representation of the frequency of a certain colour or tonal value occurring [120]. It can be defined as:

$$p(r_k) = \frac{n_k}{n}, \quad \text{Eq. 6.3}$$

where n is the total number of pixels within an image, n_k is the number of pixels of with greyscale level k and $p(r_k)$ is the probability of a pixel belonging to colour class r_k . In Figure 6.24, an example of deriving a greyscale histogram using Eq. 6.3 is shown.

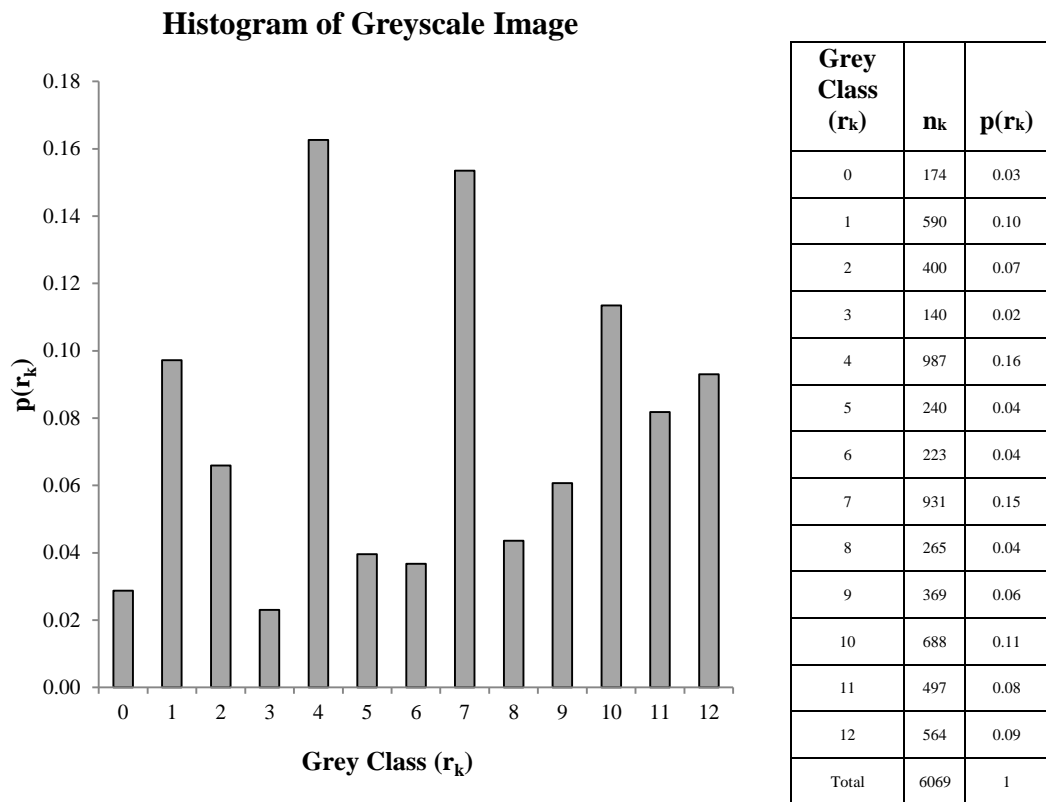
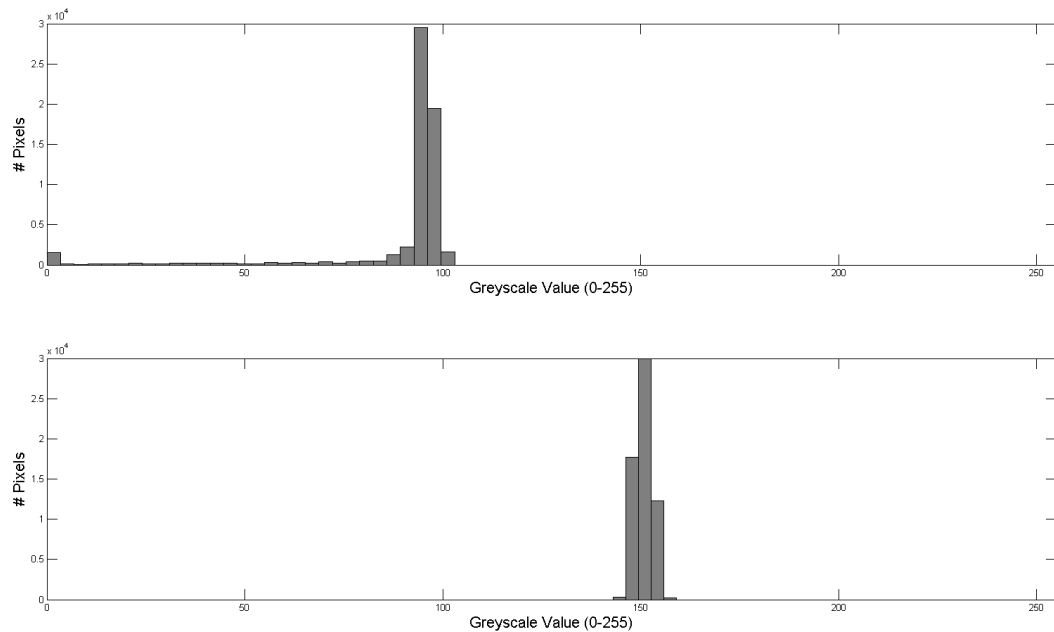


Figure 6.24. Example of histogram based on number of probability of pixels belonging to certain grey levels.

Histograms can be used visually to illustrate image parameters such as contrast and brightness. They also function as a powerful analytical tool that can be used in image processing for identifying key features. Wear particles have significantly different greyscale histograms when compared with the lubricant. An example of the difference

is shown in Figure 6.25. It can be seen that the histogram of the greyscale image containing a single particle surrounding by lubricant has greyscale values ranging from 0 to 80, indicating much darker pixels within the image. In the image with only clear lubricant the histogram has higher values overall (N.B. The graph shows total pixel number, rather than probability and the total class number is the full greyscale range of 0-255).



Upper histogram represents image to the left - a particle in lubricant. Darker lubricant is an effect of having large particles skewing average greyscale value.



Lower histogram shows the histogram of image shown to the left. The image contains no particles.

Figure 6.25. Difference in greyscale histograms for images with and without particles.

However, information regarding individual particles cannot be easily discerned with a global histogram applied across the entire image. Certain inferences may be made regarding the total mass or area of particles occupying the particular image but none regarding particle morphology. Individual histograms may be applied to objects which have been detected, but are unlikely to indicate particle morphology. However, greyscale histograms can be used to assess the ideal value in which conversion to bi-modal black and white occurs during binary conversion [120].

6.7.4 Binary Conversion

Binary images are those that only have two values (1 and 0) to represent information. Commonly 1 represents white and 0 represent black, but other situations such as text documents use the opposite (any two different colours may be used). Binary images are often used where high contrast is desired and the need to determine object morphology such as shape is not dependent on colour values. This method is therefore ideal for wear particle analysis in that the background lubricant has a very different colour than the suspended wear. Particle morphology can also be determined in the converted binary image as illustrated in Figure 6.26. The image to the left shows a greyscale image with a particle shown in black and lubricant shown in grey. Determining where the object ends is uncertain as the average greyscale pixel value changes gradually when traversing from the centre of the object to the lubricant. The blue arrow indicates the area where the object is darkest and so may be taken to the diameter approximately. The red line shows the maximum extent which may be considered as part of the particle. The image on the right shows a binary conversion where particle is approximated into black and white. Determining the diameter or any other object parameter is far less ambiguous as the boundary between the foreground object and background lubricant is well defined. However, the accuracy of the object parameters is now dependent on the accuracy of the conversion method.

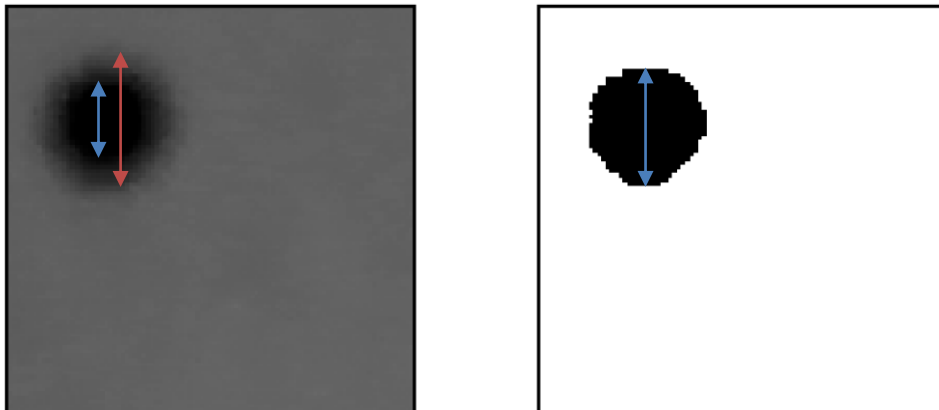


Figure 6.26. Example showing the uncertainty in estimating object size using greyscale (left) compared with binary (right).

The main problem with converting greyscale images into binary is the selection of a suitable greyscale boundary which can divide the range of 0-255 greyscale values at

an appropriate level. The boundary must allow dark objects and features to be classed as black and lighter objects to be classed as white. To achieve this, Otsu's method of minimising weighted within-class variance for greyscale histogram is often used [121]. It is assumed the image has a bi-modal intensity histogram consisting of background pixels and foreground pixels and determines the optimal greyscale threshold value, t , which separates these 2 classes. Pixels equal to or greater than t will have value 1, otherwise the pixel value will be 0. No spatial coherence is used to define the object structure and uniform illumination is assumed so the class variance is determined only by object appearance in terms of intensity [122]. It is therefore important that the light source for illumination during data capture is as uniform as possible.

The method first requires a histogram to be calculated on a greyscale image that holds the total number of pixels in each grey intensity class. The between class variance, $\sigma_B^2(t)$, for $t \in \{1 \dots 256\}$ can then be evaluated and is defined as

$$\sigma_B^2(t) = \omega_b(t)\omega_f(t)[\mu_b(t) - \mu_f(t)]^2, \quad \text{Eq. 6.4}$$

where weights $\omega_b(t)$ and $\omega_f(t)$ are the probabilities of a pixel belonging to the background and foreground classes (1 and 0) when separated by, t , the threshold. $\mu_b(t)$ and $\mu_f(t)$ are the mean values of background and foreground class when the probability of each histogram bin value occurring within the given class is evaluated for threshold t . The maximum inter-class variance is then evaluated and the corresponding value of t is selected as the threshold. Recursion can be used to calculate values of $\sigma^2(t)$ using values of t to reduce processing time.

An issue during binary conversion is the introduction of noise during thresholding. Some pixels may be incorrectly classed due to the relative proximity of pixels with significantly different greyscale values.

6.7.5 Edge Detection

An edge in digital image processing is defined as a boundary between two image regions that have distinct characteristics such as colour, texture or shade [123]. For data capture, it has been determined that the images will be converted to greyscale, then to black and white. This reduces the complexity of object detection as the change

between the background lubricant and the foreground wear particles will be between white and black pixels. Within greyscale images, edges are determined by analysing the intensity function across the area of interest. Ideally edges within images are two contrasting regions with a definite short transition from one colour or texture to the next as illustrated in Figure 6.27.

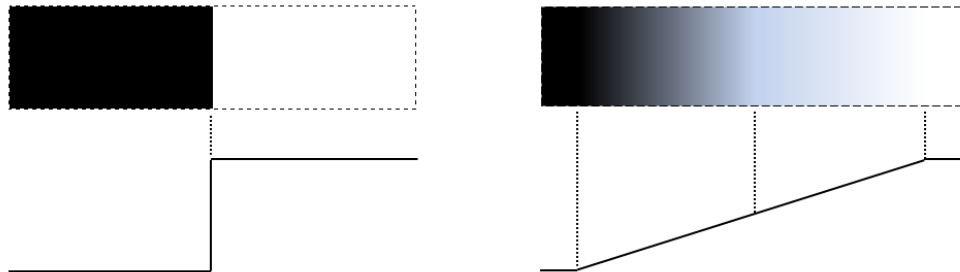


Figure 6.27. Left - Ideal digital edge with sharp change in grey level profile. Right - Ramped digital image with a ramped change in grey level profile.

Normally first order and second order derivatives of the grey level profiles are used to approximate the image gradient at any point in order to determine the edge. However, the majority of digital images have multiple variations that can prevent these derivations from yielding meaningful information. An example of this is shown in Figure 6.28.

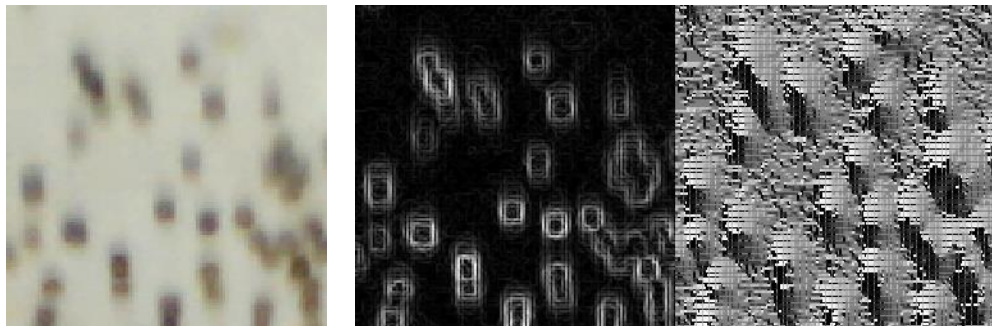


Figure 6.28. Left – Image of multiple particles in lubricant. Right(L) – Magnitude of gradient between pixels. Right(R) – Direction of gradient using Prewitt method.

The original image has multiple small particles shown in dark surrounded by lubricant. The gradient and direction of the particles using the Prewitt method are shown [124]. It can be seen that the gradient is effective in highlighting the particle boundaries. However, the gradient direction is more complex to understand visually due to the

noise from numerous changes across the entire image. This noise can be reduced by applying image smoothing with low pass filters (LPFs). In this process, all greyscale values within certain small pixel regions can be homogenised using a median LPF:

$$F(x, y) = \text{med}_{3 \times 3}[I(x, y)], \quad \text{Eq. 6.5}$$

where $F(x, y)$ is a pixel of the new image, $\text{med}_{3 \times 3}$ is the median filter and $I(x, y)$ is the a pixel in the original image [125]. The process is illustrated in Figure 6.29.

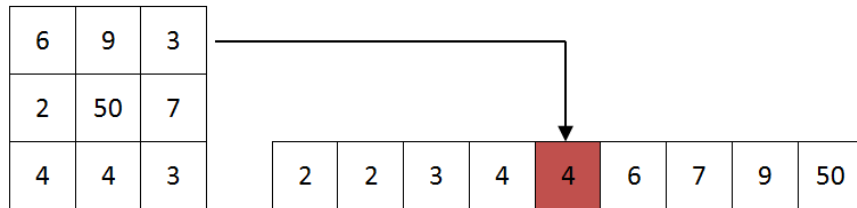


Figure 6.29. Median filtering of a 3x3 pixel array where the individual pixel values are sorted and the median is found.

Once the image has been filtered, edge points can be identified using local operators that respond strongly to edges such as the Sobel masks [126]. A typical Sobel operator consists of two 3x3 kernels that are convolved on a 2D image consisting of greyscale values to determine the approximate gradient magnitude at each point (see Figure 6.30).

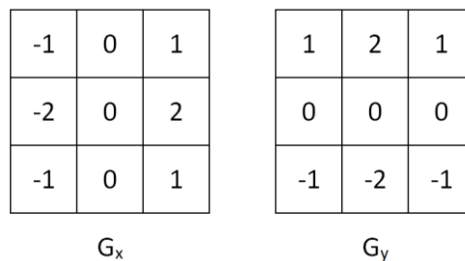


Figure 6.30. Left – X-direction operator (columns), Right – Y-direction operator (rows).

If the image is defined as a matrix A , then to apply these masks, each Sobel kernel can be convolved with A :

$$O_x = G_x * A \quad \text{Eq. 6.6}$$

$$O_y = G_y * A, \quad \text{Eq. 6.7}$$

where O_x is the output matrix of the convolution of Sobel operator G_x and A. O_y is the output matrix of the convolution of operator G_y and A. The convolution operation consists of moving the mask across the image and at each pixel computing the product of sums and writing this to a new output image (see Figure 6.31).

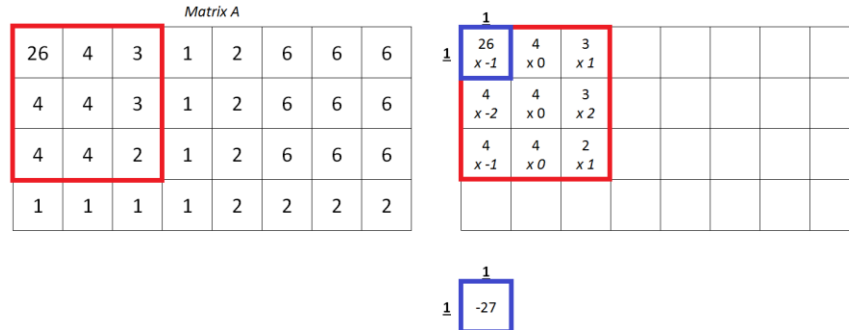


Figure 6.31. G_x (in red) is applied to matrix A, values are calculated by multiplying each value of G_x to corresponding A value, each product is summed into $O_x(1,1)$.

The new matrices O_x and O_y may have different dimensions from A as the operators may only be applied where they fully fit the image. Several methods can be used to ensure the new matrices have the same dimension, such as padding the original image with pixels around the boundary with the same value as those pixels in the original boundary. In some cases, the operator may be applied so it overlaps A on the bottom and right edges (as the convolution begins in top left corner and sums value into top left cell). O_x and O_y now contain the approximate gradients between pixel values in their given direction. The gradient magnitude is then defined as:

$$G = \sqrt{G_x^2 + G_y^2}. \quad \text{Eq. 6.8}$$

Regions that are likely to be edges have relatively high values of G. The exact threshold value can be varied depending on the requirements of the user. For example some images may be high contrast with well-defined edges and so the threshold may be set low. In complex images, careful selection of the exact boundary is required to prevent loss of important edge features. Edge detection is an important feature for wear particles as they are likely to flow in close proximity which will result in complications when evaluating the boundary. Discrete particles may be classed with as a single object with one boundary in the converted image despite being reasonably

distinct in the raw image. Well defined particle boundaries within a converted image that closely resemble the actual wear particles will improve the accuracy of morphological analysis.

6.7.6 Morphological Image Processing

Morphological image processing is a broad subject area within digital image processing that describes mathematical operations related to the shape of features in an image. The approaches of morphology image processing are diverse and may be used for a wide variety of application such as identify or transforming objects within an image. For the purposes of the novel sensor development, the focus will be on operations that are used to for to aid particle detection and shape categorisation.

When analysing groups of particles within an image, the most fundamental morphological operations are dilation and erosion [127]. Dilation of an object involves thickening an object in a binary image using a structuring element and is defined in the exclusive or statement:

$$A \oplus B = \{z \mid (\hat{B})_z \cap A \neq \emptyset\}, \quad \text{Eq. 6.9}$$

where A is the original set (a binary object), B is the structuring element, B_z is the translation of B by vector z , the location of transform. If a pixel of A with value 1 intersects a part of element B with a value of 1, the value of the pixel at the origin point of B becomes 1. The process is demonstrated in Figure 6.32 where the application of the structuring element at two different locations is shown.

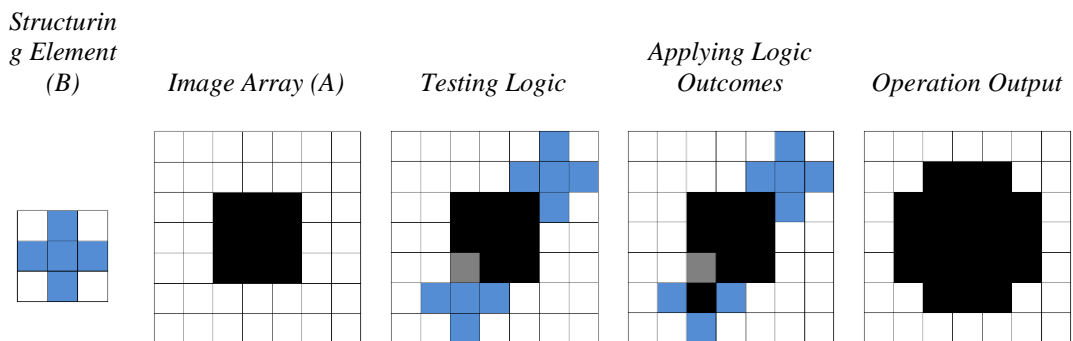


Figure 6.32. The process of object dilation. Note the structuring element has its origin at centre of blue cross.

The final output is an object that has been incrementing by 1 pixel in all directions except in the corners. If the structuring element was a 3x3 square, the output would be a 5x5 square.

In erosion, a similar process is used to reduce an image by a structuring element using symmetric difference [128]:

$$A \ominus B = \{z \mid (\hat{B})_z \cup A^c \neq \emptyset\}, \quad \text{Eq. 6.10}$$

where A , B and B_z are the same as in Equ. 6.9 and A^c is the background of the original set. If a pixel of A with value 1 intersects with the origin of B but a part of the element B is intersecting with a pixel A with value 0, the pixel at the origin loses its value of 1 and become 0. The process is illustrated in Figure 6.33.

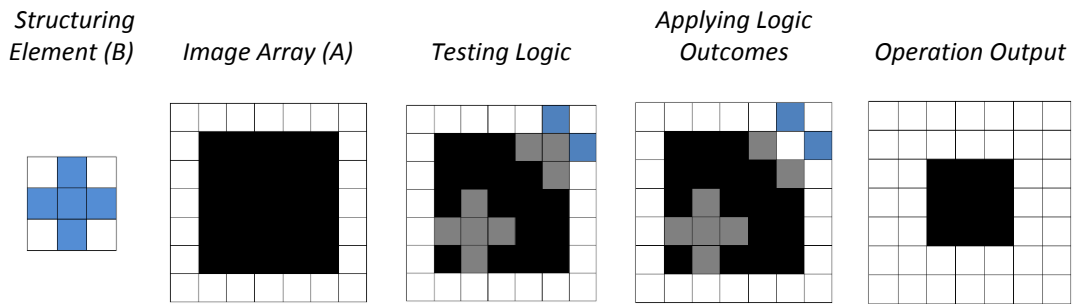


Figure 6.33. The process of object erosion. Note that it is not the exact inverse of dilation.

The final output is a 3x3 pixel that has been reduced by 1 pixel in all directions including corners. The structuring element is important as its shape and size will have a large effect on the operation output.

When considering two objects within close proximity, erosion can be used to reduce particle size and separate them into discrete objects. However, this can reduce the overall size of the object. In the context of wear particles suspended within lubricant, the total particle size is proportional to mass which as discussed in Chapter 5. Reducing the object size (and hence particle size) through erosion may cause an error in assessing total liberated wear. This can be accounted for when deriving total wear mass but during the development stage, it was considered appropriate to maintain a close approximation to the captured image as possible. The operations of erosion and

dilation can be combined into 2 compound operations known as opening and closing. Despite the apparent similarity in operation, opening and closing have significantly different effects on objects. During opening, an object is first eroded and then dilated:

$$A \circ B = (A \ominus B) \oplus B, \quad \text{Eq. 6.11}$$

where A is the original image, B is the structuring element and $A \circ B$ is the opening operation. During closing:

$$A \bullet B = (A \oplus B) \ominus B, \quad \text{Eq. 6.12}$$

where $A \bullet B$ is the closing operation. The difference in effect between opening and closing is best visualised with example in Figure 6.34. In opening, objects regions with dimensions comparable with the structuring element may disappear entirely [129]. This feature is useful in reducing noise surrounding particle images but other features like curves may be thickened to such an extent that they cannot be distinguished. During closing, objects in close proximity can become fused together and small holes within objects can disappear. For the application of detecting wear particles from binary images, opening was expected to be of greater value for images with a large number of objects.

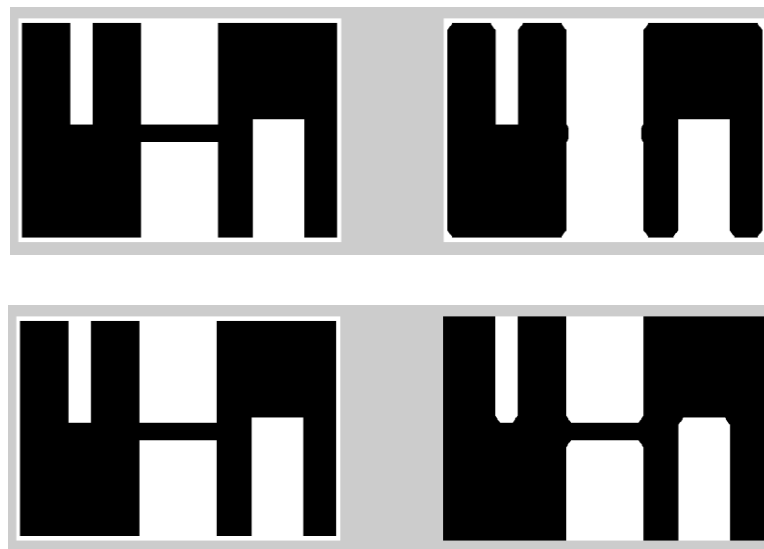


Figure 6.34. *Above* – Opening operation on left image. *Below* – Closing operation on left image.

6.8 Development of Image Capture and Analysis Software

MATLAB was selected to design the program that would underpin the wear sensor and conduct analysis on the images using the Image Processing Toolbox. This contained a large number of digital image processing techniques reducing the time required to develop the program. The advantages of this platform include:

- Basic functions such as erosion and dilation are included with quick manipulation of the defining parameters of these functions possible.
- MATLAB also allows code to be developed relatively quickly and was flexible with regard to the format of the data.
- Data could be stored in a number of ways such as variables or exported to other software for different analysis.
- Analysis program could be split into several subroutines or run as a single function. Subroutines allowed different parts of the program to be altered and validated individually.

6.8.1 Sensor Calibration and Adjustments

The centre camera, aligned with the midpoint of the pipe, used a MATLAB program that returned the captured image to the user computer. This allowed the APS sensor to be moved until the camera was in the correct location and orientation. Using a reference point on the base of the acrylic pipe, camera was manually focussed to the bottom of the pipe.

Once the camera was in place, it was secured to the rig assembly. Lubricant was then pumped through the rig and the sensor was tested by visually inspecting the returned images to check for any misalignments during operation or for changes in focus.

6.8.2 Main MATLAB Program Image Capture Subroutine

Initially the program clears any images cached from previous operations and resets APS sensor parameters. Next the APS characteristics are detected such as resolution and maximum frame rate (so that ideally a different camera may be attached). The interval between each captured image is set based on the selected flow rate of the test rig. This interval equated to a frame rate that could be recognised by the webcam:

$$FR = Q/L_{FOV} \quad \text{Eq. 6.13}$$

where FR is the frame rate, Q is the flow and L_{FOV} is the axial length of the field of view. The capture area used corresponded to the inner dimensions of the acrylic pipe of 6mm x 6mm. The APS sensor had a relatively large field of view (FOV) that was unnecessary due to the small width of the pipe. This was reduced to capture a 6mm x 6mm section by setting an area of interest (AOI) as shown in Figure 6.35. This reduction had an additional advantage of reducing the data size of the image. It was expected that several thousand images would be captured and logged which may result in slow processing or saturating available memory. By keeping the images to less than 500 KB, test runs were unlikely to experience such problems.

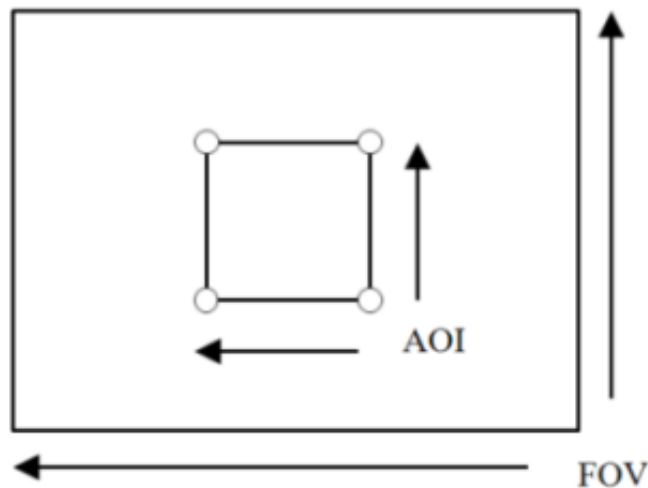


Figure 6.35. Total FOV for webcam and AOI used in image acquisition.

Setting the appropriate frame rate was important as it could lead to two types of error. A high frame rate could potentially capture the same particle multiple times during traverse of the field of view. A low frame rate could allow particles to pass undetected,

particularly at high flow rates. In addition, particles did not traverse the pipe at uniform speeds due to wall surface roughness and resulting shear flow within the pipe.

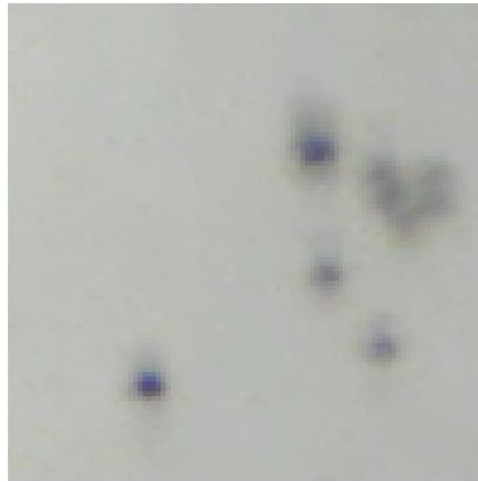


Figure 6.36. 465KB sample image showing the 6x6 mm area of interest and several particles.

Larger, heavier particles tended to flow along the bottom of the pipe at a slower rate compared to light particles that were suspended slightly above. As the system presented here was intended to demonstrate the principle of operation it was decided to use a low frame rate with the risk of some particles being undetected rather than counted multiple times. In an integrated condition monitoring system, it may be more appropriate to over count particles rather than undercount. For a typical flow rate was 12 ml s^{-1} , a particle would pass the 6 mm x 6 mm field of view in approximately 0.5 s, requiring 2 frames per second (FPS) capture rate (see Figure 6.36). This would mean a frame is captured every 0.5 s, matching the expected period for a particle to cross the FOV, if the particle travels at the same speed at the fluid. The flow of a liquid within a pipe is not uniform, with the fastest flow found in the centre, reinforcing the need to use a lower frame rate.

The images were initially recorded as an $m \times n \times 3$ array, where m and n are corresponding to the image height and width and 3 is the number of colour channels (red, green, blue or RGB). In this format, the colour perceived by the webcam pixel is represented as combination of 3 colours. The data class used was *uint8* which meant that RGB values varied between 0 and 255 [130]. The MATLAB code can be found in Appendix B.1.

6.8.3 Initial Image Processing Subroutine and Object Detection

The RGB image was converted into greyscale by averaging the individual uint8 values of red green and blue for each pixel using:

$$GS_{pixel} = (R_{pixel} + G_{pixel} + B_{pixel})/3, \quad \text{Eq. 6.14}$$

where GS_{pixel} is the greyscale image consisting of an $m \times n$ matrix populated with uint8 grey intensity classes (0 – black, 255 - white) [131]. Otsu's method was then used to calculate the optimum greyscale threshold for each image that would separate the particles and lubricant. Once this threshold was calculated, the image was able to be converted into black (pixel value 0) and white (pixel value 1). An example of the Otsu's method is shown in Figure 6.37.



Figure 6.37. 2x 750 μm particles. *Left* – Image from APS, *Right* – Conversion of image using Otsu's method into bi-modal.

An issue when using Otsu's method of bi-modal image thresholding is that when the threshold, t , is applied, some pixels can be above this limit but separated from the main object by a number of pixels whose value is below t [132]. The result is small objects consisting of a few pixels clustered around the edges of larger objects that represent particles. This distorted the total particle count and the wear profile estimated later in the program. To prevent this, objects fewer than 10 pixels were removed as this would correspond to an approximate circular particle with diameter of 5 μm . This was significantly lower than the smallest test particle size that is described later in Section 6.10.

Objects were identified by counting the number of edge boundaries that existed between black and white pixels in each image [133]. The program scanned each line of pixels until a change value occurred: pixels with value 1 (white) were considered as background so that no objects consisting of these pixels were counted.

Pixel values of 0 were assessed for connectivity to determine the outline for individual objects. An example of different types of connectivity is shown in Figure 6.38. 4-face connectivity allowed faster image processing but reduced detail. However, at 30FPS, it was found that 8-face connectivity was possible to determine an accurate outline of particles in the range of 300 to 500 μm . At sizes less than 300 μm , outlines became less accurate until particle morphology was significantly reduced. Objects were considered to have no internal boundaries by not recognising any pixel change once object connectivity had been established. This prevented small light discrepancies on particles from manifesting as object structure (for example donut shapes).

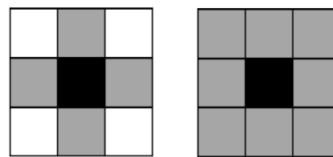


Figure 6.38. *Left* - 4 connectivity, *Right* – 8 connectivity for centre pixel.

To improve the identification of discrete particles, opening was applied to each image where the objects were eroded and then dilated. The structuring element chosen was initially a disk 5 pixel radius (giving a total pixel number of 49 pixels) as shown in Figure 6.39.

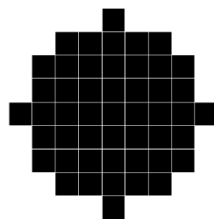


Figure 6.39. Initial ‘disk’ structuring element with radius of 5 pixels (diameter of 9).

Once all discrete objects were identified in the image, each was assigned a unique number (1 to n^{th} number of particles). Individual objects could then be logged for each image with all measured parameters, allowing all particles to be tracked and assessed. This identification also allowed the particles to be displayed as unique colour on the user interface. The MATLAB code for the initial image processing and object detection subroutine can be found in Appendix B.2.

6.8.4 Object Analysis Subroutine

An object analysis subroutine was developed to test the ability of real time data capture and analysis. The key aspects of the particle to measure were size and shape. As the data was logged, further analysis may be achieved in an 'offline' mode.

Particle size was determined by measuring the overall area and the major axis length of the objects identified in each image. Area was established by summing the total pixel count for each object. Images of 2000 graded particles (125-150 μm and 475-500 μm) were captured and the individual areas measured. The pixel to area ratio was found to be 1:260 (measured in μm^2) with an error bound of $\pm 15\%$. The calculation of the error bound is detailed in Appendix B.3.

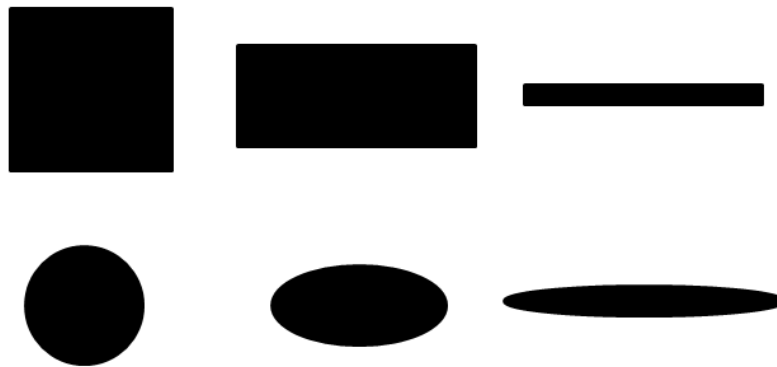


Figure 6.40. Example images of regular objects used to test shape parameters.

The percentage error was found by binning objects into area classes of 20 pixel increments for the two sets of graded particles. The average pixel to area ratio was found for each bin, with the highest and lowest ratios used to estimate error bounds. The process was repeated using the binned ratios to find the average pixel to area ratio with the error bounds carried through to weigh the total error bounds. A similar process was used to develop a pixel to length ratio which was found to be 1:16.1 with an error bound of $\pm 17\%$. Particle morphology was determined using object area, eccentricity, major axis length and minor axis length.

Using these, 4 parameters were developed to quantify the overall object shape [134]. The first parameter, P_C , estimated how circular the object was, and is defined as:

$$P_C = (1 - M_{ecc})/(L_{min}/L_{maj}), \quad \text{Eq. 6.15}$$

where M_{ecc} is the object eccentricity, L_{min} is the object minor axis length and L_{maj} is the object major axis length, both in μm . If P_C is approximately 1, the object will display circular characteristics. The second parameter, P_S , estimated how square the object was, defined as:

$$P_S = ((L_{min}/L_{maj}) + M_{ext})/2, \quad \text{Eq. 6.16}$$

where M_{ext} is the object extent, the ratio of the object area to the bounding box area. The bounding box is the smallest possible rectangle that may fit inside the object. If P_S is approximately 1, the object will display square characteristics. The third parameter, P_E , estimated how ellipsoidal the object was, defined as:

$$P_E = 1 - (L_{min}/L_{maj}). \quad \text{Eq. 6.17}$$

If P_E is approximately 1, the object will display ellipsoidal characteristics. The last parameter, P_R , estimated how rectangular the object was, defined as:

$$P_R = ((1 - (L_{min}/L_{maj})) + M_{ext})/2. \quad \text{Eq. 6.18}$$

If P_R is approximately 1, the object will display rectangular characteristics. The 4 parameters allowed a shape profile to be developed for each object and allowed non-regular shaped objects to be categorised. In Figure 6.40, regular test objects with the same formatting as the images produced by the program are shown to demonstrate how objects are characterised.

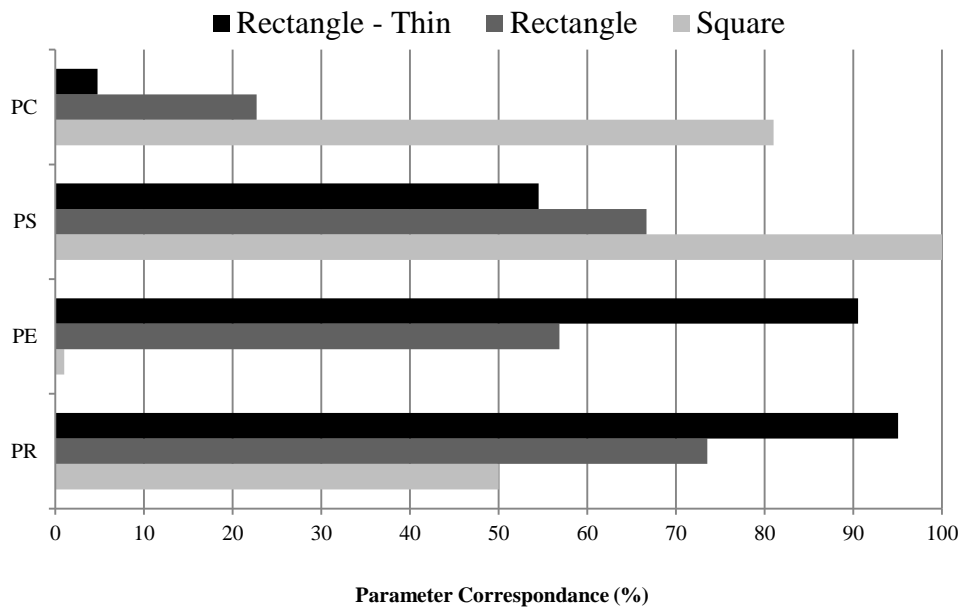


Figure 6.41. Object shape parameters for square and rectangular test objects.

In Figure 6.41, it can be seen that the thin rectangular object best fit P_R , closely followed by P_E . The rectangular object also best fit P_R and was followed by P_S . The square object best fit P_S but was instead followed by P_C which indicates that the square fits the profile of a circle better than a rectangle due to the similar axis lengths. In Figure 6.42, the results for the circular and ellipsoidal objects are expressed as a percentage correspondence.

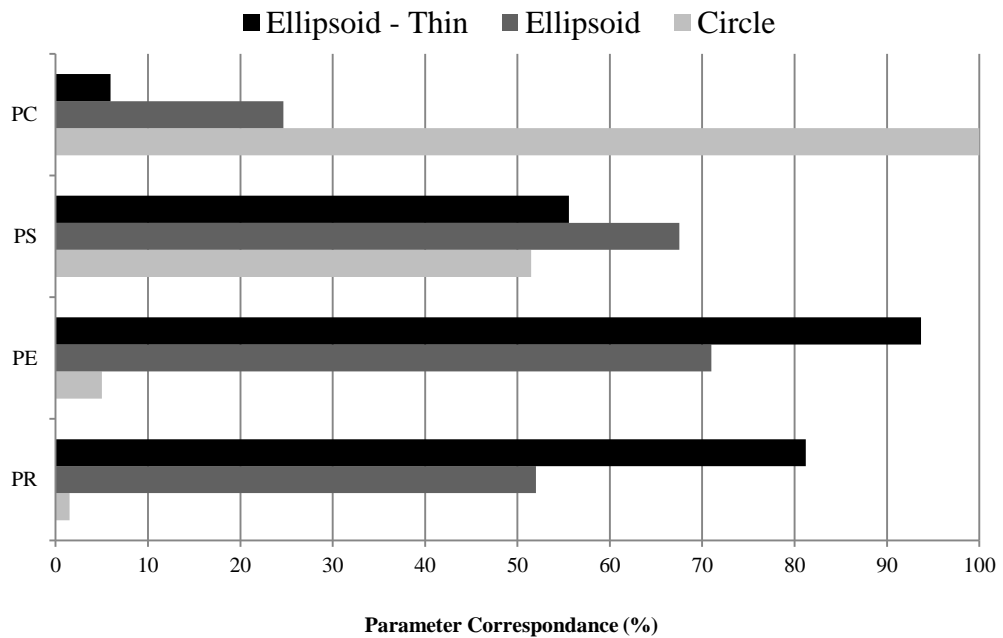


Figure 6.42. Object shape parameters for circular and ellipsoidal test objects.

It can be seen that the thin ellipsoidal object best fit P_E closely followed by P_R due to the close resemblance to the thin rectangle. Similarly the circle best matched P_C and P_S due to the close resemblance of these shapes in terms of the measured characteristics. The MATLAB code for the object analysis code is shown in Appendix B.3.

6.8.5 Data Export Subroutine

All data was stored as variables within the MATLAB code which were then exported to an Excel spreadsheet for analysis and presentation. For every new frame, the particle number, area, eccentricity, extent, major and minor axis length were stored in the appropriate column. An example of the data exported is shown in Table 6.3.

Table 6.3. Sample of data shown in Excel worksheet

	Object Characteristics (12 ml s ⁻¹ , 2 FPS)				
Frame Number	Area (µm ²)	Eccentricity	Major Axis Length (µm)	Minor Axis Length (µm)	Extent
1	947	1.00	128.68	10.49	0.18
1	18	0.87	6.93	3.46	1.00
1	484	0.96	48.18	13.90	0.44
2	115	0.84	16.76	9.10	0.77
2	52	0.48	8.76	7.69	0.93
2	41	0.53	7.99	6.79	0.98
2	65	0.50	9.87	8.54	0.90
2	47	0.66	9.12	6.82	0.98
2	71	0.62	10.81	8.50	0.89
2	55	0.49	9.15	7.96	0.98
3	40	0.51	7.83	6.71	0.95
3	75	0.60	11.06	8.81	0.94
3	47	0.66	9.12	6.82	0.98
3	72	0.77	12.11	7.72	0.94

6.8.6 User Interface

The user was presented with a real time feed of the particles as they passed and the image processing that was conducted. This allowed the user verification that a wear regime had begun and also would indicate any faults that may be occurring such as camera misalignment or poor light source. An example of the returned image for the user is shown in Figure 6.43.

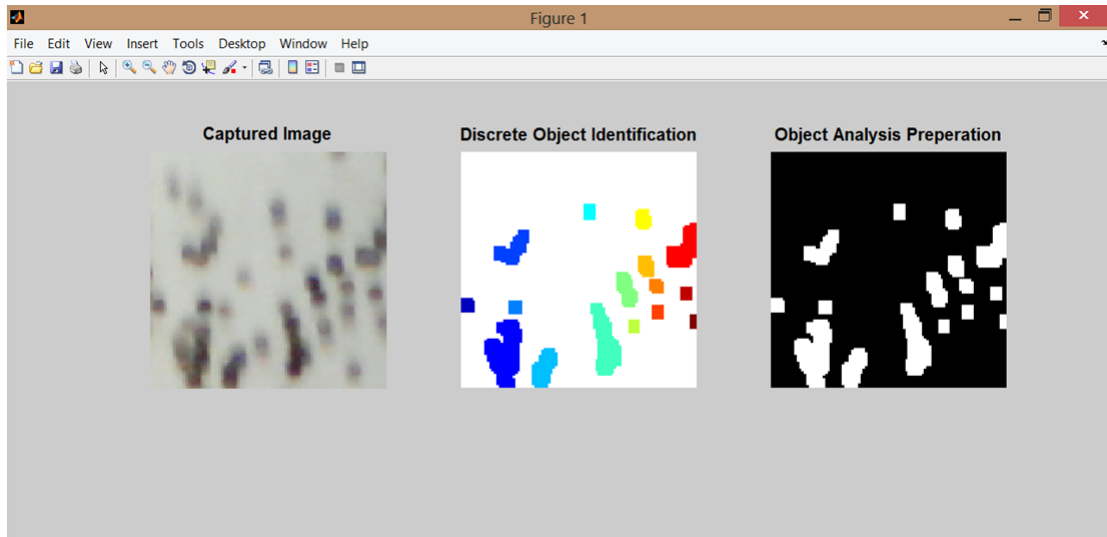


Figure 6.43. User interface showing current image, bi-modal conversion and particles classed as discrete objects by the morphology subroutine.

6.9 Testing Methodology

The APS sensor tests were primarily aimed to demonstrate the ability of the system to categorise particle size and identify shape.

6.9.1 Lowest Particle Size Testing

Basalt spherical particles were used as the first test material to determine experimentally the smallest distinguishable object possible (see Figure 6.44). The particles were graded by sieve fractions with the largest being 475-500 μm and the smallest being 125-150 μm . Particles within these grades could have a diameter value anywhere between the two limits. Basalt spheres were used for calibration as they could be sourced with known diameter distributions and uniform shape. Graded metallic particles with similar characteristics could not be sourced as readily. As the sensor operates purely on visual properties, the dark colour of the basalt particles was considered an appropriate match.



Figure 6.44. Basalt spherical particles used for size testing and other experiments.

The particle size ranges were selected after the camera was initially tested using a series of printed dots on plain white paper. The same analysis program, light source and camera positioning were used. It was found that particles larger than 500 μm appeared very clearly on the output images. Particles less than 100 μm were difficult to distinguish. Therefore it was decided to limit initial testing to this range.

Table 6.4. Individual Particle Mass for Diameter Limits

Particle Diameter (µm)	Particle Radius (m)	Particle Volume (m ³)	Particle Mass (mg)
125	0.0000625	1.0227 x10 ⁻¹²	0.00297
150	0.000075	1.7671 x10 ⁻¹²	0.00512
475	0.0002375	5.6115 x10 ⁻¹¹	0.163
500	0.00025	6.545 x10 ⁻¹¹	0.190

The mass of particles was selected to determine the number of particles in a given sample size. Using spherical volume and a basalt density of 2900 kg/m³, the individual particle masses for each grade limit was found, shown in Table 6.4. 50 mg test samples were used for each grade. A significant degree of error existed within each sample group as each had an upper and lower limit corresponding to the sieve fractions. To compensate, a geometric mean, D_{ave} , was used to calculate an average diameter for use in volume-based calculations [135], defined as

$$D_{ave} = \sqrt{(D_L D_U)}, \quad \text{Eq. 6.19}$$

where D_L is the lower sieve limit and D_U is the upper sieve limit, both measured in microns. Using the geometric mean the total number of particles per 50 mg was estimated and is presented in Table 6.5. These values were used to calculate the detection rate.

Table 6.5. Total number of particles for 50mg samples.

D_L (µm)	D_U (µm)	D_{ave} (µm)	Particle Volume (m ³)	Particle Mass (mg)	Particles per 50mg
125	150	136.9	1.3443 x10 ⁻¹²	0.0039	12825
475	500	487.3	6.0603 x10 ⁻¹¹	0.1757	285

To verify the size and shape of the basalt particles a microscope at 20x zoom was used to capture images. From visual inspection, it was found that the general shape was circular. It was also found that for each grade, a variety of particle sizes could be found within the limits. This was confirmed by running the sensor program and finding the major axis length. An example of the images obtained using a microscope and their processed form can be seen in Figure 6.45.

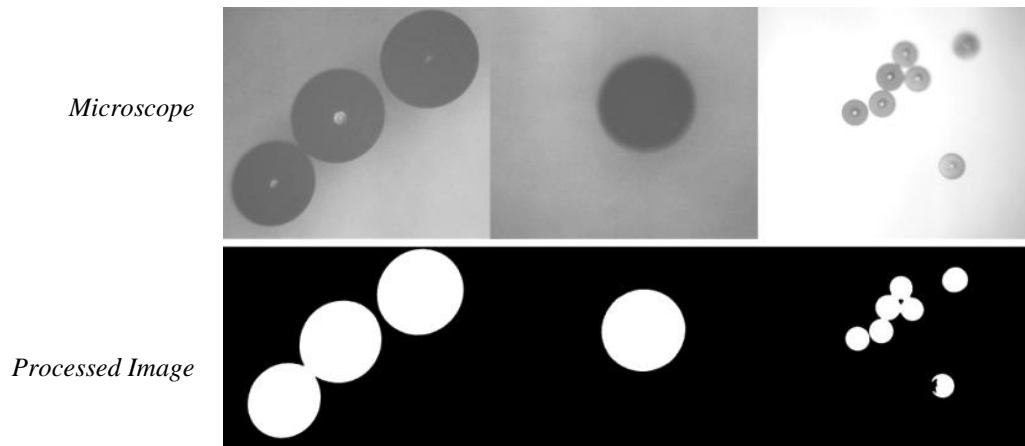


Figure 6.45. Basalt spheres particles suspended in oil under microscope inspection. Left – 476 μm , 490 μm and 498 μm particles. Centre – 483 μm particle. Right – clustered particles ranging from 127 – 145 μm .

Samples were pre-mixed with the same lubricant in a tube that could be connected to the test rig. This minimised clustering and also allowed the particles to enter the flow at a more uniform rate. The flow rate was set at a uniform 12 ml s^{-1} , requiring a 2 FPS image capture rate.

6.9.2 Particle Morphology Detection

Shape analysis capacity was assessed by introducing steel particles of varying sizes into the lubricant flow. In the absence of lubricant samples from gearboxes with known wear characteristics the particles were obtained from a machine tool workshop as they had similar sizes and shapes of those found in gearbox lubrication systems (see Figure 6.46).



Figure 6.46. Sample of wear particles used for testing morphology.

Four 50mg samples consisting of various particle shapes and sizes (validated through microscopy) ranging from approximately 100 to 500 μm were used to test

morphological detection. The sensor was not assessed for detection rate due to the unknown sample composition. Instead the sensor was tested in its intended operation format: inline collection and sorting of data in real time. Objects were initially sorted into 50 μm size bins, ranging from 100 to 500 μm and above. The shape with the highest percentage parameter would then determine what shape class they were binned. Within each object bin, the objects were further sorted by their highest shape correspondence. For example, an object with a major axis length of 265 μm would be counted in the 250-300 μm bin. If the shape parameter with the highest percentage was P_C , the object would be classed as square within the 250-300 μm bin.

To assess the effectiveness of the shape classification system, all captured images were stored with the corresponding object area, major axis length, minor axis length and eccentricity. This allowed a comparison between the measured parameters and the actual particles. Images with a large number of particles and a variety of shape classifications were sampled to verify the accuracy of the 4 measured parameters.

6.9.3 Flow Rate Limits

The rig was set to pump lubricant at 2 different flow rates, 12 and 24 ml s^{-1} , to test the effect upon the APS sensor. For each flow rate, 4 particles regimes were introduced: 2 regimes consisting of 50 mg basalt particle samples (125-150 μm) and 2 regimes consisting of 50 mg basalt particle samples (475-500 μm). A summary of the flow rate test is shown in Table 6.6. The capture rate for 12 ml s^{-1} was 2 FPS whilst at 14 ml s^{-1} it was 4 FPS.

Table 6.6. Summary of flow rate test regimes

Flow Rate (ml s^{-1})	Test 1	Test 2	Test 3	Test 4
12	50mg 125-150 μm	50mg 475-500 μm	50mg 125-150 μm	50mg 475-500 μm
24	50mg 125-150 μm	50mg 475-500 μm	50mg 125-150 μm	50mg 475-500 μm

6.9.4 Lower Light Level

Lubricants degrade over time and the most obvious manifestation of this change is a change in colour. To run the test rig under these conditions would involve switching

the current clean XMP320 with approximately 12 litres of severely degraded lubricant and procuring such a large quantity proved to be difficult. Additionally, the test rig would need to be run for an extended period of time with fresh XMP 320 to remove all traces of the degraded lubricant. The process would be too costly and unrealistic in the available time frame. To simulate degradation on the clean XMP 320, the background light for the APS sensor may be dimmed or removed to reduce the contrast between particles and lubricant. This was confirmed by running an initial test where the LEDs were switched off. Two wear regimes consisting of 50 mg samples of 125-150 μm basalt particles were run under normal light conditions and with the LED light source removed. The results of these tests are shown in Chapter 8, Section 8.18.

6.10 Conclusions

Following the development and testing of the wear particle sensor, a critical analysis of the results would allow an assessment of performance. These results and relevant discussion are detailed in Chapter 8. The next Chapter details the development and testing methodology of the lubricant quality sensor in a similar format to the wear particle sensor.

Chapter 7 – Development of Lubrication Quality Sensor

Development of a lower cost lubricant quality sensor has been identified as a valuable element of a condition monitoring system. The lubricant condition sensor described in this chapter is based on the principle of using absorption spectra of infra-red radiation within a narrow spectral band which coincides with lubricant condition degradation due to contamination or ageing. Initially absorbance spectra tests were conducted that would determine certain characteristics of the lubricant under different conditions.

7.1 Gearbox Lubrication for Experiments

In Chapter 6, the lubricant used in the test rig was described as XMP 320. This same lubricant was used for all experiments. In addition to this lubricant, samples of XMP 320 from an operational wind turbine gearbox were obtained from David Brown Gear Systems Ltd. The lubricant had been in use for approximately 18 months and was significantly darker than fresh samples (see Figure 7.1). However, it was still considered to be functional for use in a gearbox lubricant system, albeit with a higher probability of requiring replacement within the next 3 months. These samples offered potential to test the sensor with a lubricant under similar conditions found within operational gearboxes.



Figure 7.1: *Left* - New sample, *Middle* - Used test rig sample, *Right* - Used gearbox sample.

7.2 FTIR Analysis of XMP 320

Fourier Transform Infrared spectroscopy (FTIR) was used to create absorbance spectra of experimental samples (the process is described in Chapter 5, Section 4.2). A FTIR spectrometer (model number Bomem™ DA3.002) from the University of Strathclyde's Department of Physics was used to conduct the experiments. The spectra produced consisted of total absorbance against wavenumber. Total absorbance of IR radiation was defined as using the Beers-Lambert law:

$$A_{\lambda} = -\log_{10}\left(\frac{I}{I_0}\right), \quad \text{Eq. 8.1}$$

where A_{λ} is the total absorbance, I is the intensity of the transmitted light and I_0 is the intensity of the incident light [136]. An absorbance of 2.5 equates to 0.1% of incidence radiation passing through the sample, normally signifying that a certain chemical compound or bond type is present in large quantities. Smaller absorbance values from 0.2 and above indicate the presence of a bond or compound but the quantity is smaller. A typical absorbance spectrum for XMP 320 lubricant is shown in Figure 7.2.

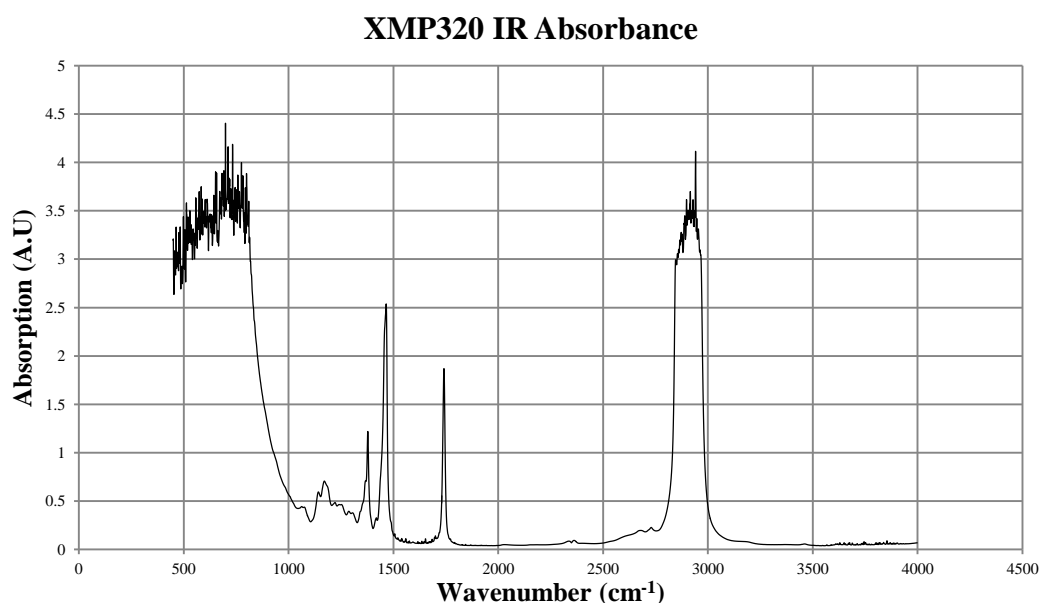


Figure 7.2. IR absorbance spectrum of XMP 320 lubricant using FTIR analysis.

7.2.1 Experimental Samples

The first stage experiments were intended to determine the differences between XMP320 samples taken from different stages of use and consisted of the following:

- 3 samples of unused XMP320 from a new container.
- 3 samples of unused XMP320 from a storage barrel (approximately 6 months old).
- 3 samples of used XMP320 from an operational wind turbine gearbox (approximately 18 months usage).

It was expected that there would be significant differences between the unused new container samples and the used lubricant. The effect of storage would also be tested by sampling unused lubricant which had been sealed for 6 months. Over time lubricant can become more oxidised in the presence of air.

7.2.2 Sample Preparation

Each sample was prepared in accordance with standard FTIR analysis [137]. All equipment was cleaned with acetone and allowed to dry. An individual drop of lubricant of 0.05 ml was collected using a volume handle single channel pipette. This was then placed between two glass plates which were separated by 25 μm thick wax paper. Thick wax paper would determine the pathlength of the IR light. Samples were secured in a collar holder which could then be placed within the FTIR. The accuracy of each sample is based on the number of different wavebands which analyse the sample. For example if the full range of IR wavebands were used to analyse the sample, the produced spectra would be most representative but would take the longest time (5 min). If a smaller number of wavebands are used, the spectra is less representative. A decision is usually made regarding the most acceptable level of representation for a given sampling regime. For example, a large number of samples may be analysed by less representative spectra (hence less accurate) so that the experiment may be conducted in a reasonable time period.

The pathlength of the samples is important in achieving appropriate results for the experiments. An example of the effect is illustrated in Figure 7.3. When using wax

paper measuring 50 μm in thickness, the lubricant acts as a thicker barrier to transmission of IR light (hence increased pathlength). This allows greater absorbance at responsive waveband. The effect is particularly pronounced between 2700-3000 cm^{-1} where significantly more absorbance occurs. 25 μm was the minimum thickness available and produced clear spectra and was used for all subsequent experiments. 50 μm may have been used but the lack of clear definition at the 2700-3000 cm^{-1} wavebands was undesirable. An enlarged version of Figure 7.3 can be found in Appendix C.1.

IR Spectra of XMP 320 Lubricant Samples

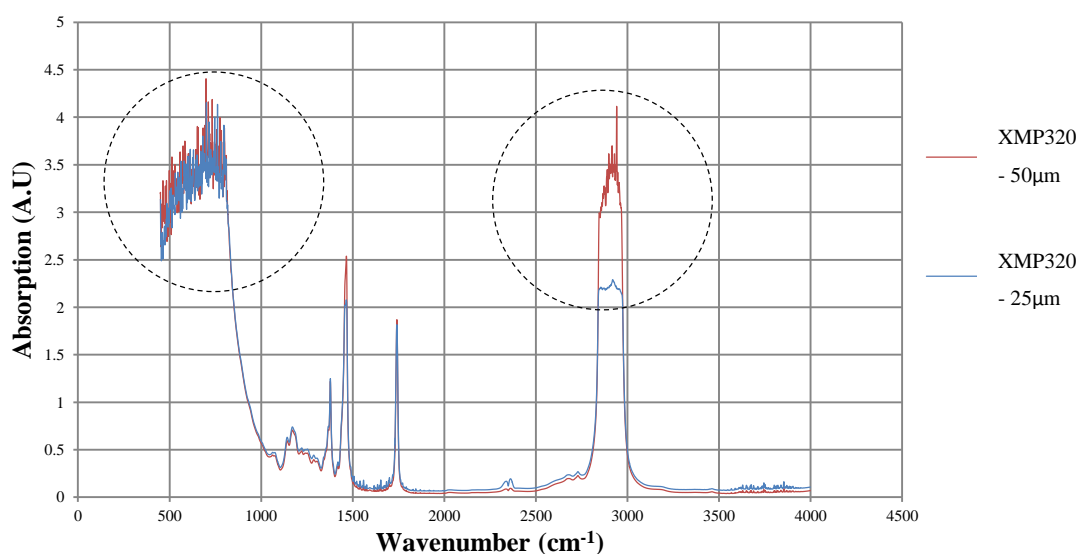


Figure 7.3. IR spectra of new XMP 320 lubricant samples.

An interesting feature of both spectra shown in Figure 7.3 is the presence of ester additives indicated with dotted circles. This manifests as an increase in absorbance bands below 1000 cm^{-1} . This additive is not present in the experimental tests and the XMP320 with this additive was only used for initial testing of FTIR. This was due to the availability of XMP320 lubricant at this stage of experimentation.

7.2.3 Comparison XMP 320 Experiments

In Figure 7.4 the IR absorbance spectra compared within each of the 3 samples is shown to verify that there were no significant variations within each group. It can be seen that the spectra within each experiment are nearly identical suggesting that the results were highly repeatable. A difference can be noted in Plot 2 (unused XMP320 stored for 6 months) but was small enough to be attributed to an error in creating the samples. As the experiments were highly repeatable, it allowed any of the 3 spectra within each group to be compared for difference in peaks. The individual spectra for each sample can be seen in Appendix C.2.

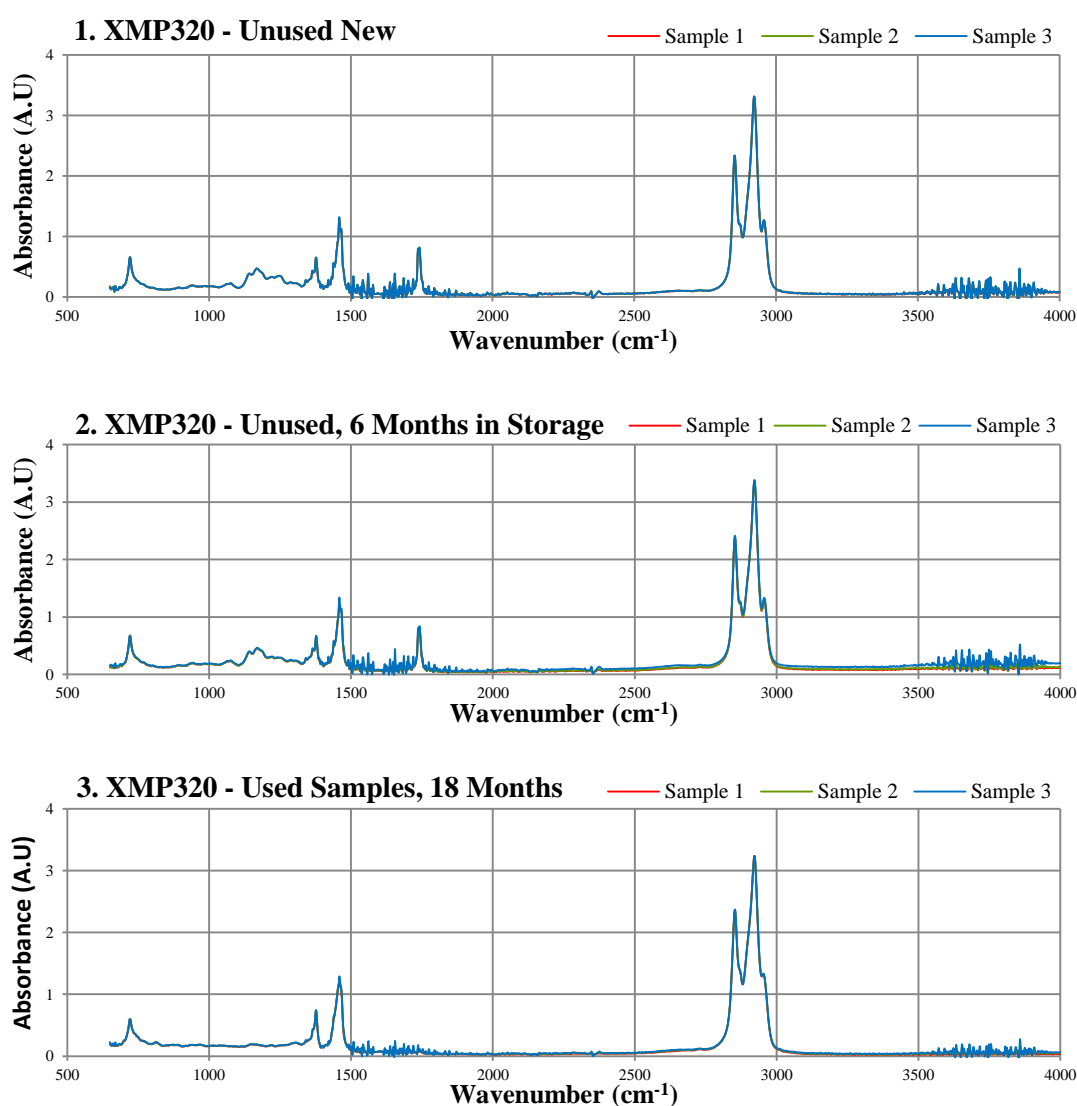


Figure 7.4. IR Spectra for 3 samples of unused XMP320 from a new container.

One spectrum from each group was plotted to compared difference in the peak and identify regions of interest. The plot is shown below in Figure 7.5. The difference between the unused new samples and the unused 6 month old samples were slight. The 6 month old XMP320 samples were excluded from comparison to focus on the difference between the unused new and used 18 month old samples.

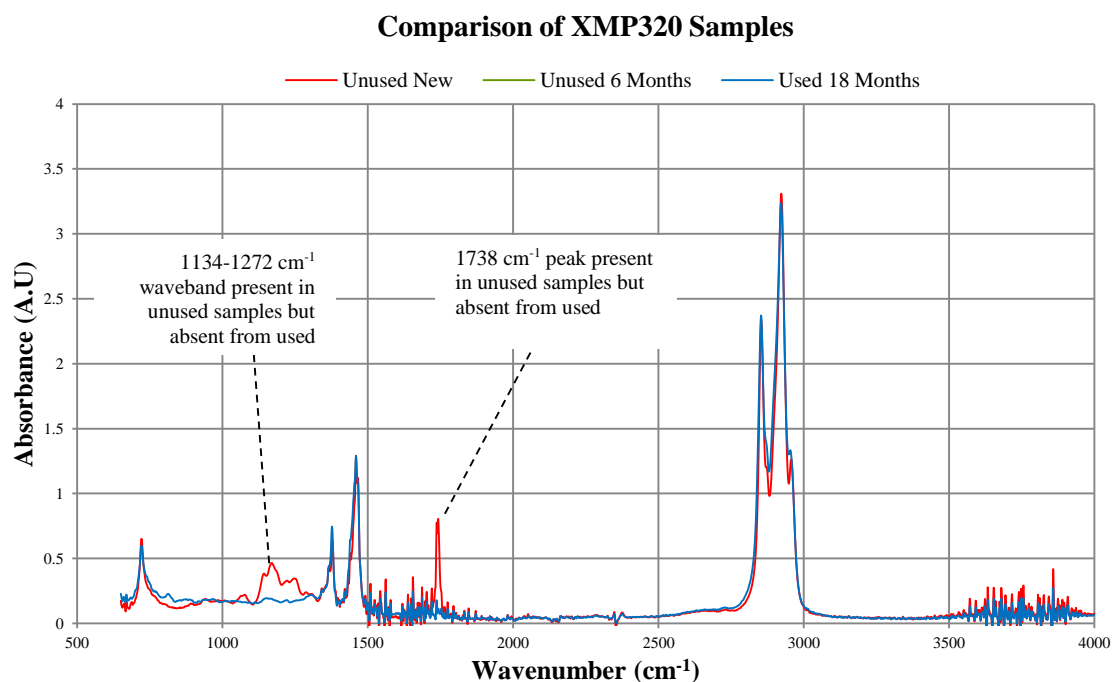


Figure 7.5. Comparison of XMP 320 Spectra from each group of lubricants.

A significant difference is the absence of the deterministic peak at 1738 cm⁻¹ and the board waveband peak between 1134 cm⁻¹ and 1272 cm⁻¹. Smaller variations in were also noticed in other regions but were not as significant or as clear.

The decrease in absorbance at 1738 cm⁻¹ is attributed to the absence of carbonyl. This result was unexpected as lubrication theory described in Chapter 5 Section 4.2 indicated that a carbonyl peak tends to appear in older lubricants due to the increase in acidity. However, the presence of additives can complicate IR spectra. The XMP320 samples all contained additives which were not published which complicated analysis of the spectra. However, as there is a noticeable difference and this peak is related to acidity, it was still considered of interest when considering the sensor deign [138].

7.3 Sensor Design

The next stage was to develop a sensor that would use the principles of IR absorbance to detect changes in the lubricant quality. The final sensor would use an IR source that would correspond to one of the two identified wavebands of $1134\text{-}1272\text{ cm}^{-1}$ and 1730 cm^{-1} described in the previous section. This source would be projected across a lubricant channel and a sensor that responds to this waveband would be used to indicate the change in transmittance.

A small prototype sensor was developed that used a widely available laser diode and photodetector. However, specific lasers at the wavebands identified were unavailable. To demonstrate the principle, a laser diode was selected that emitted IR at a waveband that would be partially absorbed by XMP 320 lubricant, but did not correspond to the identified wavebands in the previous section. However, if the principle could be demonstrated, the sensor could be modified once a laser with the correct waveband becomes available [139].

7.3.1 Sensor Layout

The main novelty of this sensor concept was the potential ability to measure inline samples. The IR source and detector would be placed across the entire lubricant channel which would be 15 mm in the case of the test rig. To minimise errors arising from lubricant transition from the rig and into the sensor, the same standard piping was used and would be adapted to allow the pairs of lasers and photodiodes to be attached (see Figure 7.6).

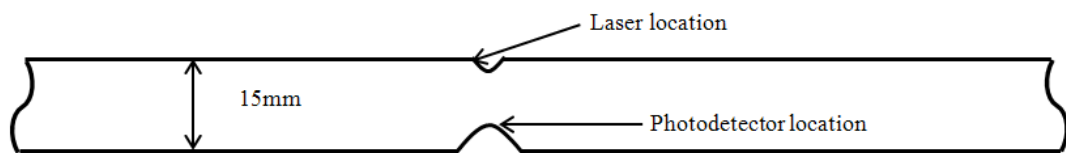


Figure 7.6. Layout of pipe and desired location of main components.

It was necessary to separate the lubricant from direct contact with the light source and photodiode for several reasons. If both were immersed directly, there was potential for wear debris to become caught on each component face, preventing accurate data

capture. In addition the varying temperature of the lubricant (18-75 °C) was expected to detrimentally affect the small voltage and current signals that are generated within each component. Small glass windows consisting of 1mm thick microscope slide glass cut to 5mm x10mm rectangles were used as separators. Each was secured using epoxy resin and self-adhesive silicone tape to prevent leaks and offer a secure point of contact for mounting the components.

7.3.2 Selection of Light Source

The light source was required to transmit the correct wavelength through 3 separate layers of material before falling on the photodetector: 2 layers of 1mm thick glass and lubricant. Several issues needed to be considered before selection. Beam divergence from the light source was the primary concern as it could affect the integrity of the generated signal from the photodetector (see Figure 7.7).

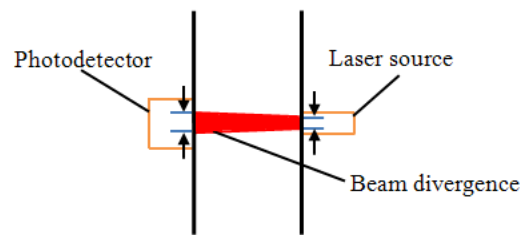


Figure 7.7. Beam divergence across lubricant and glass.

The cross-sectional area of the beam at point of incidence ideally should closely match the photodetector chip to ensure that the maximum sensitivity to changes in the total optical intensity. The optical intensity of light from diffuse sources such as standard LED's and halogen bulbs are greatly affected by the distance from source to detection point as the intensity is defined as:

$$I_{detected} = \frac{P_{emitted}}{4\pi r_{dif}^2}, \quad \text{Eq. 8.2}$$

where $I_{detected}$ is the intensity of light detected, $P_{emitted}$ is the power of the source light and r_{dif} is the distance between the light source and the measurement point. As r_{dif} doubles in value, the intensity reduces to 25% of the original value. This may lead to

poor signal quality and it was concluded that diffuse light sources would not be suitable.

Non-dispersive infrared (NDIR) is an absorbance method that uses a broadband heat source and filters to produce a specific IR waveband that can be used for analysis. The source typically generates all IR wavebands and a filter lens is used to select the desired waveband for the given purpose. NDIR has been demonstrated as a viable analysis method for creating a low cost inline lubricant detection system [140]. In the described system created, NDIR detection is shown to be feasible for small gap sizes of 2 mm. However, NDIR can suffer from higher signal to noise ratios when compared with sources such as lasers due to the use of filters which reduce the total excitation energy.

Lasers operate by reflecting light of a specific wavelength or small waveband between two highly reflective surfaces such as mirrors. In the gap between the surfaces is a gain medium consisting of a material with properties that allow amplification of the light. In this process known as stimulated emission, electrical energy or a separate light source forces the electrons in the material into a lower energy state and yield the lost energy to the light passing through. An initial light source is passed through the gain medium and reflected continually between the mirrors and is amplified with each pass. One of the mirrors has partial transparency so that light may pass through and be utilised. The emitted light has similar wavelength and phase, giving it high coherence. This property makes laser suitable for the sensor design as the higher light intensity falling on the photodetector will in turn create a stronger signal. However, small lasers with low power consumption which are most suitable for this application have higher beam divergence profiles compared to larger more powerful ones.

The next consideration was the absorption of light by the lubricant and glass which would lead to signal degradation. The microscope slide was composed of BK7 glass which has a well-characterised transmission spectrum [141]. The main region of electromagnetic radiation that allowed a high level of total transmission was found to be in the visible and near infrared region as shown in Figure 7.8. The selection of the laser source was limited to regions between 500 and 1900 cm^{-1} due to the high transmittance of 96.8% for 1mm thick BK7 glass.

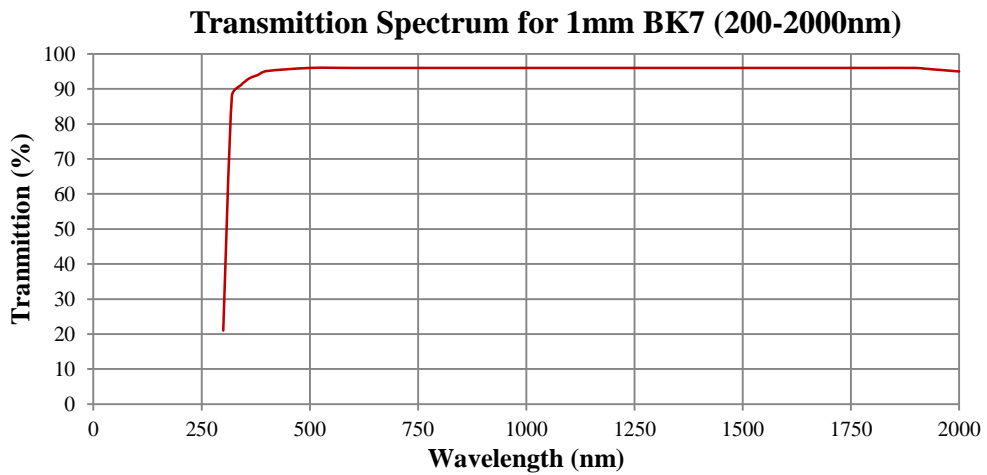


Figure 7.8. Transmittance spectrum for BK7 glass.

The transmission spectrum for gearbox lubricants is highly variable which made selecting a laser of a suitable wavelength difficult. XMP320 gearbox lubricant was used as the test lubricant for the duration of research. Therefore the main areas where transmission in XMP320 is low or significantly reduced corresponded to the near-IR to mid-IR spectral range (2500-16000 cm^{-1}) were found (see Figure 7.9). This allowed the spectral range limited by the BK7 glass slide to form the sole restrictive factor in selection of laser wavelength.

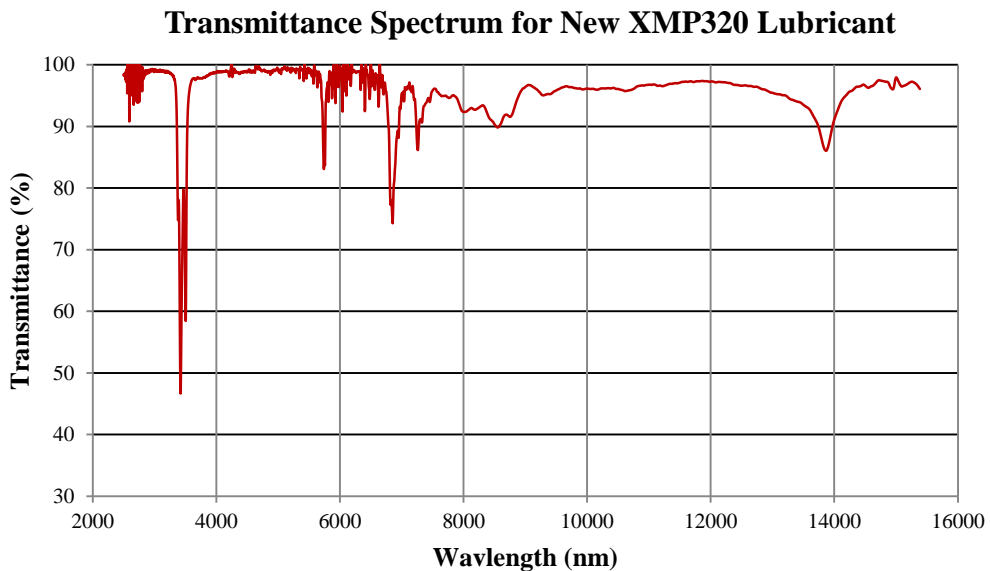


Figure 7.9. Sample transmittance spectrum for XMP320 test lubricant

From reviewing commercially available laser diodes, it was found that none existed that could provide a waveband at the targets of 1738 cm^{-1} and $1134\text{-}1272\text{ cm}^{-1}$. Laser diodes at 12376 cm^{-1} were available which was situated in the near IR spectrum. The FTIR analysis of the XMP320 lubricant samples was conducted in the mid IR spectrum. Despite the difference and the inability to track the target wavebands, the principle of the laser in operation may be demonstrated using near IR laser diodes and comparing the absorption spectra of XMP320 and a highly IR absorbent liquid such as water. Laser diodes with new wavelengths are being created so there is potential for future development [142].

Two types of 12376 cm^{-1} (808 nm) IR laser diode were selected (summary of the main characteristics can be seen in Table 7.1). Selection was based on based several factors such as low power consumption. Each could be supplied by a standard 9V DC battery and draw currents between 200 and 500 mA. In addition, the price was approximately 8 GBP per laser which was in line with the concept of low cost condition monitoring.

Table 7.1. Summary of laser diode characteristics used in selection process.

Laser Code	TO-808-0.5	TO-808-0.6	Units
Peak Wavelength	12376	12376	cm^{-1}
Slope Efficiency	≥ 0.95	≥ 0.95	W/A
Vertical Beam Divergence	38	40	deg. C
Horizontal Beam Divergence	8	12	deg. C
Output Power	200	500	mW
Operating Temperature	10-40	20-35	$^{\circ}\text{C}$
Operating Voltage	≤ 2.2	≤ 2	V
Emitting Area	40	50	μm

Final selection was based on the combined vertical and horizontal beam divergence as this would affect the photodetector's sensitivity to the incident light. The laser's initial profile was approximately circular but would diverge into an increasingly elliptical shape the further the light travelled. Eq. 7.3 was used to determine the exact beam divergence change in both horizontal and vertical directions. The initial beam diameter was found to be 1mm and the length over which the laser would diverge was 19 mm. This included the thickness of the BK7 slides (1mm) and the pipe thickness ($\approx 1\text{mm}$). The total beam divergence could be obtained using the following relationship:

$$\theta = 2\arctan\left(\frac{D_f - D_i}{2l}\right), \quad \text{Eq. 7.3}$$

where θ is the total beam divergence angle, D_f is the vertical projection, D_i is the horizontal projection and l is the length which the laser is projected across. Beam profiles were then established and are summarised in Table 7.2. TO-808-0.5 was selected as the initial test laser due to its smaller beam profile and consequently higher illuminance. However, since the photodetector had not been selected yet, it was conceivable that TO-808-0.6 could be used at some stage.

Table 7.2. Resultant beam profiles for at length $l = 19\text{mm}$.

	Parameter (mm)	θ (Deg)	D_i (mm)	D_f (mm)	Resultant Bean Profile
TO-808-0.5	Vertical	38	1	12.08	
	Horizontal	8	1	1.66	
TO-808-0.6	Vertical	40	1	12.83	
	Horizontal	12	1	2.99	

7.3.3 Selection of Photodetector

The sensor's accuracy would depend on the changes in the voltage output of the photodetector so several factors had to be considered. Sensitivity to the incident light was the main concern as the photodetector was required to respond to a particular wavelength of IR light. The peak output of the lasers selected was 12376 cm^{-1} so only photodetectors made of silicon and germanium were initially considered due to their spectral range responsivity (190-1100 nm and 400-1700 nm, respectively).

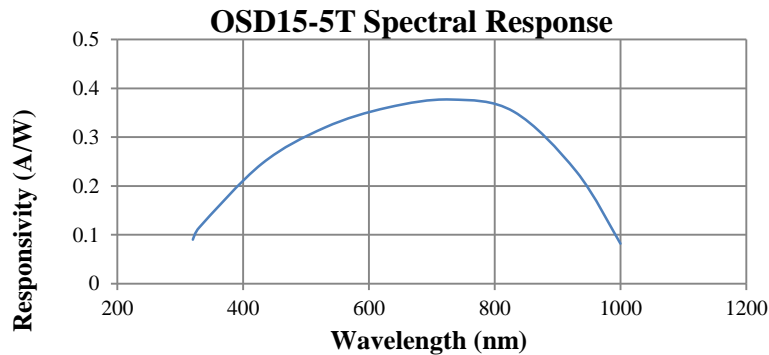


Figure 7.10. Responsivity/wavenumber relationship of a photodetector OSD15-5T.

Germanium photodiodes were found to have higher signal to noise and the larger spectral range was unnecessary for the selected lasers. Responsivity is the measure of the electrical output in amperes per incident radiant power input in watts and is used to assess photodiode sensitivity. A higher responsivity is preferred as the electrical output that is generated is larger, with the difference between signal and noise therefore being larger. If a low responsivity is used, noise fluctuations can prevent meaningful data from being extracted from the signal. For a given wavenumber and p-n junction, an optimum responsivity can be found. A short review of appropriate photodiodes was conducted on RS Components' OSD series with the details summarised in Table 7.3.

Table 7.3. Main OSD photodiode characteristics used in selection process.

Laser Code	1-5T	5-5T	15-5T	35-5T	Units
Active Area	1	5	15	35	mm ²
Responsivity (L=436cm ⁻¹)	0.21	0.21	0.21	0.21	W/A
Dark Current	0.5	2	3	3	nA
Capacitance (V _r = 0V)	30	130	390	950	pF
NEP WHz ^{-1/2} (L=436cm ⁻¹)	1.2x10 ⁻¹³	2.4x10 ⁻¹³	3.0x10 ⁻¹³	3.0x10 ⁻¹³	MΩ

OSD5-5T was selected due to its low capacitance, similar responsivity and an active area with equivalent diameter of 2.52 mm. This corresponded approximately with the beam profile diameter of the selected laser. The responsivity relationship for OSD5-5T is shown in Figure 7.10. It can be seen that the peak responsivity region corresponds approximately with the laser wavenumber of 12376 cm⁻¹.

7.3.4 Circuit Design

A driver circuit was built to power the laser and photodiode by providing the necessary voltage and current for optimal operation. The circuit layout for the laser portion of the circuit is shown in Figure 7.11. The laser required at least 200 mA of current at approximately 2.0V, however, it was considered desirable to allow small changes in these values to test effectiveness. A 10μF 16V capacitor was connected in parallel

with the laser to protect it from large voltages that can occur due to battery inactivity. The capacitor charges when a spike occurs, preventing the excess voltage from affecting the laser. A single LM317 chip regulator was used to ensure the maximum 500 mA was not exceeded by drawing the maximum available current and dissipating the excess through a steel heat sink. A 100Ω potentiometer was connected to the output of the LM317 to allow the output voltage to be adjusted whilst maintaining a stable current. Standard 1N4001 diodes were used to protect the LM317 and laser reversed biased voltages arising from incorrect battery connection. A digital multimeter was used to check voltage and current values at key locations such as the laser and the potentiometer.

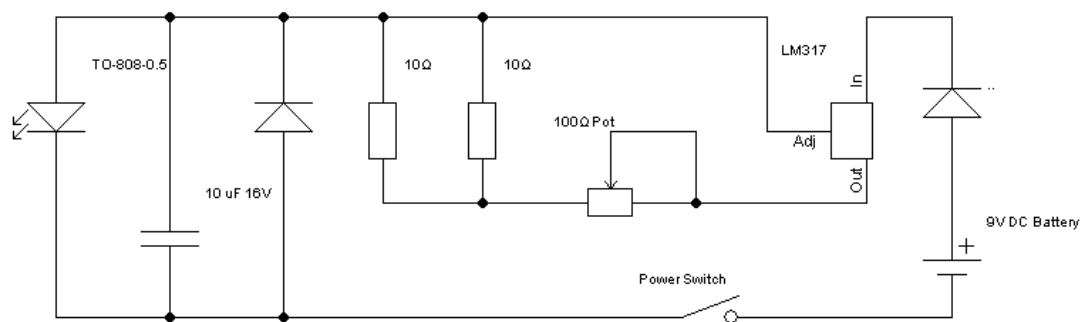


Figure 7.11. Driver circuit for laser diode using TinyCAD® open source software.

The circuit design for the detector circuit was slightly more complex due to the need for accurate signals to be generated by the photodetector. Photodetectors can have a variety of operational modes, with the two most commonly used being photovoltaic and photoconductive [143]. In photovoltaic mode, the photodetector has zero bias meaning no external voltage is applied. When light strikes the p-n junction, the photons liberate electrons and generate current but this is restricted by a resistor in series. Due to this resistance a voltage is generated. However, as the voltage is generated only by the incident light, the signal tends to be relatively small. The advantage of the system is the simple circuit design that can be used to monitor the signal. Theoretically, the photodetector in photovoltaic mode could be connected by itself to a microcontroller with a suitable resistor and the generated signal could be monitored.

In photoconductive mode, the photodetector is biased with a voltage. Reverse bias is commonly used, where the p-type material of the junction is connected to the negative terminal and the n-type material to the positive. This reverse bias increases the depletion zone of the p-n junction which decreases the junction capacitance.

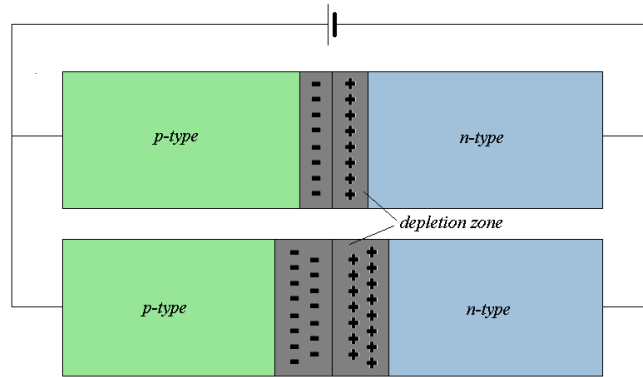


Figure 7.12. Increasing depletion zone due to reverse bias of voltage.

The effect of this decrease in capacitance is to increase the responsivity and linearity of the photodetector voltage to the incident light. For this reason, it was decided to use reverse bias as fast signal generation was considered to be important for sensors operating inline within the condition monitoring system.

To achieve photoconductive mode, a reverse bias circuit was designed as shown in Figure 7.12. A key consideration of this circuit was the use of an operational amplifier (op-amp) and the feedback resistor used. These will determine the gain-bandwidth product (GBProd) of the circuit which is a measure of the gain at particular frequencies. In the case of the circuit, it was desired to amplify the signals significantly to improve the detection of changes to the incident light. The first stage was to consider the desired range of output voltages for analysis. It was intended to use a microcontroller that could interface with a computer. In general, microcontrollers operate between 0-5V with maximum current in the order of 200mA so this was set as the target range. The output voltage for a generic reverse bias circuit is defined as:

$$V_{out} = I_S R_f, \quad \text{Eq. 7.4}$$

$$V_{out} = R P_o R_f, \quad \text{Eq. 7.5}$$

where V_{out} is the output voltage for monitoring, I_s is the photodetector light signal current, R_f is the feedback resistance, R is the responsivity of irradiance of the photodetector and P_o is the power of light incident on active area. Using the expected values of $R = 0.21\text{A/W}$ and $P_o = 0.5\text{W}$ at light of 12376 cm^{-1} at maximum irradiance, it was found:

$$V_{out} = 0.042R_f. \quad \text{Eq. 7.6}$$

This means for the largest value V_{out} to be in the range of 0-5V, the value of R_f needed to be approximately 100Ω ($V_{out} \approx 4.2\text{V}$). To achieve a stable circuit at this gain, a suitable value of GBProd must be used. To determine the GBProd, first the feedback capacitance C_F must be derived:

$$C_F = \frac{1}{2}\pi f R_f, \quad \text{Eq. 7.7}$$

where R_f is the feedback resistance and f is the maximum operating frequency of the circuit. The maximum operating frequency of the circuit was calculated from the photodetector characteristics:

$$f_{max} = \frac{0.35}{t_r}, \quad \text{Eq. 7.8}$$

where t_r , is response time required for the photodetector to increase its voltage output from 10% to 90% of final output level. This was stated to be approximately 20 ns for biased mode operation for incident light less than 900cm^{-1} . This gave a maximum operating frequency of 1.75MHz. Using Eq. 7.7, it was found that C_F should be 1nF. The GBP was then derived using:

$$GBP = 2f^2\pi R_f(C_F + C_J), \quad \text{Eq. 7.9}$$

where C_J is the junction capacitance of the photodetector ($80\mu\text{F}$ at 0V and $390\mu\text{F}$) and all other values remain as in previous equations. It was found when using C_F of 1nF, the GBProd 5V was 4.29MHz. A CA3140 op-amp was selected used as it had an approximate GBProd of 4.5MHz, high operational temperature of 125°C and inbuilt noise dampening (see Figure 7.13).

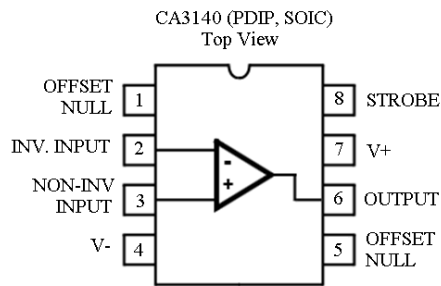


Figure 7.13. CA3140 op-amp with pin connections indicated [144].

The final circuit layout of the photodetector driver portion is shown in Figure 7.14. A separate DC battery supply was used due to the large current demand required by the laser diode and to allow isolation of any errors that may occur in either circuit. One of the main considerations for this circuit was the selection of a suitable operational amplifier (op-amp). This would allow a 100 k Ω resistor to be used to bias the photodetector to its optimal responsivity.

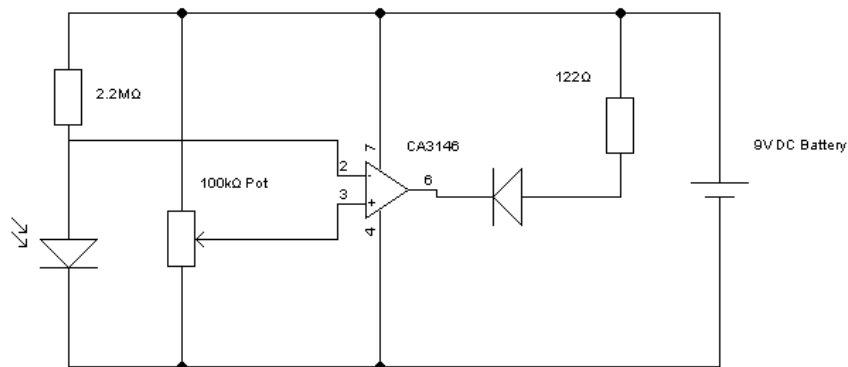


Figure 7.14. Reverse bias photodetector driver circuit using TinyCAD[®] open source software.

7.3.5 Circuit Mounting on Pipe

The circuit boards were secured to the 15mm copper pipe using electrical tape. The laser was secured using a laser mounting bracket that also acted as a heat sink which itself was secured to the BK7 glass using epoxy resin. The photodetector was secured directly opposite on the BK7 glass with epoxy resin also.



Figure 7.15. Circuit mounted on copper pipe.

7.4 Testing Methodology

The pipe was sealed at one end using solder (see Figure 7.16) and a rubber bung fitted for the other. This would allow samples to be tested without having to incorporate the sensor fully into the test rig. Initially the pipe was filled with XMP320 to determine if the 12376 cm^{-1} could be detected across the diameter.



Figure 7.16. Sealed end of pipe to allow samples to be held while IR sensor transmits voltage signal.

Once the samples were entered into the pipe, the output from the photodetector circuit was connected to an Arduino Uno microcontroller (see Figure 7.17). This converted the analogue output voltage of the photodetector circuit and the input voltage of the laser circuit into a digital signal. The Arduino consists of small microcontroller with 6 analogue to digital (ADC) pins and 14 digital output pins. By using the open source integrated development environment (IDE), it is possible to write software and upload it to the Arduino to operate independently of the computer. The data can be transferred between the Arduino and a computer using a serial port and the necessary communication protocols within the software. The advantage of this system is the analogue voltage could be converted into a 1024 bit signal.

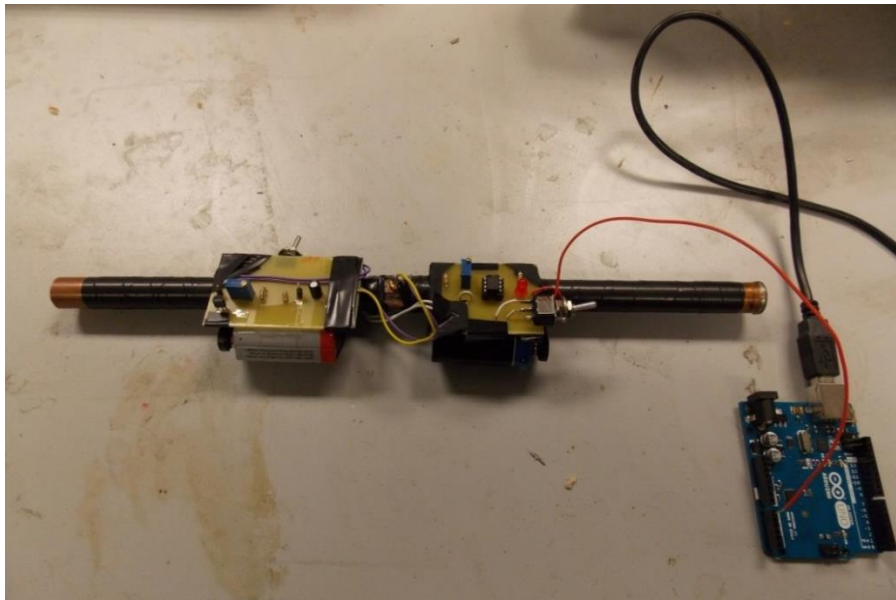


Figure 7.17. Photodetector output connected to ADC1 of Arduino microcontroller.

The voltage is applied at ADC pin 1 of the Arduino where it is read into the program loop. The ADC value is converted back into a voltage value using the internal voltage reference of 5V. The program displays the voltage and the time at which it was recorded. The program then increments the time by 100ms and repeats the process indefinitely. The code used is shown in Figure 7.18.

```
Photodetector_Signal | Arduino 1.0.5-r2
File Edit Sketch Tools Help
Photodetector_Signal$
int photodetector_in = A1;
int ADC_val;
double voltage_photo;
unsigned long time = 0; //declare time variable

void setup(){
  Serial.begin(9600); //Set communication speed
  analogReference(DEFAULT); //Default reference is 5V
}

void loop(){
  ADC_val = analogRead(photodetector_in);
  voltage_photo = ADC_val*(5/1024); //conversion from ADC to voltage
  time = millis();
  Serial.print("Photodetector Signal: ");
  Serial.print(voltage_photo);
  Serial.print(", Time: ");
  Serial.println(time);
  delay(100);
}

Done compiling.

Binary sketch size: 4,370 bytes (of a 32,256 byte maximum)
21 Arduino Uno on COM1
```

Figure 7.18. Arduino program used to view and log voltage signal.

Chapter 8 – Experimental Results

The experimental tests conducted using both sensors produced a variety of results. The active pixel sensor demonstrated the ability to capture particles inline, in real time at a variety flow rates and under different lighting conditions. Shape classification and major dimension binning was possible on particles that were successfully identified. The lubricant quality sensors did not yield discernible results.

8.1 Wear Particle Sensor Experimental Results

The testing methodology for the wear particle sensor was intended to identify the limitations of the system. Overall the system performed as expected, in that it was able to discern particles from the surrounding lubricant in real-time, analyse the particles for morphology and log the data. The main issue for the system was separating particles in close proximity.

8.1.1 Particle Size Testing

A series of wear regimes were introduced to assess the detection capabilities of wear particles with 2 different size classes: 136.9 μm and 487.3 μm . The sensor was assessed on the number of particles it could detect from 50 mg samples. When considering only the APS, the largest detectable particle relied on the focal length of the sensor, the field of view for that given length and the camera offset distance as shown in Figure 8.1.

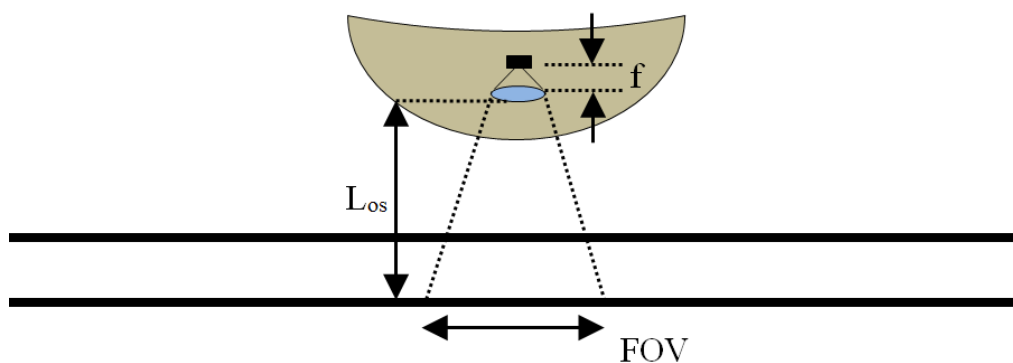
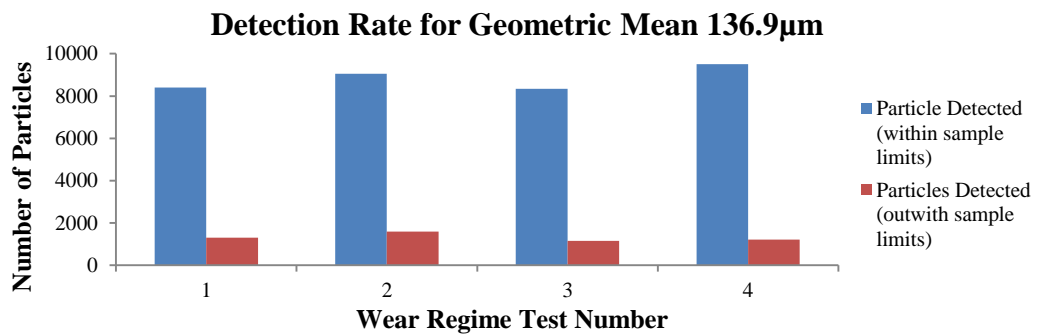


Figure 8.1. Focal length, f , field of view, FOV , and camera offset length, L_{os} .

Using a camera offset of 24 mm with a 1.5 MP APS array, it was possible to capture an object with a major dimension of 16 mm. Particles of this magnitude are not of interest but can occur with catastrophic failures where gearbox teeth fragments fully detach. However, this would require a significantly larger pipe diameter and so the limiting factor becomes the pipe diameter of 6 mm. By increasing L from the standard distance of 2.4 mm it was possible to capture larger particles but with fewer pixels, requiring a different conversion factor.

A significant requirement of the sensor was detecting particles with small dimensions. The lowest detectable particle size was determined with 8 wear regimes of 50 mg: 4 regimes used spherical particles with a geometric mean diameter of 136.9 μm and 4 of 487.3 μm . A constant flow rate of 12 ml s⁻¹ was used, with each wear regime flushed with clear lubricant for 15 min to reduce the risk of cross contamination.



Test Number	Particles Introduced	Particles Detected (within sample limits)		Particles Detected (outwith sample limits)	
		Number	% of total	Number	% of total
1	12825	8401	65.5	1309	10.2
2	12825	9056	70.6	1596	12.4
3	12825	8337	65.3	1147	8.9
4	12825	9502	74.1	1208	9.4

Figure 8.2. Summary of 50 mg samples of geometric mean 136.9 μm .

In Figure 8.2 the results of the 136.9 μm diameter particles are shown. The total number of particles within the sample limits was used to calculate an average percentage detection rate of 68.8% for particles with a geometric mean 136.9 μm . Particles that were detected but were either smaller than 125 μm or greater than 150 μm were excluded from this average. Examples of the returned images can be seen in Figure 8.3.

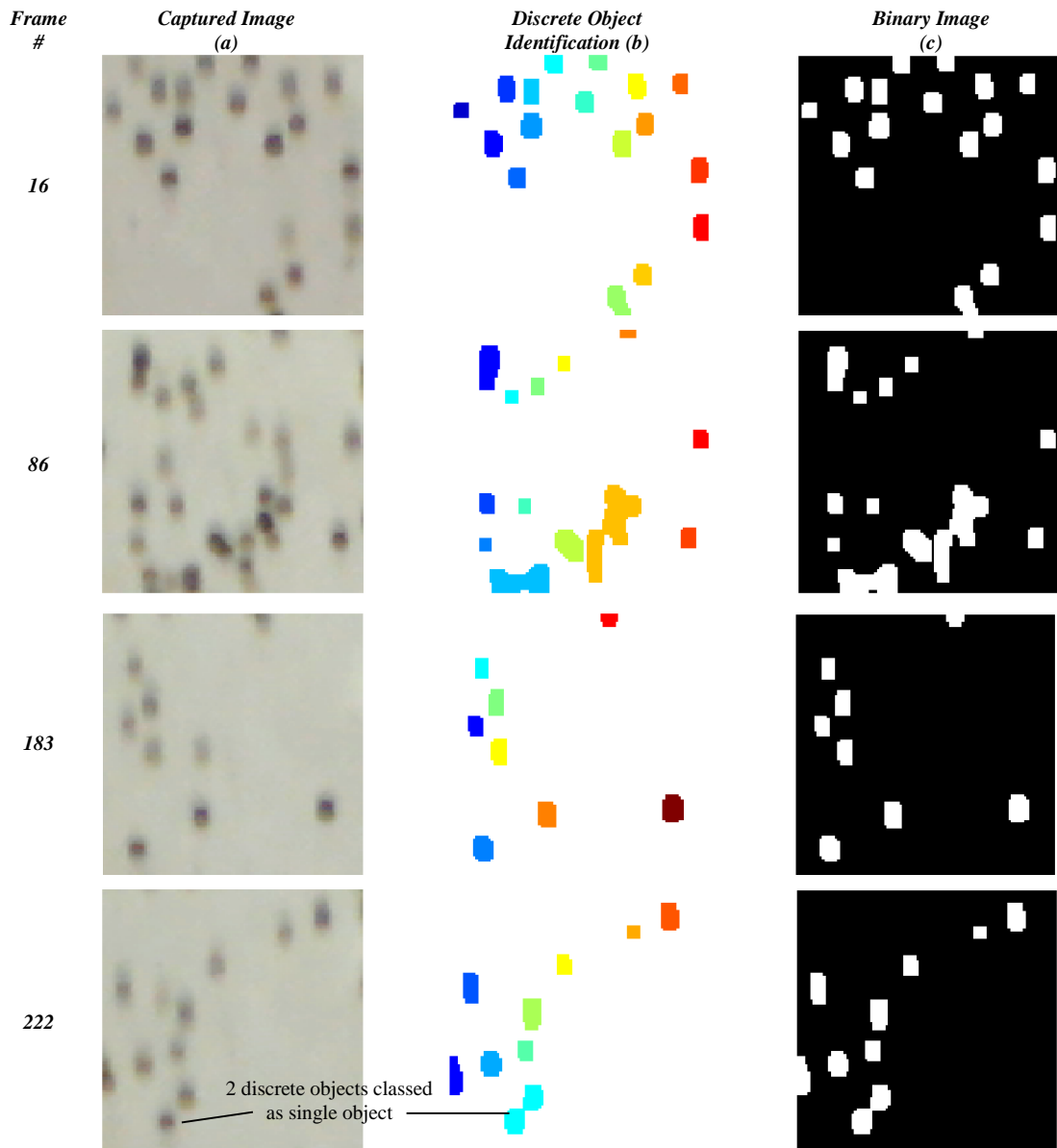
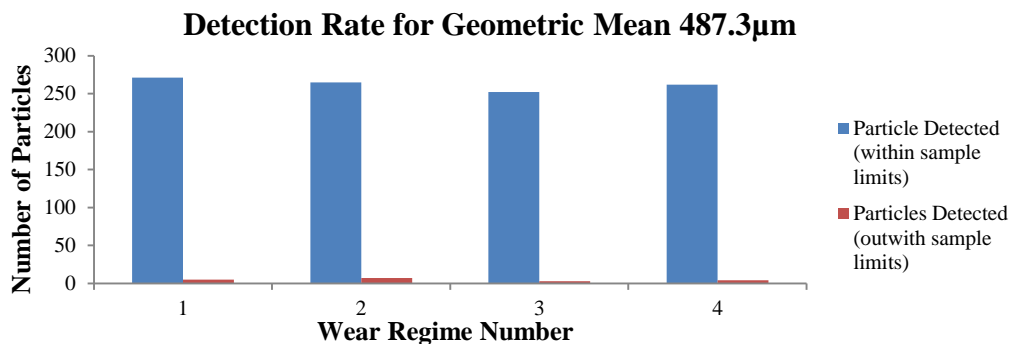


Figure 8.3. Sample of images from Test #1 of 125 - 150 μm particles to determine detection rate.

Particles within the sample limits were determined by checking the total number of pixels a discrete object contained and comparing that to the limits of the particle regime. On average, 62.1% fell into this category which was considered reasonably acceptable as the majority of particles within the given low size range were detected using a low cost imaging sensor. The sensor had been set to capture images at a slightly lower frequency than was considered adequate for the given flow rate of 12 ml s^{-1} . One reason why the detection rate was lower is that objects were often identified that consisted of 2 particles in close proximity, as shown in Frame 86 in Figure 8.3. Three

objects within that image were significantly larger than the given limits and so were not included in the main detection rate. On average 10.2% of objects were either too large or small. Another source of error is that some particles which could be viewed manually were not classed as a discrete object, for example the light blue object in Frame 222 in Figure 8.3. Despite these errors, a total detection rate of 72.3% was considered a success due to the low cost of the sensor equipment and the relatively small particles that were able to be discerned as part of a real-time acquisition and analysis system.

In Figure 8.4 the results of the 487.3 μm diameter particles are shown. It was expected that the detection rate for these particles should be significantly higher due to the greater object size that would manifest in each image. The average detection rate was found to be 92.0%. It was found that a smaller proportion of particles out with the minimum/maximum range of 475-500 μm when compared to the 136.9 μm diameter tests. The particles appeared clearly on the original images and also maintained the circular shape features after processing. The centre image (Figure 8.5(b)) is the intermediate stage of image processing where different objects are assigned different numerical values. This is represented by different colours for discrete objects. The majority of particles appeared clearly on the original images.



Test Number	Particles Introduced	Particles Detected (within sample limits)		Particles Detected (outwith sample limits)	
		Number	% of total	Number	% of total
1	285	271	95.1	5	1.8
2	285	265	93.0	7	2.5
3	285	252	88.4	3	1.1
4	285	262	91.9	4	1.4

Figure 8.4. Summary of particles detected for 50mg samples of geometric mean 487.3 μm . In Figure 8.5, sample images of particles are shown for the 487.3 μm

diameter experiments. The detection rate of the particles is higher for a number of reasons. The larger size means that the conversion of objects using Otsu's algorithm has a much steeper gradient when moving from the centre of a particle to the surrounding lubricant. The lower number of particles also reduces the effect of clustering that was significant for smaller particles.

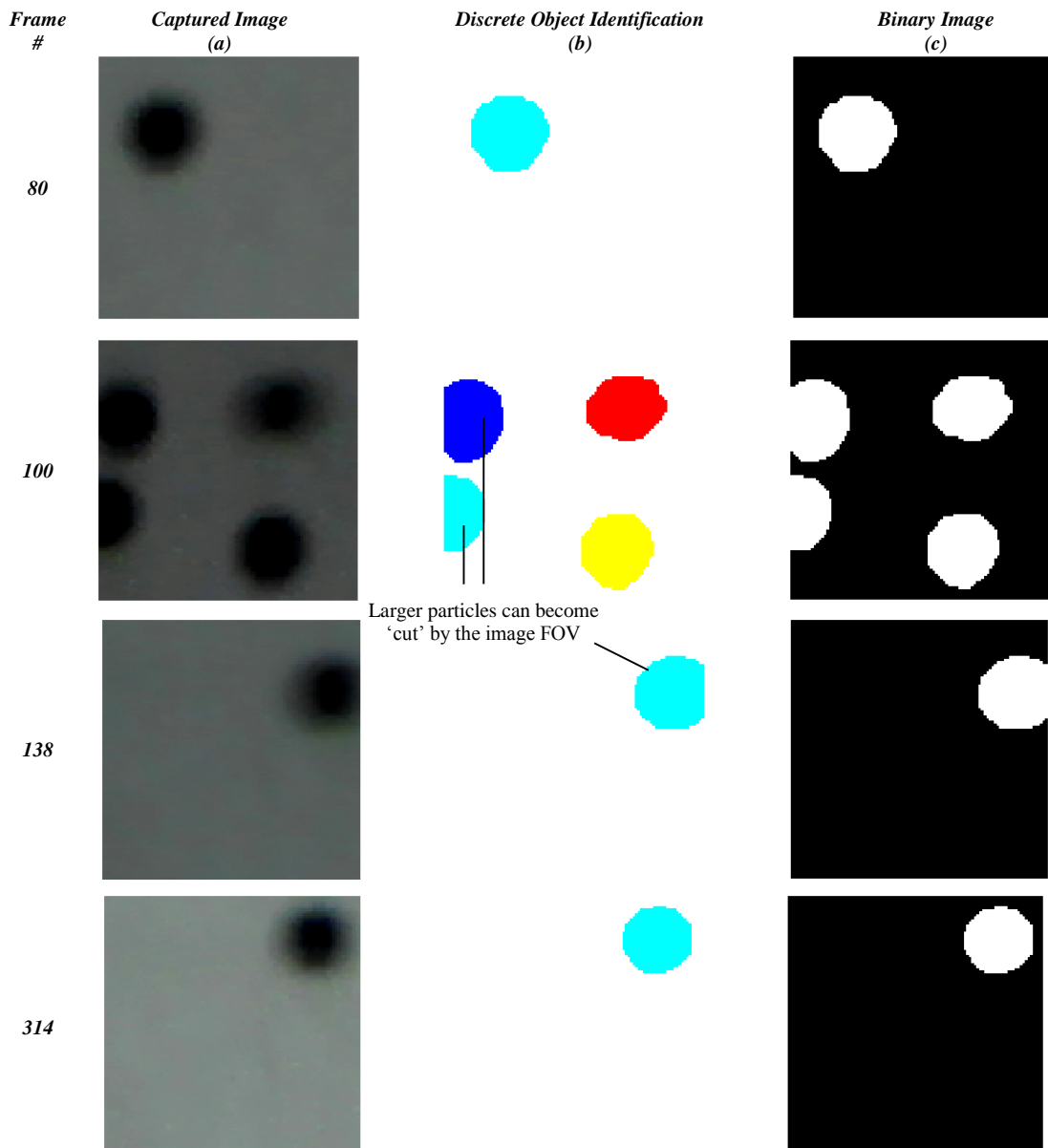


Figure 8.5. Single 475 - 500 μm particle in original, binary and unique identifier.

However, particles were still not counted due to being too small. If a particle was only partially within the FOV, it may be ‘cut’ as shown in Frame 100 in Figure 8.5. Two particles shown with shades of blue have just entered the FOV when the APS was active as indicated. This may be a source of the particles detected out with the given sample limits. The other source of error is the lack of clarity surrounding certain objects like in Frame 312 in Figure 8.5(a).

A solution to particle ‘cutting’ may be to increase the FOV and introduce particle tracking. In this system, each particle would be assigned a unique identify as it fully enters the FOV by measuring when the object is fully surrounded by background pixels. The pixel would be assessed for shape and then removed from tracking as the required information has been captured. The main issues of this system will be laminar flow causing particles to appear as a single object but then separate into discrete objects over the tracking period.

Coincidence limits (or coincidence losses) refers to the maximum particles that can be within detectable range before the sensor cannot differentiate between individual particles. Two discrete particles may be counted as one even if few particles are within detectable range. However, the coincidence limit usually denotes the point that an unacceptable number of particles will not be individually counted. The standard used to in calculating coincidence limits for light extinction sensors detecting particles suspended in liquid is BS ISO 21501-3:2007 [145]. The following assumptions are made for calculating limits (see Figure 8.6):

- Particles are uniformly distributed within liquid in all dimensions.
- Particles in lubricant have constant mean density.
- Particles contained in 2 unconnected regions are independent.

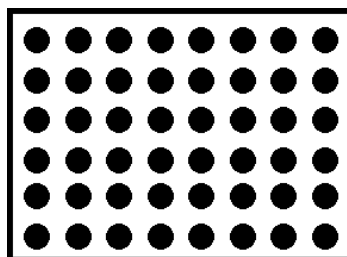


Figure 8.6. Assumed particle distribution in ISO 21501-3:2007.

The format for reporting the performance of an industrial particle sensor based on light extinction is the maximum concentration of particles of a given size whilst experiencing $\leq 10\%$ coincidence loss. For the APS sensor, the lowest particle size detectable with a high degree of consistency is $125\ \mu\text{m}$. At a flow rate of $12\ \text{ml s}^{-1}$ a particle of this size will take approximately $0.5\ \text{s}$ to fully traverse the area of interest. A coincident event will occur if an image is captured when a particle is close enough to another particle to be miscounted as a single particle. When trying to evaluate the performance of the sensor using BS ISO 21501-3:2007, problems occurred as the standard was used to classify sensors that report a voltage signal indicating the major dimension of the particle [146]. This meant that the sensor could only be evaluated against certain standards such as coincidence loss:

$$L(\%) = [1 - \exp(-Q \cdot t \cdot C_{\text{max}})] \times 100 \quad \text{Eq. 9.1}$$

where L is the coincidence loss, Q is the flow rate, t is the time taken to pass through sensing region and C_{max} is the maximum particle concentration. At a flow rate of $12\ \text{ml s}^{-1}$ with particles taking $0.5\ \text{s}$ to cross through the sensing region was used for all calculations. The maximum number of particles was calculated to be 20 by averaging the number of $125\text{-}150\ \mu\text{m}$ particles per image captured over the regimes used to test lowest particle size. Using these values, the coincidence loss was calculated at 24.25% meaning approximately a quarter of all particles captured within an image will experience a coincidence event. An average of 10.2% of all particles that were detected during the four $125\text{-}150\ \mu\text{m}$ tests were outwith the expected particle limits. The large coincidence loss of nearly 25% is likely the cause of this as particles may group together and be classed as a single object and hence excluded from the detection rate.

8.1.2 Misidentification of Particles

During image processing, it was found that images with no particles present would occasionally detect an ‘object’ within the image. An example of this effect is shown in Figure 8.7. In most circumstances, the detection subroutine would show lubricant only images as black during binary conversion.

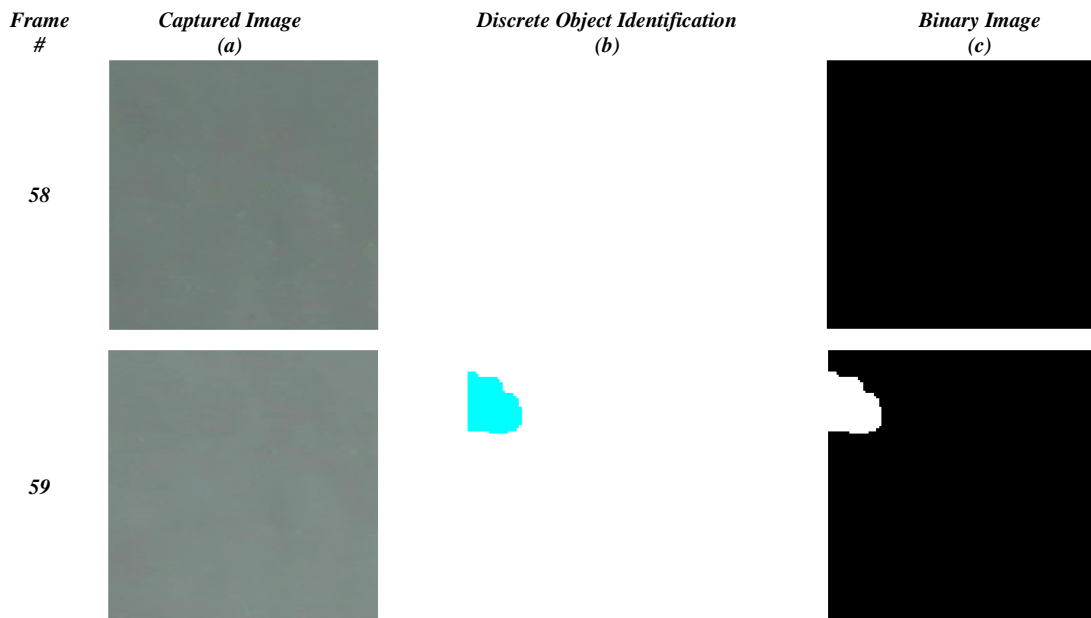


Figure 8.7. Misidentification of lubricant as an object.

Misidentification occurs during the conversion between greyscale to binary where the relative weighting of lighter and darker regions means a boundary is found, despite visually appearing similar. The issue may be resolved by introducing a second condition for object detection where a minimum number of pixels over a certain threshold of greyscale must be detected before an object can be declared. The exact greyscale level would be determined by the lowest particle size detectable as these objects are significantly lighter than larger objects. From manual inspection of sample images, misidentification of particles was a rare occurrence. The most common error is coincidence losses where multiple particles are classed as a single object, causing a misidentification of shape and overall size.

8.1.3 Effect of Mixed Samples on Detection Levels

A problem identified during mixed particle regime runs was the effect large particles has on the overall number of particles detected. It was found that when 500 μm were mixed with smaller particles, a significant portion of the smaller particles were not identified by the object analysis subroutine (see Figure 8.8).

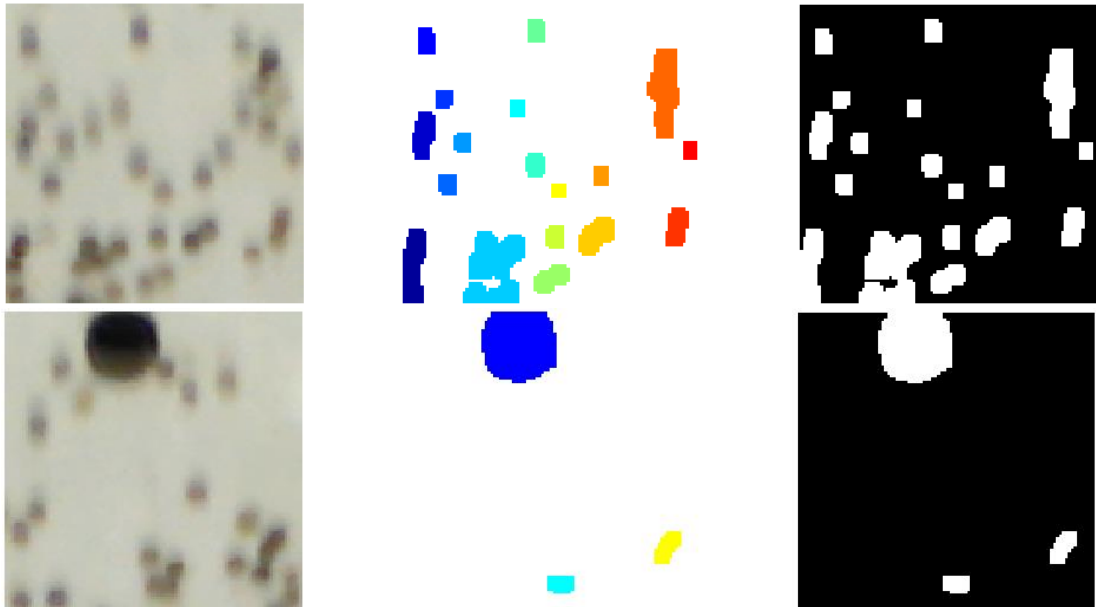


Figure 8.8. Large 500 μm particles disrupt ability for detection subroutine to discern smaller particles.

The problem may occur during the evaluation of the greyscale level used to divide the image into bi-modal regions during the application of Otsu's method. The larger particles tend to have an average greyscale level approximately in the region of 210-255 whilst smaller particles may have greyscales averages approximately in the region of 110 to 240 levels. To improve the detection rates of mixed particle images, Otsu's greyscale level may be calculated normally and then a second manually altered level may be applied to check if any smaller particles appear once the detection routine is applied again.

8.1.4 Closing and Opening

Another significant problem was the low coincidence limits observed during all testing regimes. The clustering of particles is a problem associated with all light extinction wear sensors and also others based on electromagnetic parameters. Unlike those systems, a number of mathematical operations can be conducted on the captured image to reduce this problem.

In Chapter 6, erosion and dilation were described as operations used to reduce or thicken objects by structuring elements for the purpose of improving image quality or assessing geometric features. These operations are useful in reducing noise surrounding particle images but other features like curves may be thickened to such an extent that they cannot be distinguished.

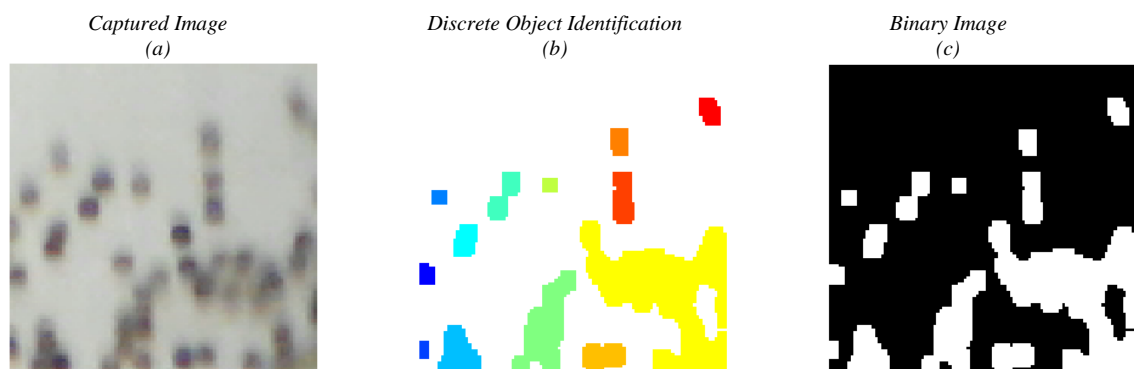


Figure 8.9. 125-150 μm particles in clusters. Image was passed into closing/opening operations to improve number of discrete particles.

A series of different structuring elements were applied to sample images that contained groupings of particles that appeared separate when viewed by the user, but appeared as a single mass when the object detection subroutine was applied. An example of a selected image is shown in Figure 8.9. The structuring elements used included disk, line, octagon and square, a summary of the types and size is shown Table 8.1.

Table 8.1. Summary of structuring elements applied and various differences in parameters.

Structuring Element Shape	Image of Shape	First Test	Second Test	Third Test
Line		Length = 6 Direction = 0	Length = 15 Direction = 0	Length = 6 Direction = 0
Square		Diameter = 6	Diameter = 20	Diameter = 16
Circle		Radius = 3	Radius = 15	Radius = 7
Octagon		3	15	8

The opening operation used a circle structuring element with radius of 8 pixels was able to separate some of the particles in the sample images. Closing tended to exacerbate the problem as small gaps between discrete particles often disappeared and formed a single object. Examples of the individual operations are shown in Figure 8.10 based on the captured image in Figure 8.9. Despite functioning better than closing in reducing particle clusters, opening often caused small particle to disappear.

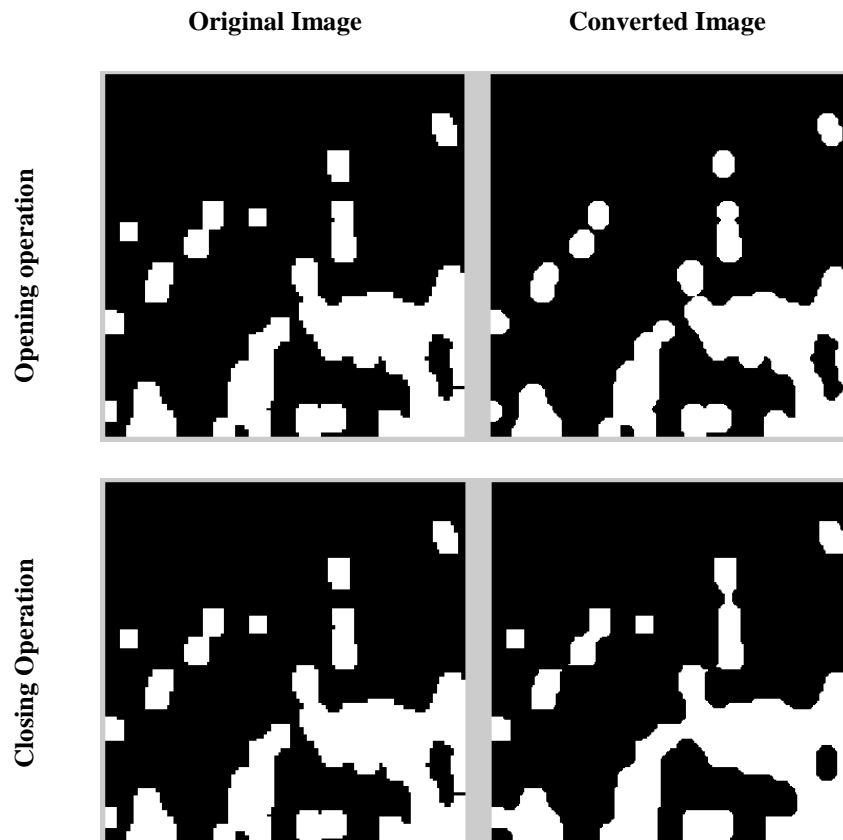


Figure 8.10. Conversion of image with clustered particles using closing and opening with circle structuring element.

Object erosion performed best but parameters such as size and shape were changed which would alter the correlation to the type of wear that is passing through the lubricant. To increase the number of particles detected whilst maintaining the shape and size analysis, the image may be initially process under the existing program but would also be eroded. If a significant number of discrete particles were found during erosion, the difference may be added to the cumulative total for the original image. These additional particles would have no shape or size parameters associated with them but would indicate to the user that higher rate of wear has been liberated that is being reported.

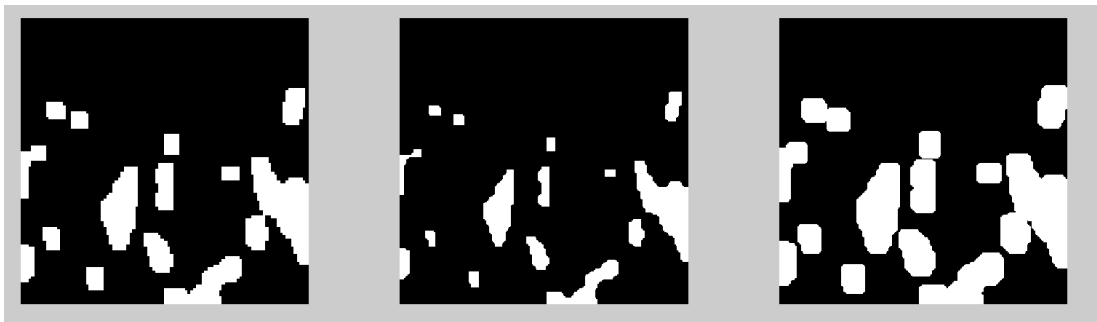


Figure 8.11. Opening operation of captured wear particle image.

8.1.5 Improvements for Particle Detection

Increasing the total pixel number used to capture the same area of interest would allow higher levels of detail to be captured. Particles with major dimension of less than 50 μm were rarely detected as the analysis program would not count particles that measure a few pixels in size. If the total number of pixels that represented these particles were increased, the capture rate for this size class could be improved without any major modifications to the current program.

The detection rate for particles of grade 125-150 μm was lower than expected. From analysing sample images, it was found that the majority of particles were captured by the sensor. However, clustered particles manifested as much larger particles and so were not included in detection rate for that grade. Further signal processing would be required to eliminate this problem. Particles at this grade had much less clarity. This meant that a large number of greyscale levels existed within each object after processing. When Otsu's method is then applied some grey levels were considered as black or white incorrectly. This resulted in inaccurate object representation of the particle size, preventing their inclusion in the detection rate.

Altering the detection parameters may result in improved detection limits. In the current program, objects less than 5 pixels in size were removed to improve the clarity of larger objects. By lowering the detection limits to 1 pixel, a significant number of sub-50 μm may be captured at the expense of reducing the overall accuracy and particle clarity for larger objects.



Figure 8.12. Image with no particles present with application of Otsu's finding difference in greyscale and applies boundary conditions.

Otsu's method relies on weighting the various levels of greyscale contained within an image and deciding upon the single boundary value (Figure 8.12). Images with no

particles could suffer from miscalculations when variations in background light level existed. The effect could be mitigated by specifying that a certain greyscale value must be detected within the image before applying Otsu's method. Particles generally contained pixels with greyscale values of 80 and above which may be a suitable minimum level. However, as the lubricant colour degrades, this boundary would need to be shifted or be removed to ensure the object detection routine is applied.

Compared to optical particle counters, the smallest detectable particle was 2 orders of magnitude greater. This would preclude early wear trending offered by current systems. However, the detectable particle size range is still relevant for failure diagnosis. 150-400 μm particles give strong indications of the type and source of wear when morphology is known, and this size range corresponds to that used by several commercial metallic particle counters. Therefore there is potential for its inclusion in a multi-sensory lubricant condition monitoring system that also included an industrial optical particle sensor. The accurate detection of optical sensors could be used to verify data obtained from an improved APS sensor.

8.1.6 Particle Morphology Detection

The main advantage of using APS was the ability to discern particle morphology through image processing. The sensor was able to determine shape based on the images that were obtained.

200 mg of wear particles that consisted of a number of shapes and sizes were introduced into the rig. In Figure 8.13 the particle size classification for the wear regime is shown. In total, 4677 objects were detected, with the most common classification being square (over 3000). Square particle detection was dominant classification, in particular within the 100-150 μm region (over 1100). The other categories had approximately the same totals: ellipsoidal shape accounted for 622 particles, rectangular for 564 and circular for 413. These shape classifications were also mainly found in the sub 300 μm ranges.

Total Particles Detected for Each Shape Category

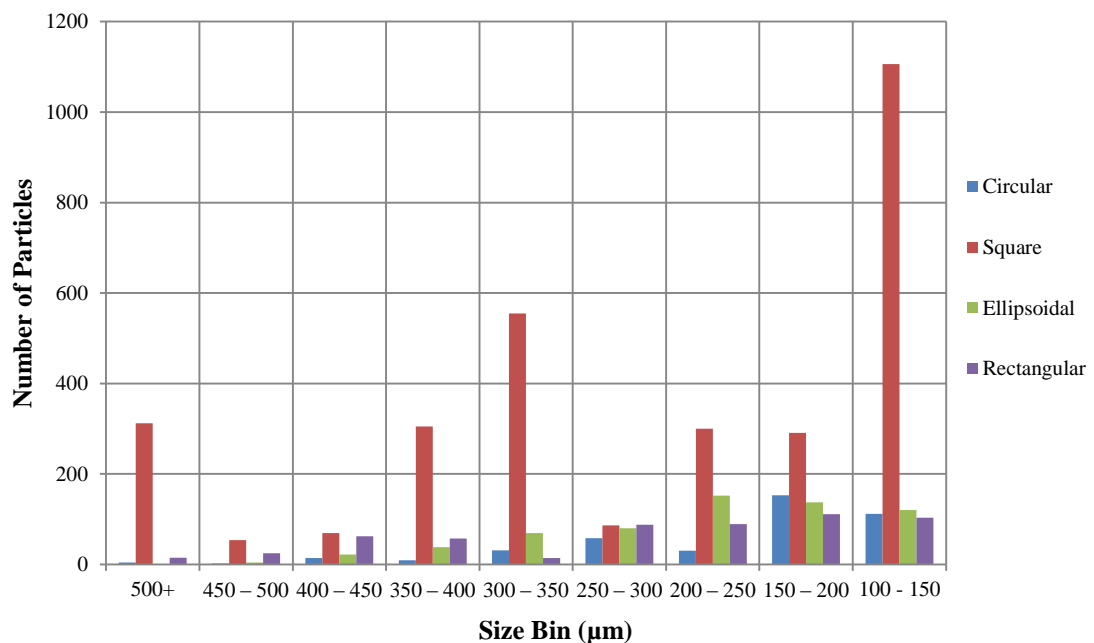


Figure 8.13. Total particles detected for different size ranges for mixed particle samples.

Square particles were expected to dominate classification of small particles (sub 150 μm) as this was approaching the detection limits of the sensor. It was observed during

the minimum size tests that circular particles often manifested as square during processing as the number of pixels representing each particles was limited. This meant that morphology was not adequately represented in small particles.

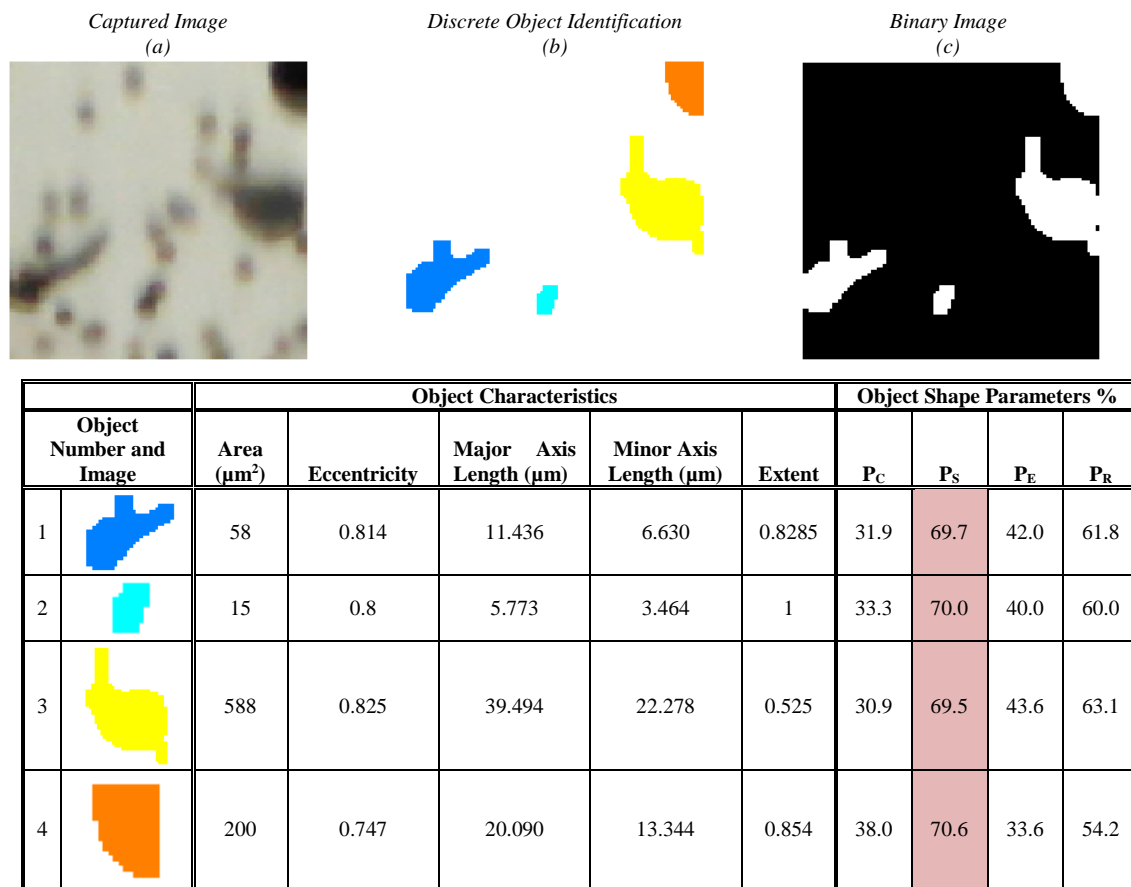


Figure 8.14. Summary of morphology detection for frame #32 during of Test 1.

Determining the effectiveness of the shape analysis subroutine involved sampling a large number of individual frames and comparing the shape classifications to the actual objects to determine if they were appropriate. In Figure 8.14 a sample image from the first 50 mg test run is shown. The following observations can be made of the captured image (a):

- A large number of particles are present in the image.
- The particles vary in shape and overall size.
- A significant number of particles are in close proximity to each other.
- 3 large particles are quite distinct in terms of size and colour.

When the image is converted using the MATLAB program, 4 discrete objects remain. Several discrete particles have been also classed as part of the same object.

During morphological testing, the conversion was not assessed and so it was assumed that the discrete object identification image (b) was an accurate representation. The objects were reasonably complex in shape, with different features. The 5 object characteristics that were used were logged. The shape parameters P_C , P_S , P_E , and P_R , defined in Eq. 7.15, 7.16, 7.17 and 7.18 were then applied to the discrete objects within each image to identify which shape classification was most appropriate.

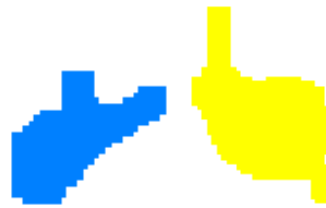


Figure 8.15. Objects 1 and 3 with non-standard morphological features.

The shape parameter the highest percentage correspondence for all 4 objects in Frame 32 for Test 1 was square (P_S). Objects 2 and 4 fit this description reasonably well although rectangular is also appropriate (which is also the second best fitting parameter). However, 1 and 3 would not normally be classed as square due to the unusual features that make their classification difficult (see Figure 8.15). Ellipsoidal may be an improved classification to account for the overall roundness of the particle and the minor axis/major axis ratio. Adding other object characteristics such as solidity may allow different shape parameters to be determined that are more representative. Improving the existing object shape parameter equations may also improve shape analysis.

Overall the shape analysis routine did perform adequately in Frame 32 as circular (P_C) was determined to be the least appropriate shape parameter for object 1-3. In object 4, ellipsoidal (P_E) was determined to be the least appropriate, followed closely by circular.

In other frames, the shape parameters were able to distinguish particles with more uniform shapes. In Figure 8.16 the summary of morphological analysis on Frame 108 of Test 2 is shown.

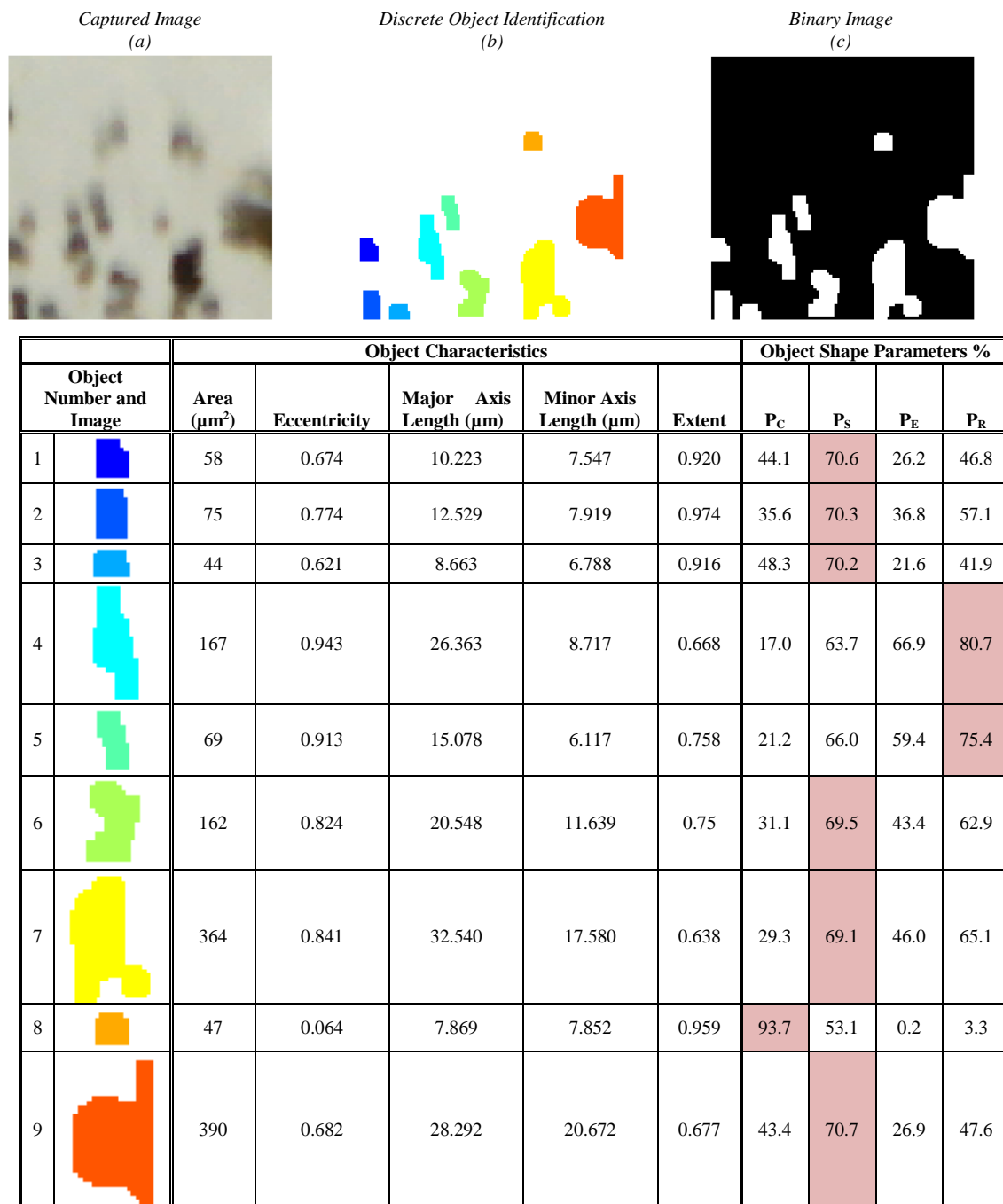


Figure 8.16. Summary of morphology detection for frame #108 during of Test 2.

Whilst square classification dominated as the most appropriate shape parameter, objects 4-5 were classed as rectangular which was confirmed visually.

Circular (P_C) was determined to be most appropriate classification for object 8 due to the small occlusions. Ellipsoidal was also found to be the least appropriate with an almost 0 classification.

The classification process requires improvements in multiple areas to ensure accurate identification. In size ranges less than 150 μm , greater distinction between circular and square particles is required to prevent false classification. The cause of this error is a combination of clarity loss and basic shape parameters based on a small number of objects characteristics. This error in identification may account for the particularly large number of particles classed as square for range 100-150 μm .

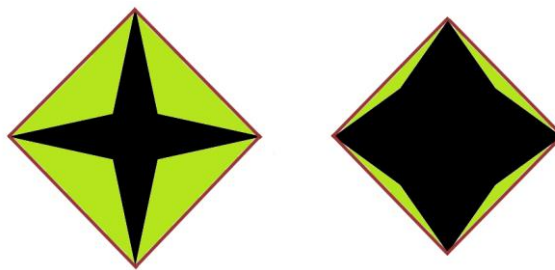


Figure 8.17. Left - Object with low solidity. Right - Object with high solidity. Green indicates convex area. Outer red line indicates bounding box.

Improvements may be made by recording a larger number of object characteristics. Solidity is based on the total area and convex area, defined as:

$$S_{object} = \frac{A_{object}}{A_{convex}}, \quad \text{Eq. 9.2}$$

where S_{object} is the solidity of the object, A_{object} is the area of the object and A_{convex} is the convex area of the object. The convex area is defined as the number of pixels that are not classed as part of the object (i.e. lubricant) but fall within the bounding box (the smallest possible rectangle which encompasses the entire object). Particles with low solidity have a large amount of convex area as shown in Figure 8.17.

The intention of analysing particle morphology was to determine the type of damage and wear affecting gearbox components. The wear regime introduced to test shape classification capabilities of the sensor system was for test purposes only and was not intended to represent a particular fault type of failure as real samples with known faults

were not available. However, if a large number of 150 μm particles are misclassified as square (but were actually circular), analysis of the wear regime may incorrectly indicate cutting bearing wear. The high number of small circular particles could indicate bearing wear whilst the large number of small ellipsoidal and rectangular particles may indicate cutting upon the bearing surface. The larger number of particles classed as square for particle size groups $>250 \mu\text{m}$ indicates that an advanced gear tooth fault has developed which is associated with large angular particles.

8.1.7 Flow Rate Limits

Each flow rate had 4 wear regimes introduced which were averaged and plotted against frame number, shown in Figure 8.18. The average number of particles captured for flow rate 12 ml s^{-1} was 11 whilst the average for 24 ml s^{-1} was 7, an approximate 36% detection reduction for a 50% increase in flow rate. The capture frame rate for 24 ml s^{-1} was 4FPS, double the frame rate used for 12 ml s^{-1} . The altered frame rate was used to compensate for particles travelling faster across the AOI. In both experiments the average particle number per frame diminishes with time.

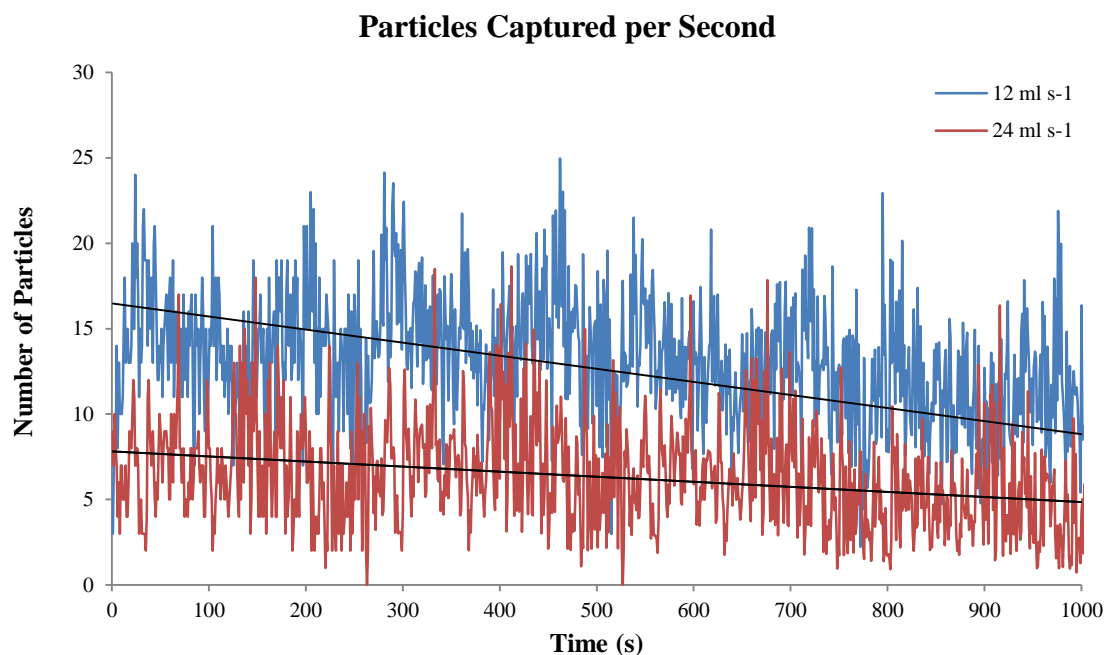


Figure 8.18. Average number of particles captured for flow rates of 12 and 24ml s⁻¹.

The lower detection rates found at 24 ml s^{-1} were expected to become severe at higher flow rates. Industrial wind turbine gearbox lubricants are pumped at 200 ml s^{-1} or greater to ensure adequate cooling of gears and bearing. The large difference between this and the test flow rates indicate that the sensor in its current configuration would be unable to track particles moving at these speeds. The diminishing detection rate can be investigated further by running the experiments for a longer period of time. The system currently operates inline but may be modified so that lubricant is sampled online instead. To maintain inline analysis, APS capable of rendering images at a faster shuttering rate may be used [147,148]. This aspect of the sensor was considered a limitation of the chosen hardware, rather than a limitation of the technique as fast image capture technology is widely used. The current APS sensor is low cost and was used to demonstrate the principle of this type of analysis.

8.1.8 Lower Light Level

Gearbox lubricant changes colour over time due to chemical changes to additives and the base hydrocarbons. In addition the increased presence of wear material reduces the amount of visible light can be transmitted. If the sensor is unable to discern the difference in greyscale or RGB value between the lubricant and particles, the detection rate is reduced. When the sensor was run with a reduced light level, particles can be still be discerned to a relatively high degree as shown in the blue trace in Figure 8.19. A drop in the average number of particles per frame can be seen towards the end of the test run, indicating a normal reduction of particles within the regime.

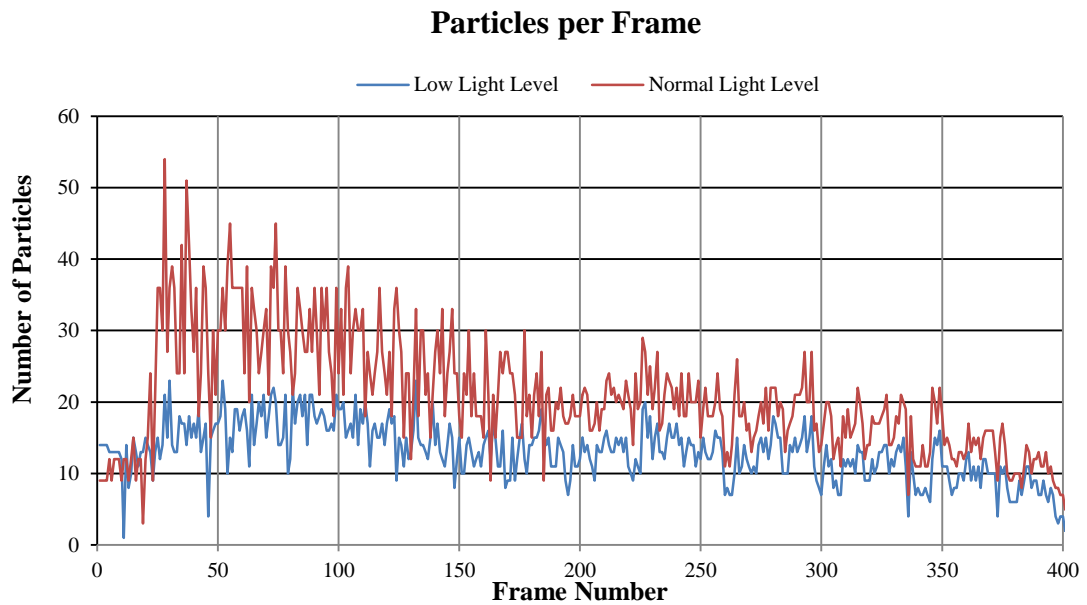


Figure 8.19. Comparison of linear trend lines for low and normal light level conditions.

To assess the impact of low light conditions, a comparison was made with normal light conditions with same particle sample size and flow rate with the results shown in Figure 8.19. Examples of images from each light level are shown in Figure 8.20.

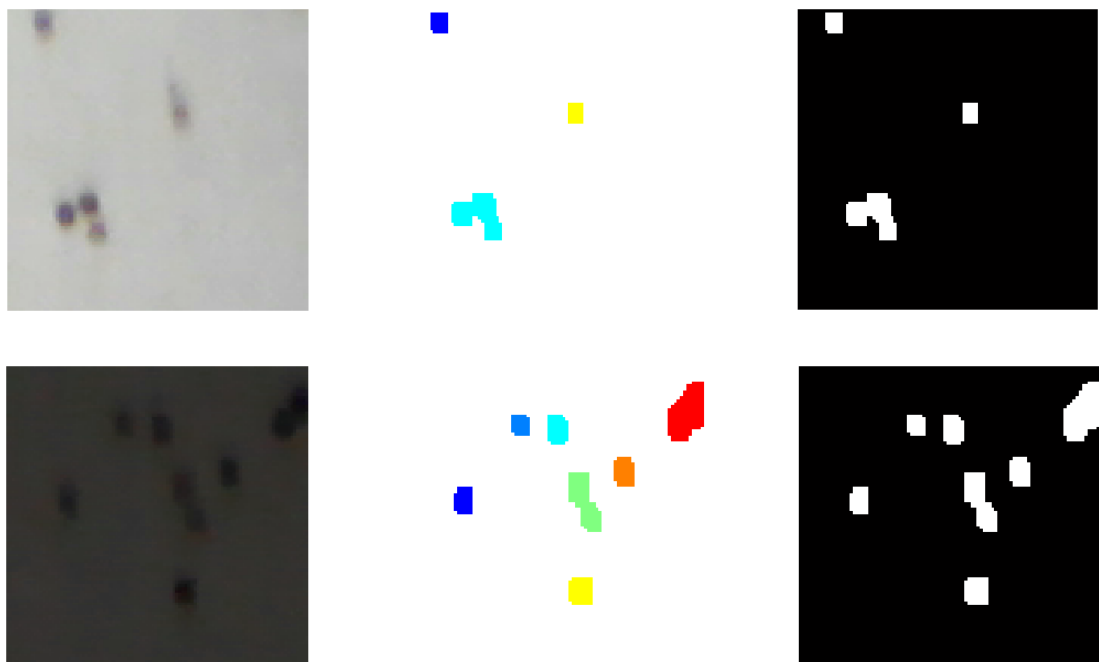


Figure 8.20. Above - normal light level conditions. Below - reduced light level conditions.

The gradients of each trend line are similar, indicating that the particle regimes used are similar. The overall detection rate is significantly higher with an approximate percentage increase of 41.34% weighted over the entire sample range for normal light level. An exception to this trend is found between the first 25 frames where similar detection rates can be noticed which may be attributed to the higher particle concentration during the period.

Otsu's method separated the lubricant and particles by finding the optimum weighted greyscale level between them. An observed additional benefit of this method was that under low light conditions, particles may still be identified as long as a difference exists between the particles and the lubricant (see Figure 8.21). A significant difference in average greyscale between lubricant and particles does increase the accuracy of the method by allowing a more defined outline to enter the object recognition subroutine. However, the system has demonstrated that it is able to function under degraded lubricant conditions. Degradation may continue to a point where particles are indistinguishable. To counter this, the light source may be modified so it can have a variable intensity that is suited for the current lubricant condition.

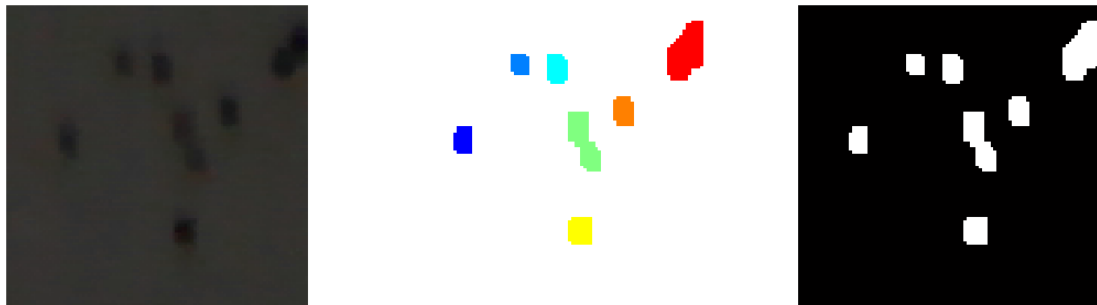


Figure 8.21. Despite low light levels, small 125 μ m particles could be distinguished from lubricant.

8.2 Lubricant Quality Sensor Experimental Results

The sensor was designed to identify changes in the lubricant chemistry by tracking the absorption of specific IR wavebands. The prototype used a laser diode and was tested using three medium: air, XMP320 lubricant and water. An example of the returned voltage signals can be seen in Figure 8.3.

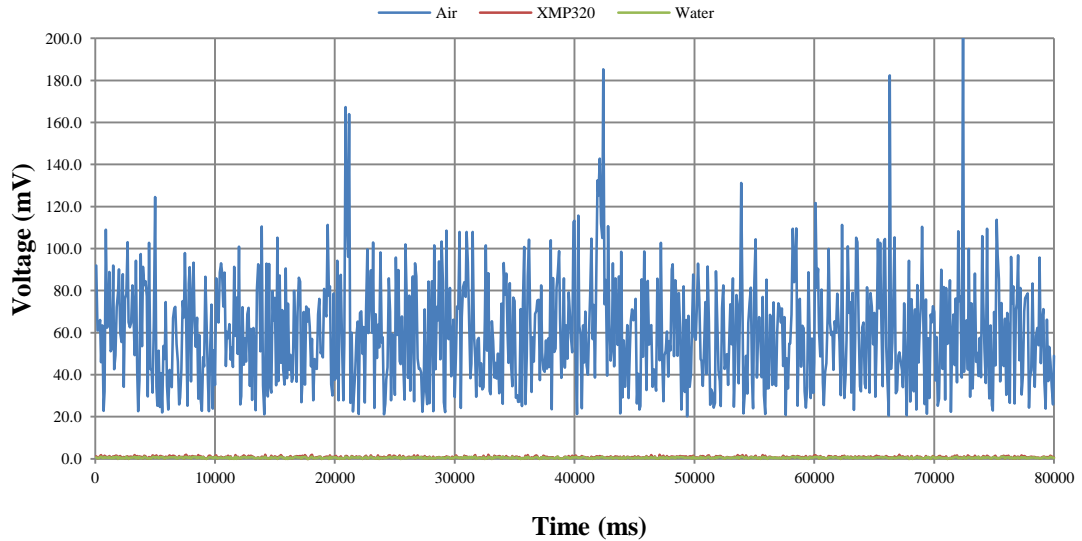


Figure 8.22. Returned voltages signals from microcontroller for all 3 fluid types.

With only air within the sensor, an average voltage signal of 60 mV could be detected by the photodiode when the laser diode was switched on. The voltage value was determined by averaging the sum of all the signals over the 80 s time period. The signal varied significantly over the measurement period, indicating that the transmittance of laser light was not uniform over time. Various factors may lead to this fluctuation over time. The laser diode and photodiode used in the sensor are susceptible to small temperature changes, despite the use of separating BK7 glass. For the laser diode, temperature variations can lead to small changes in the intensity of the generated beam. The photodiode's reactive surface produces current when photons strike its surface. Small increases in temperature can increase the local resistance of the surface, impeding the flow of current. The combined effects of these may lead to errors.

The issue may also be related to the supply of current to the laser diode. The driver circuit was intended to supply between 200-500 mA. The potentiometer incorporated

into the circuit to allow tuning was manually adjusted using the outer dial which may not have been appropriately robust. The issue may be solved by redesigning the driver circuit with an exact resistance value so that source of error may be removed.

The most significant issue arose when testing the target liquid: XMP320 lubricant. When the pipe was filled with XMP320, the voltage signal dropped to an approximate average of 1 mV as shown in Figure 8.22. This indicated that no light was reaching the photodetector surface as the value was too low to suggest it was related to incident light. This may be related to the absorbance of XMP320 at the wavenumber of 12376 cm^{-1} (808 nm). To verify this result was positive as it indicated that the light was no longer reaching the photodetector. This was confirmed by removing the XMP320 and cleaning the sensor with acetone that removed all liquid and then evaporated. The sensor was then filled with water as at 12376 cm^{-1} (808 nm), the water should transmit over 97% of all transmitted light. However, as shown in Figure 8.22, water produced an average voltage signal of 1mV.

Initially beam divergence was considered as a source of error. When light changes from one medium to another with different material properties, the beam of laser light may diverge or converge. In the sensor assembly, the laser passes from air to BK7 glass, to the test fluid, back to BK7 glass and finally onto the photodetector (which is flush with the glass). By applying Snell's law, the beam of laser light should diverge more in air than in water due to the latter's higher refractive index. This should result in a more concentrated beam of laser light on the photodiode when water is in the sensors, rather than air.

This lead to the conclusion that the laser beam became misaligned when liquid was introduced into the sensor. The may be attributed to the sensor assembly having insufficient robustness when additional pressure was introduced into the glass surface within the pipe. An alternative conclusion is that the laser diode was misaligned even during the tests with air, but the effect of reflectance of the copper piping mitigated the effect in the photodiode. When liquids were introduced, a higher degree of light scattering may have occurred within the sensor, causing severe signal degradation.

The underlying principle of using one of the specific IR wavebands to monitor changes found between new and 18 month used XMP320 lubricant is still valid. In a similar system demonstrated by Parker et al, a much narrower channel of 2 mm (compared with 19 mm in sensor layout) was able to detect changes in XMP320 lubricant due to oxidation. The sensor differed in terms of the light source used and its intention to be used as part of an online period sampling system, rather than an inline one. The main issue with the system described by Parker is that increased the channel width above 2 mm produced anomalous results.

By combining the more robust sensor assembly described within the work of Parker with a laser diode that matches a key waveband, the sensor concept may be developed further with more positive results. The work should focus on increasing the maximum sensor channel diameter so that the system could function inline to provide accurate information on the state of the lubricant in terms of its chemical composition. This may lead to improved condition monitoring of the wind turbine gearbox based on a novel inline data source.

Chapter 9 – Conclusions and Future Work

A review of condition monitoring systems applicable for determining the state of wind turbine gearbox lubricants was conducted. The results of the review indicated that there was potential to develop small low cost sensors that would target novel lubricant characteristics such as wear particle morphology and infrared absorption of specific wavebands related to changes in chemical composition.

The principle of using active pixel sensors as a wear particle sensor that can capture images of wear particles for further analysis was successfully demonstrated. Particle morphology is an important parameter to monitor in wind turbine gearboxes as the size and shape can indicate the type of wear that is occurring and the source. To achieve detection standards equivalent to current commercially available sensors the system must be able to detect particles in the order of 5 μm consistently. The system was able to detect particles with a major dimension in the order of 125 μm consistently. However, considering the low resolution of the webcam when compared with other APS sensors customised for fast shuttering the system performance exceeded expectations.

A number of improvements to the hardware would significantly improve the quality of images and allow smaller particles to be captured. The system uses a relatively simple APS sensor with a low number of megapixels. Using an APS sensor with smaller pixel size would increase the clarity of images, especially for small particles. The architecture of the webcam pixels is also not optimised for video capture; rather it is designed to capture images at a relatively high frequency for video calls. Digital video cameras with APS sensors may allow faster snapshot processing, reducing the effect of flow and ultimately allow a higher flow rate whilst maintaining a given detection rate.

Another design consideration would be the use of multiple APS sensors focussed at different depths and levels. The sensor could not change focus automatically during operation as it required the lens to be moved manually. Larger particles had more clarity than those under 150 μm which affected the ability of the sensor to determine the

circular shape of the particles. In most case, small particles were rendered as square under the current object transformation subroutine.

Particle tracking would be useful feature to introduce where unique particles are tagged and tracked as they traverse across the FOV. This would allow changes to be identified (in shape or size) based on the expected velocity of the particle. Problems will occur with particles in close proximity which may cause issues with tracking but the expected benefits are high.

The sensor used built in MATLAB functions for image processing such as structuring elements. Further work should include research into creating customised structuring elements that would produce more representative images during the binary conversion.

If sufficient improvements can be made to raise the detection standards to conform to ISO 21501-3:2007, the sensor could form part of a multi-sensory condition monitoring system that bases its signals on a new data source. Reporting wear particle morphology would give wind turbine operators a larger data pool from which they can base the need for maintenance or give advanced warning of fault development.

Fourier-transform infra-red (FTIR) analysis of wind turbine lubricants under different operational conditions allowed analysis of changes to the spectra. This allowed identification of particular IR wavebands that changed during the operation of the gearbox. These wavebands formed the basis of development a low cost targeted IR sensor that would monitor the lubricant inline. Future development of a similar sensor would assess new laser diodes with relevant wavenumber that could track these changes.

References

- [1] European Commission (2009), "Directive of the European Parliament and the Council - on the promotion of the use of energy from renewable sources", European Union National Archives [Online]. Available: <http://eur-lex.europa.eu/LexUriServ/LexUriServ.do?uri=Oj:L:2009:140:0016:0062:en:PDF> "
- [2] S. Faulstich, *et al*, "Wind Turbine Downtime and Its Importance for Offshore Deployment," in *Wind Energy*, vol. 14, pp. 329, 2012.
- [3] K. Scott, D. Infield, "Effects of Extreme and Transient Loads on Wind Turbine Drive Trains" in *30th ASME Wind Energy Symposium*, Nashville, USA, 2012.
- [4] B. Al-Najjar, I. Alsyuf, "Enhancing a company's profitability and competitiveness using integrated vibration-based maintenance: a case study," COMADEM, San Sebastian, Spain, Jun 9-11, 2009.
- [5] C. Crabtree, "Survey of commercially available condition monitoring systems for wind turbines". Technical Report of the University of Durham, May 2010. [Online]. Available: <http://www.supergen-wind.org.uk/docs/Survey%20of%20commercially%20available%20CMS%20for%20WT.pdf>
- [6] Allianz Global Corporate & Specialty (2012), "Extension of the scope of Condition Monitoring Systems formulti-MW and offshore wind turbines", Allianz Center for Technology. [Online]. Available:http://www.agcs.allianz.com/assets/Global%20offices%20assets/Germany/Risk%20Consulting/Allianz%20Condition%20Monitoring%20System_final.pdf
- [7] European Commission (2006), "Renewable Energy Road Map - Renewable energies in the 21st century: building a more sustainable future", European Union Library Archives [Online]. Available: <http://eur-lex.europa.eu/LexUriServ/LexUriServ.do?uri=COM:2006:0848:FIN:EN:PDF>
- [8] European Commission (2009), "Directive of the European Parliament and of the Council - on the promotion of the use of energy from renewable sources", European Union National Archives [Online]. Available: <http://eur-lex.europa.eu/LexUriServ/LexUriServ.do?uri=Oj:L:2009:140:0016:0062:en:PDF> "
- [9] Department of Trade and Industry (2007), "Meeting the Energy Challenge - A White Paper on Energy". UK National Archives, [Online]. Available: http://webarchive.nationalarchives.gov.uk/20121205174605/http://www.dec.gov.uk/assets/decc/publications/white_paper_07/file39387.pdf
- [10] Civil Service Capability Reviews (2011), "Department of Energy and Climate Change: Baseline Assessment", UK Civil Service Archives

- [Online]. Available: <http://www.civilservice.gov.uk/wp-content/uploads/2011/09/DECC-phase2-Dec2009.pdf>
- [11] Department of Energy and Climate Change (2011), "Review of the generation costs and deployment potential of renewable electricity technologies in the UK". UK Energy Statistics, [Online]. Available: https://www.gov.uk/government/uploads/system/uploads/attachment_data/file/42843/3237-cons-ro-banding-arup-report.pdf
- [12] Office of Gas and Electricity Markets (2012), "Energy Capacity Assessment 2012", Ofgem [Online]. Available: <https://www.ofgem.gov.uk/ofgem-publications/40203/electricity-capacity-assessment-2012.pdf>
- [13] Department of Energy and Climate Change (2013), "Fuel used in electricity generation and electricity supplied", UK Energy Statistics, [Online]. Available: <https://www.gov.uk/government/publications/electricity-section-5-energy-trends>
- [14] European Offshore Statistics (2012), "The European offshore wind energy industry key trends and statistics 2013", European Wind Energy Association, [Online]. Available: http://www.offshorewindenergy.org/reports/report_026.pdf
- [15] G. Corbetta, *et al*, "The European offshore wind industry - key trends and statistics 2013", EWEA. [Online]. Available: http://www.ewea.org/fileadmin/files/library/publications/statistics/European_offshore_statistics_2013.pdf
- [16] T. Burton, N. Jenkins, *et al.*, "The Wind Resource", in *Wind Energy Handbook*, 2nd ed., Chichester, UK: John Wiley & Sons Ltd, 2011, ch. 2, sec. 1, pp. 9-10.
- [17] J. Kaldellis, D. Zafirakis, "The wind energy (r)evolution: A short review of a long history," in *Renew Energ*, vol. 36, no. 7, pp. 1887-1901, 2011.
- [18] T. Burton, N. Jenkins, *et al*, "Introduction", in *Wind Energy Handbook*, 2nd ed., Chichester, UK: John Wiley & Sons Ltd, 2011, ch. 1, sec. 1, pp. 2.
- [19] Siemens 3MW 3 bladed HAWT wind turbine, Siemens Wind Power [Online]. Available: <http://www.energy.siemens.com/hq/en/renewable-energy/wind-power/>
- [20] T. Burton, N. Jenkins, *et al.*, "Aerodynamics of horizontal axis wind turbines", in *Wind Energy Handbook*, 2nd ed., Chichester, UK: John Wiley & Sons Ltd, 2011, ch. 3, sec. 8, pp. 75.
- [21] Siemens Wind Power (2013), "SWT-4.0-130 wind turbine specifications", Siemens [Online]. Available: <http://www.energy.siemens.com/hq/en/renewable-energy/wind-power/>
- [22] Drivetain Innovation Awards, "A typical Vestas 2MW layout, with main shaft supported in two main bearings", Wind Power Monthly [Online]. Available: <http://www.windpowermonthly.com/article/1225352/turbines-year---drivetrains>

- [23] T. Burton, N. Jenkins, *et al.*, “Component Design,” in *Wind Energy Handbook*, 2nd ed., Chichester, UK: John Wiley & Sons Ltd, 2011, ch. 7, sec. 4, pp. 425.
- [24] “Illustration of an epicyclic gear effecting a gear reduction/increase”, by Wapcaplet, under Creative Commons Licence: CC BY-SA 3.0. [Online]. Available at:
http://commons.wikimedia.org/wiki/File:Epicyclic_gear_ratios.png
- [25] David Brown Gear Systems, “Gear Foundation Course Notes”, from *David Brown Gear Academy Handbook*, 2009, Version 2. Retrieved from <http://www.davidbrown.com/gear-academy>
- [26] SKF Bearing Products, “Hybrid bearings”, SKF UK Ltd [Online]. Available: <http://www.skf.com/uk/products/bearings-units-housings/engineered-products/hybrid-bearings/index.html>
- [27] NREL, “Wind Turbine Gearbox Wear and Failure Modes and Detection Methods”, *Wind Turbine Condition Monitoring Workshop Proceedings*, Sept, 2011, [Online]. Available:
http://www.nrel.gov/wind/pdfs/day1_sessioniv_02_9-19-2011.pdf
- [28] T. Burton, N. Jenkins, *et al.*, “Component Design,” in *Wind Energy Handbook*, 2nd ed., Chichester, UK: John Wiley & Sons Ltd, 2011, ch. 7, sec. 4, pp. 425-429.
- [29] K. Scott, “Effect of Transient Loading on Wind Turbines Drivetrains”, Ph.D thesis, University of Strathclyde, 2014.
- [30] W. Musial, *et al.*, “Improving Wind Turbine Gearbox Reliability,” *European Wind Energy Conference*, Conference Paper NREL/CP-500-41548, Milan, Italy, 2007.
- [31] P. Tavner, *et al.*, "Reliability of different wind turbine concepts with relevance to offshore application," in *European Wind Energy Conference & Exhibition*, 2008, pp. 166-170.
- [32] Whittle, M., *et al.*, "A Parametric Study of the Effect of Generator Misalignment on Bearing Fatigue Life in Wind Turbines," *European Wind Energy Association (EWEA) Conference*, Brussels, 2011.
- [33] B. McNiff, “The Gearbox Reliability”, in *Proceedings 2nd Sandia National Laboratories Wind Turbine Reliability Workshop*, 2007.
- [34] National Grid, Round 3 Offshore Wind Farm Connection Study, [Online] Available: http://www.thecrownstate.co.uk/round3_connection_study.pdf.
- [35] Davis, J. R., “Gear Failure Modes and Analysis” in *Gear Materials, Properties and Manufacture*, OH: ASM International ch. 3, sec. 1, pp 257, 2005
- [36] Davis, J. R., “Gear Tribology and Lubrication” in *Gear Materials, Properties and Manufacture*, OH: ASM International, ch. 2, sec. 1, pp 21, 2005.
- [37] *Rolling bearings – Damage and failures – Terms, characteristics and causes*, BS ISO 15243:2004.

- [38] Figure 3.1, *g_01c.jpg* (2013), *Broken gear tooth*. [Photograph; Side view of a metallic gear with helical teeth, one of which has cracked at base]. [Online] Accessed: http://www.tribology.co.uk/image/g_01c.jpg
- [39] A. Wöhler, “Über die Festigkeitsversuche mit Eisen und Stahl”, in *Zeitschrift für Bauwesen*, vol. 20, pp. 73-106, 1870.
- [40] M. Miner, "Cumulative Damage in Fatigue," in *Journal of Applied Mechanics*, pp. 159-164, 1945.
- [41] A. Heege, et al. “Fatigue load computation of wind turbine gearboxes by coupled finite element, multi-body system and aerodynamic analysis”, in *Wind Energy*, vol. 10(5), pp. 395-413, 2007.
- [42] W. Dong W, “Time domain-based gear contact fatigue analysis of a wind turbine drivetrain under dynamic conditions”, in *International Journal of Fatigue*, vol. 48, pp.133–146, 2012.
- [43] S. McArthur, E. Davidson, “Multi-agent systems for diagnostic and condition monitoring applications”, in *IEEE Power Engineering Society General Meeting*, vol.1, pp.50-54, 6-10 June, 2004.
- [44] S. Ebersbach, *et al*, “The investigation of the condition and faults of a spur gearbox using vibration and wear debris analysis techniques”, in *Wear*, vol 260(1-2), pp.16-24, Jan, 2006.
- [45] H. Hertz, “Über die berührung fester elastischer Körper” in *Miscellaneous Papers*. Jones and Schott, Editors, *J. reine und angewandte Mathematik* 92, Macmillan, London, pp. 156, 1896.
- [46] J. Davis, “Gear Tribology and Lubrication” in *Gear Materials, Properties, and Manufacture*, OH: ASM International, 2005, ch. 2, sec. 1, pp 22-24.
- [47] Figure 3.3, *Backup_200409_contamctrl-fig6.jpg* (2004), *Destructive Pitch-Line Pitting of Gear Teeth from Subsurface Defect Origin*. [Photograph; Top down view of helical gear profile with macro pitting evident on side faces of teeth]. [Online] Accessed: http://media.noria.com/sites/archive_images/Backup_200409_contamctrl-fig6.jpg
- [48] G. Totten, *et al*, “Gear Lubricants” in *Fuels and Lubricants Handbook: Technology, Properties, Performance, and Testing*, Volume 1, Glen Burnie, MD: ASTM International, 2003, ch. 13, pp. 434.
- [49] G. Maitra, “Spur Gears” in *Handbook of Gear Design*, India: Tata McGraw-Hill, New Delhi, 1994, ch. 2, sec. 23, pp 2.93.
- [50] A. Tedric, *et al* “Failure and Damage Modes in Rolling Bearings” in *Advanced Concepts of Bearing Technology; Rolling Bearing Analysis*, 5th Edition, FL: CRC Press, Boca Raton, 2007, ch. 10, sec. 8, pp 295.
- [51] S. Ghosh, “Wear Characterization by Fractal Mathematics for Quality Improvement of Machine,” in *J. Qual. Maint. Eng.*, vol. 11(4), pp. 318–332, 2005.

- [52] B. Rao, "Condition Monitoring of Power Plants", in Handbook of Condition Monitoring, 1st ed, UK: Elsevier Advanced Technology, 1996, pp 303.
- [53] A. Hamilton A, *et al*, "Development of a Novel Wear Detection System for Wind Turbine Gearboxes" in IEEE Sensors Journal, vol. 14(2), pp. 465–473, 2014.
- [54] M. Hourani, *et al*, "Alkylated Naphthalenes as High-Performance Synthetic Lubricating Fluids", Tribology Transactions, 50, pp 82-87, 2007.
- [55] E. Niedzielski, "Neopentyl Polyol Ester Lubricants-Bulk Property Optimization", in Industrial & Engineering Chemistry Product Research and Development, vol. 15(1), pp. 54-58, 1976.
- [56] M. Kaurav, "Lubrication and Lubricants" in Engineering Chemistry with Laboratory Experiments, India: PHI Learning Private Limited, New Delhi, 2011, ch. 7, sec. 7, pp. 199.
- [57] R. Rudnick, "Automotive Gear Lubricants" in Synthetics, Mineral Oils, and Bio-Based Lubricants: Chemistry and Technology, FL: CRC Press, 2013, ch. 28, sec. 4, pp. 469.
- [58] R. Gohar, H. Rahnejat, "Lubricant Properties" in Fundamentals of Tribology, UK: Imperial College Press, London, 2008, ch. 5, sec. 2, pp. 78-81.
- [59] ASTM D2422 – 97, 2007, Standard Classification of Industrial Fluid Lubricants by Viscosity System, ASTM International.
- [60] C. Seeton, "Viscosity-Temperature Correlation for Liquids", in Tribology Letters, vol. 22(1), pp. 67-78, 2006.
- [61] S. Mia, *et al*, "High-pressure behavior and tribological properties of wind turbine gear oil", in Journal of Mechanical Science and Technology, vol. 24, pp. 111-114, 2010.
- [62] G. Totten, *et al* "Gearbox Lubrication" in Handbook of Lubrication and Tribology: Theory and Design, Second Edition, Volume 2, FL: CRC Press, 2012, ch.50, sec. 6, pp. 13.
- [63] M. Neale, "Mineral Oils" in Lubrication and Reliability Handbook, UK: Arrowsmith Ltd, Bristol, 2001, ch. A2, pp. A2.6.
- [64] W. Al-Akhdar, *et al*, "Lubricating oil compositions comprising phenolic antioxidant", US Patent CA2575502, 2004.
- [65] H. McCormick, *et al*, "Poly-alkylstyrene viscosity index improver", US Patent US3318813, 2004.
- [66] L. Carbognana, "Preparative isolation and characteristics of zinc dialkyldithiophosphates from commercial antiwear additives", in Journal of Separation Science, vol. 26(17), pp. 1575-1581, 2003.
- [67] S. Wen, P. Huang, "Additives and Properties" in Principles of Tribology, N.J.: John Wiley & Sons Inc. 2012, ch. 11, pp. 455-484.

- [68] G. Totten, *et al*, “Gear Lubricants” in Fuels and Lubricants Handbook: Technology, Properties, Performance and Testing, Volume 1, Glen Burnie, MD: ASTM International, 2003, ch. 16, pp.216.
- [69] E. Booser, “Lubricants and Their Application” in Handbook of Lubrication: Theory and Practice of Tribology, vol.2, N,W: CRC Press LLC, 1983, ch.2 , sec.2 , pp. 262.
- [70] D. Ebbing, D. Gammon, “Organic Chemistry,” in General Chemistry, 9th ed., MA: Houghton Mifflin Company, 2009, ch. 23, sec. 6, pp. 991.
- [71] R. Mortier, S. Orszulik, “Industrial lubricants” in Chemistry and Technology of Lubricants, 2nd ed, UK: Blackie Academic and Professional Ltd, 1997, ch. 8, sec. 5, pp. 210.
- [72] Z. Pawlak, “Analytical Techniques in Lubricating Practices” in Tribochemistry of Lubricating Oils, Amsterdam, Netherlands: Elsevier Ltd, 2003, ch. 6, sec. 4, pp. 225-234.
- [73] G. Totten, *et al*, “Additives and Additive Chemistry” in Fuels and Lubricants Handbook: Technology, Properties, Performance and Testing, Volume 1, Glen Burnie, MD: ASTM International, 2003, ch.9, pp. 203.
- [74] D. McMillan, G. Ault, “Quantification of Condition Monitoring Benefit for Offshore Wind Turbines”, in Wind Engineering, vol. 31(4), pp. 267-285, 2007.
- [75] P. Tavner, “Monitoring Wind Turbines,” in Offshore Wind Turbines: Reliability, Availability and Maintenance, Stevenage, UK: IET, 2012, ch. 7, sec. 6, pp. 137.
- [76] D. Lekou, *et al*, “Emerging Techniques for Health Monitoring of Wind Turbine Gearboxes and Bearings”, Proceedings EWEC, Scientific Track – Operation and Maintenance, Marseille, France, 2009.
- [77] S. Sheng, “Investigation of Oil Conditioning, Real-time Monitoring and Oil Sample Analysis for Wind Turbine Gearboxes”, in AWEA Project Performance and Reliability Workshop, San Diego, CA, Jan 12-13, 2011, [Online]. Available: <http://www.nrel.gov/docs/fy11osti/50301.pdf>
- [78] P. Tavner, “Monitoring Wind Turbines,” in Offshore Wind Turbines: Reliability, Availability and Maintenance, Stevenage, UK: IET, 2012, ch. 7, sec. 2, pp. 115.
- [79] S. Sheng, *et al* “Use of SCADA Data for Failure Detection in Wind Turbines”, Energy Sustainability Conference and Fuel Cell Conference, Aug 7-11, 2011, NREL/CP-5000-51653
- [80] R. Randall, “Types and Benefits of Vibration Analysis”, in Vibration-based Condition Monitoring: industrial, aerospace and automotive applications, Chichester, UK: John Wiley & Sons Ltd, 2011, ch. 1, sec. 5, pp 8.
- [81] Y. Zhan,V. Makis, “A Robust Diagnostic Model for Gearboxes Subject to Vibration Monitoring”, Journal of Sound and Vibration, vol. 290(3-5), pp. 928-955, 2006.

- [82] L. Gelman, et al, “Adaptive Vibration Condition Monitoring Technology for Local Tooth Damage in Gearboxes”, in *Insight: Non-destructive Testing and Condition Monitoring*, vol. 47(8), pp. 461-464, 2005.
- [83] A. Davies, “Wear debris analysis methods” in *Handbook of Condition Monitoring: Techniques and Methodology*, UK: Chapman and Hall, London, 1998, ch. 15, sec.5, pp. 401.
- [84] C. Crabtree, *et al* “Survey of commercially available condition monitoring systems for wind turbines”. Technical Report of the University of Durham, May 2014. [Online]. Available: <http://www.supergen-wind.org.uk/download/Survey%20of%20commercially%20available%20CMS%20for%20WT.pdf>
- [85] Y. Iwai, *et al*, “Quantitative Estimation of Wear Amounts by Real Time Measurement of Wear Debris in Lubricating Oil”, in *Tribology International*, vol. 43(1-2), pp. 388-394, 2010.
- [86] R. Xu, “Optical Particle Counting” in *Particle Characterization: Light Scattering Methods*, Netherlands: Kluwer Academic Publishers, Dordrecht, 2001, ch. 4, pp. 189.
- [87] T. Hunt, “Classification of Debris” in *Handbook of Wear Debris Analysis and Particle Detection in Liquids*, UK: Elsevier Applied Science, Barking, 1993, ch.3, pp. 46.
- [88] G. Stachowiak, *et al* “Wear Particle Analysis” in *Experimental Methods in Tribology*, Netherlands: Elsevier, Amsterdam, 2008, ch. 10, sec. 3, pp. 269.
- [89] T. Hunt, “Methods of Detecting Particles” in *Handbook of Wear Debris Analysis and Particle Detection in Liquids*, UK: Elsevier Applied Science, Barking, 1993, ch.6, pp. 121-122.
- [90] J. Bird, “Inductance of a Coil” in *Electrical Circuit Theory and Technology*, UK: Elsevier Ltd, Kidlington, 2010, ch. 9, sec. 7, pp. 99.
- [91] Hunt, T. M., “Methods of Detecting Particles” in *Handbook of Wear Debris Analysis and Particle Detection in Liquids*, UK: Elsevier Applied Science, Barking, 1993, ch.6, pp. 151.
- [92] Hunt, T. M., “Quantifying Debris” in *Handbook of Wear Debris Analysis and Particle Detection in Liquids*, UK: Elsevier Applied Science, Barking, 1993, ch.7, pp. 123.
- [93] Y. Freng, *et al.*, “Use of SCADA and CMS for failure detection and diagnosis of a wind turbine gearbox,” 2011 European Wind Energy Association, Brussels, Belgium, Mar 14-17.
- [94] P. Tavner, “Monitoring Wind Turbines,” in *Offshore Wind Turbines: Reliability, Availability and Maintenance*, Stevenage, UK: IET, 2012, ch. 7, sec. 7, pp. 127.
- [95] M. Mauntz, J. Gegner, “A Sensor System for Online Oil Condition Monitoring of Operating Components” in *Tribology - Fundamentals and Advancements*, 2013, [Online]. Available: <http://cdn.intechopen.com/pdfs-wm/44606.pdf>

- [96] T. Hunt, "Methods of Detecting Particles" in Handbook of Wear Debris Analysis and Particle Detection in Liquids, UK: Elsevier Applied Science, Barking, 1993, ch.6, pp. 115.
- [97] A. Hamilton, "Detailed State of the Art Review for the Different Online/Inline Oil Analysis Techniques in Context of Wind Turbine Gearboxes", in Journal of Tribology, vol. 133(4), pp. 044001-044014, 2010.
- [98] T. Wu, *et al*, "A New On-Line Visual Ferrograph", in Tribology Transactions, vol. 52(5), pp 623-631, 2009.
- [99] B. Stuart, "Experimental Methods", in Infrared Spectroscopy: Fundamentals and Applications, UK: John Wiley and Sons Ltd, Chichester, 2004, ch. 2, sec.3 , pp. 16- 18.
- [100] C. Párkányi, "Analysis and Prediction of Intermolecular Interactions", in Theoretical Organic Chemistry, Netherlands: Elsevier Science B. V, Amsterdam, 1998, ch. 3, sec.3, pp. 65- 71.
- [101] I. Poljanšek, M. Krajnc, "Characterization of Phenol-Formaldehyde Prepolymer Resins by In Line FT-IR Spectroscopy", Acta Chimica Slovenica, 52, pp. 238–244, 2005.
- [102] L. Toms, "Analysis Methods" in Machinery Oil Analysis Methods, Automation and Benefits, 3rd ed., FL: STLE, Virginia Beach, 2008, ch. 7, sec.2, pp. 108.
- [103] SpectroInc. QinetiQ North America, FluidScan Q1000, accessed from <http://www.spectroinc.com/products-fluidscan.htm> on August 25th, 2010.
- [104] MONO CMM263 415V Pump, mono-pumps.com, Mono™. [online] Available at: <http://www.hss-online.co.uk/mono-cmm263-415v-pump-2972-p.asp> [Accessed: 28 Aug 2013].
- [105] Freescale Semiconductor, Data Sheet: Technical Data for MPX5700 Integrated Silicon Pressure Sensor On-Chip Signal Conditioned, Temperature Compensated and Calibrated. [Online] Available at: http://www.freescale.com/files/sensors/doc/data_sheet/MPX5700.pdf
- [106] Flownetix, Product Data Sheet for flownetix 100series flowmeter. [Online] Available at: <http://www.flownetix.co.uk/products/110v3>
- [107] RS Components, Data Sheet for RS 409-4908 (PTFE) Thermocouple Type 'K'. [Online] Available at: <http://docs-europe.electrocomponents.com/webdocs/112a/0900766b8112a28e.pdf>
- [108] National Instruments, Data Sheet for NI CompactRIO data acquisition and FPGA module. [Online] Available at: <http://www.ni.com/compactrio/>.
- [109] Mobilgear™ XMP, Mobil.com (1996) Mobilgear™ XMP. [online] Available at:http://www.mobil.com/Australia-English/Lubes/PDS/GLXXENINDMOMobilgear_XMP.aspx [Accessed: 26 Sep 2012].

- [110] P. Noble, "Self-scanned silicon image detector arrays", in IEEE Trans. Electron Devices, vol. 15(4), pp. 202-209, 1968.
- [111] J. Webster, H. Eren, "Image Sensors" in Measurement, Instrumentation and Sensors Handbook, 2nd Ed, FL: CRC Press, Boca Raton, 2004, ch. 4, sec. 1, pp. 4.
- [112] S. Mendis, *et al*, "A 128 x 128 CMOS Active Pixel Image Sensor for Highly Integrated Imaging Systems," *IEDM '93. Technical Digest.*, International, pp.583-586, Dec. 1993.
- [113] R. Coath, *et al.*, "Advanced Pixel Architectures for Scientific Image Sensors," Proc. Topical Workshop Electronics for Particle Physics, Paris, 2009, pp. 57-61.
- [114] Mathworks, List of functions available for R2015a MATLAB Image Processing Toolbox Functions. [Online] Available at: <http://www.mathworks.co.uk/help/images/functionlist.html;jsessionid=f9329d33f3a91779675b4a7f334a>
- [115] S. Canaan, R. Hornsey, "Inverted Logarithmic Active Pixel Sensor with Current Readout", 2001, IEEE Workshop on CCDs and Advanced Image Sensors, Crystal Bay, Nevada, June 2001.
- [116] D. Lim, *et al* "Automated detection of all kinds of violations at a street intersection using real time individual vehicle tracking," Image Analysis and Interpretation, 2002. Proceedings. Fifth IEEE Southwest Symposium, vol., no., pp.126, 129, 2002.
- [117] B. Cyganek, "Introduction" in Object Detection and Recognition in Digital Images, N.J: John Wiley & Sons Ltd, 2013, ch. 1, sec. 1, pp. 54.
- [118] R. Gonzalez, R. Woods, "Light and the Electromagnetic Spectrum" in Digital Image Processing, 3rd ed., N.J: Pearson Education Inc., 2008, ch.2, sec 2. pp. 41-42.
- [119] K. Hunt, "Digital Images" in The Art of Image Processing with Java, MA: A K Peters Ltd, Natick, 2010, ch. 3, sec. 2, pp. 32.
- [120] O. Marques, "Image Histogram," in Practical image and video processing using MATLAB, Hoboken, N.J: John Wiley & Sons Ltd, 2010, ch. 9, sec. 2, pp. 171.
- [121] N. Otsu, "A Threshold Selection Method from Gray-Level Histograms," IEEE Sys Man Cybern, vol.9, no.1, pp.62-66, Jan. 1979.
- [122] M. Petrou, C. Petrou, "Binary Conversion," in Image Processing: The Fundamentals. 2nd ed., Chichester, U.K: Wiley, 2010, ch. 4, sec. 5, pp. 140.
- [123] O. Marques, "Edge Detection," in Practical image and video processing using MATLAB, Hoboken, N.J: John Wiley & Sons Ltd, 2010, ch. 14 sec. 2, pp. 336.
- [124] J. Prewitt, "Object enhancement and extraction," Picture Processing and Psychopictorics, B. Lipkin and A. Rosenfeld, Eds., New York: Academic Press, 1970, pp. 75-149.

- [125] O. Marques, "Median and other Nonlinear Filters," in Practical image and video processing using MATLAB, Hoboken, N.J: John Wiley & Sons Ltd, 2010, ch. 10, sec. 3, pp. 217.
- [126] M. Nixen, A. Aguado, "Low level feature extraction," in Feature Extraction and Image Processing, Oxford, UK: Elsevier Ltd, 2008, ch. 4, sec. 2, pp. 123.
- [127] F. Shih, "Binary Morphology," in Image Processing and Mathematical Morphology: Fundamentals and Applications, Boca Raton, FL: CRS Press, 2009, ch. Sec. 2, pp. 15-19.
- [128] O. Marques, "Erosion," in Practical image and video processing using MATLAB, Hoboken, N.J: John Wiley & Sons Ltd, 2010, ch. 13, sec. 3, pp. 307.
- [129] R. C. Gonzalez, R. E. Woods, "Morphological Image Processing" in Digital Image Processing. 3rd ed., N.J: Pearson Education Inc., 2008, ch.9, sec 3. pp. 635-639.
- [130] M. Petrou, C. Petrou, "Image Segmentation and Edge Detection," in Image Processing: The Fundamentals. 2nd ed., Chichester, U.K: Wiley, 2010, ch. 3, sec. 2, pp. 37.
- [131] L. Kirkup, "Dealing with uncertainties", in Experimental Methods, Milton, Australia: John Wiley and Sons Ltd, 1994, ch. 4, sec. 3, pp. 58.
- [132] O. Marques, "Morphological Image Processing," in Practical image and video processing using MATLAB, Hoboken, N.J: John Wiley & Sons Ltd, 2010, ch. 13, sec. 2, pp. 301.
- [133] M. Petrou, C. Petrou, "Image Segmentation and Edge Detection," in Image Processing: The Fundamentals. 2nd ed., Chichester, U.K: Wiley, 2010, ch. 6, sec. 1, pp. 542-544.
- [134] S. Ghosh, et al, "Wear Characterization by Fractal Mathematics for Quality Improvement of Machine," in J. Qual. Maint. Eng., vol. 11(4), pp. 318–332, 2005.
- [135] J. Carsetensen, M. Dali, "Particle size distribution in mesh cuts and microscopically estimated volumetric shape factors," Drug Dev Ind Pharm, vol. 25, no. 3, pp. 347-352, Mar. 1999.
- [136] C. Smith, "The Basics of Infrared Interpretation," in Infrared Spectral Interpretation: A Systematic Approach, Boca Raton: FL: CRC Press LLC, ch. 1, pp. 5, 1999.
- [137] B. Stuart, "Experimental Methods" in Infrared Spectroscopy: Fundamentals and Applications, Chichester, UK: John Wiley & Sons Ltd, ch. 2, pp 30, 2004.

- [138] T. Ooi, K. Maruoka, "Carbonyl Recognition", in *Modern Carbonyl Chemistry*, Germany: Wiley-VCH, Weinheim, 2000, ch. 2, sec. 2, pp. 37.
- [139] J. Coleman, "The development of the semiconductor after the first demonstration in 1962," in *Semiconductor Science and Technology*, vol. 27, pp. 90207-90217, 2012.
- [140] M. Parker, et al, "Practical Online Condition Monitoring of Gearbox Oil Using Non-Dispersive Infra-Red Sensors" Renewable Power Generation Conference, Naples, Italy, 2014.
- [141] H. Bach, and N. Neuroth, "The properties of optical glass". 2nd corr. print. ed. Schott series on glass and glass ceramics. 1998, Berlin ; New York: Springer. xvii, 414 p.
- [142] Pike, E., Abbiss, J., "New Opto-Electronic Technologies for Photon Correlation Experiments" in *Light Scattering and Photon Correlation Spectroscopy*, Poland: NATO ASI Series, Krakow, 1995, ch. 4, sec. 3, pp. 265.
- [143] A. Maini, "Optoelectronic Devices and Circuits," in *Laser and Optoelectronics: Fundamentals, Devices and Applications*, Chichester, UK: John Wiley & Sons Ltd. ch. 10, sec. 6, pp. 333.
- [144] TinyCAD, TinyCAD Open Source Software. [Online]. Available at <http://sourceforge.net/apps/mediawiki/tinycad/index.php?title=TinyCAD> [Accessed: 12 May 2013].
- [145] Determination of particle size distribution – Single particle light interaction methods – Part 3: Light extinction liquid-borne particle counter, BS ISO 21501-3:2007.
- [146] F. Scholar, *et al.*, "Person tracking in three-dimensional laser range data with explicit occlusion adaption," *Proc. IEEE International Conference on Robotics and Automation*, 2011, Shanghai, pp.1297-1303.
- [147] M. El-Desouki, *et al.*, "CMOS Image Sensors for High Speed Applications," in *Sensors*, vol. 9(1), pp. 430-444, 2009.
- [148] A. Krymski, *et al.*, "A High-Speed, 240-Frames/s, 4.1-Mpixel CMOS Sensor", in *IEEE Trans. Electron Devices*, vol. 50, pp.130, 2003.
- [149] P. Worsfold, "Photoacoustic Spectroscopy", in *Encyclopaedia of Analytical Science* 2nd ed, 2005, ch. 7, sec. 3 pp. 174-180.
- [150] N. Foster, *et al.*, "Detection of Trace Levels of Water in Oil by Photoacoustic Spectroscopy", in *Sensors and Actuators*, vol. 77, pp. 620-624, 2001.
- [151] MICEPAS: Miniaturised Cell Enhanced Photoacoustic Spectroscopy, 2009, [Online], Available: <http://www.micepas.basnet.by/> on August 10th 2010.

- [152] S. Firebaugh, *et al*, “Miniaturization and Integration of Photoacoustic Detection with a Microfabricated Chemical Reactor System”, *Journal of Microelectromechanical Systems*, vol. 10(2), pp. 232-237, 2001.
- [153] F. Sotelo, *et al*, “Application of Fluorescence Spectroscopy for Spectral Discrimination of Crude Oil Samples”, in *Brazilian Journal of Petroleum and Gas*, vol. 2(2), pp. 63-71, 2008.
- [154] T. Liang, “Portable Fluorescence Sensor for On-line Monitoring of Lubricant Oils”, in *Sensors the Proceedings of IEEE*, vol. 1(24-27), pp. 8-11, 2004.
- [155] D. Patra, “Total Synchronous Fluorescence Scan Spectra of Petroleum Products”, in *Analytical and Bioanalytical Chemistry*, vol. 373, pp. 304-309, 2002.
- [156] B. Patel, “Graphite Rod Atomization and Atomic Fluorescence for Simultaneous Determination of Silver and Copper in Jet-engine Oils”, in *Analytical Chemical Acta*, vol. 64, pp. 135–138, 2004.
- [157] G. Mignani, “Optical Fiber Spectroscopy for Measuring Quality Indicators of Lubricant Oils”, in *Measurement Science and Technology*, vol. 20, pp. 7-13, 2009.
- [158] Goldstein, J., Newbury, D., Joy, D., Lyman, C., Echlin, P., Lifshin, E., Sawyer, L., Michael, J., 2003, *Scanning Electron Microscopy and X-ray Microanalysis* (3rd Edition), Plenum Publishing Corporation, New York.
- [159] Scanning Electron Microscope, Purdue University, Department of Radiological and Environmental Management, accessed from <http://www.purdue.edu/rem/rs/sem.htm>, on 2nd August 2010.
- [160] B. Wiesent, *et al*, “Suitability of tunable Fabry-Perot spectrometers for condition monitoring purposes of gear oils in offshore wind turbines”, in *Proc. IRS2 SENSOR+TEST Conferences*, 2011.
- [161] C. Lord, “Determination of Trace Metals in Crude Oil by Inductively Coupled Plasma Mass Spectrometry with Micro-emulsion Sample Introduction”, in *Analytical Chemistry*, vol. 63, pp. 1594–1599, 1991.
- [162] M. Escobar, *et al*, “Determination of Metallo-organic Species in Lubricating Oil by Electrothermal Vaporization Inductively Coupled Plasma Mass Spectrometry”, in *Analytica Chimica Acta*, vol. 320, pp. 11–17, 1996.
- [163] R. Aucelio, *et al*, “The Determination of Trace Metals in Lubricating oils by Atomic Spectrometry”, *Spectrochimica Acta Part B*, vol. 62(9), pp. 952-961, 2007.
- [164] I. Goncalves, *et al*, “Determination of Metals in Used Lubricating Oils by AAS using Emulsified Samples”, in *Talanta*, vol. 47, pp. 1033–1042, 1998.

- [165] R. Brown, "Determination of Trace Metals in Petroleum and Petroleum Products Using an Inductively Coupled Plasma Optical Emission Spectrometer", *Spectrochimica Acta Part B*, vol. 38(1-2), pp. 283–289, 1983.
- [166] E. Jansen, "Rapid and Accurate Element Determination in Lubricating Oils Using Inductively Coupled Plasma Optical Emission Spectrometry", in *Journal of Analytical Atomic Spectroscopy*, vol. 7(2), pp. 127–130, 1992.
- [167] P. Yaroshchuk, *et al*, "Quantitative Determination of Wear Metals in Engine Oils Using LIBS: The Use of Paper Substrates and a Comparison Between Single- and Double-pulse LIBS", in *Spectrochimica Acta Part B*, vol. 60, pp. 1482–1485, 2005.

Appendix A: Applicable Lubrication Analysis Techniques

A review of other applicable lubrication analysis techniques was conducted to assess if other technologies may be adapted for wind turbine gearbox condition monitoring. The following technologies were considered but were not selected for further development due to the measurement method, expense or complexity of adaptation.

A.1 Photoacoustic Spectroscopy

Photoacoustic spectroscopy (PAS) is a photothermal technique in which a sample is hit with light. When the light hits, it is absorbed into the sample as heat, changing the thermal structure. The change can be observed by measuring temperature or density of the sample. Eventually the sample will return to its original energy state due to environmental heat transfer with the surrounding environment. The process of hitting the sample with light can be modulated, so that there is a constant cycle of energy absorption and emission. This cycle of modulated light can be increased so that the sample does not have time to expand and contract to the modulated light source, resulting in a change in pressure which causes an acoustic wave that can be detected with hyper sensitive microphones or piezoelectric devices. Figure A.1.1 shows the layout of a PAS sensor.

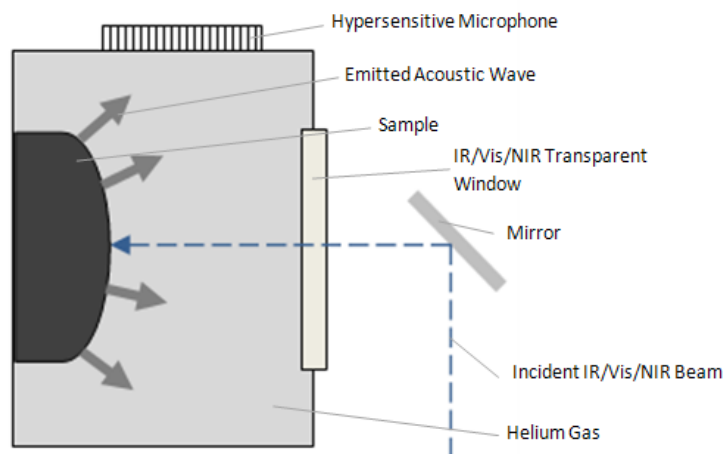


Figure A.1.1. Diagram of classic PAS sensor equipment.

The method for detecting which chemicals are present is similar to IR spectroscopy. In standard PAS, the modulated light source is usually a high powered xenon or halogen lamp which is passed through a monochromator to allow selection of the

desired wavelength of light [149]. If the sample absorbs a particular wavelength, the molecules will become excited and then relax, generating heat. This occurs for every cycle of modulated light that hits, resulting in a series of thermal waves that travel through the sample until reaching the surface. At this point the heat is transferred to the contacting gas (usually helium) as an acoustic wave which then travels to the microphone. Individual chemicals and elements are identified by the amplification of this sound. Compounds that have a higher absorption coefficient will generate a wave with greater amplification. To fully analyse a sample, a range of monochromatic wavelengths can be used. Since PAS analyses the thermal waves that generate acoustic waves, it is unaffected by surface scattering effects unlike other types spectroscopy. This allows the analysis of lubricants which have suspended solid particles.

PAS has the ability to detect trace levels of water within a sample (≤ 50 ppm) in lubricants which is very desirable in the context of gearboxes [150]. However, these detection levels have so far been only achieved as an offline experimental system.

There is potential to develop PAS into an inline/online sensor for gearbox condition monitoring. There is currently significant research into miniaturising the technology, with sensors cells ranging in size from 5mm^2 to 500mm^2 that can be integrated as part of a remote system [151]. Currently, the accuracy of miniaturised devices for detecting the desired oil parameters has not been established. However, the accuracy of miniaturised PAS sensors has been tested in other fields such as chemical reactors. Several PAS sensors measuring 14.4cm^2 have demonstrated considerable accuracy in detecting shifts between levels of gas such as CO_2 and propane [152]. As PAS analyses thermal waves that propagate through the sample and manifest themselves as acoustic waves, smaller samples actually increase the detection capabilities, meaning that it is very suitable for micro sensors.

A.2 Fluorescence Spectroscopy

Fluorescence spectroscopy uses light to excite electrons that then emit electromagnetic radiation which is detected by a spectrometer. The wavelength emitted and its intensity is characteristic of the molecules present and their amount in the sample. A single wavelength of light is selected to excite the sample by using a source that emits

only one wavelength such a laser or using a halogen lamp can be combined with a monochromator. The light hits the sample, causing an increase in the energy of the molecule which results in a vibrational mode. The molecule then drops back down to its ground state, releasing photons of a particular wavelength in the process. The wavelength emitted is dependent on several factors such as the molecule structure, its vibrational modes and the surrounding molecules.

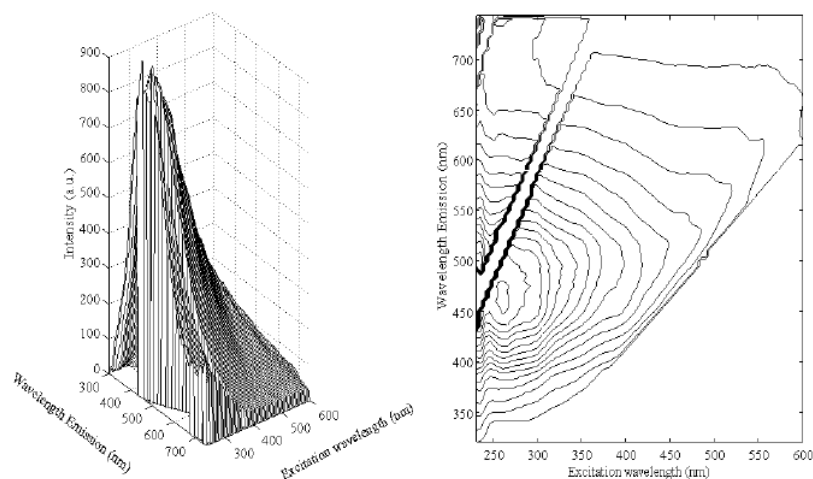


Figure A.1.1. Total Fluorescence spectra of a crude oil sample [153].

There are three methods of analysing the sample. The first is to use Total Fluorescence Spectroscopy (TFS), where the sample is hit with one wavelength of electromagnetic radiation and all emitted wavelengths are measured. This process is repeated for different excitation wavelengths until a full profile is created. The data is presented as a 3D plot of excitation wavelength against emission wavelength with fluorescence intensity as the z-axis or as a 2D contour plot, as shown in Figure A.2.1. The main disadvantage is that Raman and Rayleigh scattering of the excitation light can cause false signals [153]. The excitation light wavelength is basically reflected and then detected by the spectrometer, giving an inaccurate emission spectrum. It is necessary to remove these as shown in 2D contour diagram in Figure A.2.1.

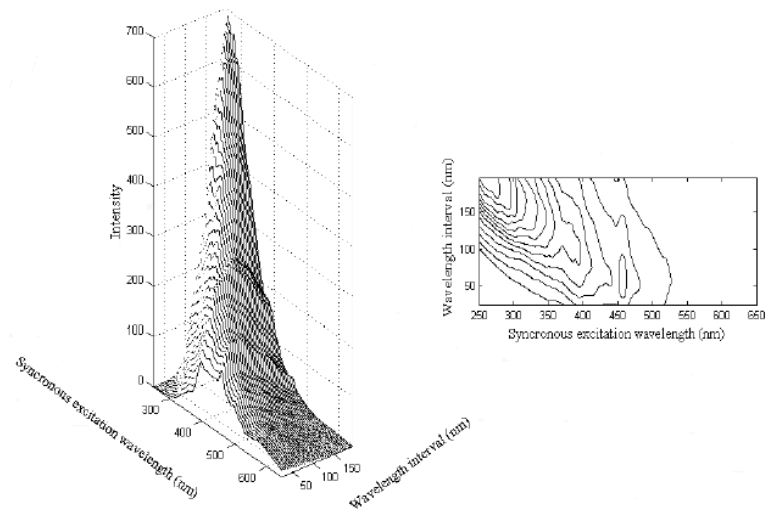


Figure A.2.2. Synchronous Fluorescence spectra of a crude oil sample [153].

The second method is Synchronous Fluorescence Spectroscopy (SFS). This combines two different methods of fluorescence spectroscopy into one analysis. The first is to use an emission spectrum where the sample is analysed by using a beam of monochromatic light and measuring the resulting emitted wavelengths. The second is to use an excitation spectrum where the sample is analysed by hitting the sample with different wavelengths of light and measuring the emission of a single wavelength of light. SFS combines these by setting an initial emission wavelength (λ_{exc}) to bombard the sample and an initial excitation wavelength (λ_{em}), with $\Delta\lambda$ being the difference between λ_{exc} and λ_{em} . $\Delta\lambda$ is varied after each bombardment and a similar 3D plot to TFS can be created. The main advantage of SFS is clearer spectra when compared to TFS due to the reduced effect of Raman and Rayleigh scattering. Figure A.2.2 shows the spectra obtained from SFS.

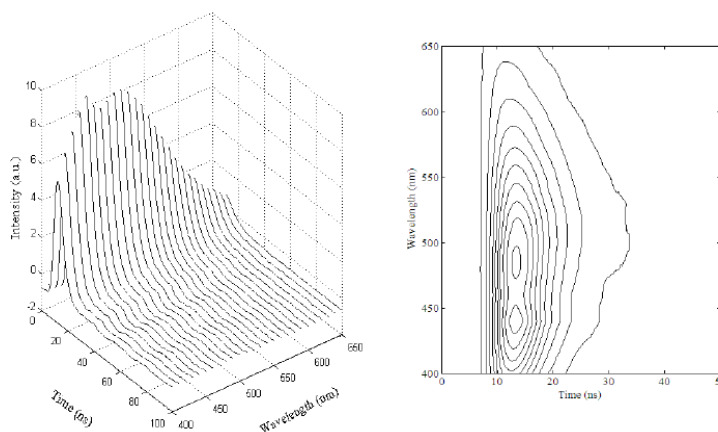


Figure A.2.3. Time Resolved Fluorescence spectra of a crude oil sample [153].

The third method is Time Resolved Fluorescence Spectroscopy (TRFS) which measures the time a molecule remains excited for once it has absorbed a particular wavelength of light. A pulsed light source is used to excite the sample which will then emit different wavelengths of light at different times depending on the molecular structure. The data can be presented in a similar manner to TFS and SFS as shown in Figure A.2. A.2.3.

There is potential to develop fluorescence spectroscopy as a sensor system. Experiments have already been conducted demonstrating its ability to analyse lubricants from lubricant sumps [154]. The system used UV light with 404 nm wavelength which was produced using a GaN laser diode and transmitted using optical fibre. Lubrication degradation was not classified by individual parameters, but an overall change in the condition over time. Similar studies have shown its use for identifying various different products of petrochemicals with similar composition to synthetic lubricants [155]. Fluorescence spectroscopy has also been used extensively to identify iron, molybdenum, and copper wear particles in jet engine oils [156].

It is likely that fluorescence spectroscopy would not be used as an individual system but would be combined with other types of spectroscopy such as absorption as described by Mignani [157].

A.3 Karl Fischer Water Test

The Karl Fischer water test analyses the volume of water in a sample by quantifying the oxidation of sulphur dioxide (SO_2) by iodine (I_2) in the presence of water. There are two methods of achieving this reaction: volumetric or coulometric titration.

The coulometric titration cell consists of two parts, a main and an anode compartment as shown in Figure A.3.1. The reason for the separation is to prevent the reaction from reversing and giving an inaccurate result. In the main, the sample which is to be analysed is mixed with an alcohol, a base, SO_2 and I_2 which is known as the anode solution and also contains the electrical cathode. The alcohol used is generally methanol or diethylene glycol monoethyl ether while the base may be imidazole or primary amines.

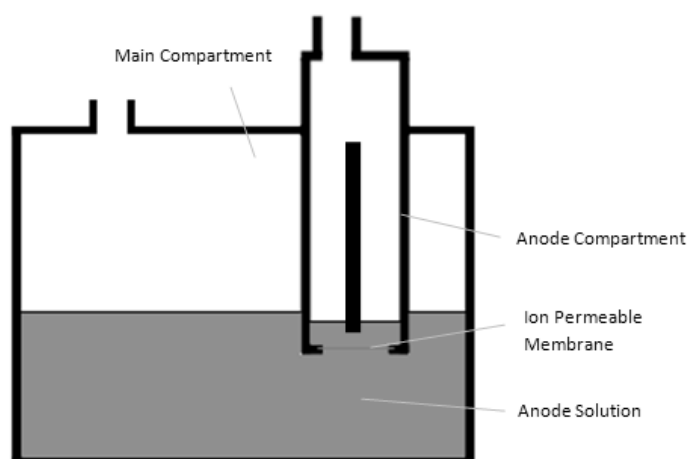


Figure A.3.1. Coulometric titration diagram.

The anode compartment contains the electrical anode which is submersed in the solution but is separated from the main compartment by an ion-permeable membrane. In the reaction, water and iodine are consumed in a 1:1 ratio, which means when excess iodine starts to appear, all the water in the sample has reacted. The excess iodine is detected using a second pair of indicator electrodes maintain a constant current. When the reaction has finished, the excess iodine causes a sharp decrease in voltage across the electrodes. The amount of water that is in the sample is determined by measuring the charge required in order to fully complete the reaction: $1 \text{ mg H}_2\text{O} = 10.72 \text{ C}$. This

method of titration can detect water as low as 1 ppm which is suitable for gearbox condition monitoring.

The method of volumetric titration operates in the same manner as coulometric but instead the iodine is added into the solution until no more reacts with water. This point is established using a double platinum pin indicator electrode. A microprocessor is used to determine the volume of water in the sample from the amount of iodine that consumed in the solution. This method of titration however, is not suitable for <100 ppm, which would make it unsuitable for the low level water detection in gearboxes.

There is low potential to develop a Karl Fischer coulometric titration module as an online or inline sensor system. Water detection is highly accurate, but other systems would be needed to identify other parameters. Also the system needs a supply of iodine, alcohol and reagent base which would have to be incorporated. When the supplies run out, the system would have to be replenished which would be undesirable in the context of offshore wind farms.

A.4 Viscometers

A number of viscometers are currently used for offline measurement with some developments of online/inline capabilities.

A.4.1 Capillary Tube Viscometers

Capillary tubes are the most common method of offline viscosity measurement. A lubricant sample is contained in a U-shaped capillary tube and is then moved by suction so that the volume on either side of the bend is uneven. Figure A.4.1 shows the layout of a classic capillary tube viscometer. The suction is then released, allowing the oil to flow back to the equilibrium position and the time taken is measured. The flow rate is proportional to the kinematic viscosity of the oil sample, with less viscous oils flowing faster than more viscous.

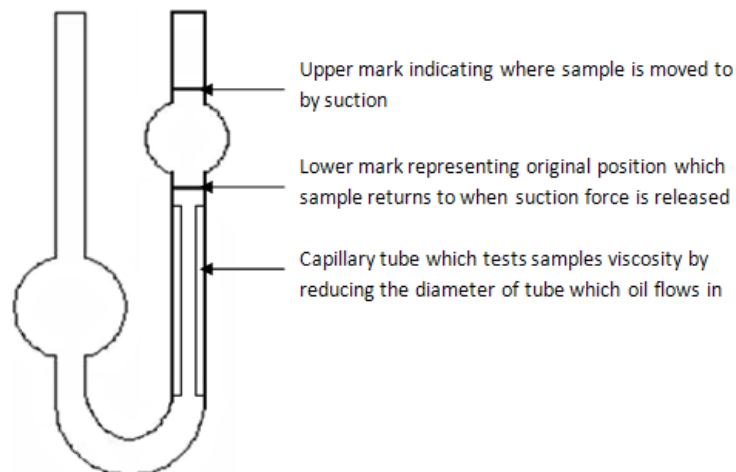


Figure A.4.1. Diagram of capillary tube viscometer.

A capillary tube viscometer is highly effective at establishing viscosity. The equipment required is not costly, but relies on constant gravity to establish accurate viscosity measurements.

A.4.2 Rotary Viscometers

In rotary viscometers, a lubricant sample is placed in a glass tube which is encased in a chamber with a constant temperature. A metal spindle runs through the lubricant and can only rotate at a constant rpm so in order to turn the spindle, sufficient torque must

be applied. If a lubricant sample has high viscosity, it will require a larger amount of torque to turn the spindle.

There is low potential to develop the rotary viscometer into a remote sensor. Despite simple technology, the additional costs to have a separate system that requires moving parts, a relatively large lubricant sample and accurate calibration that may be affected by vibration makes it unsuitable for deployment in a wind turbine.

A.4.3 Solid State Viscometers

Solid state viscometers measure the acoustic viscosity of a given sample using the properties of shear wave propagation. A shear wave is a type of energy transfer through a material, where the direction of wave propagation is perpendicular to the direction of motion. These waves can move through most materials but changes occur when the wave transfers between materials. At the transition point, the amount of energy that is lost from the wave is directly proportional to the frequency of the wave, the density of the new material and the absolute viscosity of the new material.

If an acoustic wave resonator is placed in contact with a lubricant and a low frequency shear wave is transmitted through it, a layer of the lubricant will hydrodynamically couple to the surface of the resonator. Since the frequency and amplitude of the wave is fixed (frequency is set by the design of the sensor and the amplitude is set by the power of the electrical signal sent), the layer thickness and energy dampening (power loss) will be determined by the viscosity and density. If the original power in the wave is known and the power that is left once the wave enters the lubricant, the difference can be found and subsequently, the viscosity. In order to make this comparison, the wave in the lubricant must be measured.

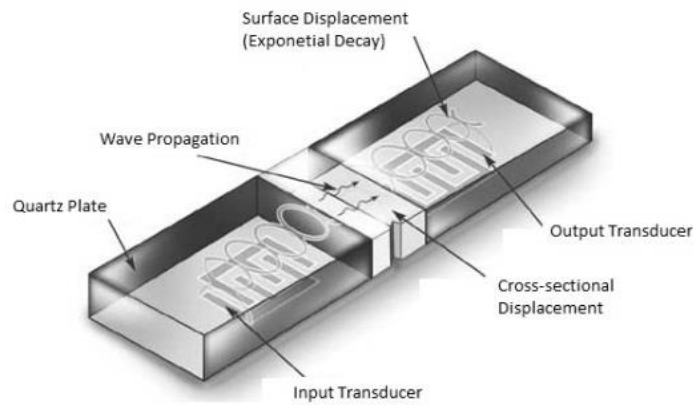


Figure A.4.2. Layout of acoustic wave resonator sensor.

To achieve this, a set of electrodes are sealed from the oil, but are situated below the lubricant sample (see Figure A.4.2). When the wave passes through, the power will be attenuated and the new wave value is measured by the electrodes. The value of acoustic viscosity can be determined from this and then converted to a more useful term such as absolute viscosity using a previously determined relationship for the particular lubricant. The lubricant is not adversely affected by the process as the area which forms the hydrodynamic coupling in the micron scale. As mentioned previously, it is essential to report the temperature of the oil sample before an assessment of the viscosity can be made.

There is high potential to develop a solid state viscometer as an online or inline system. Since it is not standard practice to state the acoustic viscosity of a sample, a conversion must be made to either kinematic or absolute viscosity. In addition, the sizes of these sensors are small, measuring approximately 12 to 24 cm³ which would be ideal for integration into a wind turbine gearbox. The accuracy of solid state viscometers in analysing lubricants for gearboxes would have to be investigated further to ensure additives, vibrations in the nacelle and temperature variations do not have adverse effects on measurements.

A.5 Scanning Electron Microscope

A scanning electron microscope (SEM) analyses materials by hitting the sample with a beam of high energy electrons. This causes various different types of signals: back scattered electrons (BSEs), secondary electrons, x-rays, light and transmitted electrons. These signals can be interpreted in different manners to allow information about the chemical composition and shape of the sample to be determined. The types of signals that are produced can be divided into those that give information about the material composition and those which can be used to create an image of the material surface. The sample itself must be electrically conductive as this will prevent electrons from building up at the surface and disrupting scattering [158]. Standard SEM requires the sample to be contained within a vacuum as any presence of gaseous substances can disrupt the beam of electrons as shown in Figure A.5.1. This poses problems for samples that contain water and some oils as these would need to be dried. Environmental SEM (ESEM) allows samples to be prepared in a gaseous environment (i.e. not a vacuum), enabling samples to contain water and oil. The types of liquids that are allowed vary with the pressure inside the sampling region. Many modern ESEM allow variable pressure so that fluid samples may be analysed. The disadvantage with this system is that more complex algorithms are required to compensate for the presence of gas, leading to longer analysis.

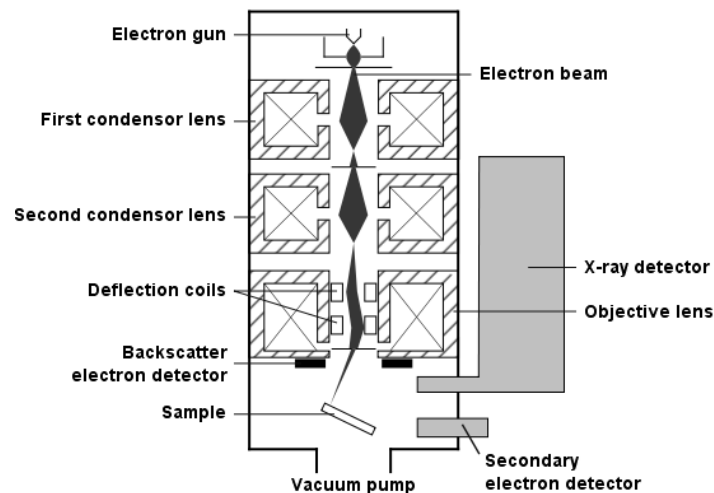


Figure A.5.1. SEM operation with EDS detector [159].

For surface imaging, secondary electrons are analysed. These are the original electrons which are present in the sample before the beam of high energy electrons hits. Due to the presence of extra higher energy electrons, the original electrons are displaced and will be emitted in a pattern related to the surface of the sample. An Everhart-Thornley detector is used to identify these secondary electrons which give signals that can be interpreted by software. The SEM scans in a raster pattern at high speed, allowing a highly detailed image to be created. The resolution and magnification of these images varies greatly between each type of machine but generally ranges from 10nm to 100nm with 10 to 500,000x magnification. To put in context, if a square wear particle in the order of 20x20 μm (microns) is magnified 10,000x by SEM, an image 20x20 CMS with a resolution of 15nm could be displayed on screen. This could allow analysis of the type of wear occurring, for example shear or abrasion. Small personal SEM's (PSEM's) that are of similar size to laser printers can have the capability of 10 to 24,000x magnification with resolution of 30 nm. In terms of imaging, SEM is unparalleled for accuracy even when compared to laser imaging.

For composition analysis, there are two signals which can be used: BSE's and x-rays. BSE's are electrons from the beam which are deflected. The intensity at which this deflection occurs is proportional to the atomic number of the specimen. If the sample has a high atomic number (i.e. a large number of protons), the electrons will encounter a strong resistance to their negative charge which results in a strong repelling force. The BSE's are detected with sensors similar to the Everhart-Thornley device but positioned above the sample in concentric rings to ensure maximum capture. Since the intensity of the BSE's depends on the atomic number, the image produced will also indicate the material that is being analysed. In order to identify the sample's composition, image analysis software is now required. Generally a grey scale image will be produced which darker greys indicating higher atomic numbers.

X-rays that are emitted from the sample after being hit by the high energy electrons can also be analysed. Each material and element has its own unique characteristic x-ray which can be used to identify the sample in a process known as Energy Dispersive X-Ray Spectroscopy (EDS). When compared with BSE analysis EDS provides the most accurate results due to the uniqueness of the x-ray signature whilst taking slightly

longer. However, EDS has to be considered a separate system from SEM as it can actually be applied on its own. All it requires to carry out spectroscopic analysis are characteristic x-rays which are conveniently produced as a result of SEM bombardment. Many materials laboratories will only use EDS if the actual image is unimportant, using an x-ray exciter to produce the required signals.

The price of a new SEM varies between manufacturers and specifications. However, recently there have been developments in PSEM devices for small scale laboratories and industrial use. These devices do not include EDS and are generally used for their imaging capabilities, with some including BSE detectors for material analysis.

There is low potential to develop SEM as an online or inline gearbox lubricant sensor. It is clear that a system that can identify materials and elements with such accuracy and the ability to create images for wear and damage analysis would be a great asset to CM. However, the cost of the equipment and the problems in integrating SEM as a functional sensor are too great to justify it as a candidate.

A.6 Atomic Spectroscopy

A variety of atomic spectroscopic methods exist for use in lubricant analysis [160]. Several of these techniques are currently used to identify metals in lubricant oil in laboratory tests. However, samples often require preparation to be compatible with the instrumentation; complex hydrocarbons with relatively high viscosities generally cannot be analysed directly. Methods include dissolving lubricants in acid to mineralise the lubricant matrix and allow metals to form aqueous solutions. This allows far easier calibration for the particular spectroscopic method. However, it is clear that these complex preparations will be unsuitable for a robust online system which will have to operate continuously for periods in the order of years.

A.6.1 Inductively Coupled Plasma Mass Spectroscopy (ICP MS)

ICP MS converts a sample into ionic plasma by extreme heating. In this state, ions can be displaced by a magnetic field due to the overall positive charge. Since ions with larger atomic numbers will have a greater positive charge, the value of displacement will be characteristic of the atom [161]. By using mass spectrometry to distinguish different elements, it is possible to identify the composition of material wear [162]. However, ICP MS is unsuitable for development as an online/inline sensor. It requires expensive and large equipment such as the mass spectrometer and requires sample preparation so would be unfeasible as a solution [163].

A.6.2 Flame Atomic Absorption Spectroscopy (FAAS)

FAAS uses a flame to atomise an oil sample which is then scanned with different wavelengths of light. The values of absorbed wavelength correspond to particular elements similar to other absorption spectroscopic methods. Generally samples must be converted into an emulsion to reduce the organic elements of the sample (hydrocarbons) [164], although direct introduction into the flame atomiser is possible [163]. The main problem with FAAS is the process of atomising and destroying the sample. Lubricant supplies are limited in wind turbine so destructive sampling methods are not recommended.

A.6.3 Optical Emission Spectroscopy (OES)

OES relies on the excitation of the sample by flame, inductively coupled plasma or by arc discharge to emit characteristic wavelengths of light. Inductively coupled plasma optical emission spectroscopy (ICP OES) is the most widely used method due to its reliability and accuracy. The sample generally requires dilution in an organic solvent before it can be converted into a plasma [165]. An online system using ICP OES has been demonstrated with detection limits of 10 μm [166]. However, the system still requires sample dilution and large expensive equipment.

A.6.4 Laser-Induced Breakdown Spectroscopy (LIBS)

LIBS is a branch of atomic emission spectroscopy that uses a high powered laser to cause emissions of light. When the laser beam contacts the sample, a small amount of the material at the surface detaches and becomes plasma with an incredibly high temperature. The high thermal energy causes the material to break down into individual elements and ions. When the sample cools, it emits characteristic wavelengths which can be detected by a spectrometer. Nd:YAG lasers with a wavelength of 1064 nm are generally used to create the plasma [167]. LIBS identifies particles in the same manner as other emission spectroscopic technologies. The main difference is the formation of the plasma layer. By creating this, the state of the material does not matter (solid liquid, gas) as all can be converted to plasma. There is low potential to develop LIBS as an online solution due to the cost.

A.7 Summary of Technologies Reviews

Technology	Principle	Key Parameters	Accuracy	Online/Inline Capability	Advantages	Disadvantages
Karl Fischer Water Test	Chemical reaction with iodine determines water concentration	- Water	Water: very high (1 ppm)	Poor – requires chemicals and sensitive apparatus unsuitable for wind turbine nacelle	- High accuracy - Cheap	- Poor sensor development - Identification of single parameter. - Slow analysis
Calcium Hydride Water Test	Chemical reaction with calcium hydride determines water concentration	- Water	Water: high (50 ppm)	Poor – requires chemicals and sensitive apparatus	- High accuracy - Cheap	- Poor sensor development, - Identification of single parameter. - Slow analysis
Infrared Spectroscopy	Infrared radiation is absorbed by sample, absorbed wavelengths representative of key parameters	- Water - Oxidation - Acid Content	Water: medium (100 - 500 ppm) Oxidation: very high (deterministic peak) Acid Content: very high (deterministic peak)	Good – already proven as online sensor and handheld portable sensor	- Multiple parameters measured - High accuracy - Fast analysis	- Expensive (several thousands) - Poor water analysis
Photoacoustic Spectroscopy	Conversion of thermal waves to acoustic waves that are characteristic of sample parameters	- Water - Possible Acid Content - Possible Oxidation	Water: high (<50 ppm)	Good – sampling method still to be determined	- High accuracy - Fast analysis - Extremely small	- Unknown cost of implementation - Unclear accuracy in determination of other parameters
Capillary Tube Viscometer	Time taken for liquid to re-establish volumetric equilibrium correlates to viscosity	- Viscosity	Viscosity: high (used as industrial standard measurement)	Poor – requires delicate apparatus unsuitable for use in wind turbine nacelle	- High accuracy - Cheap	- Poor sensor development - Identification of single parameter.
Rotary Viscometer	Shear forces acting on a moving spindle increase as viscosity increases	- Viscosity	Viscosity: high (used as industrial standard measurement)	Moderate – simple technology but effects of adverse forces in wind turbine nacelle require investigation	- High accuracy - Cheap	- Identification of single parameter. - Delicate measurement
Solid State Viscometer	Acoustic shear wave transmitted between a resonator and liquid loses power proportional to viscosity of liquid	- Oxidation	Viscosity: high (however uses acoustic viscosity that must be correlated to kinematic or dynamic viscosity)	Good – unobtrusive inline measurement possible	- High accuracy - Simple, small design	- Currently expensive - Vibrations in wind turbine may reduce accuracy
Fluorescence Spectroscopy	Radiation is used to excite sample which re-emits light characteristic of sample composition	- Water - Oxidation - Acid Content	Overall change in fluorescent spectrum is observed over time period	Moderate – complicated online sampling method but new systems under development	- Reasonable accuracy - Multiple parameters measured - Cheap	- Potentially expensive - Fluorescence spectrum difficult to analyse quickly - Poor accuracy
Electrical Conductance	Changes to electrical conductance indicative parameter changes	- Water - Oxidation - Acid Content	Overall change in conductance indicates changes, poor as distinguishing between each is not possible	Good – unobtrusive inline measurement possible	- Cheap - Proven technology	- Poor accuracy

Table A.8.1. Summary table of oil quality analysis technologies

Technology	Principle	Key Parameters	Accuracy	Online/Inline Capability	Advantages	Disadvantages
Scanning Electron Microscope	Beam of electrons hits sample, two effects are measured to create images of sample and identify composition	- Source - Composition - Type of wear - Number	All very high	Poor – equipment is large, sample requires preparation	- Very high accuracy - Identifies all particle parameters	- Extremely expensive - Poor sensor development
Ferrography	Particles removed from oil sample through magnets, images of particles are taken to identify size and shape	- Ferrous particles only - Type of wear - Number	High	Moderate – sensor has been developed as online sensor, but requires technician to analyse images	- High accuracy - Relatively simple technology	- Identifying other particles relies on high concentrations of ferrous particle - Required image processing software
Atomic Spectroscopy	Several methods consisting of dissolving samples in acid matrices before combusting to identify metals	- Source - Composition - Type of wear - Number	All very high	Very poor – nearly all methods require complicated sample preparation	- Very high accuracy - Identifies all particle parameters	- Unsuitable for sensor development
Particle Counters	Particles passing a light source block light from falling on detector, voltage drop indicates size and quantity	- Number - Indication of size and type of wear	High	Good – unobtrusive inline sampling method	- High accuracy - Already used in industry	Only quantity can be identified to any great accuracy
Radioactive Tagging	Certain components are lightly irradiated, when particles are liberated, emitted radiation can be detected and used to identify wear	- Source - Number	Medium	Good – sensor unobtrusive inline sampling method	- Accurate - Component specific	- Added complications of lightly irradiated components - Safety issue
Electromagnetic Detection	Various electromagnetic properties change when metallic particle pass through sensors	- Number - Indication of composition	High	Good – unobtrusive inline sampling method	- Medium accuracy - Cheap	- Identification of single parameter

Table A.8.2. Summary table of particulate analysis technologies

Appendix B: MATLAB Code for Wear Sensor

B.1 Main MATLAB Program Image Capture Routine

```
clear all;
close all;

imaqreset;
cam = videoinput('winvideo', 1, 'YUY2_640x480');

TP = datenum(clock + [0,0,0,0,0,15]);
FC = 0; %frame count for export
TM1 = 0;
TM2 = 0;
TM3 = 0;
TM4 = 0;
TM5 = 0;
PNT = 0;

filename = 'D:\Main Root\PhD Root\MATLAB\Data - Testing\2D
(10.06.13)\2D Test (22.05.13).xlsx';

while datenum(clock)<TP

    FC = FC+1;

    imagefile = ['D:\Main Root\PhD Root\MATLAB\Data - Testing\2D
(10.06.13)\Frame ' num2str(FC) '.tif'];

    data = getsnapshot(cam_set);
    level = graythresh(data);
    bw = im2bw(data, level);
    bw = bwareaopen(bw, 5);
    se = strel('disk',5);
    bw = imclose(bw,se);
    bw = ~bw;
    ci = bwconncomp(bw);
    L = labelmatrix(ci);

    [L,M1,M2,M3,M4,M5,WS,OI,PN,bw,data]=SUB_Particle_Number_Parameters
(cam_set,FC,imagefile);
    [TM1,TM2,TM3,TM4,TM5,PNT]=SUB_Cumulative_Matrix(M1,M2,M3,M4,M5,PN,
TM1,TM2,TM3,TM4,TM5,PNT);
    SUB_Plot_Data(L,data,bw);

end
SUB_Export_Data(TM1,TM2,TM3,TM4,TM5,filename);
display('Export Complete');
```

Figure B.1.1. Main MATLAB code with image capture routine.

B.2 Initial Image Processing Subroutine and Object Detection

```
function
[L,M1,M2,M3,M4,M5,WS,OI,PN,bw,data]=SUB_Initial_Proc_Object_Detection (cam_set,FC,imagefile)

data = getsnapshot(cam_set);
level = graythresh(data);
bw = im2bw(data, level);
bw = bwareaclose(bw, 5);
se = strel('disk',5);
bw = imopen(bw,se);
bw = ~bw;
ci = bwconncomp(bw);
L = labelmatrix(ci);

F2 = figure('visible','off');
subplot(1,3,1);
imshow(data);
subplot(1,3,2);
imshow(label2rgb(L));
subplot(1,3,3);
imshow(bw);
saveas(F2,imagefile);

end
```

Figure B.2.1. Initial image processing and object detection MATLAB code.

B.3 Object Analysis Subroutine

Calculation of Pixel to Area Ratio

Average Values of 2000 Graded Particle Images			
(px/ μm^2)	(px/ μm^2)	(px/ μm^2)	Ratio (px/ μm^2)
125-150	14972	57	263
475-500	186778	723	257
		Average Ratio:	260
Error			
Actual Ratio (px/ μm^2)	Measured Ratio (px/ μm^2)	Error (%)	
226	260	14.956	

MATLAB Script for Object Analysis Subroutine

```
function
[L,M1,M2,M3,M4,M5,WS,OI,PN,bw,data]=SUB_Object_Analysis(cam_set,FC,
imagefile)

OI = bw;
WS = regionprops(L,'all');
PN = size(WS,1);

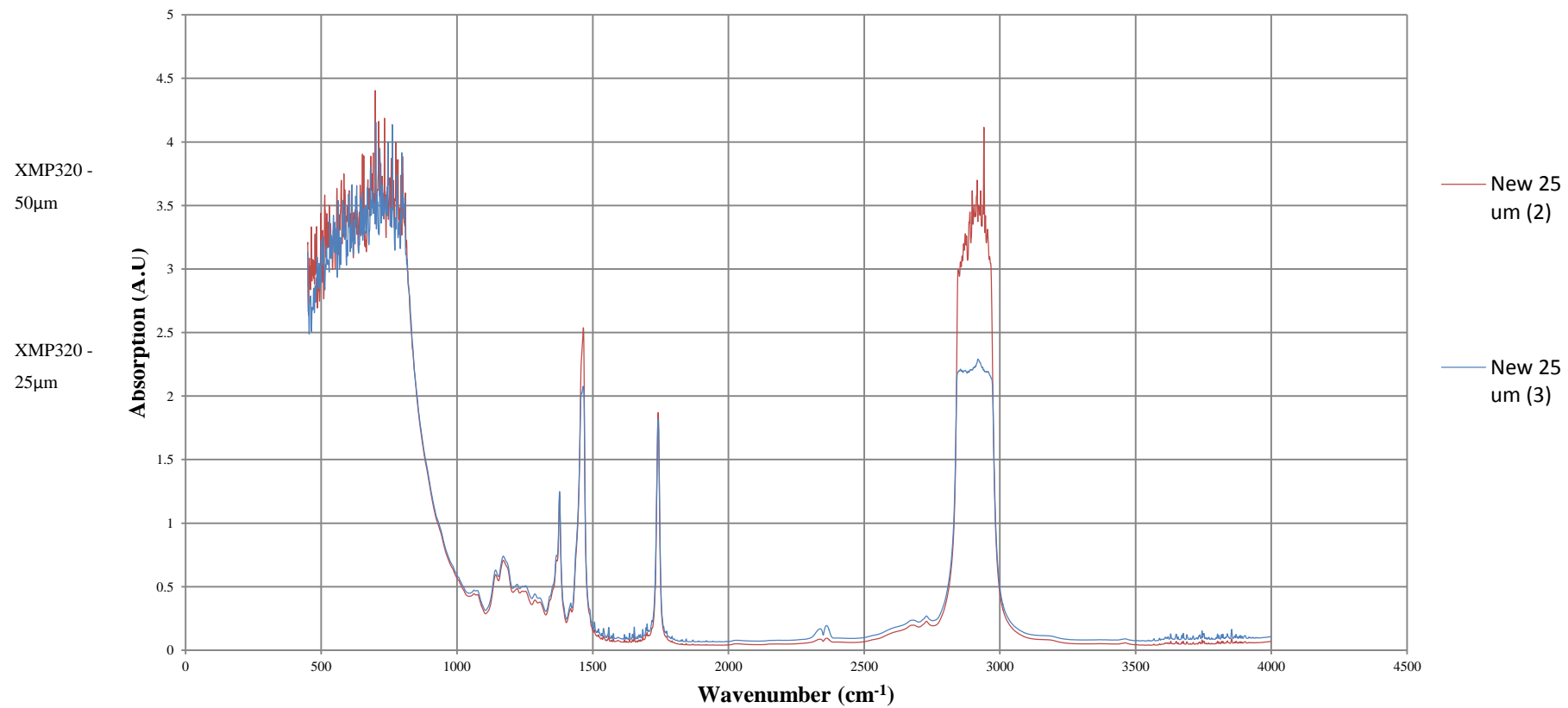
STATS1 = regionprops(L,'area'); %area
CELL1 = struct2cell(STATS1);
M1 = cell2mat(CELL1);
M1 = M1';
STATS2 = regionprops(L,'eccentricity'); %eccentricity
CELL2 = struct2cell(STATS2);
M2 = cell2mat(CELL2);
M2 = M2';
STATS3 = regionprops(L,'majoraxislength'); %major axis length
CELL3 = struct2cell(STATS3);
M3 = cell2mat(CELL3);
M3 = M3';
STATS4 = regionprops(L,'minoraxislength'); %minor axis length
CELL4 = struct2cell(STATS4);
M4 = cell2mat(CELL4);
M4 = M4';
SM = size(M4,1); %use to get 'm' value of matrix dimensions
M5 = repmat(FC,SM,1);

end
```

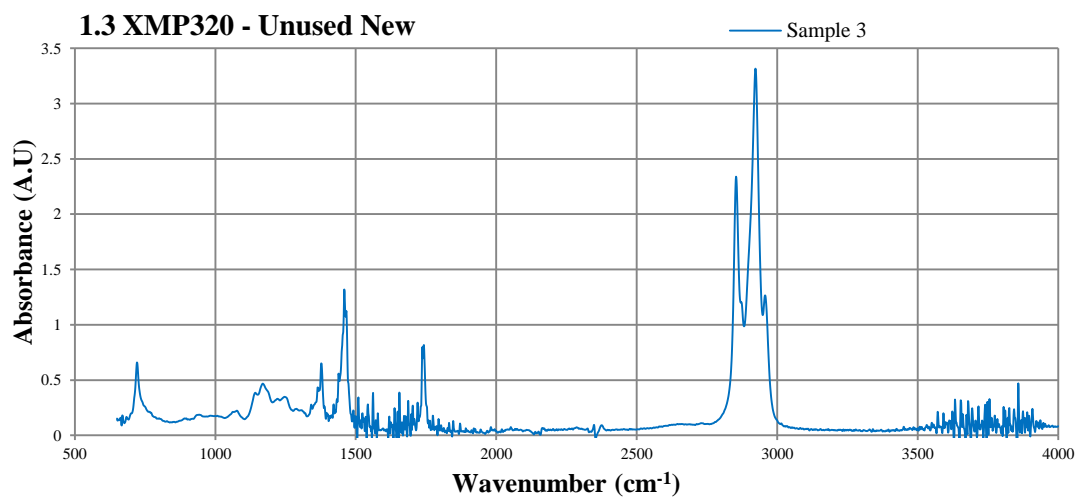
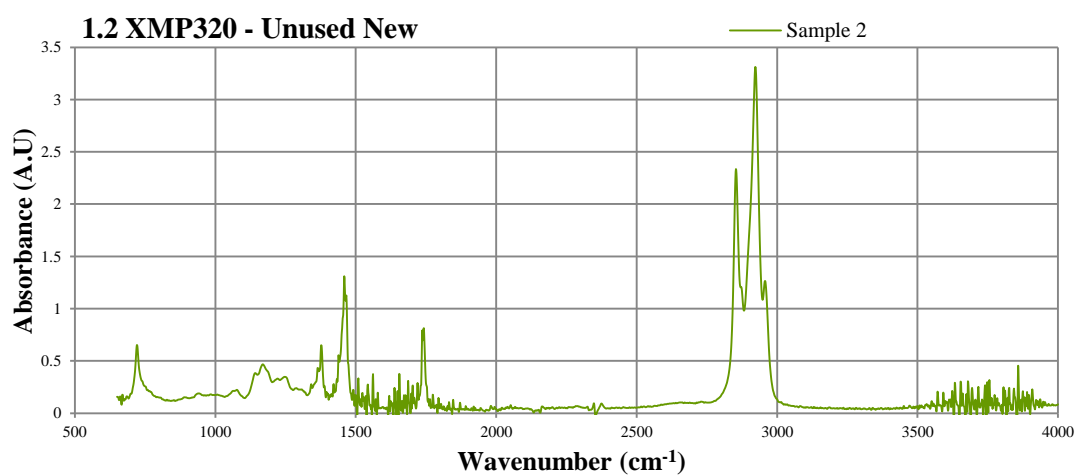
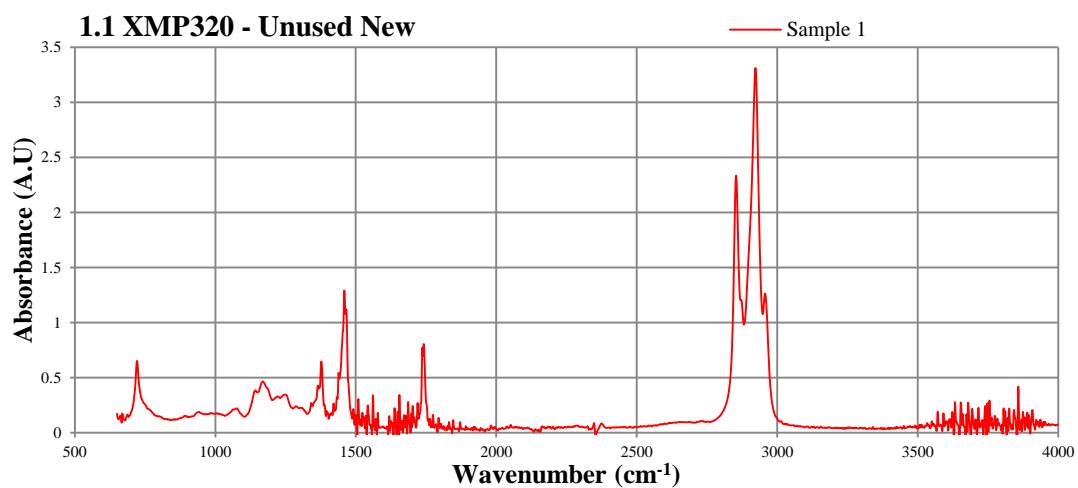
Figure B.3.1. MATLAB code developed for object analysis.

Appendix C: IR Absorbance Spectra and Additional Information

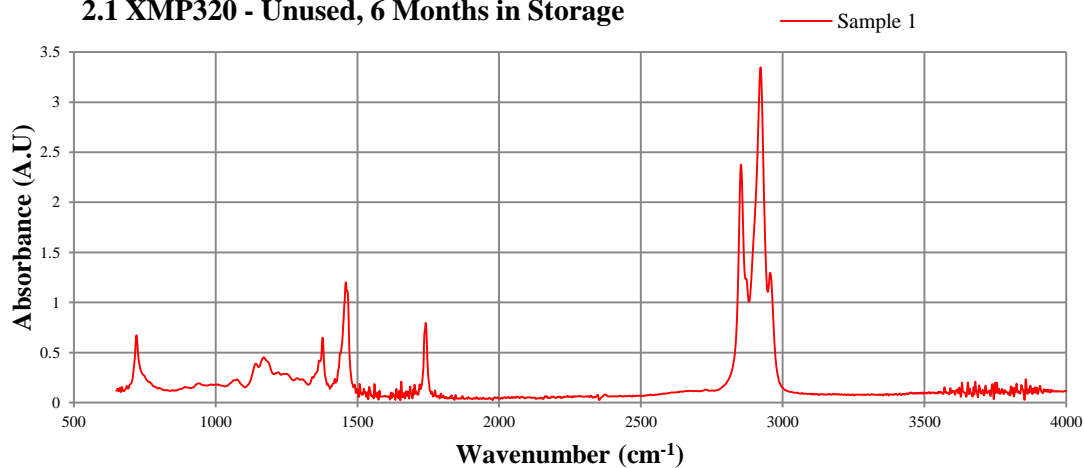
C.1 Enlarged IR Spectra of XMP



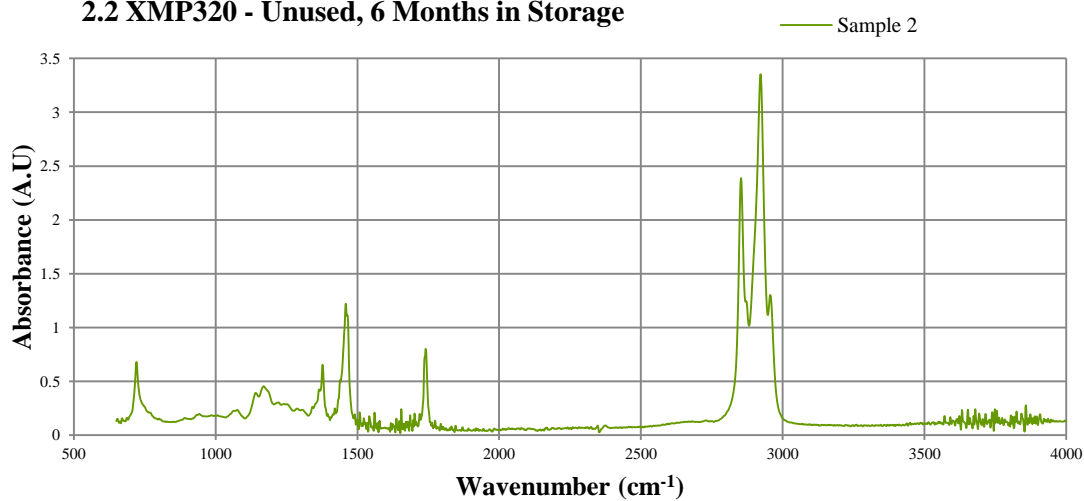
C.2 XMP320 Individual Spectra



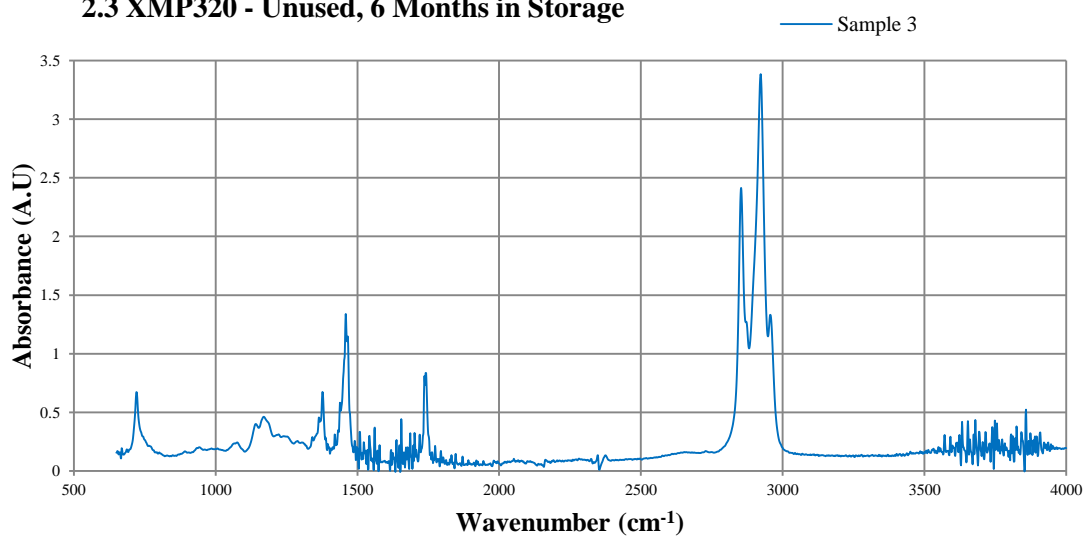
2.1 XMP320 - Unused, 6 Months in Storage



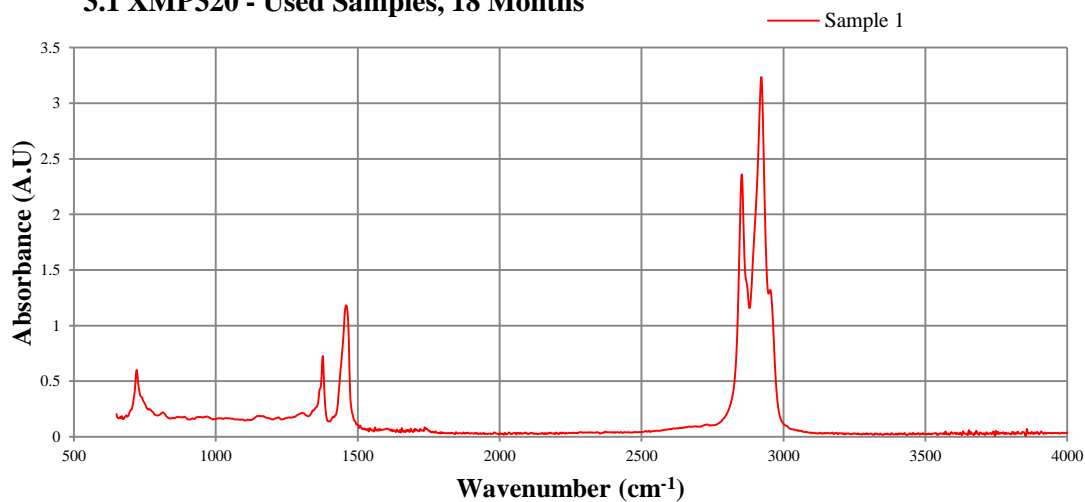
2.2 XMP320 - Unused, 6 Months in Storage



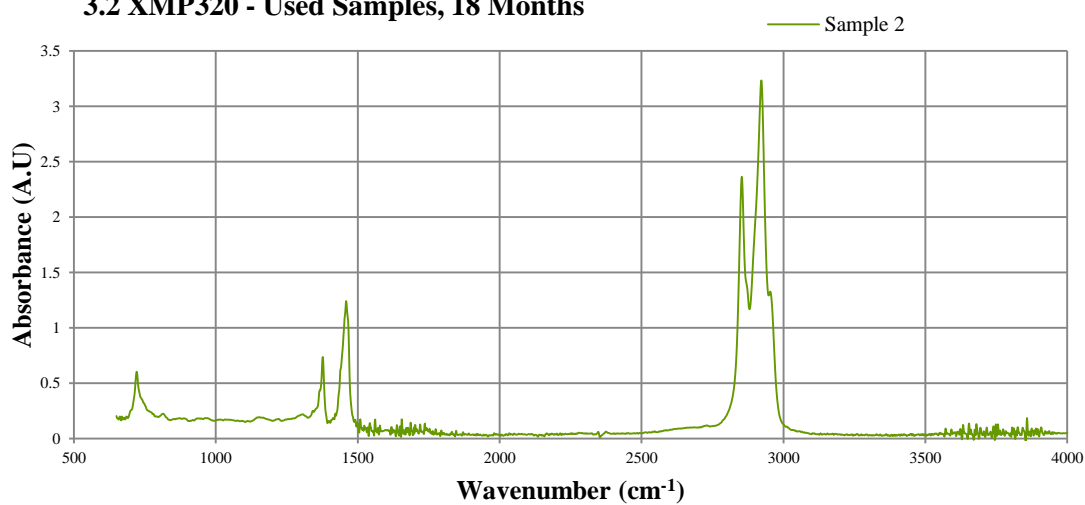
2.3 XMP320 - Unused, 6 Months in Storage



3.1 XMP320 - Used Samples, 18 Months



3.2 XMP320 - Used Samples, 18 Months



3.3 XMP320 - Used Samples, 18 Months

